Faculty of Science and Engineering

Department of Physics and Astronomy

Synthesis and Characterisation of Nanostructured TiO_2 for Photocatalytic Applications

Hani Manssor Mohammed Albetran

This thesis is presented for the Degree of

Doctor of Philosophy

Of

Curtin University

March 2016

Declaration

To the best of my knowledge and belief this thesis contains no material previously published by any other person except where due acknowledgment has been made.

This thesis contains no material which has been accepted for the award of any other degree or diploma in any university.

ALBETRAN, HANI MANSSOR M

Signature:

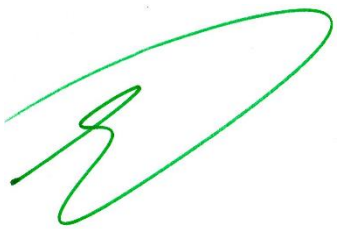

Date: 18th March 2016

Abstract

This thesis focused on both synthesis and characterisation of nanostructured TiO_2 mainly for photocatalytic application, as well as other applications in general. TiO_2 nanofibres, nanopowders, and nanotubes were synthesised using the electrospinning, sol-gel, and anodisation methods, respectively.

The electrospun TiO_2 nanofibre, sol-gel TiO_2 nanopowders, and anodised TiO_2 nanotubes were synthesised and characterised with different analytical techniques, including scanning electron microscopy (SEM), energy dispersive X-ray spectroscopy (EDS), transmission electron microscopy (TEM), X-ray diffraction (XRD), *in-situ* high temperature synchrotron radiation diffraction (SRD), differential thermal analysis (DTA), thermogravimetric analysis (TGA), differential scanning calorimetry (DSC), X-ray photoelectron spectroscopy (XPS), and UV/ Visible spectrophotometer.

This thesis is prepared following the style of a series of published papers, and provides a comprehensive introduction as well as overview to link the published papers together so that a coherent story was told. It is hoped that this thesis would provide valuable resources for researchers, postgraduate students in the fields of physics, chemistry, and engineering.

This study considers seven published journal papers which are related to the main themes of interests. Brief summaries of these papers are given below:

The first paper examined how phase transformations in electrospun TiO_2 nanofibres are affected by both atmospheric air and argon environments. The study, based on high temperature SRD results, shows that although initially the as-synthesized TiO_2 nanofibres were amorphous, they crystallized to form anatase and rutile when thermal annealing air or argon environment. There was a delay of anatase's crystallization temperature by 100 °C in argon as compared to in air enviroment. In argon environment, the anatase-to-rutile transformation was faster than in air environment due to formation of oxygen vacancies.

The second paper, which is basically a sequel to the first one, discussed relative phase concentrations from the measurements of SRD. In this paper, the transformation of absolute phase levels of titania (amorphous, anatase and rutile forms) contained in

electrospun amorphous titania nanofibres was reported based on the change in temperature over the range 25–900 °C according to the controlled environments for calcination as the material is heated non-isothermally. For extracting the absolute levels of amorphous titania and crystalline anatase and rutile from the SRD data, a new method was developed. In both air and argon environments, the estimation of the activation energies for amorphous-to-anatase, and anatase-to-rutile transformations was facilitated by the determination of absolute phase levels. The variation in activation energies for heating in air and argon can be attributed to the occurrence of a substantial amount of oxygen vacancies, the number of which is higher in argon than in air, during the annealing of material in argon. From the SRD data, the estimates of the site occupancies of anatase and rutile oxygen suggest that (i) there is discernible oxygen vacancies for anatase in argon in correspondence with the stoichiometry TiO_{2-x} with $x < 0.4$; (ii) the stoichiometry of anatase in air at these temperatures is TiO_2; and (iii) no significant oxygen vacancies for rutile exist in either argon or air environments.

In the third paper, the focus was on how V-ion implantation influences the thermal response of electrospun amorphous TiO_2 nanofibres, particularly with regard to structural phase transformation behaviour, applying *in-situ* SRD measurements ranging from the room temperature to 1000 °C. The SRD data enabled the determination of activation energies for both amorphous-to-anatase and anatase-to-rutile transformations. It also provides assessments of the V-ion implantation's influence on the development of microstructure during of calcinations. Both crystallite size and microstrain were estimated. The V-ion implantation resulted in a lowering of the temperature for forming anatase and rutile, the temperature having been initially observed at 500 °C. In the process, the anatase-to-rutile transformation was accelerated compared to the non-implanted sample. The V ion implantation's effect was observed through the substantial reduction of activation energies.

The fourth paper, using ultraviolet-visible absorption spectrometry at room temperature, identified the relationship between the nature of air-argon atmosphere in which the material has been heated non-isothermally to 900 °C and the band gaps in electrospun titania nanofibres at ambient temperature. From the results of different air-argon mixtures' heating suggest that the UV-region band gap contained in unheated as-spun amorphous nanofibres, 3.33 eV, could be transferred into the visible region

through calcinations under different air-argon mixtures. The heating of material in an air-argon mixture reduced the band gap of 3.09 eV found for heating in air, while the band gap in pure argon remained at 2.18 eV. The cumulative lowering of the band gap depended on crystallinity development in the fibres. This is because the material was heated and the related oxygen vacancies were developed during the heating in argon, and as a result, the defect states formation stays below the conduction band.

The aim of paper five was to optimise the smallest fibre diameter with a minimum electrospun TiO_2/PVP nanofibre variation. It showed the preparation of TiO_2 nanofibres within polyvinylpyrrolidone (PVP) polymer, by utilising a combination of both sol-gel and electrospinning techniques. It evaluates the effects of sol-gel and electrospinning on the TiO_2/PVP nanofibres' diameter, particularly titanium isopropoxide (TiP) concentration, flow rate, needle tip-to-collector distance, applied voltage, and needle size. The evaluation was done through applying the Taguchi design of experiment (DoE) method. It was demonstrated from the DoE experiments of nanofibre diameters, that the most significant factor for optimum combination was TiP concentration. Through conducting a confirmation experiment where it used two different needles to study the effect of needle size, the optimum combination was further validated. According to the optimum condition, as Taguchi DoE method estimated, both needle sizes resulted in the same average nanofibre diameters.

Paper six and seven studied the synthesis of titania nanotube arrays which were electrochemically produced by the anodization of titanium foils, followed by implantation them with chromium (Cr) and indium (In) ions. The effect of ions implantation on the crystallization titania phase transformation was investigated using *in-situ* high-temperature X-ray diffraction (XRD) and SRD from room temperature to 1000 °C. Diffraction results show that crystalline anatase first appeared at 400 °C for non-implanted and In-implanted materials, but at 300 °C for Cr-implanted TiO_2 nanotubes. The crystallisation temperature for rutile increased from 600 °C for non-implanted materials to 700 °C for In-implanted materials, whereas it decreased to 500 °C for Cr-implanted materials. The anatase-to-rutile transformation was inhibited by the In-ions and Cr-ions implantation. Although In^{3+} and Cr^{3+} are expected to increase oxygen vacancy concentration and then the rate of titania transformation, the observations are consistent with implanted In-ions and Cr-ions occupying the Ti

sublattice substitutionally and thus inhibiting the transformation. The relatively difficult anatase-to-rutile transformation in the implanted material appears to result from the relatively large In^{3+} radius (0.080 nm) and Cr^{3+} radius (0.0615 nm), which partly replaces the Ti^{4+} (0.061 nm), thus providing greater structural rigidity and allows for no relaxation in the Ti bonding environment.

Acknowledgments

This thesis would have not been possible without the guidance and help of several individuals who in one way or another have contributed and extended their valuable assistance and time in the preparation and completion of this research.

I heartily owe my deepest gratitude to Professor It-Meng (Jim) Low, who has provided me exceptionally supervision with considerable patience and proper guidance, and helped in advancing my understanding and skills throughout this research work. His encouragement, support and advice have been a great source of motivation enabling me to face any challenging situations. I must say that I would not be able to complete the thesis without the friendly cooperation that he has extended towards me all the time.

I also wish to express my sincere gratitude to Emeritus Professor Brian O'Connor for his resourceful guidance, encouragement, experimental directions, critical discussions, patience and sincere support throughout the course of my PhD study. His continuous mentoring has been the most critical for the completion of the thesis and the advancement of my research career.

I also gratefully acknowledge highly useful suggestions from my associate supervisor Dr. Yu (Roger) Dong. I would like to express my deepest gratitude to him for his timely guidance, support and help.

I am indebted to Dr. Brendan McGann as the Chairperson of Thesis Committee and Postgraduate Coordinator of the Department of Physics and Astronomy. I would like to take the opportunity to thank him for the extraordinary periods of time that he made available to support and guide me, and to organise regular meetings to help me resolve any issues raised during my postgraduate studies.

Special thanks to Ms. E. Miller of John de Laeter Centre, Curtin University for her kind assistance with SEM work. I would like to acknowledge Dr. C. Kealley, Dr. A. Halfpenny, Ms. V. Avery, and Ms. K. Merigot of John de Laeter Centre, Curtin University, and Ms. K. Haynes, Mr. A. Vireck and Mr. J. Xiao Hua from the Departments of Chemical Engineering, Curtin University for their laboratory assistance.

I would like to thank Dr. Justin Kimpton of the Australian Synchrotron for advice on instrumentation at the Powder Diffraction Beamline, Prof. Victor Prida from Department of physics, University of Oviedo for specialist technical service advice and samples for anodization experiments, and Dr. Mihail Ionescu from Institute for Environmental Research, Australian Nuclear Science and Technology Organisation (ANSTO) for helpful assistance with ion implantation and SRIM simulation of RBS data.

I wish to express my deepest thanks to all my colleagues, in particular, Ahmed Hakamy, Hasan Assaedi, and Thamer Alomayri for their friendship and emotional support.

Finally and most importantly, I would like to express my ultimate gratitude and thanks to my family who supported me with everything they had to help me achieve this degree, my first teacher, my mother, Rabab Aldarwish, my wife, Anhar Almohanna, my son, Mohammed, my daughters, Zahra and Sukaina, six brothers, and six sisters; only to them I attribute my success in life. Moreover, my kindest regards and special thanks would go to one person whom I did not see during my PhD study: my late father Manssor Mohammed Albetran.

ALBETRAN, HANI MANSSOR M

March 2016

List of Publications Included as Part of the Thesis

ALBETRAN, H., HAROOSH, H., DONG, Y., PRIDA, V. M., O'Connor, B. H., & LOW, I. M. 2014. Phase Transformations and Crystallization Kinetics in Electrospun TiO_2 Nanofibers in Air and Argon Atmospheres. *Applied Physics A*, 116, 161–169.

ALBETRAN, H., O'Connor, B. H., & LOW, I. M. 2016. Activation Energies for Phase Transformations in Electrospun Titania Nanofibers: Comparing the Influence of Argon and Air Atmospheres. *Applied Physics A*, 122, 1–9.

ALBETRAN, H., O'Connor, B. H., PRIDA, V. M., & LOW, I. M. 2015. Effect of Vanadium Ion Implantation on the Crystallization Kinetics and Phase Transformation of Electrospun TiO_2 Nanofibers. *Applied Physics A*, 120, 623–634.

ALBETRAN, H., O'Connor, B. H., & LOW, I. M. 2016. Effect of Calcination on Band Gaps for Electrospun Titania Nanofibers Heated in Air–Argon Mixtures. *Materials & Design*, 92, 480–485.

ALBETRAN, H., DONG, Y. & LOW, I. M. 2015. Characterization and Optimization of Electrospun TiO_2/PVP Nanofibers Using Taguchi Design of Experiment Method. *Journal of Asian Ceramic Societies*, 3, 292–300.

LOW, I. M., **ALBETRAN, H.,** PRIDA, V. M., VEGA, V., MANURUNG, P., & IONESCU, M. 2013. A Comparative Study on Crystallization Behavior, Phase Stability, and Binding Energy in Pure and Cr-Doped TiO_2 Nanotubes. *Journal of Materials Research*, 28, 304–312.

ALBETRAN, H., & LOW, I. M. 2016. Effect of Indium Ion Implantation on Crystallization Kinetics and Phase Transformation of Anodized Titania Nanotubes. *Journal of Materials Research*, 31. 1588–1595.

Statement of Contribution of Others

ALBETRAN, HANI MANSSOR M's input into this project and the associated papers included the execution of all the experimental work and a major contribution to the intellectual input involved in the project. As is almost always the case in the physical sciences, other scientists made contributions to the work that were significant enough to warrant co-authorship on the resulting journal articles. These are specified below:

I. M. Low, who provided project supervision and manuscript editing.

B. H. O'Connor, who provided specialist technical advice, project associate supervision and manuscript editing.

Y. Dong, who provided specialist technical support for instrument usage (electrospinning machine at Curtin University).

H. Haroosh, who provided specialist technical support for instrument usage (electrospinng machine at Curtin University).

V. M. Prida, who provided specialist technical support for instrument usage (XPS laboratory at University of Oviedo).

M. Ionescu, who provided specialist technical service, advice on instrument usage (Ion implantation at ANSTO).

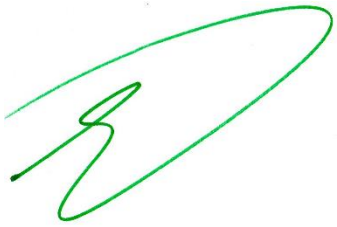

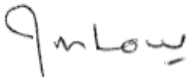

ALBETRAN, HANI MANSSOR M

Prof. It-Meng (Jim) Low

List of papers and presentations by the Candidate Relevant to the Thesis but not Forming Part of it

Conference papers (See Appendix IV)

ALBETRAN, H., ALSAFWAN, A., HAROOSH, H., DONG, Y., & LOW, I. M. 2013. X-ray Diffraction Study on the *In-Situ* Crystallisation Kinetics in Electrospun PVP/TiO_2 Nanofibers. Nanostructured Materials and Nanotechnology VII: Ceramic Engineering and Science Proceedings. *The American Ceramic Society*, 34, 35–49.

ALBETRAN, H., HAROOSH, H., DONG, Y., O'Connor, B. H., & LOW, I. M. 2014. Effect of Atmosphere on Crystallization Kinetics and Phase Relations in Electrospun TiO_2 Nanofibers. *Ceramics for Environmental and Energy Applications II: Ceramic Transactions*, 246, 125–133.

LOW, I. M., **ALBETRAN, H.,** PRIDA, V., MANURUNG, P., & IONESCU, M. 2013. Effect of Chromium Doping on the Crystallization and Phase Stability in Anodized TiO_2 Nanotubes. Developments in Strategic Materials and Computational Design III: *The American Ceramic Society*. 151–158.

Journal paper

AZMAN, N. Z. N., SIDDIQUI, S. A., HAROOSH, H. J., **ALBETRAN, H.,** JOHANNESSEN, B., DONG, Y., & LOW, I. M. 2013. Characteristics of X-ray Attenuation in Electrospun Bismuth Oxide/Poly-Lactic Acid Nanofiber Mats. Journal of Synchrotron Radiation, 20, 741–748.

Journal papers in preparation

ALBETRAN, H., O'Connor, B. H., & LOW, I. M. Effect of pressure on TiO_2 crystallization kinetics using *in-situ* sealed capillary high temperature synchrotron

radiation diffraction. This manuscript is in the advanced stage of preparation. It will be submitted to *Ceramics International*.

ALBETRAN, H., & LOW, I. M. Effect of Aluminum ion implantation on the crystallization kinetics and phase transformation of electrospun TiO_2 nanofibers. This manuscript is in the advanced stage of preparation. It will be submitted to *Journal of Alloys and Compounds.*

ALBETRAN, H., O'Connor, B. H., & LOW, I. M. *In-situ* high temperature synchrotron radiation diffraction study of the crystallization kinetics of In-doped and In-Cr co-doped TiO_2 nanopowders. This manuscript is in the advanced stage of preparation. It will be submitted to *Journal of Alloys and Compounds*.

Oral presentations

ALBETRAN, H., HAROOSH, H. J., DONG, Y., & LOW, I. M. 2013. Effect of Doping on In-Situ Crystallization and Crystal Growth in Electrospun TiO_2 Nanofibres. Paper ID# ICACC-S7-014-2013, The 7th International Symposium on Nanostructured Materials and Nanocomposites at The 37th International Conference and Expo on Advanced Ceramics and Composites (ICACC'13), January 27– February 1, 2013. Daytona Beach, Florida, (USA).

ALBETRAN, H., O'CONNOR B. H., & I. M. LOW. 2015. Band-gap engineering of electrospun TiO_2 nanofibers for visible light photocatalysis. Paper ID# H2-001, International Conference on High-Performance Ceramics (CICC-9), Guilin, China, November 4 – 7, 2015.

ALBETRAN, H., & I. M. LOW. 2015. Effect of indium ion implantation on crystallization kinetics and phase transformation of anodized titania nanotubes. Paper ID# H2-101, International Conference on High-Performance Ceramics (CICC-9), Guilin, China, November 4 – 7, 2015.

ALBETRAN, H., B. H. O'CONNOR, Y. DONG, & I. M. LOW. 2015. Effect of ion implantation and atmospheres on the crystallization kinetics, phase transformation,

and band gap of electrospun titania nanofibers using In-situ high-temperature synchrotron radiation diffraction. Awarded ***second prize*** at the Australian X-ray Analytical Association (AXAA), Western Australian Student Seminars, held at CSIRO laboratories in Waterford, Perth, 10 December, 2015.

Poster presentations

ALBETRAN, H., B. H. O'CONNOR & I. M. LOW. 2015. Effect of atmosphere on the band gap of electrospun titania nanofibers. Paper ID# H2-102, International Conference on High-Performance Ceramics (CICC-9), Guilin, China, 4 – 7 November, 2015.

ALBETRAN, H., O'CONNOR B. H., & I. M. LOW. 2015. Activation energies for phase transformations electrospun titania nanofibers: comparing the influence of argon and air atmospheres. Paper ID# 40, Asia Oceania Forum for Synchrotron Radiation Research (AOFSRR), Australian Synchrotron, Melbourne, Australia, 25 – 27 November, 2015.

Table of Contents

List of Abbreviations

ANSTO	Australian Nuclear Science and Technology Organization
CB	Conduction Band
CIF	Crystallographic Information File
CNT	Carbon Nanotubes
DSC	Differential Scanning Calorimetry
e^-	Electron
EDS	Energy Dispersion Spectrometry
FIBSEM	Focused Ion Beam Scanning Electron Microscopy
FWHM	Full Width at Half Maximum
GOF	Goodness of Fit
h^+	Hole
HR-TEM	High-Resolution Transmission Electron Microscopy
ICDD-PDF	International Centre for Diffraction Data-Powder Diffraction File
ICSD	Inorganic Crystal Structure Database
MB	Methylene Blue (Dye)
MO	Methyl Orange (Dye)
ND	Neutron Diffraction
P-25	P-25 Nanoparticulate TiO_2 (Degussa)
PECs	Photoelectrochemical cells
PVP	Poly-Vinyl Pyrrolidone
R_B	Derived Bragg, R-factors
RBS	Rutherford Backscattering Spectroscopy
R_{exp}	Expected R-factor
rmsε	Root-Mean-Square Strain
R_p	Profile R-factor
R_{wp}	Weighted Pattern R-factor
SEM	Scanning Electron Microscopy
SRD	Synchrotron Radiation Diffraction
SRIM	Stopping and Range of Ions in Matter

TEM	Transmission Electron Microscopy
TGA	Thermogravimetric Analysis
TiO_2	Titanium oxide (titania)
TIP	Titanium Isopropoxide
TNF	TiO_2 Nanofibres
TNN	TiO_2 Nanoneedles
TNP	TiO_2 Nanoparticles
TNR	TiO_2 Nanorods
TNT	TiO_2 Nanotubes
TNW	TiO_2 Nanowires
TOPAS	Total Pattern Analysis Solutions
UV/Vis	Ultraviolet-Visible (spectroscopy)
VB	Valence Band
XPS	X-ray Photoelectron Spectroscopy
XRD	X-ray Diffraction
χ^2	Chi-square = GOF
Ω	Ohm
0-D	Zero-Dimensional
1-D	One-Dimensional
2-D	Two-Dimensional
3-D	Three-Dimensional

List of Figures

List of Tables

1 Introduction to Project

1.1 Introduction

Although several decades have yet to pass before fossil fuel depletes on Earth, climate has changed quickly since the industrial revolution a century ago. The contaminant species, chemical pollutants, dust, gusty winds and sandstorm are harmful to human beings and for the environment as well. In air, these harmful substances can exist in the form of liquid droplets, particulate or gass, whereas, in water, they are present as dissolved substances. The level of air pollution inside houses is often two to five times higher than the outdoor level (Augugliaro *et al.* 2010). Indoor air pollution has been confirmed by the Environmental Protection Agency, because it is one of the top human health risks. Household products, including paints, wood preservation, aerosol sprays, disinfectants and cleaners, automotive products, and dry-cleaned clothing are some major or potential sources of indoor air pollution. Moreover, the rapid depletion of both fossil fuels and safe drinking water could result in severe political and economic conflicts among countries with rapidly growing population and increasing environmental pollution (Augugliaro *et al.* 2010).

Green energy and other sustainable alternative sources have become a major issue. Solar energy is estimated to play a crucial role in the world's energy consumption in the future. It can be used for solving global warming or climate change induced problems since, solar energy sources can generate electricity without giving emitting carbon dioxide and other greenhouse gases. The first practical solar cells was fabricated in 1954 using silicon, and then the numbers of efficient solar cells with varied materials and structures have been developed looking for high power conversion efficiency with low cost (Kim *et al.* 2010).

TiO_2 has attracted considerable attention as a promising inorganic material and an attractive raw material for various applications such as water purification, gas sensing, storage and delivery, and energy generation. It exhibits a range of advantageous chracteristics such as inexpensiveness, nontoxic nature, stability, and excellent photocatalytic activity (Bavykin and Walsh, 2010; Dransfield *et al*., 2000; Kandavelu

et al., 2004; Landmann *et al*., 2012; Low *et al*., 2012; Park *et al*., 2010; Pfaff and Reynders, 1999; Tang *et al*., 2011a, Weir et al., 2012, Zhang *et al*., 2012).

TiO_2 offers two important polymorphs, anatase and rutile in the nature, which are considered mainly in this thesis. The anatase and rutile exhibit different properties and consequently different photocatalytic performances. Anatase is a metastable phase, which transforms to the stable rutile phase at an elevated temperature.

In recent years, research into heterogeneous photocatalysis has been accelerated with the rapid emergence of new materials and devices, suggesting promising performance characteristics. To achieve further in a safe photocatalytic reaction, it is necessary to choose a suitable photocatalyst, fabricate a device with a proper nanostructure, and to understand the physics and chemistry behind the photocatalyst. Thus, this study focuses on both synthesis and characterisation of nanostructured TiO_2 for photocatalytic and other related applications.

1.2 Project Aim and Significance

The purpose of this thesis was to synthesis nanostructured TiO_2 (nanofibres, nanopowders, and nanotubes) and gain a fundamental understanding of synthesis, physical and chemical characteristics for potential application in photocatalysis, photovoltage, and other related fields. To achieve this purpose, TiO_2 nanostructures were synthesised to reduce the band gaps of TiO_2, and hence ensuring activation at wavelengths, from ultraviolet (UV) to visible light.

The specific project objectives cover the following fundamental issues:

- Synthesis of nanostructured TiO_2 photocatalysts through electrospinning, sol-gel and anodisation methods;

- Investigate the effects of sol-gel and electrospinning parameters on the electrospun TiO_2 nanofibres' diameter, which include: collector-to-needle distance, solution concentration, applied voltage, flow rate, and needle size;

- Investigate the influence of ion implantation on phase transformation, crystal growth and band gaps of TiO_2 nanofibres, nanopowders, and nanotubes.

The importance of titanium oxide has increased because it can lead to fascinating applications in the areas of environment and alternative energy sources. It is an attractive material due to its wide-ranging applications, for example, in ceramic interference coatings, paints, sunscreens, optical devices, gas sensing, solar cells and biomedical products (Bavykin and Walsh, 2010, Dransfield *et al*., 2000; Pfaff and Reynders, 1999; Kandavelu *et al*., 2004; Lee *et al*., 2008; Weir et al., 2012, Zheng *et al*., 2008,). With the advent of nanotechnology, nanostructured semiconducting TiO_2 has also attracted considerable attention, particularly due to its high potential of being applied in diverse areas, including photocatalysis of pollutants, photo-splitting of water and as transparent conducting electrodes for dye-sensitised solar cells. In particular, elongated TiO_2 nanostructures (nanofibres or nanotubes) and nanopowders have generated much interest because of their high photoactivity and photo-durability (Barzykin and Tachiya, 2002, Nalwa, 2004). In addition, electrospun nanofibres have a wide range of applications, including water filtration, because of the ease and simplicity of the fabrication process together with the high porosity and high surface area of these fibres. Electrospun TiO_2 nanofibres rapidly and drastically degrade various contaminants in water and wastewater to remove the organic pollutants (Doh *et al*., 2008; Lee *et al*., 2012; Lee *et al*., 2013; Thavasi *et al*., 2008; Yun *et al*., 2010).

1.3 Research Methodology

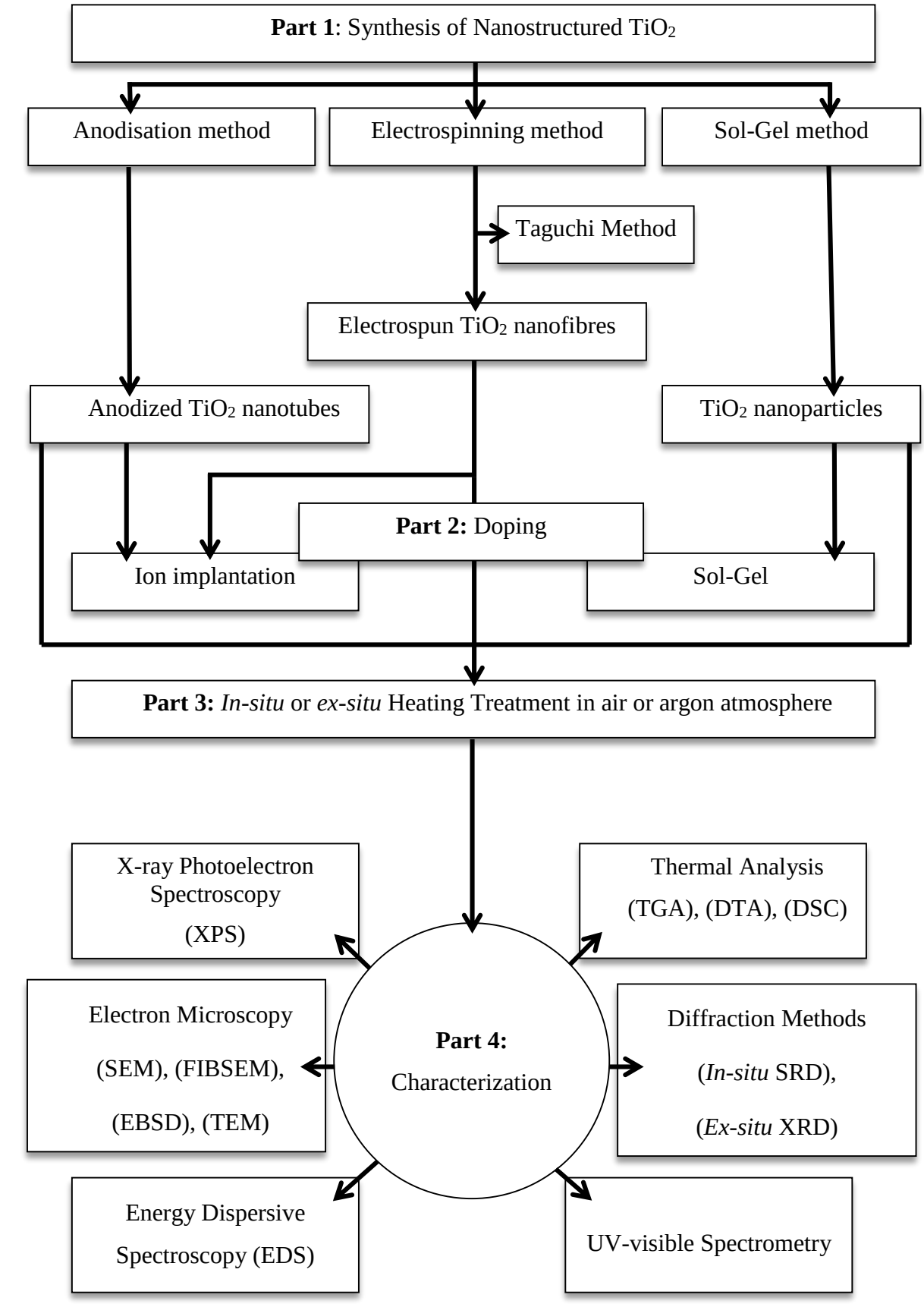

As shown in the flowchart, this thesis specifies four major parts for research and development in order to achieve the objectives. The research methodology is as follows:

Part 1: Synthesis of Nanostructured TiO_2

A. Electrospinning method

A titania sol-gel precursor solution was prepared by mixing titanium isopropoxide (TiP) (M_w = 284.22 g/mol, 97% purity), ethanol (M_w = 46.07 g/mol, 99.5% purity), and acetic acid (M_w = 60.05 g/mol, 99.7% purity). The titania sol–gel was stirred, and then Poly-Vinyl Pyrrolidone (PVP) (M_w = 1300000 g/mol, 100% purity) was dissolved in the solution. The solution was loaded into a plastic syringe with a stainless steel needle. A syringe pump was used to control the solution flow rate during the process of electrospinning. A high voltage power supply was used to provide 14-25 kV between the stainless steel needle and an aluminium collector, which was covered by aluminium foil, approximately at 8-12 cm.

A L_9 orthogonal array along with signal to noise (*S/N)* ratios and ANOVA in Taguchi DoE method was used to investigate applied voltage, needle tip-to-collector distance, flow rate, and TiP concentration, at three different levels on the electrospun TiO_2/PVP nanofibre diameter. The TiO_2/PVP solutions were prepared by mixing 40, 50 or 60 wt% TiP with a constant mixed acetic acid and ethanol with PVP polymer. The needle tip-to-collector distances were from 8 to 11 cm, and a syringe pump was used to control the solution flow rate at 0.5, 1, or 2 ml/h during the electrospinning process.

B. Anodisation method

To synthesis the titania nanotube arrays, (99.6% purity) titanium foils with dimensions of 10 × 10 × 0.1 mm^3 were anodized. In the anodization cell, the titanium foil acted as a cathode, and platinum was used as an anode, with the electrolyte consisting of water, ethylene glycol, and ammonium fluoride (NH_4F). The electrolyte was kept at a constant room temperature and a pH of 6, and the anodizing conditions were set at a constant applied voltage of 10-60 V for several hours at room temperature. The as-anodized titania nanotube arrays were rinsed/washed with ethanol and water, then were dried in air.

C. Sol-Gel method

TiO_2 nanopowders were synthesised via a conventional sol–gel method using titanium (IV) isopropoxide ($C_{12}H_{28}O_4Ti$, *Mw* = 284.22 g/mol). To evaporate any organic material, the TiO_2 solution was mixed through a magnetic stirrer for one hour at 100 °C and then left to dry at room temperature for 48 hours.

Part 2: Doping (Ion implantation)

As-anodized titania nanotube arrays, and nanofibres were implanted with Cr, In, and V ions using the MEVVA ion implanter at the Australian Nuclear Science and Technology Organization (ANSTO). The average implantation energy of ions was 25-63 keV, and the peak penetration depth of ions in the titania nanosturcure was close to the stopping and range of ions in matter (SRIM) prediction based on the implantation parameters. The near-surface composition depth profiling was measured by Rutherford backscattering spectrometry (RBS) using He^{+1} ions at about 2 MeV.

Part 3: *In-situ* or *ex-situ* heating treatment

In-situ high temperature synchrotron radiation diffraction (SRD) was used as the main tool for investigating the titania crystallization behaviour, which was evaluated using the Powder Diffraction Beamline at the Australian Synchrotron. The titania nanotube arrays, and nanofibres were mounted and heated in air and argon atmospheres using an Anton Parr HTK 16 hot platinum stage. Synthesised TiO_2 powders were ground and loaded into a sealed capillary, and then heated using a hot air blower placed directly below the capillary. The SRD data were acquired at a grazing incidence angle of approximately 3° and with a wavelength of 0.085-0.1126 nm, and recorded using a Mythen II microstrip X-ray detector.

To consider the effect of capillary pressure due to heating in sealed capillaries for the SRD measurements, laboratory XRD diffraction patterns were measured after heating TiO_2 powders in air at atmospheric pressure from ambient temperature to 700 °C at 10 °C/min, and then cooled to room temperature. Powder XRD patterns were collected over 2θ = 7–120° with a Bruker D8 advance diffractometer using Cu Kα

radiation (λ = 0.15419 nm) and an accelerating voltage of 40 kV, tube current of 40 mA, sample spinning speed of 30 rpm, and scanning speed of 0.0149°/s.

Synchrotron radiation diffraction (SRD) and X-ray diffraction (XRD) were used to determine phase composition and phase evolution of TiO_2 nanostructure. The SRD patterns were collected at the Australian Synchrotron. The SRD patterns were analysed by Rietveld pattern-fitting using the *Rietica* program (version 2.1) or Topas (version 4.2). In order to determine absolute levels of the amorphous and crystalline anatase and rutile, a novel technique was developed using the temperature-dependence of the SRD pattern background levels. The SRD results were used to obtain the activation energies of amorphous-to-crystalline TiO_2 (anatase and rutile) transformation, and anatase-to-rutile transformation.

Part 4: Other Characterisation

A. Electron microscopy

Transmission electron microscopy (TEM), scanning electron microscopy (SEM), field emission scanning electron microscope (FESEM), and electron backscatter diffraction (EBSD) were used to characterise the morphologies of the nanostructured titania. TEM was used to examine the interfaces, crystallinity, morphology and particle size. SEM, FESEM and EBSD were used to investigate the structure, diameter, and the morphology of the nanostructures.

B. Energy Dispersive Spectroscopy (EDS)

The qualitative and quantitative EDS analyses were determined to ascertain the presence of TiO_2 in the material.

C. X-ray photoelectron spectroscopy

X-ray photoelectron spectroscopy was used to investigate the surface properties and the valence band spectra of the TiO_2 materials. The XPS measurements were carried out in two stages: first, a survey spectrum was measured to obtain a global measurement; second, high-resolution spectra were used to acquire more detailed analysis.

D. Thermal analysis

Thermal analysis calcination measurement of DTA, TGA, and DSC were used to determine the thermal behaviour and activation energies of the titania transformation. The change in the weight of TiO_2 nanofibres was indicated by TGA results. DTA results were used to show the maximum decomposition temperature for solvent, polymer loss, and crystalline titania. DSC measurements were made non-isothermally from 25 to 900 °C using different heating rates in order to determine the titania activation energies.

E. UV-visible Spectrometry

Electrospun titania band gap assessments were made from absorption spectra recorded using a UV-visible spectrometer. The main instrument settings were: absorbance photometric mode, wavelengths of 200 to 750 nm, and 200 nm/min scanning speed.

2 Literature Review (Background)

Titanium dioxide or titanium (IV) oxide, also known as titania, is the naturally occurring oxide of titanium, with the chemical formula is TiO_2. It is a white pigment that can provide a basic white background colour, capable of making paints, inks, plastics, paper, ceramics, candy coating, glazed fruit, toothpaste, sunscreen and cosmetic products impenetrable by light as well as reflecting light across most of the visible spectrum. It is widely used in the food industry as a colorant and classified as E171, which has long been used in many different industrial fields as a white pigment in foodstuffs. For instance, it can be used in Mozzarella cheese to give the whole appearance and colouring of skim milk and flour (Pfaff and Reynders, 1999; Dransfield *et al*., 2000; Kandavelu *et al*., 2004; Weir *et al*., 2012).

Following the discovery of photocatalytic water splitting using TiO_2 in the late 1970s by Fujishima and Honda (Fujishima and Honda, 1972), a new era of TiO_2-based materials has begun. TiO_2 has emerged as a novel material of choice for a variety of applications, because it is inexpensive and both chemically and biologically stable. TiO_2 has drawn more and more attention from researchers in the past few decades, owing to its wide range of potential environmentally friendly applications. Since the synthesis the Nano TiO_2, the amount of published material has been growing exponentially every year. Figure 1 shows the number of published papers increased from 23 papers in 2000 to 4099 papers in 2015, and these numbers are likely to grow even faster in the coming days.

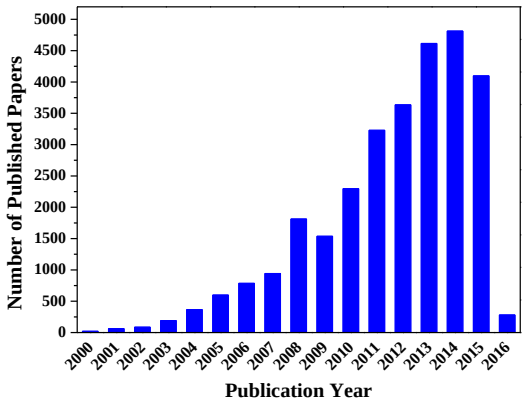

Figure 1: The number of published papers related to nano TiO_2 for the year range 2000–2016.

Data were collected from ProQuest Database using "Nano TiO_2" as keywords.

The introduction review section provides a brief review of the titania fabrication, assembly, and application that focus on the most comment TiO_2 phases, namely anatase and rutile. Anatase and rutile are found in nature and particularly play a significant role in industrial applications (Chuangchote *et al*., 2009; Liu *et al*., 2010). They are popular industrial or engineering materials with promising prospects for everyday human life because of their wide existing and potential applications along with their low cost advantage (Landmann *et al*., 2012; Low *et al*., 2012; Zhang *et al*., 2012). Figure 2 shows the average price of anatase to be ~ 2.3 US$ per kg, whereas the average price of rutile is ~ 2.4 US$ per kg, which is slightly higher for rutile than the anatase price. This difference in prices of the two, suggests TiO_2 phases could be related to the type of their applications. Anatase phase is utilised in the industrial sector as an efficient photocatalyst, whereas rutile phase is used for photovoltage application. (*See Applications and Potential Applications, Section 2.6*).

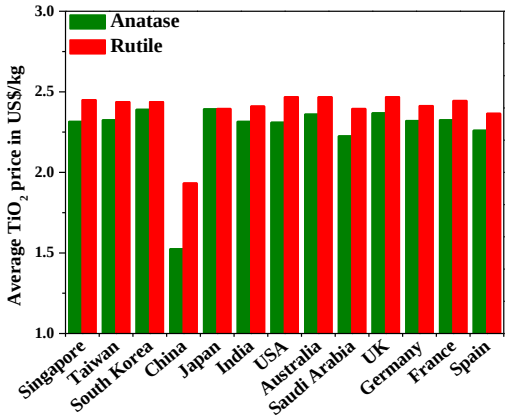

Figure 2: The prices of anatase and rutile with different countries.

Data were taken from Pertrosil on 5th May 2016 (www.petrosil.com).

2.1 Crystal Structured of TiO_2

TiO_2 occurs in a variety of crystal structures and exhibits diverse electronic and optical properties. It has four polymorphs in nature, namely anatase, rutile, brookite, and bronze (TiO_2 (B)) (Carp *et al*., 2004). Moreover, Columbite (TiO_2 II) and Hollandite (TiO_2 (H)) are two additional high-pressure rutile polymorphs which have been synthesised in the laboratory (Simons and Dachille, 1967; Latroche *et al*., 1989). Baddeleyite (TiO_2 III), and Ramsdellite (TiO_2 (R)) or any other TiO_2 modifications have been synthesised in the laboratory too (Sato *et al*., 1991; Takahashi *et al*., 2006). The composition is the same for TiO_2 phases, but each titania phase represents a different arrangement of the atom, making up a different crystal structure.

The application of TiO_2 is usually based on one or a mixture of TiO_2 crystalline phases. Since then, the study of TiO_2 crystalline phase has also become important for TiO_2 applications. The three common polymorphs of titanium dioxide, namely, anatase (tetragonal), rutile (tetragonal) and brookite (orthorhombic) are considered in this section; even bronze (monoclinic) is rare because it is mostly synthesised by high-pressure treatment and can be readily synthesised in the laboratory.

In 1916, a structural investigation of anatase (tetragonal) and rutile (tetragonal) was originally conducted by Vegard applying Bragg's ionisation method (Vegard, 1916), whereas the brookite crystal structure (orthorhombic) was first determined by Pauling and Sturdivant using powder XRD in 1928 (Pauling and Sturdivant, 1928). In 1955, the acceptable crystal structures of anatase and rutile were revised by Cromer and Herrington using powder X-ray Diffraction as well (Cromer and Herrington, 1955).

In the common titania forms, titanium (Ti^{4+}) atoms are coordinated to six oxygen (O^{2-}) atoms, forming TiO_6 octahedra. Crystalline anatase and rutile are tetragonal structure, with which the octahedra share edges at (001) and (001) planes, respectively. On the other hand, both edges and corners of brookite are shared to give an orthorhombic structure. Anatase and rutile appear more often than brookite in lab synthesised materials and in many other device applications involving titania (Beltran *et al*., 2006).

2.1.1 Anatase

Anatase is one of the most widely studied TiO_2 polymorphs. It is widely employed as a photocatalyst because it is the most photoactive amongst the three common TiO_2 polymorphs (Fujishima *et al*., 2000). It has the highest density of localised state and consequent surface-adsorbed hydroxyl radicals and the slowest charge carrier recombination compared to rutile and brookite. This is due to the differences in crystal structures and associated exposed planes among the titania phases, where anatase has a lower surface enthalpy and lower surface free energy than that of rutile (Banfield, 1998).

Anatase and rutile have a tetragonal structure as shown in Figure 3 and 4, respectively, but the distortion of the TiO_6 octahedron is slightly larger in anatase than in rutile, and have different space groups and atoms per unit cell (Z) (Linsebigler *et al*., 1995; Mo and Ching, 1995). Table 1 shows the structural parameters, as well as physical and mechanical properties of anatase. The lattice anatase parameters are $\boldsymbol{a}$ = $\boldsymbol{b}$ = 0.3784 nm, and $\boldsymbol{c}$ = 0.9515 nm at room temperature. Anatase has higher unit cell symmetry when compared with brookite, since there are only five different bond lengths in its representative octahedron. There are four Ti-O distances of 0.1937(3) nm and two Ti-O distances of 0.1964(9) nm.

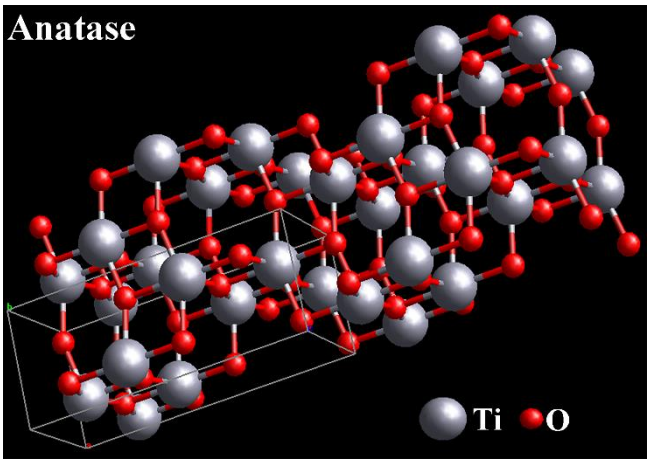

Figure 3: The basic unit cell crystal structure of anatase (ICSD 202242).

Table 1: Structural parameters, and physical and mechanical properties of anatase.

Property		**Value**	**Reference**
Crystal System		Tetragonal	(Cromer and Herrington, 1955; Bokhimi *et al.*, 2001; Burdett *et al.*, 1987; Matsui and Akaogi, 1991; Mo and Ching, 1995; Kim *et al.*, 1996; Wunderlich *et al.*, 2004; Lin *et al.*, 2006; Hummer *et al.*, 2007; Reyes-Coronado *et al.*, 2008)
Space Group		$I4_1/amd$	
Atoms per Cell (Z)		4	
MD Basic Cell		32 ($4\boldsymbol{a}\times4\boldsymbol{a}\times2\boldsymbol{c}$)	
Lattice Parameters (25 °C) (nm)	***a***	0.3784(5)	
	c	0.9515(5)	
Volume of Cell (25 °C) (nm^3)		0.1363	
Density (25 °C) ($kg.m^{-3}$)		3894	
O-Ti-O Bond Angle (°)		77.7 92.6	
Mean Interatomic Distances (nm)	Ti–Ti	0.304	
	Ti–O	0.195	
Thermal Expansion Coefficients (TECs) $\times10^{-5}$ ($°C^{-1}$) at 900 °C	Linear (α_a)	0.53	
	Linear (α_c)	1.04	
	Volumetric (β)	2.17	
Molecular Weight ($g.\ mol^{-1}$)		79.88	
Molar Volume ($\times10^{-6}\ m^3.\ mol^{-1}$)		20.51	
Optical Band Gap (eV)		3.20(5)	
Light Absorption (nm)		~ 388	
Refractive Index		2.52(3)	
Mohs Hardness		5.5-6.0	
Resistivity (25 °C) (Ω. cm)		10^5	
Conductivity (25 °C) (1/Ω. cm)		10^4-10^7	
Bulk Modulus, K (TPa)		0.21	
Melting Point (°C)		Transformation to rutile	
Solubility in Water		Insoluble	

2.1.2 Rutile

Rutile has been studied extensively because it has the simplest TiO_2 structure, and most common and stable TiO_2 form. The tetragonal rutile structure is defined by three crystallographic parameters: two lattice parameters ***a***, ***c*** and the oxygen fractional coordinate. Anatase and rutile have the same tetragonal crystal structure, but they have a different space group and atoms per cell (Z), $P4_2/mnm$ sharing two edges for rutile, and, $I4_1/amd$ sharing four for anatase (see Table 1 and 2). Figure 4 shows the basic unit cell crystal structure of rutile. The cell parameters are ***a*** = 0.45936(5) nm and ***c*** = 0.29587(3) nm, and the oxygen parameter is 0.03056(6) nm at room temperature. There is four Ti–O distances of 0.1946(3) nm, and two Ti–O distances of 0.1984(4) nm (see Table 2).

The rutile phase is most stable at elevated temperature and pressure up to 50 kbar. Both anatase and brookite structure transformed to the rutile phase with a certain condition and parameter (*See Kinetics of TiO_2 phases Transformation, Section 2.3*).

Among the three common polymorphs of TiO_2, the highest symmetric structure is possessed by rutile. It contains six atoms per unit cell with the TiO_6 octahedron slightly distorted. The rutile crystal structure is defined as sharing of two edges and two vertices of the octahedron, which leads to a higher symmetry of the crystal structure.

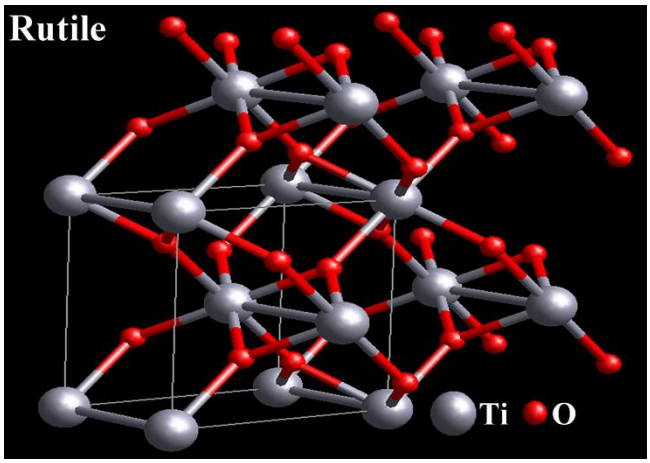

Figure 4: The basic unit cell crystal structure of rutile (ICSD 64987)

Table 2: Structural parameters, and physical and mechanical properties of rutile.

Property	**Value**		**Reference**
Crystal System	Tetragonal		(Cromer and Herrington, 1955; Burdett *et al.*, 1987; Matsui and Akaogi, 1991; Tang *et al.*, 1994; Mo and Ching, 1995; Kim *et al.*, 1996; Bokhimi *et al.*, 2001; Ohno *et al.*, 2001; Wunderlich *et al.*, 2004; Lin *et al.*, 2006; Hummer *et al.*, 2007; Reyes-Coronado *et al.*, 2008)
Space Group	$P4_2/mnm$		
Atoms per Cell (Z)	2		
MD Basic Cell	96 ($4\boldsymbol{a}\times4\boldsymbol{a}\times6\boldsymbol{c}$)		
Lattice Parameters (25 °C) (nm)	***a***	0.45936(5)	
	c	0.29587(3)	
Volume of Cell (25 °C) (nm^3)	0.0624		
Density (25 °C) (kg. m^{-3})	4130		
O-Ti-O Bond Angle (°)	81.2 90.0		
Mean Interatomic Distances (nm)	Ti–Ti	0.296	
	Ti–O	0.196	
Thermal Expansion Coefficients (TECs) $\times10^{-5}$ ($°C^{-1}$) at 900 °C	Linear (α_a)	0.87	
	Linear (α_c)	1.01	
	Volumetric (β)	2.83	
Molecular Weight (g. mol^{-1})	79.9		
Molar Volume ($\times10^{-6}$ m^3. mol^{-1})	18.80		
Optical Band Gap (eV)	3.00(5)		
Light absorption (nm)	~ 413		
Refractive index	2.9 or 2.75		
Mohs Hardness	7.0-7.5		
Resistivity (25 °C) (Ω. cm)	10^{12}		
Conductivity (25 °C) (1/Ω. cm)	10^4-10^7		
Bulk modulus, K (TPa)	0.23		
Melting point (°C)	1825		
Boiling point (°C)	2500–3000		
Solubility in water	Insoluble		

2.1.3 Brookite

Brookite has an orthorhombic crystal structure (see Figure 5). Its titanium atom is located near the centre, with oxygen atoms at the vertices. The Brookite unit cell is octahedral, and a crystal structure is formed when the octahedron shares three edges. The Ti-O and O-O bond lengths differ, which leads to a distorted octahedron. The Brookite cell volume is larger than the anatase or rutile cell volumes, with eight atoms per cell (Z), compared with four for anatase and two for rutile. The brookite cell volume is 0.32172 nm^3, whereas it is 0.1363 nm^3 and 0.0624 nm^3 for anatase and rutile, respectively (See Table 3).

Although many reports have interest in brookite structure, only few of them present the synthesis of pure brookite (Bokhimi *et al*., 2001). The metastable anatase may transform into brookite thermodynamically under standard condition, and then the metastable brookite transforms to the stable rutile upon calcination at an elevated temperature, but this is rare due to the fact that it is difficult for brookite crystal structure to form (*See Kinetics of TiO_2 phases Transformation, Section 2.3*).

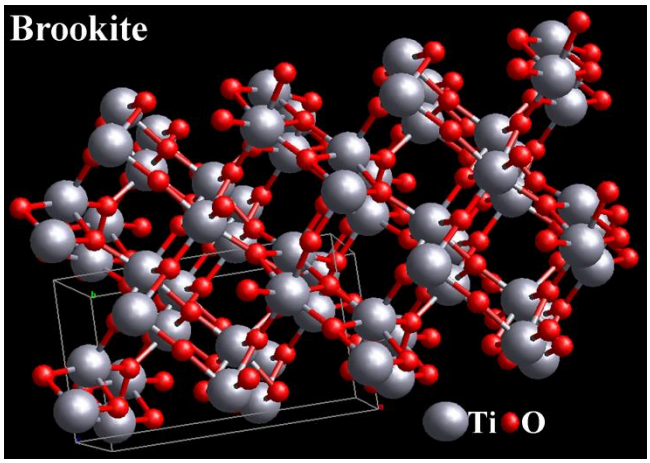

Figure 5: The basic unit cell crystal structure of brookite (ICSD 015409)

Table 3: Structural parameters, and physical and mechanical properties of brookite.

Property		**Value**	**Reference**
Crystal System		Orthorhombic	(Meagher and Lager, 1979; Mo and Ching, 1995; Kim *et al.*, 1996; Bokhimi *et al.*, 2001; Ohno *et al.*, 2001; Wunderlich *et al.*, 2004; Reyes-Coronado et al. 2008; Matsui and Akaogi 1991)
Space Group		P b c a	
Atoms per Cell (Z)		8	
MD Basic Cell		18 (2***a***×3***b***×3***c***)	
Lattice parameters (25 °C) (nm)	***a***	0.9174(5)	
	b	0.5439(5)	
	c	0.5163(5)	
Volume of Cell (25 °C) (nm^3)		0.32172	
Density (25 °C) (kg. m^{-3})		4250	
O-Ti-O Bond Angle (°)		77.0 ~ 105	
Mean Interatomic Distances (nm)	Ti–Ti	0.302	
	Ti–O	0.196	
Thermal expansion coefficients (TECs) $\times 10^{-5}$ ($°C^{-1}$) at 900 °C	Linear (α_a)	0.68	
	Linear (α_b)	0.69	
	Linear (α_c)	1.05	
	Volumetric (β)	2.40	
Molecular Weight (g. mol^{-1})		79.866	
Molar Volume ($\times 10^{-6}$ m^3. mol^{-1})		19.35	
Optical Band Gap (eV)		3.35(5)	
Light absorption (nm)		~ 370	
Refractive index		2.63	
Mohs Hardness		5.5-6	
Resistivity (25 °C) (Ω. cm)		10^5	
Bulk modulus K (GPa)		0.22	
Melting Point (°C)		Transformation to rutile	
Solubility in Water		Insoluble	

2.2 TiO_2 Band Gap, Doping, and Modifying

Figure 6 presents the schematic illustration of the energy band gap. An electron (e^-) from the valence band (VB) is excited to the conduction band (CB) with the formation of a hole (h^+) by light radiation of energy equal or greater to the TiO_2 band gap.

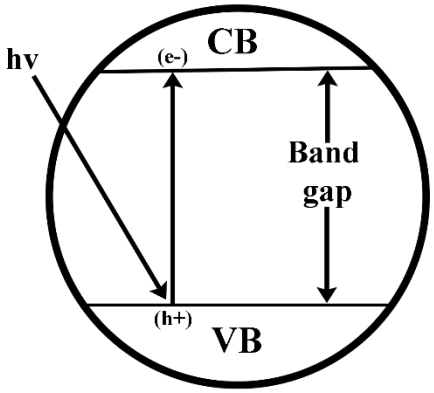

Figure 6: Schematic illustration of energy bands.

Figures 7 and 8 show the band gap energy with valence band (green) and conduction band (red) positions for several semiconductors including anatase and rutile. The conductance band of the semiconductor must be more negative than the reduction potential of the chemical species, whereas the valence band of the semiconductor must be more positive than the oxidation potential of the chemical species (Mills and Le Hunte, 1997). Among these semiconductors, titania phases have received the largest attention as a photocatalytic material because of its superior photocatalytic activity, chemical stability, low cost, and nontoxicity. Titania (TiO_2) is an n-type semiconductor because of oxygen deficiency. TiO_2 valance band is O_{2p} in one character, while the conduction band is $Ti_{3d\&4s}$ in the other character. It is a large band gap semiconductor, and the optical band gap of amorphous TiO_2 was found to be in the range of 3.30-3.50 eV (Eufinger *et al*., 2007). This value decreased slightly for single-crystalline anatase (3.20 eV), and crystalline rutile (3.00 eV).

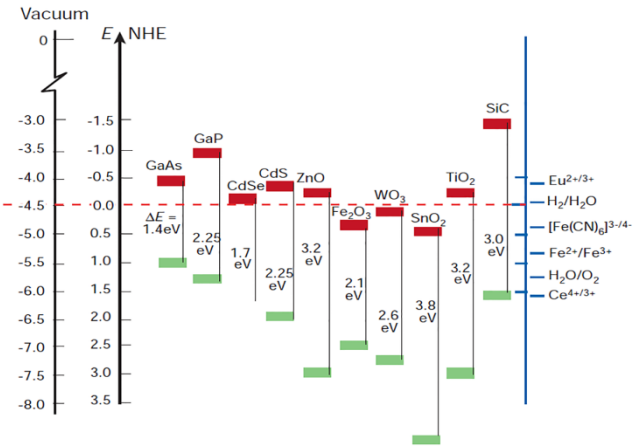

Figure 7: Band gap energy with valence band (green) and conduction band (red) positions for several semiconductors.

(Gratzel, 2001).

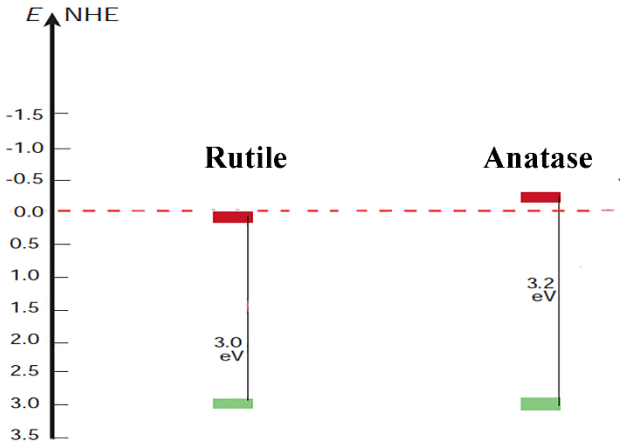

Figure 8: Band gap energy with valence band (green) and conduction band (red) positions for pure crystalline anatase and rutile.

Data take from (Mills and Le Hunte, 1997).

The rutile band gap is slightly lower than the anatase band gap at absorbing the solar spectrum, but both of them can only be excited under ultraviolet irradiation, which occupies only 3-5 percent of the total solar irradiation at the Earth's surface. For anatase, a wavelength (λ) shorter than 387 nm is required for the absorption of a photon

to excite an electron to the conduction band (e_{CB-}) in order to generate a positive hole in the valence band (h_{VB+}) according to:

$$TiO_2 + hv \longrightarrow h_{VB^+} + e_{CB^-} \qquad (1.1)$$

Controlling the electrical conductivity of TiO_2 is an important step towards the application of electronics and photo-electronics. If the TiO_2 semiconductor with any forms is irradiated with photons of energy more than their band gap, the electron is promoted from the valence band to the conduction band (see Figure 6).

Many of the TiO_2 uses are closely related and dependent on its optical properties, and one drawback appears because of its wide band gap. Several approaches for TiO_2 modification have been proposed to realise an efficient TiO_2 by changing the absorption edge from UV to visible region, including metal loading, metal-ion doping, anion doping, metal ion-implantation, organic dyes, polymer attachment, and hydrogen plasma reduction (Hsu *et al*., 2007).

Coating the TiO_2 surface with a thin layer of dye is one strategy for the TiO_2 modification and for reducing the band gap. This method is called a dye sensitisation and has been successfully applied to solar cell devices. Photodegradation of organic pollutants in water has been achieved on the TiO_2 surface modified with thionine and eosin Y dyes using visible light. The dyes (sensitiser) adsorbed on titania surface are excited by absorbing visible light and affect charge injection into the conduction band (CB) at sub-band gap excitation and the catalytic processes follow through an interfacial electron transfer (Chatterjee and Mahata, 2001).

Doping of TiO_2 with metal (Cr, Cu, Ni, Mn, Mo, Nb, Ru, Au, Ag, Pt Co, V, and Fe) or nonmetal elements (N, B, P, I, F, C, and S) is a common method and currently attracting considerable interest as a promising route to extend the absorption of TiO_2 from UV light to visible light range (Anpo, 2000; Asahi *et al*., 2001; Umebayashi *et al*., 2002; Yu *et al*., 2002; Ohno *et al*., 2003; Sakthivel and Kisch, 2003; Yamashita *et al*., 2003; Yu *et al*., 2003; Hong *et al*., 2005; Chen *et al*., 2007; Lam *et al*., 2007; Liu *et al*. 2010; Zhang *et al*., 2010; Kamat, 2012).

Figure 9 shows five possible origins of visible light absorption in non-metal doped anatase TiO_2. These five electronic mechanisms can explain different optical absorptions of metal and non-metal doped TiO_2 (Liu *et al*. 2010). (**a**) narrowing of band gap by the newly formed valance band (VB) by mixing O_{2p} of TiO_2 with a doping states; (**b**) and (**c**) doped TiO_2 with a localised a and new dopant level near the valence band (VB) and the conduction band (CB), respectively; (**d**) formation of colour centres in the band gap as the origin of the visible light absorption band; and (**e**) sensitisation mechanisms in which melamine condensation products as visible light sensitiser.

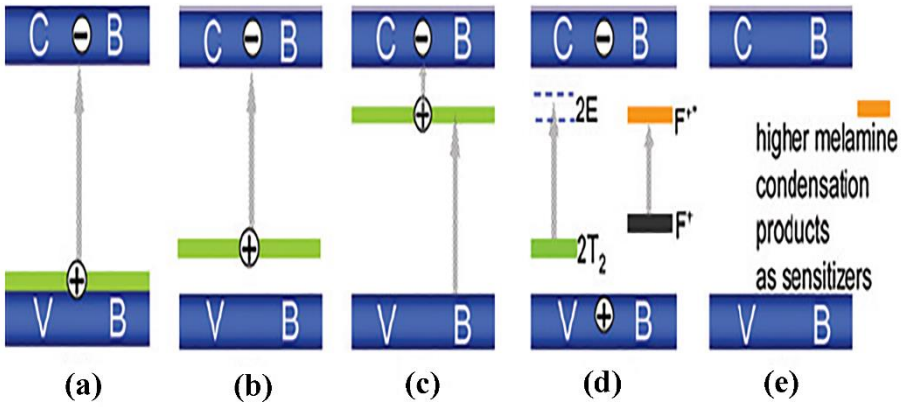

Figure 9: Various schemes of band gap structure change of non-metal doped anatase TiO_2.

(CB: Conduction band, and VB: Valence band)

(Liu *et al*. 2010)

Next section reviews methods of reduced TiO_2 band gap with metallic and non-metallic species, including ion implantation, sol-gel, and heterostructure methods.

2.2.1 Ion Implantation Method

In 2000, Anpo used the application of the ion implantation method to improve the electronic properties of the TiO_2 and present second titania generation photoactivity under the visible light (Anpo, 2000). In ion-implantation method, metal ions including

V^+, Cr^+, Fe^+, V^+, Mn^+, among others, are accelerated in the electronic field and injected into the deep bulk of TiO_2 sample target as the ion beam (see Figure 10). The interaction of implanted ions with the sample surface depends on the kinetic energy. High kinetic energy from 150 to 200 keV are accelerated enough to implant metal ions (Fe^+, Mn^+, V^+, etc.) into TiO_2 bulk samples by the ion-implantation. Depending on the metal ions implanted type and amount, UV-VIS absorption spectra of TiO_2 photocatalysts were found to shift towards visible light regions (Yamashita *et al*., 2003). The UV light to visible light (UV–Vis) absorption spectra of some metal ion-implanted TiO_2 photocatalysts such as V, Cr, Mn, Co, Ni, and Cu, were shifted to near the visible light regions (Lam *et al*., 2007; Zhang *et al*., 2010; Kamat, 2012). However, ion-implantation with Ti, Ar, or Na, was not effective at all to modify the TiO_2 properties to make a shift of absorption band to the longer wavelength region (Yamashita *et al*., 2003).

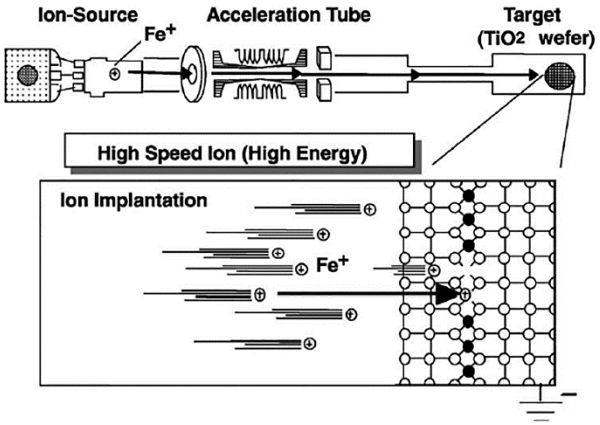

Figure 10: Systematic diagram of ion implantation into TiO_2 samples.

(Yamashita *et al*., 2003).

2.2.2 Sol-Gel Doing Method and Other Methods

Doping with metal and non-metal using the sol-gel method is a powerful strategy for modifying the electronic structure of TiO_2 for two reasons. Firstly, depending on the type and amount of metal used, TiO_2 can be activated at a range of wavelengths from ultraviolet to visible light. Secondly, the sol-gel process is one of the most versatile methods to prepare titania nanopowder materials since it has a high ratio of

surface area in proportion to volume, which increase the decomposition rate of water and air pollutants and allows for photocatalytic reactions to occur more rapidly on the titania photocatalyst surface. It is found that some doped elements and types play a significant role in the TiO_2 band gap.

Sol-gel doping of TiO_2 with non-metals has been investigated intensively, such as nitrogen-doped TiO_2 films (Asahi *et al*., 2001). The nitrogen-doped TiO_2 which narrowed the TiO_2 band gap contributed to the visible light absorption, because the N_{2p} state in nitrogen hybrids with the O_{2p} state in the anatase TiO_2, in which their energies are very close.

Following N-doped TiO_2, a series of non-metal doped TiO_2 were successfully synthesised and they were photoactive under visible light such as iodine, flour, phosphorus, boron, sulfur/sulphur, and carbon (Umebayashi *et al*., 2002; Yu *et al*., 2002; Sakthivel and Kisch, 2003; Ohno *et al*., 2003; Yu *et al*., 2003; Hong *et al*., 2005).

Doping TiO_2 with anion elements such as nitrogen, carbon, sulphur can reduce the TiO_2 band gap and exhibit visible photoresponse, as the atomic orbitals of the non-metal elements (N_{2p}, C_{2p}, and S_{3p}, respectively) have higher potential energy than titania O_{2p}. This will form a new valence band instead of a pure O_{2p} atomic orbital that minimises the band gap energy without changing the conduction band level.

Among non-metal elements doped TiO_2, carbon did not receive high attention like the nitrogen, even though a C-doped TiO_2 powder was determined to be five times more active than the N-doped TiO_2 (Sakthivel and Kisch, 2003). Another study reports a preparation of carbon-doped TiO_2 nanotube arrays with high aspect ratios for maximising the photo-cleavage of water under white-light irradiation. The synthesised C-doped titania nanotube arrays showed much higher photocurrent densities and more efficient water splitting under visible light illumination (> 420 nm) than pure titania nanotube arrays (Park *et al*., 2006). Additionally, a photocatalytic performance of a composite of titania nanotubes and carbon nanotubes (TNT-CNT) was used to study benzene degradation in the gas phase as a testing reaction. The results have demonstrated that a certain amount of CNT doping into the matrix of TNT affects the conversion ratio of the benzene degradation slightly (Tang *et al*., 2011b). Moreover, N-doped TiO_2, C-doped TiO_2, and (C, N) co-doped TiO_2 with different nitrogen and carbon contents were used to reduce the TiO_2 band gap and utilize visible light more

efficiently in photocatalytic reactions (Chen *et al*., 2007). The nitrogen atoms weaved into the titania lattice and induced new band states in the TiO_2 band gap, through replacing the sites of oxygen atoms, whereas the carbon atoms could form a layer composed of a complex carbonaceous mixture on the TiO_2 surface. It was found that co-doped TiO_2 exhibited the highest photocatalytic activity under visible light than those of C-doped or N-doped TiO_2 due to the assigned synergistic effect of doped C and N atoms.

Different metal elements such as chromium, indium, and vanadium were used to prepare doped titania, and the optical absorption edge could be shifted into the visible range of solar irradiance. Chromium-doped TiO_2 was synthesised using various morphologies and methods. Mishra *et al.* (2014) synthesised low-content Cr-doped TiO_2 nanotubes by electrochemical anodisation methods of Ti-Cr alloys in ethylene glycol electrolyte. Cr^{3+}-doped TiO_2 with crystalline anatase were prepared by a combination of the sol-gel process with hydrothermal treatment (Zhu *et al*., 2006). Cr^{3+}-doped anatase TiO_2 photocatalytic activity was investigated under UV and visible light irradiation. It shows a good ability for absorbing the visible light because of the excitation of 3d electron of Cr^{3+} to the TiO_2 conduction band (CB). Doping of chromium ions effectively improves the photocatalytic activity under visible light irradiation with an optimal doping concentration of 0.15% and 0.2%, respectively. Moreover, a visible light active mesoporous Cr-doped TiO_2 photocatalyst was synthesised by applying an evaporation-induced self-assembly approach (Fan *et al*., 2008). The Cr^{3+} doping concentration effect on the photocatalytic activity of mesoporous TiO_2 was investigated from 0.1 to 1 mol percent. The Cr-doped TiO_2 extended the photoabsorption edge into the visible light region and exhibited higher photocatalytic activities when compared with pure mesoporous TiO_2 under visible light irradiation (Dholam *et al*., 2010).

Doping TiO_2 nanofibres with 1.0 and 5.0 wt.% V were also successfully incorporated into the crystal lattice of TiO_2 nanofibres, and could extend the visible light absorption of TiO_2 nanofibres. The obtained V-doped TiO_2 nanofibres possessed high activity for the photodegradation of organic pollutant methylene blue (MB) (Zhang *et al*., 2010).

2.2.3 Mixed Titania Phases, Heterojunction (Heterostructure)

Mixed-phase titania, which includes anatase/rutile, anatase/brookite, rutile/brookite, and anatase/TiO_2 (B), has been recently developed as a strategy to circumvent the wide band gap of titania (Van *et al*., 2007; Li and Liu, 2009; Xu and Zhang, 2009; Zheng *et al*., 2010).

The common mixed-phased titania photocatalyst is Degussa P25, which contains a combination of mainly crystalline anatase (~ 80%) and crystalline rutile (~ 20%). The photocatalytic activity of the mixed titania phases is better than one of them, because the rutile conduction band is more positive than that of anatase, which means that the crystalline rutile phase may act as an electron sink for photogenerated electrons from the conduction band of the anatase phase (see Figure 8). The high photocatalytic activity of this mixed titania phase enhances the separation of photogenerated electrons and holes, and results in reduced recombination.

Composites of two semiconductors with different band gaps can suppress the photocatalytic performance. Many efforts have been made in the synthesis of different heterostructure semiconductor such as CdS/TiO_2, Bi_2S_3/TiO_2, Fe_2O_3/TiO_2 and ZnO/TiO_2, which can be present as a core-sell geometry or sandwich structure (Serpone *et al*., 1995; Marci *et al*., 2001; Brahimi *et al*., 2007; Ghows and Entezari, 2011). These coupling resulted in extended photoabsorption bands in the visible form and were reported to be more effective for the photocatalytic degradation of a dye under visible light irradiation, as compared to pure TiO_2. The coupling of a smaller band gap semiconductor such as Bi_2S_3 (1.42 eV) with the TiO_2 band gap, is of great interest using solar radiation. In principle, the heterostructure of anatase and rutile with ZnO seems useful to achieve a more efficient electron-hole pair separation under visible light irradiations due to the increased lifetime of the photo produced electron-hole pairs, which is transferred between the two semiconductors.

Another researcher, Li and his co-worker reported that two semiconductors Al_2O_3/Degussa P25 TiO_2 composite exhibited visible-light absorption, which was attributed to Nitrogen-doping during high-temperature combustion, and to alterations in Ti species with the electronic structure induced by the Al addition (Li *et al*., 2012). The optimal Al_2O_3 to Degussa P25 TiO_2 molar ratio was 1:1.5, and the semiconductors

composite exhibited a large specific area of 152 m^2/g, with enhanced photocatalytic activity, and large surface positive charges. The degradation rate of anions methylene orange enhanced by the N-doped Al_2O_3/TiO_2, which was 43.6 times greater than the pure Degussa P25 TiO_2. The high visible-light photocatalytic activity of anionic methylene orange was attributed to the synergetic effects between the two semiconductors, Al_2O_3 and TiO_2, N-doping a large specific surface area (*See Nanostructured TiO_2, Section 2.4*), and low recombination efficiency of photo-excited electrons and holes.

2.3 Kinetics of TiO_2 Phases Transformation

TiO_2 (titania) belongs to the transition metal oxides family, and it is known to exist in various polymorphs and crystalline phases. Amorphous TiO_2 transforms into crystalline anatase, and the crystalline anatase transform to crystalline rutile at an elevated temperature. Rutile is the only stable phase at normal condition, whereas anatase and brookite are metastable and undergo irreversible transformations into rutile at an elevated temperature.

Some studies focused on the amorphous-to-anatase transformation (Eufinger *et al*., 2007). However, many studies were conducted on the anatase-to-rutile transformations, because crystallinity was an important parameter that influenced titania band gap narrowing, and thus the titania applications. The crystalline anatase-to-rutile transformation temperature, as reported in the literature, ranges from 400 to 1200 °C, and is affected by various conditions, including calcination time, synthesis method, level of impurities, doping, calcination time, the deviation of stoichiometry, surface area, grain and particle size, reaction atmosphere type and condition, method of synthesis, and so forth (Shannon and Pask, 1965; Eppler, 1987; Akhtar *et al*., 1992; Ding *et al*., 1996; Gennari and Pasquevich, 1998; Zhang and Banfield, 2000a; Okada *et al*., 2001; Barakat *et al*., 2005; Zhang and Banfield ,2005; Fang *et al*., 2011; Liu *et al*., 2013).

These transformations do not have a unique temperature, and the processes that are involved in the titania transformation, as well as the methods to promote or inhibit this transformation, have not yet been reviewed and discussed comprehensively.

The fraction of anatase-to-rutile transformation was estimated using the Spurr and Myers equations (Spurr and Myers, 1957):

$$A(\%) = 1/[1 + I_R/1.26I_A] \times 100\% \qquad (1.2)$$

$$R(\%) = 1/[1 + I_A/0.8I_R] \times 100\% \qquad (1.3)$$

$$A(\%) = 100 - R(\%) \qquad (1.4)$$

where *A (%)*, and *R (%)* are the relative weight fraction of crystalline anatase and rutile, respectively. I_A and I_R are the X-rays integrated intensities of anatase (101) reflection and rutile (110) reflection, respectively.

It should be noted that the crystal structure of titania is not completely understood by XRD patterns. For example, the TiO_2 nanotubes are not pure TiO_2, but crystal modifications of TiO_2 (anatase and rutile) with some polytitanic acids and organic sources, which make it difficult to identify the modified titania phases (TiO_{2-x}). The titania nanotubular structure is another difficulty because the sample is not flat, as the orientation will affect the XRD results, and hence the relative weight calculated from Spurr and Myers method will not be identified accurately, where only the peak intensities of anatase (101) and rutile (110) are used. However, for *in-situ* XRD/SRD high temperature experiments, the phase identification will be more difficult due to the thermal expansion of the lattice parameter at an elevated temperature. Moreover, the structure is relatively unstable, and can undergo further phase transformation during a thermal treatment.

This section reviews the titania phase transformation by discussing the thermodynamics of the titania phase transformation and the factors affecting its observations.

2.3.1 Temperature

Anodised TiO_2 nanotube arrays were heated at different temperatures from 300 °C to 800 °C with a step of 100 °C in an air atmosphere for 2 hours with the heating rate of 10 °C/min (Liu *et al*., 2013). The crystal structures and crystallinity of the samples were analysed using the X-ray diffraction patterns (XRD). Figure 11 shows the XRD patterns of the samples, which indicate that the diffraction peaks of the Ti foils were only observed before calcination, thus indicating the amorphous nature of TiO_2 nanotubes. The amorphous-to-anatase transformation can be seen clearly at 300 °C, which includes the characteristic peak of crystalline anatase. The anatase-to-rutile transformation started when the TiO_2 nanotubes were calcinated at 600 °C until the rutile phase began to appear in the XRD patterns.

The weight fraction of rutile increased dramatically as the temperature increased with the transformation of metastable anatase into rutile at elevated temperatures, which were 65, 91.8, and 100 percent for 600 °C, 700 °C, and 800 °C, respectively.

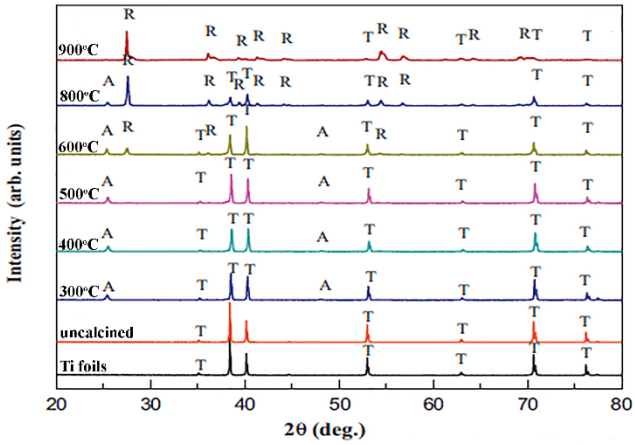

Figure 11: XRD patterns of the anodised TiO_2 nanotubes for different calcination temperatures.

[T: Titanium, A: anatase, and R: rutile]. (Liu *et al*., 2013).

2.3.2 Calcination Time

The effect of calcination time on the anatase-to-rutile transformation was studied. Anatase was heated in air at 950 °C for periods of 4, 24, and 48 h. After each treatment,

the anatase and rutile were calculated from X-ray diffraction (XRD) measurements. The analysis shows that an increase in calcination time increased the rutile percentage and decreased the anatase percentage. The relative rutile percentage was 5% for 4h, 65% for 24 h, and 92% for 48h (Gamboa and Pasquevich, 1992).

Calcination time of 1, 2, 4, 8, and 12 h at 500 °C with a heating rate of 10 °C/min were used to study the effect of calcination time for anatase-to-rutile transformation of TiO_2 nanotube arrays (Liu *et al.*, 2013). XRD patterns in Figure 12 show that only (101) anatase peak of the crystallographic plane appear following 1 h calcination. For 2 h calcination, (101) and (200) anatase crystallographic planes began to appear. The formation of rutile phase (40.5%) was observed for 4 h calcination. The anatase phase transformed completely into rutile phase when the calcination time was 12 h.

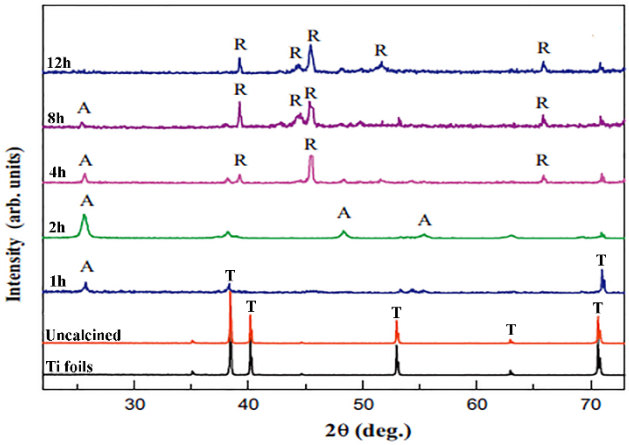

Figure 12: XRD patterns of the of anodised TiO_2 nanotubes for different calcination times.

[T: titanium, A: anatase, and R: rutile]. (Liu *et al.*, 2013).

2.3.3 Heating Rate

TiO_2 nanotube arrays were calcined for 2 h at 500 °C in an air atmosphere with heating rates of 1, 5, 10, and 20 °C/min to determine the crystalline phases (see Figure 13) (Liu *et al.*, 2013). Crystalline anatase was just observed for all different heating rates, which only affected the (101) and (200) crystallographic planes intensity, and

the amorphous-to-anatase transformation. The relative anatase crystallinity was the highest for the 10 °C/min heating rate. It should be noted that the nanotubes intensity was affected by the morphology of nanotubes. Moreover, the crystallite size varied from 50.9 to 90.4 nm with the increasing heating rate from 1 to 20 °C/min, indicating that the higher heating rate promoted the anatase grain growth.

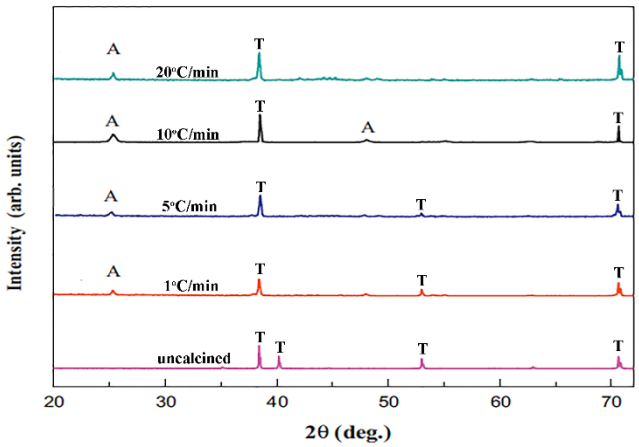

Figure 13: XRD patterns of the anodised TiO_2 nanotubes for different heating rates.

[T: titanium, and A: anatase].

(Liu *et al*., 2013).

2.3.4 Atmospheres

The effect of different reactive atmospheres including air, argon, nitrogen, hydrogen, vacuum, hydrogen-nitrogen, chlorine, argon-chlorine atmospheres on TiO_2 transformation were reported by various reasearchers (Shannon and Pask, 1965; Gamboa and Pasquevich, 1992; Fang *et al*., 2011; Varghese *et al*., 2003; Plugaru *et al*., 2004; Huang and Wong, 2011).

For instance, it was reported that the anatase-to-rutile transformation rate was lower in a vacuum than in a hydrogen atmosphere, whereas an increase in the oxygen partial pressure decreased the transformation rate (Iida and Ozaki, 1961). It was also reported that the anatase-to-rutile transformation was lower in a vacuum than in air (Shannon and Pask, 1965). Various studies showed that the atmosphere enhanced the TiO_2

transformation due to the formation of oxygen vacancies and the diffusion necessary for the crystallographic rearrangement (Shannon and Pask, 1965). The oxygen vacancy defects in TiO_2 acted as colour centres, changing from white to grey or dark blue, with increasing non-stoichiometry (TiO_{2-x}) (Shannon and Pask, 1965; Cornaz *et al*., 1966).

The oxygen vacancies, which lower the anatase-to-rutile transformation temperature, can be created by annealing TiO_2 under certain atmosphere. Effects of oxygen vacancies on the anatase-rutile transformation of TiO_2 thin films were studied and annealed at various temperatures of 400–800 °C in air, vacuum and H_2 atmosphere. In both H_2 and vacuum atmosphere, the oxygen vacancies concentration increased with increasing temperature, whereas it remained constant in air. The amorphous-to-anatase and the anatase-rutile transformations occur at lower temperatures in hydrogen than in air or vacuum atmosphere because of the higher oxygen vacancy concentration in the TiO_2 film (Huang and Wong, 2011).

The anatase-to-rutile phase transformation in argon-chlorine atmosphere is 300 times faster than in air atmosphere at 950 °C. The transformed rutile percentage was 5, 65, and 92%, when anatase was heated in air for periods of 4, 24, and 48 h, respectively. In contrast, when the anatase was heated in argon-chlorine for just 10 min, the rutile fraction was 99% (Gamboa and Pasquevich, 1992).

2.3.5 Impurities, Presence of Foreign Elements or Doping

The presence of foreign ions affects the kinetics of the anatase-to-rutile transformation at elevated temperatures. The role of TiO_2 dopants is considered to facilitate an increase in surface-adsorbed species levels, improvement in charge carrier separation, introduction of mid-gap states, and reduction of the band gap (Hanaor and Sorrell, 2011).

The nature of the presence of foreign ions appears to control the stoichiometry of the TiO_2 by the formation of both titanium interstitial and oxygen vacancy concentration. The formation of oxygen vacancies was expected to accelerate the anatase-to-rutile transformation, whereas the titanium interstitial formation inhibited

the transformation. There are some reports that show that doping TiO_2 with Nb, Al, Ni, Ga, Ta, and W delays the anatase-to-rutile transformation, whereas, Mn, Fe, Cu, and Zn are generally believed to promote the phase transformation (Depero *et al*., 1999; Depero *et al*., 2000; Guidi *et al*., 2003).

The presence of foreign ions affects the titania defect structure and, therefore, the transformation rate, which enters either substitutionally or interstitially. The presence of interstitial ions inhibits the anatase-to-rutile transformation. However, substitutional ions may accelerate or inhibit the transformation depending on the substitutional ions type and size. Smaller ionic radius than Ti, e.g. Cu^{2+}, Li^{+}, or Co^{2+} can enter the TiO_2 structure substitutionally, and would be expected to increase the oxygen vacancy concentration, and thus the phase transformation. However, larger ions, e.g. S^{6+} and P^{5+} would be expected to decrease the oxygen concentration and the rate of anatase-to-rutile transformation, because it will be easy to make rearrangement of the TiO_2 structure (Shannon and Pask, 1965).

The anatase-to-rutile transformation in the presence of Fe_2O_3 was investigated in air and argon atmospheres (Gennari and Pasquevich, 1998). In the presence of Fe ions, the transformation rate in air is higher, and the transition temperature is lower than the corresponding one in undoped TiO_2. Moreover, the anatase-to-rutile transformation in the presence of Fe^{+3} in argon atmosphere is more rapid than in air because of the formation of oxygen vacancies. Thus, the transformation rate was strongly dependent on impurities and the weight percentage. The influence of doping on the anatase-to-rutile phase transformation of different forms of TiO_2 was studied. Table 4 shows some literature values for different titania forms and foreign elements.

The effects of silver on the phase transformation of electrospun TiO_2 nanofibre were also investigated. Pure and Ag-doped TiO_2 nanofibres were calcined for 4 h at a different calcination temperature of 0, 400, 450, 500, 600, 700, and 800 °C. An analysis of XRD patterns of the pure and Ag-doped electrospun TiO_2 nanofibre provided the influence of Ag on the anatase-to-rutile transformation. For both samples, they were initially amorphous, with crystalline anatase first appearing at 400 °C. The presence of the rutile phase was observed after calcination of pure TiO_2 nanofibre at 450 °C, and at 600 °C for Ag-doped electrospun TiO_2 nanofibre (Park *et al*., 2010).

Table 4: Compilation of literature values on the effect on impurity/doping on anatase-to-rutile transformation.

Wt. % of foreign ions	**Anatase (%)**	**Rutile (%)**	**Heating time, and temperature**	**Reference**
Pure	80	20	3 days, at 850 °C	(Rao et al., 1959; Iida and Ozaki, 1961; Shannon and Pask, 1965)
5%SrO	100	0		
5%CaO	90	10		
5%BaO	90	10		
5%K_2O	50	50		
5%Na_2O	30	70		
5%Li_2O	0	100		
Pure	5	95	3h, at 800 °C	
1%NaO	100	0		
1%MnO_2	100	0		
1%WO_3	100	0		
1%Fe_2O_3	98	2		
1%NiO	97	3		
1%Cr_2O_3	88	12		
1%MoO_3	84	16		
1%CoO	79	21		
Pure	5	95	1 h, at 708 °C	
5%Cl^-	51	49		
5%Zn^{++}	24	76		
5%$PO4^{--}$	100	0	1 h, at 870 °C	
5%SO^{4--}	71	29		
5%Al^{3+}	28	72		

2.3.6 Synthesis Method

The effect of the preparation method on titania transformation was studied and concluded that a major cause for differing transformation temperature ranges was the degree of crystallinity of the precipitate (Iida and Ozaki, 1961). It is also known that the method of anatase preparation caused the wide variation in the anatase-to-rutile temperature, which can probably be due to the impurity of anatase. Anatase can be prepared by hydrolysis of titanium sulphate, and this is possible due to the presence of sulphate ion impurity in the anatase. Thus, the transformation of impure anatase occurs at a much higher temperature than that of pure anatase (Yoganarasimhan and Rao, 1962).

Anodisation time has an appreciable affect on anatase-to-rutile transformation (Low *et al*., 2012). Uniform and highly ordered TiO_2 nanofibres were fabricated by the electrochemical anodic oxidation on Ti foil (*See Anodisation Method, Section 2.5.6*). The anodisation process was performed in Nalco solution with a concentration of 0.5M under an applied voltage of 20V for 5 or 10 minutes. The crystallisation and crystal growth of TiO_2 nanofibres were characterised using *in-situ* synchrotron radiation diffraction (SRD) at the temperature range of 25–700 °C. The anodised TiO_2 nanofibres were initially amorphous, but crystallised to anatase at ~ 400 °C and to rutile at ~ 550–600 °C. The rutile weight fraction for 5 min anodisation nanofibres were 54.2 wt% at 550 °C, 54.7 wt% at 600 °C, 54.8 wt% at 650 °C, and 56.7 wt% at 700 °C. The corresponding values for 10 min anodised nanofibres were 55.0 wt% at 550 °C, 55.2 wt% at 600 °C, 55.5 wt. % at 650 °C, and 59.2 wt. % at 700 °C. This implies that a longer anodisation time with the Nalco solution favours the fraction of anatase-to-rutile transformation (Low *et al*., 2012).

2.3.7 Particle/Grain Size

The kinetics of titania's structural transformation from anatase to rutile were studied extensively by various researchers using microcrystalline or nanocrystalline anatase. The nanocrystalline rutile is thermodynamically stable relative to nanocrystalline anatase and brookite under ambient condition. However, anatase is more stable than

rutile at particle diameters below 14 nm (Zhang and Banfield, 1998). The influence of particle size on TiO_2 phase transformation was studied using a mixed titania of anatase (5.1 nm, 46.7 wt. %) and brookite (8.1 nm, 53.3 wt. %), both isothermally and isochronally, at a reaction time of two hours in the temperature range 325–750 °C (Zhang and Banfield, 2000b). Results show that both anatase and brookite were transformed into rutile, but anatase was transformed before brookite. The anatase-to-rutile and brookite-to-rutile transformations depend on their initial particle size (Zhang and Banfield, 2000b). It was also reported by the same authors that the kinetics of nanocrystalline anatase phase transformation and the activation energy of nucleation are size dependent (Zhang and Banfield, 2000a). Anatase and brookite phases were transformed into the rutile phase after reaching a certain particle size (Zhang *et al*., 2000).

2.3.8 Surface Area

Anatase with the highest purity was used to study the effect of the surface area, which seemed to favour the anatase-to-rutile transformation. The anatase surface area of ~54 m^2/g and ~25 m^2/g was heated at 700 °C. The observation showed that the larger surface area slightly accelerated the anatase-to-rutile transformation (Yoganarasimhan and Rao, 1962).

2.4 Nanostructured TiO_2

Nanostructured materials have existed in this world for centuries. The field of nanoscience is relatively young, and a number of new terms have appeared, some of which are inconsistent. The modern boom in nanotechnology and nanoscience is to some extent a result of the recent advances in the methods of investigating and manipulating the small object. Based on the nanometre (nm), the nanoscale exists specifically from 1 to 100 nanometers, but definition can be used to some micrometers (Bavykin and Walsh, 2010).

Developing tools for probing and manipulating atomic scale objects was mostly driven by improvement in the resolution, reliability and availability of electron microscopy, including scanning electron microscopy (SEM), electron backscatter diffraction (EBSD), transmission electron microscopy (TEM), X-ray spectroscopy (EDS), X-ray diffraction (XRD), synchrotron radiation diffraction (SRD), X-ray photoelectron spectroscopy (XPS), and atomic force microscopy (AFM).

In general, TiO_2 has a low surface area compared to other semiconductors, which reduce the photocatalytic activity via influences the adsorption of organic pollutants on the TiO_2 surface (Li *et al*., 2012). The morphological modification, such as increasing surface area and porosity are one strategy that has been adopted for improving the photocatalytic efficiency of titania or other optical properties applications.

TiO_2 nanostructures have a reduced size and an increased surface area, which can lead to such interactions having a significant impact. A high surface area leads to a higher density of localised states when electrons involved from the valence band (VB) to the conduction band (CB), and the higher localised states provide valuable charge separation in a form of trapping sites for photo-generated charge carriers, by keeping electrons present due to terminated and unsaturated bonds on the surfaces (Barzykin and Tachiya, 2002). Reducing TiO_2 surface features down to the nanoscale can lead to new unique electronic, physical, and chemical properties, which can offer a development of novel application, towing to its quantum effect, regional confinement of matter, and ultra-high surface (Nalwa, 2004).

Nanostructured TiO_2 exhibits superior photocatalytic activity compared to conventional bulk TiO_2 because of its high surface area, and it is one of the most intensively researched substances of the past decade (Zhan *et al*., 2006). The TiO_2 specific surfaces are in the range of 200–300 m^2/g for nanotubes produced by hydrothermal method, 20–50 m^2/g nanofibre and nanorods produced by hydrothermal method, and < 20 m^2/g for nanotube arrays produced by the anodisation method (Bavykin and Walsh, 2010).

Nanostructured TiO_2 has been synthesised in a wide variety of shapes, including symmetrical spheres and polyhedrons, cylindrical tubes and fibres, or random and regular pores in solids. But unfortunately the nanostructured TiO_2 definition of that

various morphological forms has not been developed in a careful fashion, which has resulted in some confusion over their use. In the following sections, various shapes are discussed.

2.4.1 Zero-dimensional nanostructure (0-D)

Nanoparticles /Quantum dots

Nanoparticles are microscopic particles with size less than 100 nm, whereas quantum dots are nanoparticles scaled down to further lower dimensions between 2 and 10 nm. The most commonly used titania morphology is that of monodispersed nanoparticles/nanopowders such as Degussa P25, wherein the diameter is controlled to give benefits from the small crystallite size ~ 25 nm (high surface area, reduced bulk recombination) without the detrimental effects associated with minuscule particles.

2.4.2 One-Dimensional Nanostructures (1-D)

The one-dimensional TiO_2 nanostructures are extremely important because they can efficiently transport electron/photon and optical excitations. This enhancement of morphology has a larger specific surface and pore volume as compared to TiO_2 nanoparticles. The directional transport in one-dimensional nanostructure is vital to the function and device integration at the nanoscale.

In general, one-dimensional (1-D) TiO_2 nanostructures have received much attention recently because of their unique properties, exploitable for device applications, and structures that are ideal for studying the dependence of physical properties on directionality (Archana *et al*., 2009). Elongated structures are of particular importance, as long, thin nanotubes, nanorods, nanowire, nanoneedles, nanobelts, and nanofibres can provide a high specific surface area during the photocatalytic reaction (Bavykin and Walsh, 2010).

TiO_2 nanorods (TNR), nanowire (TNW), and nanoneedles (TNN), nanobelts (TNB)

The nanorods, nanowires, nanoneedles, and nanobelts are long and solid cylinders with a circular base. Major differences between them are the length and the thickness.

Figure 14 shows SEM images of TiO_2 nanowires (TNW) obtained by ultrasonically dispersing TiO_2 nanofibres for 0.5 h in acetic acid and thick film developed using the NW paste. NWs are produced by a bottom-up approach of having self-assembly of the target material from vapor, liquid, or solid phases through nucleation and growth under optimised conditions of pressure, temperature, and concentration.

Electrospinning is one of emerging bottom-up techniques for fabricating 1-D nanostructures (*See Electrospinning Method, Section 2.5.7*) including nanowires (NW), nanorods (NR), nanofibres (NF) and nanoneedles (NN) that work on the principle of asymmetric binding of a charged liquid jet when it is enhanced by a longitudinal electric field.

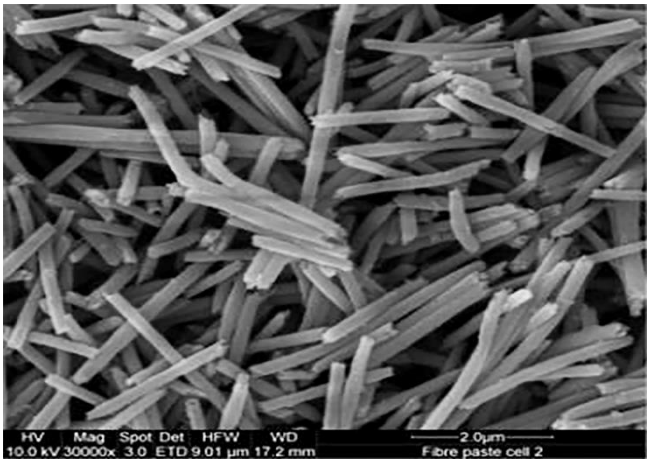

Figure 14: SEM images of the electrospun TiO_2 nanowires.

(Archana *et al*., 2009).

Figure 15 shows TEM and SEM micrographs of TiO_2 nanobelts, which were prepared by a hydrothermal method (*See Hydrothermal Method, Section 2.5.2*). TiO_2 nanobelts are 1-D nanostructures with a length of several tens of micrometers, more than 100nm width, and 20-25 nm thickness (Hu *et al*., 2010).

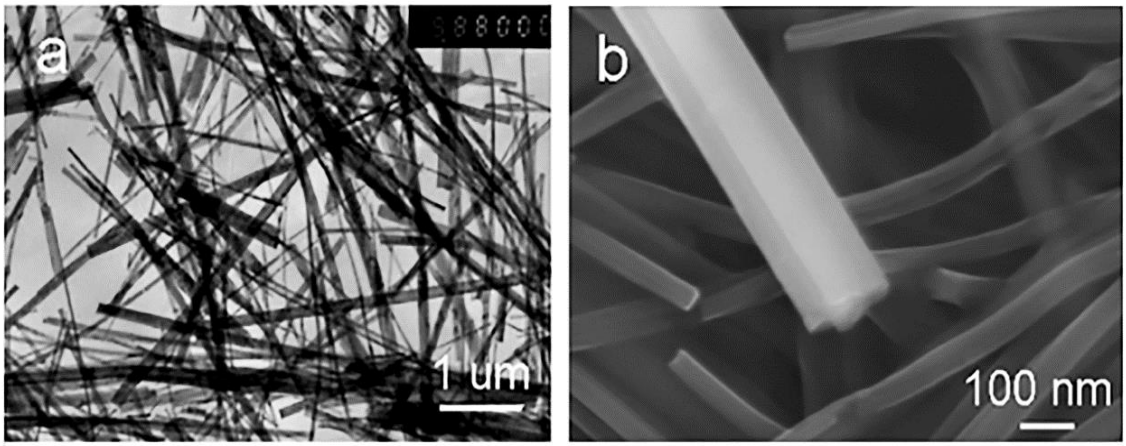

Figure 15: (a) TEM and (b) SEM micrographs of TiO_2 nanobelts.
(Hu *et al*., 2010).

TiO_2 nanofibres (TNF)

The nanofibres are one dimensional long, solid and parallel piped nanostructures like other elongated TiO_2 structures with a diameter which is typically in the nano-range, but the length can be several tens of micrometers. Figure 16 illustrates the SEM image of electrospun nanofibres. The nanofibres have smooth surfaces with a random distribution.

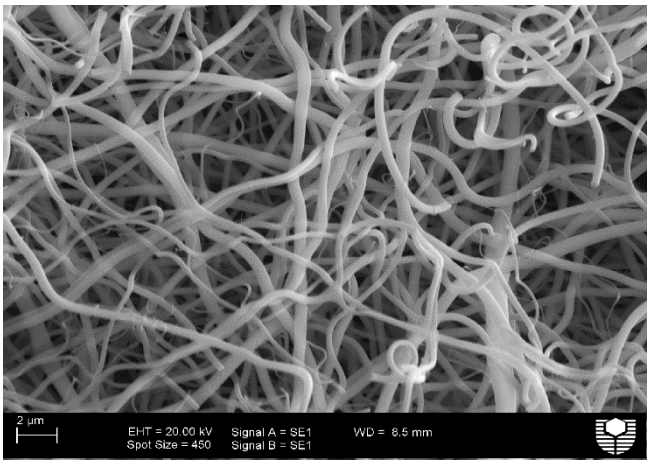

Figure 16: Electrospun TiO_2 nanofibres.

1-D electrospun nanofibres composed of well-aligned nanofibrils in the fibre direction are beneficial for the enhancement of the surface area, crystallinity, and the

photocatalytic activity for hydrogen evolution. This methodology of the electrospun TiO_2 offers a straightforward guide to the immobilisation of novel nanofibre photocatalysts for water splitting and hydrogen evolution. 1-D electrospun nanofibres with extremely aligned bundled nanofibrils are beneficial for the enhancement of the higher photocatalytic activity, large surface area, and crystallinity. The 1-D electrospun Polymer/TiO_2 nanofibres were prepared by combining electrospinning and sol-gel techniques. For example, electrospun PVP/TiO_2 nanofibres were formed with lengths up to several centimetres and nanometre diameter size (Li and Xia, 2003). These amorphous PVP/TiO_2 nanofibres were converted into crystalline titania phases (anatase, and rutile) without changing their morphology via calcination at elevated temperatures. Pure TiO_2 nanofibres with smaller diameter size were obtained from calcination of the as-spun nanofibre at elevated temperatures. These nanofibres were utilised in the photocatalytic activity for hydrogen evolution, which showed the highest activity, when compared with a nanofibre prepared by other methods, e.g., hydrothermal method, and also higher than reference commercial of TiO_2 nanoparticles (Chuangchote *et al*., 2009).

TiO_2 nanotube (TNT)

Nanotubes are nanometre scale tubes, with a hollow centre, as compared to other one-dimensional nanostructure (See TiO_2 nanotube arrays in Figure 17). The nanotubes are long cylinders having a hollow cavity positioned at their centre and lying along their length. The nanotube structure is extremely attractive because of its high surface area and thermal stability against high temperature calcinations (Wang *et al*., 2009).

The first nanotubes were carbon nanotubes in 1991, which was discovered and developed into multi-walled carbon nanotubes by Sumio Ijima and many other scientists from NEC Corporation, Fundamental Research Laboratories, Japan (Iijima, 1991). The preparation of finite carbon structure consists of needle-like tubes. The nanotubes grow at a negative end of an electrode used from an arc discharge. Electron microscopy revealed that each needle comprised coaxial tubes of graphitic sheets. On each tube, the C-atom hexagons were arranged in a helical fashion around the needle axis. The carbon nanotubes formation, range in a few tens of nanometres in diameter.

Scientists have also synthesised nanotubes from various oxides such as aluminium, zinc oxide, and hafnium.

The TiO_2 nanotubes (TNT) were synthesised by many approaches such as anodic oxidation of titanium, deposition with templates, and hydrothermal treatment with concentrated alkali solutions (Hoyer, 1996; Imai *et al*., 1999; Michailowski *et al*., 2001; Du *et al*., 2001; Seo *et al*., 2001; Liu *et al*., 2002; Tian *et al*., 2003; Yu *et al*., 2010). The TiO_2 nanotubes were synthesised by hydrothermal method, where the tubes can have a multilayered onion shape with a number of two to ten layers, and are usually straight with relatively constant diameter and being open at both ends. Moreover, TiO_2 nanotubes are produced by anodic oxidation of titanium with one open end and another close end. Through anodisation methods, TiO_2 nanotubes bear similarities to alumina nanotubes. A template of aluminium or titanium can be used for the synthesis of aluminium or TiO_2 nanotubes, respectively.

TiO_2 nanotubes are highly exciting material systems, which can be employed in a wide range of applications and potential applications. TiO_2 nanotubes arrays are used as electrodes for solar cell devices and batteries, and for carbon in fuel cells due to its highly effective supporting matrix. Gas sensors, water photoelectrolysis, and photocatalyst devices are other potential applications of TiO_2 nanotube arrays. In particular, one-dimensional semiconductor TiO_2 nanotube devices suggest improved energy conversion efficiencies in DSSCs (Yang *et al*., 2008).

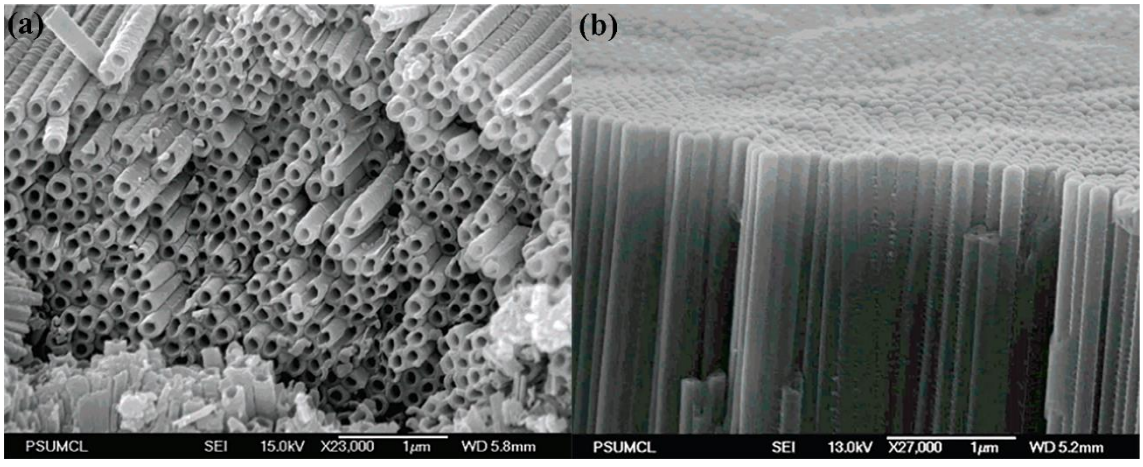

Figure 17: SEM image of the highly ordered TiO_2 nanotube arrays at (a) top view, and (b) bottom view.

(Paulose *et al*., 2006)

2.4.3 Two-Dimensional Nanostructure (2-D)

TiO_2 nanofilm and nanosheets

The nanosheets and nanofilms are very thin two-dimensional nanostructures (10 × 100 × 100 nm). They have two types of layers, namely single nanosheets, and multilayer nanosheets. The two types can be folded to make singles or multilayered nanotubes via the alkaline hydrothermal route (Bavykin and Walsh, 2010).

Nanosheets can be converted to nanofibres instead of scrolling into nanotubes under alkaline hydrothermal conditions. An increase in Ti source concentration can result in a faster rate of nanosheets growth, with less effect on the rate of nanosheets scrolling. Thus, the thicknesses of the nanosheets have a particular value where they become too rigid to bend, before curving can occur to the formation of nanofibre rather than nanotubes (Bavykin and Walsh, 2010).

TiO_2 nanosquares (TNS)

Titania nanosquares are another 2-D nanostructure, which were prepared by a mild solvothermal method (Yu *et al*., 2013). Figure 18 shows the TEM photographs of titania, which is composed of square-like crystals with a length of 10-20 nm and area of ~ 200 nm^2.

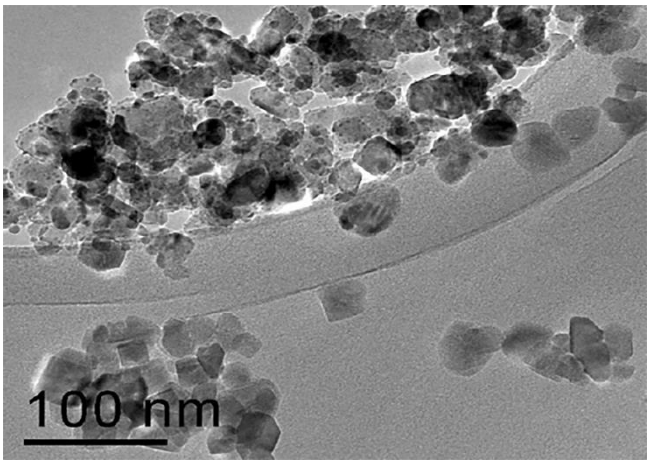

Figure 18: TEM image of titania nanosquare nanocrystals.

(Yu *et al*., 2013)

2.4.4 Three-Dimensional Nanostructure (3-D)

The three-dimensional nanostructures comprise of thin films ranging from nm to μm in dimensions with several nm in all dimensions such as metals, semiconductors, and magnetic materials. The thin films' functionality is particularly enhanced when they are made of multiple layers combining all layers' functionalities together. This structure saves cost and allows manipulation of refractive index to a higher degree (Rao and Cheetham, 2001).

Superlattices

The periodic structure of alternating thin films of a semiconductor such as TiO_2 forms an arrangement known as superlattices. This structure is made of different bandgap semiconductors and results in the formation of the quantum well, which confines the direction of charge flow through the lattice (Rao and Cheetham, 2001).

2.5 Synthesis Methods of Nanostructured TiO_2

A wide range of bulk TiO_2 synthesis techniques were used, the major ones being sol-gel, hydrothermal treatment, solvothermal, microemulsion, vapor deposition, and mechanical milling. In the last decade, nanostructured TiO_2 was an important property and was developed by utilising the same synthetic methods and creating new synthetic methods, such as the sol-gel method, hydrothermal, solvothermal, electrospinning, and anodisation. Hitherto, various techniques were used to synthesis nonporous materials, nanoparticles, nanowires, nanorods, nanotubes and nanofibres of TiO_2 (Chuangchote *et al*., 2009; Low *et al*., 2012).

2.5.1 Sol-Gel

The sol-gel is a preferred method as it is a low temperature, and cost effective process. The sol-gel method was developed as one of the most promising ways of

synthesising porous TiO_2 materials. Substances with controlled pore TiO_2 structure such as pore size distribution, porosity and pore shape are useful in photocatalytic applications. Compared to other synthesis methods of photocatalysts, the sol-gel method presents certain advantages, such as the possibility of depositing onto complex-shaped substrates, highly pure and homogeneous products at low temperature, uniform aperture size, and easy control of the doping level (Yang *et al*., 2011). The most common way to impart crystallinity of thus formed polymeric gel, is calcination at elevated temperature, but the prepared crystalline TiO_2 has increased particle size, and decreased surface area. Moreover, the sol-gel method is used to dope TiO_2 with various forms. It also is used as a combination method with electrospinning techniques for the preparation of doped electrospun TiO_2 nanofibres (Park *et al*., 2010).

2.5.2 Hydrothermal Method

In 1998, TiO_2 nanotubes were the first nanostructured TiO_2 forms, which were synthesised by applying the hydrothermal method (Kasuga *et al*., 1998). It is a simple method for the preparation of TiO_2 nanotubes, involving the treatment of amorphous with a concentrated solution of NaOH. In a typical process, several grams of TiO_2 raw material can be nanotubes at a temperature from 110 to 150 °C, followed by washing with water and HCI. The formation of TiO_2 nanotubes occurred spontaneously and was characterised by a wide distribution of morphological parameters, with a random nanotubular orientation. TiO_2 nanotubes prospered via the alkaline hydrothermal method were observed only in multilayered walls. The key factors affecting the titania nanotube structure, according to the hydrothermal method, include the washing process, calcination temperature and atmosphere, and the important role of residual sodium ions in the stabilisation of the tubular framework structure (Sun and Li, 2003).

This method can also be used to produce TiO_2 nanofibres (TNF) besides the TiO_2 nanotubes (TNT) under the hydrothermal condition through the treatment of anatase TiO_2 powder with NaOH for one week at 130 °C, and 110 °C, respectively. The nanofibre is elongated morphology with a typical width being in the range of 20–200 nm, and length of several micrometers (Lin *et al*., 2008; Kuo *et al*., 2007).

Multilayered TiO_2 nanosheets are possible to obtain by the hydrothermal treatment method. Nanosheets show an important role in the mechanism of the nanotubes formation, which are synthesised by this method. Nanotubes TiO_2 can contain a few multilayered TiO_2 nanosheets, which can be scrolled or folded into a nanotubular morphology (Bavykin *et al*., 2004; Ma *et al*., 2004).

2.5.3 Template Method

This method is called the template method, because the pores in the nanoporous membranes are used as templates. The Template method is an old approach and a classic bottom-to-up method which has become extremely popular during the last decade (Hulteen, 1997). The template is particularly suitable for the generation of thin films and powders with a well-defined porosity. Moreover, the template synthesis uses a nanoporous membrane as a template to make nanofibres, nanowires, and nanotubes. The most important feature of this method is that tubes and fibres composed of electronically conductive polymers and semiconductors can be prepared in a nanostructure such as titania nanotubes and nanofibre (Martin, 1996). Although the template is a directed method that provides a straightforward and reliable stratagem for processing 1-D nanostructured TiO_2, it involves multiple (at least three) steps: template fabrication, filling or coating of the templates surface with titania precursor, and the selective removal of the templates (Li and Xia, 2003).

The preparation of TiO_2 nanotubes involves the controlled sol-gel hydrolysis of titanium solutions, followed by the polymerisation of TiO_2 in the self-assembled template molecules or deposition of TiO_2 onto the surface of template aggregates (Bavykin and Walsh, 2010). This method has some disadvantages in most cases; the template material is sacrificial and needs to be destroyed after synthesis, leading to increased cost of materials. Moreover, it is also important to maintain a high level of surface cleanliness (Bavykin and Walsh, 2010). The template synthesis has been used to synthesis nanofibres in recent years. Templated PAN nanofibres with different diameter and densities were synthesised using the PAN precursor solution into a solidifying solution under a necessary pressure (Feng *et al*., 2002). The template can consist of a 13 mm diameter, 60 µm thick anodic aluminium oxide membrane with

straight parallel porous channels arranged in a regular hexagonal pattern with an average pore diameter of ~ 102.4 nm and a pore density of ~ 6.43×10^9 pores / cm^2.

2.5.4 Chemical Vapour Deposition (CVD)

The chemical vapour deposition (CVD) is a chemical method like the sol-gel process, but at relatively high temperatures it can form a crystalline material of solid film under certain crystal structures. The TiO_2 film can be obtained by chemical reaction between the heating TiO_2 substrate and the vapour, where increasing temperature is necessary to maintain the chemical reaction and crystalline TiO_2.

2.5.5 Layer-by-Layer Method

The layer-by-layer self-assembly method was developed to produce multilayer nanofilm structures containing semiconductor nanoparticles. In this method, polyelectrolytes are employed to provide electrostatic attractions with the inorganic material in a next layer and, therefore, reduce the defect formation within the multilayered structures (Zhang *et al*., 2010).

Nanoporous TiO_2/poly (sodium-4-styrenesulfonate) (PSS) multilayered films were synthesised by applying layer-by-layer self-assembly (Hao *et al*., 2005). A TiO_2/PSS solution was rinsed extensively with water. Then an ordered structure multilayered TiO_2/PSS film was obtained. The TiO_2/PSS films deposited on a quartz substrate were heated to elevated temperature for two hours in the ambient atmosphere. Moreover, TiO_2 nano-films assembled with TiO_2 nanoparticles with similar polyelectrolyte component (titanium (IV) bis(ammonium lactato) dihydroxide (TALH)) were fabricated by employing the layer-by-layer self-assembly method at a room temperature (Kim *et al*., 2006). Figure 19 shows the schematic illustration of the procedures of fabrication the TiO_2/TALH multilayered nano-films. In the first step, a negative substrate, glass and Si/SiO_2 were obtained by KOH treatment in ultrasonication for 5 min and then rinsed in water. The substrates were immersed into TiO_2 colloidal solution and polyelectrolyte for 10 min and TALH solution from 10 s to 10 min in the second and third steps, respectively. The second and third steps were

repeated 30 times in the fourth step. The synthesised $(TiO_2/TALH)_{30}$ multilayered nano-films showed a high transmittance in the visible range for optical applications with refractive index (ca. n=1. 75), and high photocatalytic property by decomposing methyl orange molecules gradually, according to UV light irradiation (Zhang et al. 2008).

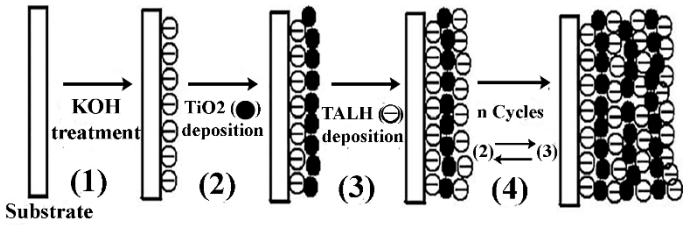

Figure 19: Schematic illustration of the procedures to fabricate the $(TiO_2/TALH)_{30}$ nano-films using the layer-by-layer self-assembly method.

(Kim *et al*., 2006)

The combination of the electrospinning method with layer-by-layer technique was used to fabricate hollow titania-containing multilayered nanofibres. In the electrospun process, 1.5 g of polystyrene (PS, M_w =185000 g/mol) was dissolved in a mixture solvent of tetrahydrofuran (THF) and N, N-dimethylformamide (DMF) with a volume ratio of 1:1. The solution was stirred for two hours to get a homogeneous sol-gel. Then, the sol-gel was loaded into a 5 gauge syringe with stainless needle, which was connected to a high voltage supply capable of generating voltage up to 15 kV. An automatic syringe pump was used to control the feeding rate of the sol-gel, and the needle-to-collector was 10 cm (*See Electrospinning Method, Section 2.5.7*). To obtain the hollow multilayer TiO_2 containing nanofibre, the synthesised electrospun PS nanofibres were selected as the template and immersed into PEI/TiO_2 solution. Four multilayered polymer of $(PEI/TiO_2)_4$ coated electrospun PS nanofibre were immersed into THF to remove the PS core. To remove the PEI solution inside the nanofibre, the nanofibre was centrifuged at 1000 rmp for 1 min and washed with a solvent (See Figure 20). The diameter of the obtained hollow multilayered nanofibre is ~ 700 nm, and its shell thickness is ~ 140 nm. This nanostructured titania nanofibres have the highest

photocatalytic activity to degrade methylene blue (MB) solution compared to with a TiO_2 film because of their unique hollow structures (Zhang *et al*., 2008).

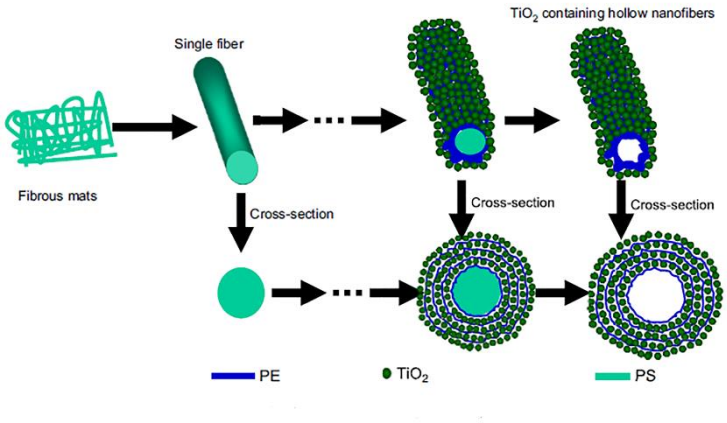

Figure 20: Schematic illustration of the procedures to fabricate the hollow titania-containing multilayered nanofibres using nano-films combination of layer-by-layer technique with electrospinning method

(Zhang *et al*., 2008).

2.5.6 Anodisation Method

An alternative method to the hydrothermal method, which facilitates a structured array of nanotubes with a narrower distribution of morphological parameters, is the anodisation method. The anodic synthesis was initially developed for the preparation of aluminum oxide nanotubes and later adapted for TiO_2 nanotube arrays. This method is an electrochemical approach for the preparation of elongated TiO_2 nanostructures.

In 1999, the first anodised TiO_2 nanotube arrays were reported by Zwilling and his co-workers (1999) using electrochemical anodisation of Ti-based alloys in an acidic, fluoride-based electrolyte. In the anodisation cell (Figure 20), platinum (Pt) foil is used as the counter anode, and the titanium (Ti) foil acts as the cathode inside H_2O-NHF electrolyte at 10-30 V for several hours at a room temperature (Gong *et al*., 2001). The nanotubes were all oriented in the same direction, perpendicular to the surface of the electrode. Anodisation of a Ti substrate in a fluoride-containing electrolyte had highly

ordered and vertically oriented titania nanotubes with an open top (facing the electrolyte) and closed bottom, and a narrow distribution of tube diameter, spacing and lengths.

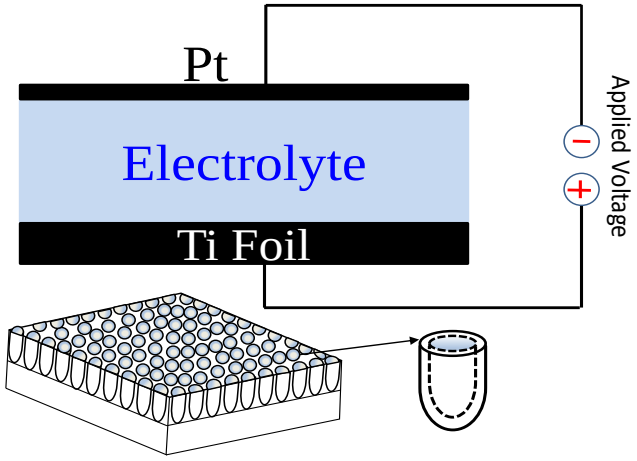

Figure 21: Schematic of the anodisation process.

Figure 22 shows SEM images of TiO_2 nanotubes taken (a) at the top (b) in the middle and (d) close to the bottom of a tube laser. As can be seen, the walls thicknesses of the nanotubes are thinner at the open end and relatively thicker at the closed end.

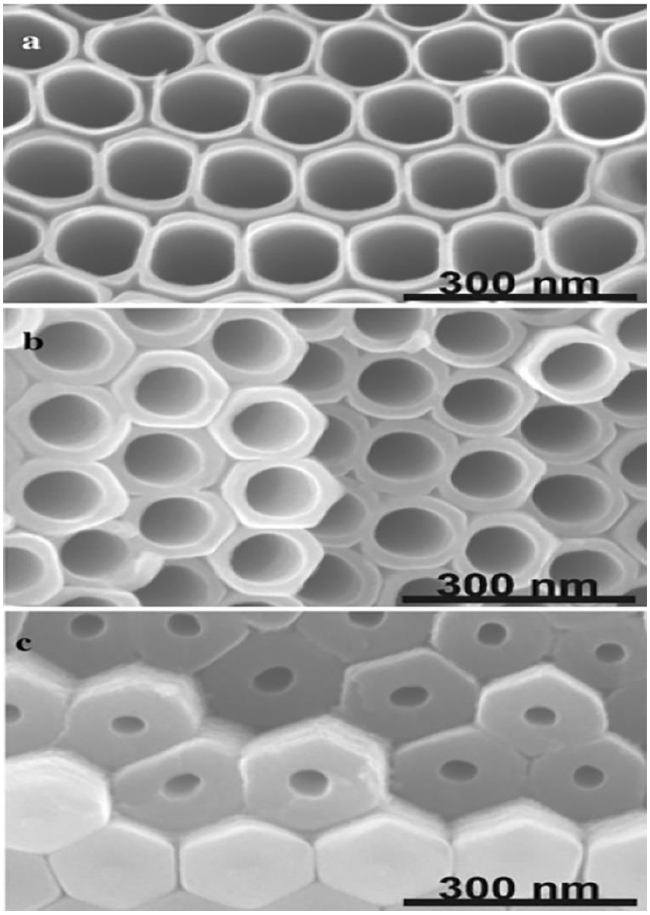

Figure 22: SEM images of TiO_2 nanotubes were taken (a) at the top (b) in the middle and (d) close to the bottom of a tube laser

(Macak *et al*., 2007).

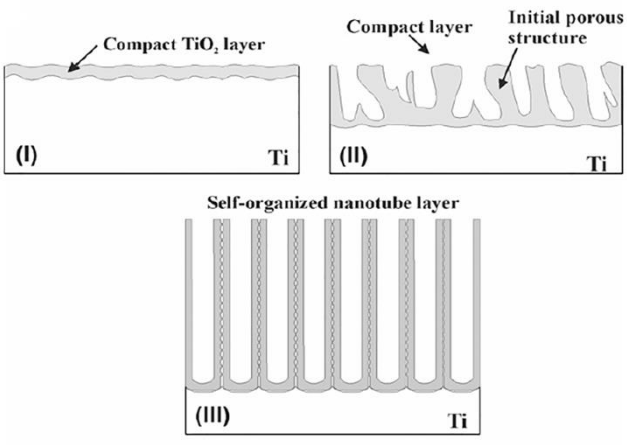

Figure 23: Schematic set-up for anodisation experiment.

(Macak *et al*., 2007).

Figure 23 shows the schematic set-up for the anodisation experiment. Anodisation of Ti using an electrolyte of fluoride containing polyhydric alcohols such as ethylene glycol or glycerol were used as it results in an ordered array of TiO_2 nanotubes with a smooth surface and a very high aspect ratio. It provides a scalable, easy and inexpensive technique for future industrial application. The anodisation method has a good degree of controlling the nanotube diameter, length, and wall thickness. Changing the dimensions of TiO_2 nanotube array have also been studied, such as the tube length, the pore diameter and the tube wall, which can influence the titania applications.

The formation, growth rate and morphology of TiO_2 nanotubes during anodisation depends on various factors such as electrode areas, the distance between electrodes, temperature, synthesis time, applied voltage, and electrolyte composition. It was found that the field emission properties also affected the TiO_2 nanotube diameter and height (Alivov *et al*., 2010). Various electrolytes were used for titanium anodic oxidation under different anodic conditions with metallic titanium existing in the close-packed hexagonal (α phase) or body-centered cubic (β phase) forms. Anodic titanium foil consists mostly of titania, but also a certain degree of non-stoichiometric TiO_2. Different researchers have different compositions (TiO_{2-x}, where x is the oxygen vacancies) due to differences in electrolyte composition used, oxidation conditions, etc. Moreover, the anodic oxide of Ti foils may contain various amounts of elements other than titanium and oxygen, depending on Ti foils and the electrolyte. Moreover, the water content of ethylene glycol as electrolyte was found to affect the formation of TiO_2 nanotube arrays (Raja *et al*., 2007).

The effects of anodising potential, anodising temperature, concentration, anodisation voltage and time of the formation of titania nanotube arrays were investigated by Xie *et al*. (2008). It was found that the anodizing temperature and concentration were significant parameters for the formation of nanotubes while the applied voltage and time mainly determined the nanotube dimensions. An active surface area was increased by increasing the anodisation time or voltage, which led to enhanced photovoltaic currents, and thereby an overall higher performance of the dye-sensitised solar cells (Xie *et al*., 2008).

Anodisation time and the fluoride electrolyte can be tuned for obtaining the tube length, whereas the tube diameter can be controlled by the anodisation voltage. Experimental results indicate that the relationship between the anodisation time and the nanotube length is present logarithmically, and the growth rate decreases with the anodisation time as the length of the nanotubes increases, whereas it is present approximately linearly between the anodisation voltage and nanotube diameter. Solvent type is another factor that can affect nanotube formation and growth including the electrolyte chemistry.

After anodisation formation, TiO_2 nanotube arrays are amorphous, which can be transformed into crystalline anatase, and then the crystalline anatase is transformed to crystalline rutile at elevated temperatures (*See Kinetics of TiO_2 Phases Transformation, Section 2.3*), but annealing can also affect the nanotube morphology, and then start collapsing.

Some reports indicate the presence of crystalline anatase, a mixture of anatase and rutile, or crystalline rutile in the tube wall, particularly if the anodisation is carried out at higher voltages (Marchenoir *et al*., 1980; Delplancke *et al*., 1994). Albu *et al.* (2010) reported that significant changes in amorphous TiO_2 nanotubes morphology and structure can be induced by TEM e-beam irradiation (operating at 200 kV). HR-TEM images of the as-anodized TiO_2 nanotubes showed that crystalline zones formed with increasing TEM observation time. Thus, the amorphous TiO_2 nanotubes seem to be affected by the electron-beam, which induced crystalline titania.

The common fabrication of titania nanostructure which was obtained through this method is nanotubes (TNT), but anodised titania with various nanostructures can also be obtained by the anodisation method. For example, anodisation of titanium in 1.0 M NaCl solution with bias 30 V applications for several minutes into a chloride anion-based electrolyte is used to synthesis anodised titania nanofibres (Beh *et al*., 2011; Low *et al*., 2012; Li *et al*., 2012).

2.5.7 Electrospinning Method

Anton Formhals (1934) patented his first invention on the electrostatic spinning of fibres. The invention did not claim e-spinning as a technique for harnessing technology, as it took more than 60 years for e-spinning to gain momentum as an effective technique for synthesising polymeric fibres, i.e., one-dimensional fibres. This method is not only employed in university laboratories but is also increasingly being applied in industry and everyday life.

As shown in Figure 24, the electrospun experimental setup mainly consists of a high voltage power supply (5–30 V), a syringe pump, a syringe with a conductive needle, and a conductive collector (e.g., a flat stand collector, or a rotating drum), copper wire, and a sol-gel solution. In a typical process, a polymer and melt solution is injected with a small needle under the influence of an electric field as strong as several kV/cm (Li and Xia, 2003; Hassan *et al*., 2012; Zhu, 2012; Wu *et al*., 2012; Li *et al*., 2012b).

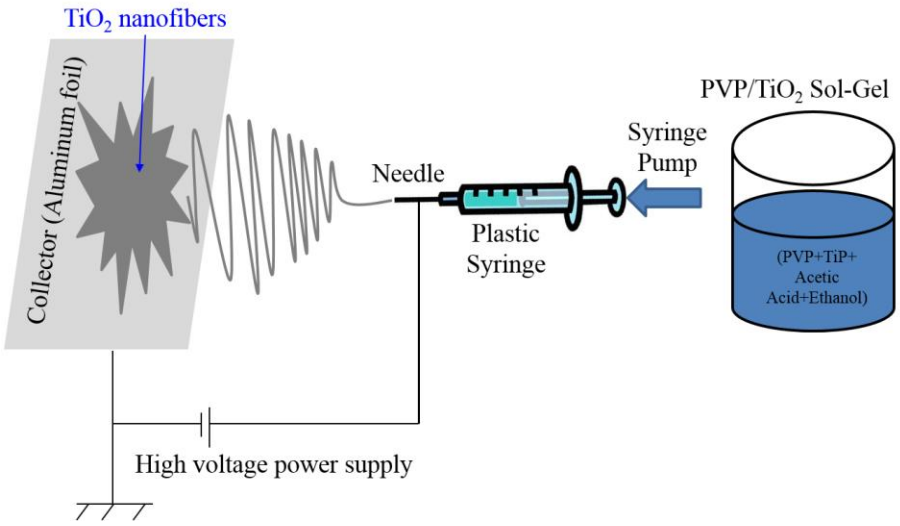

Figure 24: Schematic of electrospinning process for TiO_2 nanofibres.

The sol-gel solution is extruded from the microneedle tip at a constant rate by the syringe pump, forming a droplet, which is stretched into a conical shape by the applied voltage. It is named as Taylor cone after the researcher who reported it for the first time (see Figure 25). At the apex of the Taylor cone, a jet is spouted and breaks down into charged droplets that are sprayed out when the sol-gel does not contain any

spinning aid. This phenomenon is known as electrospraying. The breakdown of the jet into small droplets is due to the effect of surface charges that tend to create larger surfaces in order to decrease the charge density over a larger area, while the surface tension tends to keep the droplet large, to reduce the specific surface area.

At the high electric field, the effect of the surface charge is more favoured by the effect of the surface tension, which leads to smaller droplets with larger specific surface area. By adding the polymeric spinning, the viscosity of sol-gel is increased to retard the formation of droplets by the chain entanglement of the polymer. When the effect of the surface tension and the viscosity at the higher concentration overcomes the breakdown by the surface charge, the jet maintains its fibrous morphology. As the electric field is increased, the effect of the surface charge gets stronger, to result in thinner fibres with larger specific surface area. After a short flight from the ejection, the behaviour of ejected fibres gets unstable, which can be described by three different instability modes ie. the Rayleigh instability, the axisymmetric instability and the non-axisymmetric instability. In an occasion when the system is highly electrically charged by the electrospinning condition, the behaviour of the jet is governed by the non-axisymmetric instability in which the jet flies in a random whipping motion at a high frequency. The whipping instability is of crucial importance in the electrospinning process because the fibre gets elongated during the whipping motion that consequently results in the fibre thinning as well. The jet will elongate when the droplets become electrospray, if the molecular cohesion of the material is a suitable sol-gel (Hardick *et al*., 2011).

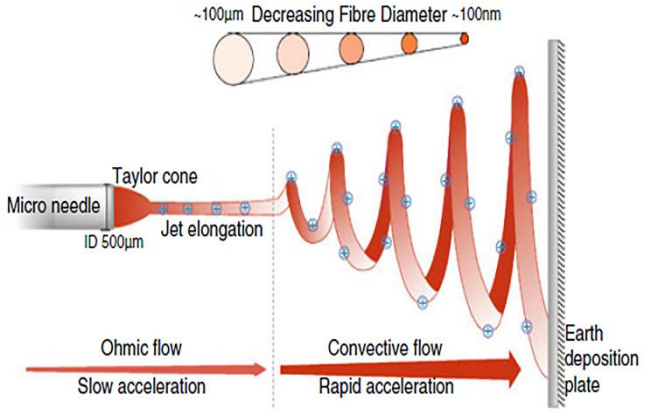

Figure 25: Nanofibre formation by electrospinning process uses an efibrescal charge to draw fibres from a polymer-solvent solution.

(Hardick *et al*., 2011).

Electrospinning has been recognised as an efficient method for 1-D nanofibres fabrication, and the diameters of electrospun nanofibres materials can shrink from micrometers to nanometers. This appears as an amazing characteristic such as a very large surface area to volume ratio with a process that attracted growing interest quickly, triggered by potential nanofibres application in the nanotechnology. The electrospinning is a relatively new and easy method for fabrication of very long nanofibres compared with other nanofibres prepared by anodisation, self-assembly, and template methods. Moreover, electrospinning is a simple, and cost-effective technique applicable at industrial levels for fabricating one-dimensional nanofibres, which have numerous and diverse potential application, including composite materials, medical materials, filtration devices, and bioengineering materials. The high surface makes the nanofibres attractive as in drug delivery, catalyst support, and even in energy cells (Hassan *et al*., 2012; Zhu, 2012; Wu *et al*., 2012).

Electrospun nanofibres can be collected on a conductive surface to form nonwoven mats, which is one of the attractive features associated with the electrospinning method. The electrospun nanowoven mats are characterised by high surface areas and relatively small pore size, making them excellent candidates for use in filtration and membrane applications. Therefore, the electrospinning method has been used for many applications and potential application, such as drug delivery, membrane, tissue engineering, protective clothing, wound dressing, filtration, and electronic application (Wu *et al*., 2012; Samadi *et al*., 2012). McCann *et al.* (2005) synthesised porous electrospun TiO_2 nanofibres using miscible solvents with immiscible polymers followed by calcination of the nanofibres at an elevated temperature. The porous TiO_2 nanofibres have a much larger surface area compared to the solid TiO_2 nanofibres, which can have potential applications such as photocatalysis, energy storage, catalysis, and fuel cells.

Because of the particular interests in the electrospun nanofibres applications, great efforts have been made to study the processing parameter effects. In general, electrospun nanofibres diameter, size, and morphology depend primarily on three processing parameters which include conditions of sol-gel solution, electrospinning, and ambient environment (Huang *et al*., 2003).

Firstly, the solution properties have important influences on electrospun nanofibre diameters, which include polymer concentration, surface tension, viscosity, electrical conductivity, molecular weight distribution and architecture of the polymer, which are related to one another (Fridrikh *et al*., 2003). The viscosity of the so-gel solution depends on the molecular weight and concentration of a polymer, solvent, and another source, where the polymer concentration is used for controlling beads and fibre diameters (Fridrikh *et al*., 2003; Patra, Easteal *et al*., 2009; Inai *et al*., 2005). A higher TiO_2 concentration in a precursor solution will increase the TiO_2 fibre diameter (Li and Xia, 2003; Li *et al*., 2012b).

Secondly, needle tip-to-collector distance, needle size, flow rate, and applied voltage are the electrospinning conditions (Fridrikh *et al*., 2003). The applied voltage is a significant factor for electrospinning conditions in the fibre diameters, where a high applied voltage (i.e., strong electrical repulsive forces) decreases the nanofibres diameter, resulting in elongated and highly stretched fibres (Kumar *et al*., 2007; Patra *et al*., 2009). One of the most important roles in determining the fibre diameter and bead formation is a flow rate, as it determines the amount of sol-gel solution available to be stretched into nanofibres (Fridrikh *et al*., 2003; Li and Xia, 2003). A large needle tip-to-collector distance, applied high voltage setting, a low flow rate, and a comparatively low concentration of polymer solutions reduce the variation in product quality of electrospun fibre mats with a minimum number of experiments (Patra *et al*., 2009). During the electrospinning process, the size and shape of the needle tip affect the formation of Taylor cone and nanofibres oscillation (Ksapabutr *et al*., 2005). Ksapabutr *et al*. claimed that a sawtooth needle shape allowed for Taylor cones of greater length than its standard and flat counterparts (Ksapabutr *et al*., 2005).

Aspects of the atmospheric environment, such as temperature, pressure, and humidity, belong to the last set of parameters. The average nanofibre diameter

decreases with decreasing atmospheric humidity and increasing atmospheric temperature (Hardick *et al*., 2011).

E-spinning produces fibres and has been shown to produce many other "one-dimensional" shapes including nanofibres, nanorods, nanowires, and nanoneedles, nanobelts and hollow tubes. The nanotubes (core-shell fibres) or hollow fibres can be produced by a special electrospinning method and complex architectures. Electrospun TiO_2 nanotubes have been synthesised by a fabrication process of core-shell nanofibres (see Figure 26). Two syringes feed, "Inner fluid" and "Outer fluid", inter-separated and coaxial to the spinneret. Under high voltage, the liquid of electrospinning is drawn out from spinneret and forms a "compound Taylor cone" with a core-shell structure. The core-shell structure is built and kept in the fibres through spinning solid and can be collected from a collector.

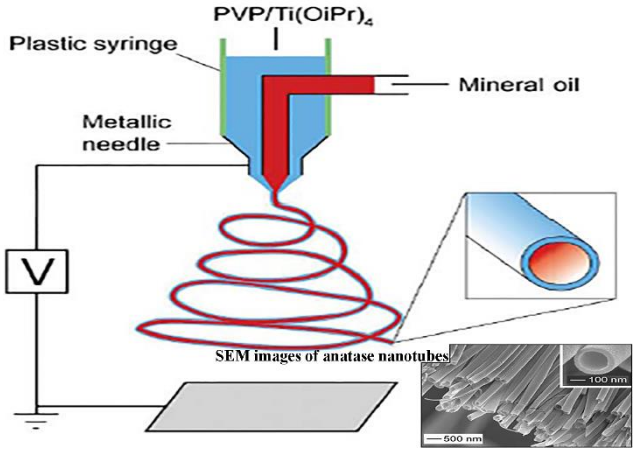

Figure 26: Schematic for fabrication of core-sheath electrospun TiO_2 nanofibres. (McCann *et al*., 2005).

A wide range of composites, polymers, and ceramic precursor solutions have been electrospun into fibres. The electrospinning technology enables the production of continuous polymer or metal oxide/ceramic nanofibres, which has been in the process of development since 1934 (Dzenis, 2004). In 2002, the first report of electrospun metal oxide composite fibres was synthesised by Dai and his co-workers (Dai *et al*.,

2002). The electrospun alumina borate solution was mixed with polyvinyl alcohol (PVA) to form composite alumina nanofibres.

Electrospun TiO_2 nanofibres were the next metal oxide into composite nanofibres (Li *et al*., 2004). Nanofibres of TiO_2 metal oxides have been prepared from a polymer solution containing suitable TiO_2 precursors, and stabilisers. The viscosity of the TiO_2 solution can be adjusted by molecular weight and concentration of the polymer, allowing sol-gel to be electrospun into a well-defined composite amorphous titania/polymer nanofibres. Crystalline TiO_2 nanofibres are obtained by removing the carrier polymer by calcination, where amorphous TiO_2 initially, with crystalline anatase TiO_2 being formed first, followed by rutile TiO_2 at an elevated temperature.

TiO_2 nanofibres can be synthesised by a combination of the electrospinning method and the sol-gel techniques (Huang *et al*., 2003). In this process, a solution of polymer (binder) and TiO_2 precursor is ejected through a needle in a strong electric field (kilovolts per centimetre), whereby composite nanofibres of polymer and amorphous TiO_2 nanofibres are formed (Wessel *et al*., 2011; Li *et al*., 2012a; Li, Zhang and Pan, 2011; Luo *et al*., 2012) (see Figure 1). The diameter, morphology and grain size of the TiO_2 nanofibres have optimal values for photocatalytic activity and are directly affected by the electro-spinning parameters (Li *et al*., 2010). Therefore, the electro-spinning parameters, such as solution concentration, applied voltage, collector distance, used solvent and solution feed rate, were extensively studied (Patra *et al*., 2009).

Electrospinning was proved to be a simple, low cost, and reliable technique for TiO_2 doping to attain modified optical, electrical, and structural properties. Doping or incorporation of foreign materials into TiO_2 is often required for several titania applications such as catalysis and chemical sensors. The electrospinning method has been used for doping TiO_2 nanofibres with metal or nonmetal elements. Doped electrospun TiO_2 nanofibres brought results that indicated that doping was successfully incorporated into the crystal lattice of TiO_2 nanofibres. Meanwhile, the doping could extend the visible light absorption of TiO_2 nanofibres (Zhang *et al*., 2010). In the electrospinning process, nanoparticles or molecules as a functional material can be easily doped or incorporated into the electrospun TiO_2 nanofibres by

adding these materials to the sol-gel solution. For example, Ag-doped TiO_2 nanofibres were fabricated using the sol-gel method and electrospinning technique. A solution of titanium isopropoxide (TiP) acetic acid and ethanol was mixed into another solution that contained ethanol, polyvinylpyrrolidone (PVP), and 0.5 N $AgNO_3$ followed by magnetic stirring for one day. The sol-gel solution was loaded into a syringe equipped with a 21 G stainless steel needle. A voltage of 20 kV was applied between the needle and a collector with the needle-to-collector distance of 15 cm, and a flow rate of 0.05 ml/min, which was controlled using a syringe pump (Park *et al*., 2010). In most electrospun experiments, electrospun TiO_2 nanofibres were synthesised at a constant flow rate, needle tip-to-collector distance, and applied voltage, but with different polymer type and Ti precursors (Ghani *et al*., 2004; Park and Kim, 2009; Park *et al*., 2010).

Various polymers have been successfully electrospun for fabrication of electrospun TiO_2 nanofibres, with typical examples, including Poly(vinyl pyrrolidone) (PVP), and Poly(vinyl alcohol) (PVA), Poly(vinyl acetate) (PVAc), Polyacrylonitrile (PAN), Poly(acrylic acid) (PAA), Polystyrene (PS), and Poly(methyl methacrylate) (PMMA) (Wu *et al*., 2012). Among of them, Poly(vinyl pyrrolidone) (PVP) is one of the most popular polymers because of its high solubility in water and its good compatibility with many salts containing a high molecular weight (1,300,000 g/mol), good solubility in water and alcohols, not chemical classified as hazardous or dangerous goods. The PVP is used considering its safety for many applications such as medical as a binder in many pharmaceuticals tablets (Buhler, 2005), toothpaste, and shampoos, as personal care products, and as a food additive with E number 1201.

Electrospun TiO_2/PVP composite nanofibres were prepared by a solution that contained titanium (diisoproproxide) bis (2, 4-pentanedionate) 75 wt. % in 2-propanol, and poly (vinyl pyrrolidone) (PVP). Diameters of 80–100 nm anatase and rutile TiO_2 nanofibre were obtained from calcination of as-electrospun TiO_2/PVP composite nanofibres at above 300 °C for 3 h in air. The results indicated a significant effect of calcination temperature on the morphology of the nanofibres, and the crystalline titania phase in the form of anatase, mixed anatase/rutile, or rutile (Nuansing *et al*., 2006). There was a decrease in diameter size, because PVP polymer, solvent and another organic source were removed at lower calcined temperature. Upon further calcination,

the nanofibres become crystalline titania nanofibres, and the polymer had been completely removed.

For Ti precursors, titanium isopropoxide is well known as a feasible parent titania material for the pure titania synthesis. It is alkoxide of titanium (IV), which is used in materials science and organic synthesis with many acquired names (See Table 5).

Table 5: Titanium isopropoxide properties

Property	**Value**
Chemical Formula Structure	$C_{12}H_{28}O_4Ti$
Molar mass (g/mol)	284.22
Appearance	Colourless to light-yellow liquid
Density (at 20 °C) (g/cm^3)	0.96
Melting point (°C)	14-17
Boiling point (°C)	232
Solubility in	Water, ethanol, ether, benzene, chloroform
Refractive index (R.I)	1.46
Synonyms	Tetraisopropyl titanate Ti(IV) isopropoxide Ti(OiPr)4 Titanium isopropoxide Titanium(IV) isopropoxide
Reference	Pubchem Open Chemistry Database http://pubchem.ncbi.nlm.nih.gov

Taguchi method

After the Second World War, the associated forces found that the quality of the Japanese telephone system was totally inappropriate and less effective for long-term communication purpose. To improve the system, the associated command recommended that Japan established research facilities similar to the Bell Laboratories

in the United States in order to develop a state-of-the-art communication system. The Japanese authority funded the Electrical Communication Laboratories (ECL) appointing Dr. Taguchi in charge of improving the R&D productivity and enhancing product quality. He observed that a great deal of money and time was invested on engineering testing and experimentation. Little importance was given to the process of creative brainstorming to minimise the expenditure of resources (Ranjit, 1990).

Dr. Taguchi started to develop new methods to improve the process of engineering experimentation. He developed techniques that are now widely known as the Taguchi Method. Taguchi approach is more than a method which layouts experiments in the mathematical formulation of the experimental design. His method has produced a powerful and unique discipline for quality improvement that differs from traditional practices by replacing a full factorial experiment with a partial factorial, faster, less expensive, and lean experiment.

The Taguchi method is highly useful as an engineering approach for designing robust experiments and selecting optimal levels of processing parameters with minimal sensitivity to variations different causes. In addition, it can also explain the effects of a large and complex number of factors on an individual and on interactive basis. An orthogonal array (OA) to simultaneously accommodate numerous experimental design factors, and signal to noise ratio (*S/N*) for measuring the most robust set of operating conditions from variations within the results are the two essential tools of the Taguchi method (Ranjit, 1990; Dong and Bhattacharyya, 2008; Ghani *et al*., 2004; Patra *et al*., 2009).

The Signal-to-Noise (S/N) concept has been used in the fields of electrical, acoustics and mechanical vibrations, and other science and engineering disciplines for several years. In a majority of cases, the quality characteristic may be a single measurable quantity such as length, weight, hours, etc. for some products with subjective measurements like ‘’low,’’ “bad,” “good” may be used. In other examples, objective and subjective evaluations may be combined into an Overall Evaluation Criteria (OEC).

Signal-to-Noise (S/N) Ratio:

$$S/N = \frac{Signal}{Noise} \qquad (1.5)$$

Three characteristic formulae have been used to identify the optimum combination of factors:

Smaller-the-Better equation:

$$S/_N = -10log_{10}\left[\frac{(\sum y_i^2)}{N}\right] \qquad (1.6)$$

Larger-the-Better equation:

$$S/_N = -10log_{10}\left[\frac{\sum\left(1/_{y_i^2}\right)}{N}\right] \qquad (1.7)$$

Nominal-the-Best equation:

$$S/_N = -10log_{10}\left[\frac{\sum(y_i - m)^2}{N}\right] \qquad (1.8)$$

where S/N is the signal-to-noise ratio, N is the number of trials, results target value, y_i is results of experiments, observation or quality characteristics such as titania nanofibres' diameter, inner diameter and length of titania nanotubes. The negative sign is used to indicate that the largest value gives the optimum value for the response variable and the robust design.

2.6 Applications and Potential Applications

TiO_2 has a wide range of environmental and energy applications. Nanostructured TiO_2 is a promising original production material for many applications because of its high specific area and electronic semiconductor properties, including photocatalytic, photochromic, photovoltaic, electroluminescence devices, electrochromic and sensors (Bavykin and Walsh, 2010; Park *et al*., 2010; Tang *et al*., 2011a).

2.6.1 Photocatalytic Applications

Various industries produce dyes pollutants which have become a major source of environmental contamination. Most industries use dyes to colour their products,

including textile, food, tannery, paper, printing, pulp and carpet industries. The discharge of dye wastewater into the environment is harmful. It adds deleterious colour to the receiving stream and inhibits sunlight penetration into the stream, as well as it is toxic to aquatic lives and food chain organisms (Chu, 2001). Some of the dyes are mutagenic and carcinogenic; any debasement that does occur may produce molecules that are alien to the environment such as amines, which also are toxic (Chu, 2001).

The pollutants removal technique from wastewater through using light is called photolysis. The photocatalytic process is a qualified technique for water purification due to its several benefits. First, in the presence of UV or near-UV illumination, many organic pollutants are decomposed into less harmful substances. Second, several non-toxic materials can be used as semiconductor photocatalyst, ZnO, Al_2O_3, and especially TiO_2. TiO_2 semiconductor photocatalyst has been the more widely used compared to CdS, SrO_2, ZrO_2, and ZnO, among others (Serpone *et al*., 1995). Third, photocatalysis is relevant to long-term situations as photocatalyst material is not consumed during the process. Last but not the least, the photocatalytic process can produce low operating cost based on the use of sunlight as the source of irradiation in addition to serving as environmental cleaning process (Jantawasu *et al*., 2009).

TiO_2 was discovered as a photocatalyst in 1972 by two Japanese scientists, Fujishima and Honda who demonstrated the potential of titania semiconductor materials to split water into oxygen and hydrogen in a photochemical cell (Fujishima and Honda, 1972). Since then, TiO_2 as a photocatalysis has received much attention and become very attractive in the application of self-cleaning, air cleaning and antibacterial effects in the construction industry. The merits of TiO_2 including high photostability, low cost and nontoxicity, have allowed its wider usage in photocatalytic applications.

The photocatalytic activity of TiO_2 depends mainly on its physicochemical properties, such as particle size, morphology, porosity, surface area and other physical characteristics (Guo *et al*., 2012).The photocatalytic applications of TiO_2 include the degradation of organic pollutions in aqueous and gaseous phases, hydrogen gas generation from photocatalytic water splitting, and removal of heavy metals from contaminated water, among others. TiO_2 semiconductor interacts with light of sufficient energy to produce reactive oxidizing species, which can lead to the

photocatalytic transformation of an air or water pollutant. At least two events must occur simultaneously during the photocatalytic process/reaction for the successful production of reactive oxidising species: first, the oxidation of dissociative adsorbed H_2O by photogenerated holes; and second, the reduction of an electron acceptor by photoexcited electrons. These reactions lead to the production of a hydroxyl and superoxide radical anion of the two events (Mills and Le Hunte, 1997).

TiO_2 with the crystal structure of anatase and rutile phases are commonly applied as photocatalysts, with anatase type showing a higher photocatalytic activity than rutile (Linsebigler *et al*., 1995). However, mixtures of anatase and rutile have been reported to exhibit superior photoactivity than that of either anatase or rutile alone (Kment *et al*., 2009; Natoli *et al*., 2012; Li *et al*., 2011). Degussa P25 TiO_2 photocatalyst reveals multiphasic material consisting of an amorphous state, together with the approximate crystalline phases 80% anatase and 20% rutile. The photocatalytic activity of the Degussa P25 is reported as being greater than the activities of either of the pure titania crystalline phases (anatase, and rutile). An interpretation of this reflection has also been given in terms of the development in the magnitude of the space-charge potential, which is created by contact between anatase and rutile crystalline phases and by the presence of localised electronic states from the amorphous phase (Bickley *et al*., 1991).

A heterogeneous photocatalytic system consists of semiconductor photocatalyst like TiO_2, which are in close contact with gaseous or liquid reaction. Doping, hetrosturctioring and crystal growth of semiconductor photocatalysts should be studied substantially (see Figure 16). The functional properties of TiO_2 photocatalyst are important for its photoreactive properties, including electronic structure, surface properties, and charge transport.

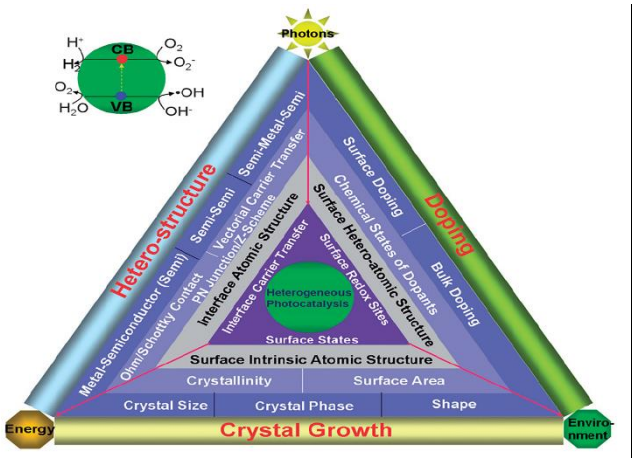

Figure 27: Doping, heterostructure and crystal growth of semiconductor photocatalysts.

(Liu *et al*., 2010)

Doh and his co-workers (2008) developed the photocatalytic of anatase particles/nanofibres. TiO_2 nanofibres (average 236 nm thick) were fabricated using the electrospinning method. Using the sol-gel method, the photocatalytic TiO_2 particles were coated on the TiO_2 nanofibres to increase effective surface area and photocatalytic activity. They claimed that the degradation rate of composite TiO_2 was much higher than that of TiO_2 nanoparticles and TiO_2 nanofibres. Therefore, they suggested that the composite TiO_2 of nanoparticles and nanofibres would be suitable for the degradation of organic pollutants (Doh, 2008).

A TiO_2 photocatalyst is a semiconducting substance that can be chemically activated under UV light radiation that results in an oxidation-reduction (redox) reaction, i.e., it has a photocatalysis action or photoactivity. Thus, various modifications were carried out to construct the photocatalytic application to be active under the visible light. Metal and non-metal doped TiO_2 photocatalyst to enable a photocatalysis under visible light was developed. Doping can exert a substantial influence on modifying the electronic structure and the construction of heteroatomic surface structures that allow high-efficiency TiO_2 photocatalysis under solar light irradiation. In 2001, the nitrogen doped TiO_2 photocatalyst was developed to enable a photocatalysis under visible light (Asahi *et al*., 2001). The nitrogen doped TiO_2

narrowed the band gap to the visible light by mixing O_{2p} states with the N_{2p} states of the substituted nitrogen atoms in the newly formed valence band (VB). Since then, it has attracted much attention with other metal and non-metal doping. Metal ion dopants such as Cr, V, Fe, Mn, Ni, Co, etc. into the TiO_2 lattices can influence the photocatalyst performance through the effects on electron/hole recombination dynamics and interfacial charge transfer (Choi *et al*., 1994).

Antifogging and Self-cleaning

The fogging on eyeglasses, cars windows and bathroom mirrors is caused by condensation of water damp that forms small droplets on the glass surface. The wetting of a solid surface with water where air is the surrounding medium is dependent on the contact angle. In general, 0° contact angle means completely wet, whereas 180° means completely non-wet. Cleaning by soap is based on low contact angle by reducing the water surface tension. The contact angle of water on glass and other inorganic materials is in the range of 20°–30°, but is not less than 10° for any surfaces under any conditions. The contact angle can be decreased without detergents, but by putting thin layer on the material surface. A hydrophobic surface is the main method to prevent this fogging by repelling the water molecules, and then removing the water drops by blowing or shaking. Materials such as ceramic tiles, glass, or plastics can develop super-hydrophilic materials by surface coating with the photocatalyst TiO_2.

The antifogging, antibacterial and self-cleaning functions of TiO_2-coated materials are obtained without using any chemicals, but with only UV sunlight and rainwater. The water contact angle of the illuminated surface with UV light of anatase TiO_2 is less than 1°. The super-hydrophilic effect of TiO_2 occurs when the surface is exposed to light, and the water contact angle approaches zero after a certain time of moderate illumination (Fujishima *et al*., 2000). Figure 28 shows a demonstration of antifogging of glass with the effect of TiO_2 coating under UV illumination.

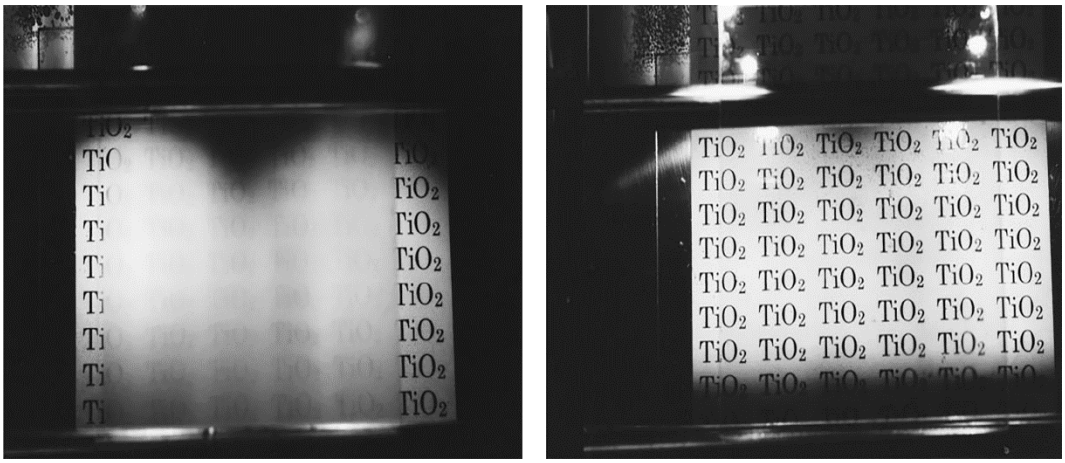

Figure 28: A photograph of steamed glass surfaces after UV illumination (a) without coating (b) with TiO_2 coating

(Watanabe *et al*., 1999).

The application of TiO_2 photocatalysis on surface materials has enabled the degradation of a range of organic and inorganic compounds that are aggressive towards material properties and the environment. TiO_2 photocatalysis was applied in different cementations materials, and the applications varied from self-cleaning to air cleaning purposes especially for indoor. TiO_2 coating on ceramic tiles was used for its antibacterial properties to increase the life-cycle of cement-based materials and to substantially reduce the air pollutant concentration in hospital rooms, care facilities, kitchens, baths, and schools (Benedix *et al*., 2000). A particularly interesting aspect was a clear synergy between TiO_2 and cement composites that makes this material an ideal substrate for environmental photocatalysis. A photocatalytic building materials used outdoors, e.g., PVC fabric, aluminum walls, glass, and exterior tiles were coated by TiO_2 where they could be easily washed by water, raining, rainwater, and rainfall. This is because water soaks between the highly hydrophilic TiO_2 surface and the materials.

Rutile has been reported to have a higher surface enthalpy and higher surface free energy than anatase due to a different crystal structures and associated exposed planes (Zhang and Banfield, 2005). Therefore, it would be expected that the anatase wetting by water would be less than that of rutile since higher surface free energies commonly contribute to hydrophilicity (Rupp *et al*., 2006). Rutile (100) and (110) faces exhibit a

higher hydrophilicity than the (001) face, which are favourable for increasing the number of OH groups. The (100) and (110) faces have two-fold oxygens, which are higher in position and energetically more reactive than their surrounding atoms and are called the ‘‘bridging site oxygen’’. On the other hand, the rutile (001) has three-fold oxygens, which are lower in position and energetically more inactive (Wang *et al*., 1999).

Photocatalysts for water treatment and air purification

The three-dimensional space by photocatalysis such as water, air, and soil is much more difficult than that of the two-dimensional surface of photocatalytic building materials. In general, the total amount of reactants in 3-D spaces is higher than on the two-dimensional surface, indicating that much more light energy is necessary for the purification of the 3-D space (Hashimoto *et al*., 2005). Moreover, the photocatalytic reactions are surface reactions, and thus the reactants must be captured by the photocatalyst surface. Fortunately, the construction of practical purification systems for wastewater from agriculture and polluted soil have been succeeded by volatile organic compounds (VOCs), which were based on TiO_2 photocatalysts and use only solar light. Nanosized TiO_2 photocatalyst powders were dispersed on substrates with extremely large surface areas, spreading them on the ground widely to collect sunlight (Hashimoto *et al*., 2005).

TiO_2 photobioreactor

In the food and environmental industries, anatase photocatalysts as a photobioreactor have attracted great attention for sterilising selected food-borne pathogenic bacteria such as *Listeria monocytogenes*, *Vibrio parahaemolyticus*, and *Salmonella choleraesuis subsp* (Kim *et al*., 2003). Various anatase concentrations and Ultraviolet (UV) illumination time were used to study the photocatalytic reaction. On all bacterial suspensions, it was found that the bactericidal effect of UV/anatase was much higher than without anatase. As the anatase concentration increased to 1.0 mg/ml, bactericidal effect increased, but it was rapidly abbreviated at higher than 1.25 mg/ml anatase concentration to all selected bacteria. The time of anatase/ UV

illumination affected the viability of bacteria with different death rates drastically. After 3 h of UV illumination, *Salmonella choleraesuis subsp* and *Vibrio parahaemolyticus* were completely killed, whereas, about 87 percent death ratio was for *Listeria monocytogenes* which was killed (Kim *et al*., 2003).

2.6.2 Photovoltaic Application

The photovoltaic is the conversion of sunlight to electrical power. In the past decade, the cost of solar cells or photovoltaics has been reduced greatly because of the fact that the conversion efficiency increases sharply with the introduction and application of more sophisticated technologies. However, the production cost of a solar cell is still higher than the fossil fuel. The high cost of silicon, which is the main solar energy material is the main reason behind the present limitation in the use of solar energy. Thus, there is an increasingly urgent need for developing environmentally friendly energy with relatively cheap price. TiO_2 semiconductor with low cost is a promising original production material, which is often related to the cost of solar energy technologies. Furthermore, recent developments in the synthesis of nanocrystalline TiO_2 with various morphologies/forms have opened up several new opportunities for the construction of efficient photovoltaic cells, and a wide range of applications.

Solar energy is available in abundance and should be used more extensively. The semiconductor has important application in renewable energy and environment fields. Nanocrystalline TiO_2 and its conductivity is being established and challenged for use as a new generation of photovoltaic cells. Sensitised nanostructured solar cells were assembled into ruthenium dye (N-719) using photoanode TiO_2 nanotube arrays. A solar cell in backside illumination mode was formed using anodic TiO_2 nanotube arrays, yielding 7.4% power conversion efficiency (PCE) (Wang and Lin, 2009).

Lithium batteries

The lithium-ion batteries (LIBs) are widely used in portable electric vehicles and electronic devices and toys. For high-performance second LIBs generation, recent

progress in advanced nanoscience and nanotechnology is paving the way to the development of diverse nanostructured electrode. It has led to improved energy density, higher cycling rate, and capability, because it has large surface area, short mass and charge-diffusion distance, numerous active sites, and efficient accommodation of volume changes (Nam *et al*., 2006). Nanostructured TiO_2 is widely used in rechargeable lithium batteries as electrodes because of their superior safety, low cost, chemical stability, and non-toxicity. Elongated TiO_2 with various morphologies [e.g. nanotubes (Zhou *et al*., 2003; Li *et al*., 2005a; Fang *et al*., 2009), nanowires (Armstrong *et al*., 2005; Li *et al*., 2005b; Wang *et al*., 2006), nanofibres (Nam *et al*., 2010), and nanorods (Gao *et al*., 2004)] have been utlised for lithium storage. These TiO_2 nanostructures attract attention as a possible negative electrode material for lithium cells, because they have open, mesoporous structure, efficient transport of lithium ions, and effective ion-exchange/properties. In terms of safety, TiO_2 is a promising anode material for the lithium-ion storage, as it alleviates the overcharge issue by moving toward a higher potential, thereby avoiding the lithium plating and parasitic electrochemical reaction (Jiang *et al*., 2004).

Photo Electrochemical Cells (PECs)

Figure 29 shows the total energy related to CO_2 emission from different fuels. Hydrogen is likely to be an alternative energy and idea fuel in the future, which is produced from clean and green energy sources. It is an environmentally friendly gas and recognised as an efficient source of fuel. Renewable hydrogen production is not common yet due to its high production cost. Photovoltaic water electrolysis can become more competitive by splitting off water using semiconductor photocatalyst. The cost of hydrogen continues to decrease with the technological advancement, but a considerable use of some semiconducting materials can cause serious life cycle impacts on environment. Fortunately, a promising semiconductor for the clean, low-cost and environmentally friendly production of hydrogen is offered by photocatalytic water-splitting (Sheppard and Nowotny 2007, Bard and Fox 1995).

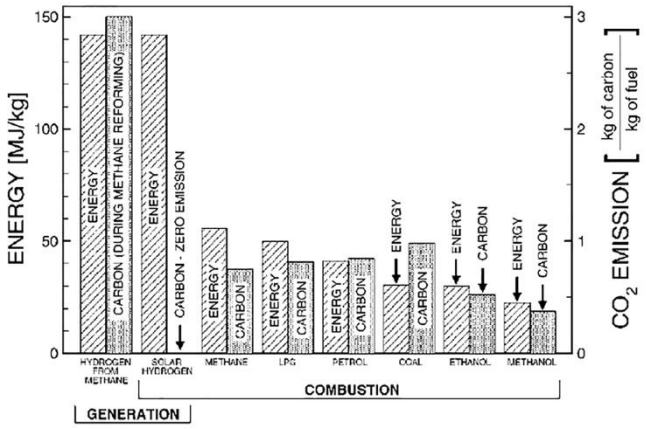

Figure 29: Energy amount in different fuels and related CO_2 emission.

(Sheppard and Nowotny, 2007)

In early 1972, the first invention of photocatalytic decomposition of water into oxygen and hydrogen used photo-excited TiO_2 as the anode and Pt as the electrode in the photoelectrochemical cells (PECs) (Fujishima, 1972). PEC technology is an environmentally safe renewable resource, since it is based on solar energy and could be used on both small and large scales and in a relatively uncomplicated manner. There are three options to make a photoelectrochemical cells (PECs) technology, which are: cathode made of metal and photoanode made of n-type semiconductor; photocathode made of p-type semiconductor and photoanode made of n-type semiconductor; and anode made of metal and photocathode made of p-type semiconductor (Bak, 2002).

Figure 30 shows a schematic diagram of photoelectrochemical cell. As the first PECs by Fujishima (1972), the surface of n-type TiO_2 (1) as a photoanode was irradiated with light consisting of energy larger than its band gap, photocurrent flowed from the platinum counter photocathode (2) to the titania through the external circuit. The direction of the current revealed that the oxidation reaction (oxygen evolution) and the reduction reaction (hydrogen evolution) occur at the TiO_2 photoanode (4 right) and the Pt photocathode (4 left), respectively (See Figure 26). Water can be decomposed into hydrogen and oxygen using UV light, without the application of an external voltage, according to the following scheme (Fujishima *et al.*, 2000; Hashimoto *et al.*, 2005).

TiO_2 excitation by light:

$$TiO_2 + hv \longrightarrow e^- + h^+ \qquad (1.9)$$

At the TiO_2 electrode:

$$2H_2O + 4h^+ \longrightarrow O_2 + 4H^+ \qquad (1.10)$$

At the Pt electrode:

$$2H^+ + 2e^- \longrightarrow H_2 \qquad (1.11)$$

The overall reaction is:

$$2H_2O + 4hv \longrightarrow O_2 + 2H_2 \qquad (1.12)$$

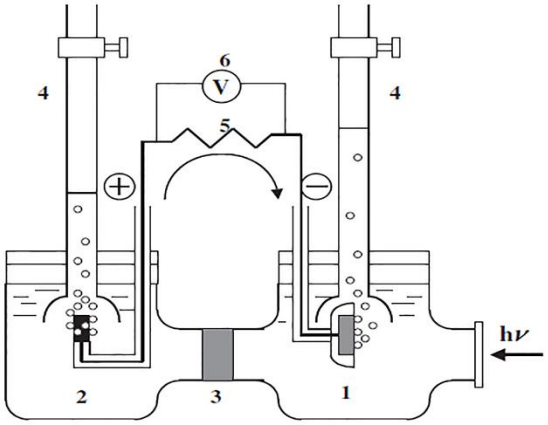

Figure 30: A schematic diagram of photoelectrochemical cell.

(Fujishima *et al*., 2000; Hashimoto *et al*., 2005).

The water splitting reaction over TiO_2 semiconductor-photocatalyst materials has attracted much attention, although TiO_2 has several advantages and remains one of the most promising because of its photostability, chemical inertness, environmentally friendly solar-hydrogen production to support the future hydrogen economy, and low cost (Fujishima and Honda, 1972). To maximise photocatalytic decomposition of water using the TiO_2 as the photoanode, the TiO_2 band gap should utilise visible-light

energy, and high contact area with the electrolyte to increase the splitting of the e^-/h^+ pairs. Thus, metal and non-metal doped nanostructured TiO_2 has great potential for photocatalytic water-splitting technology with high aspect ratios for maximizing the photocleavage of water under visible-light irradiation. The total photocurrent of carbon-doped TiO_2 nanotubes arrays was 20 times higher than the pure P-25 TiO_2 under the visible light illumination (see Figure 31) (Ni *et al*., 2007).

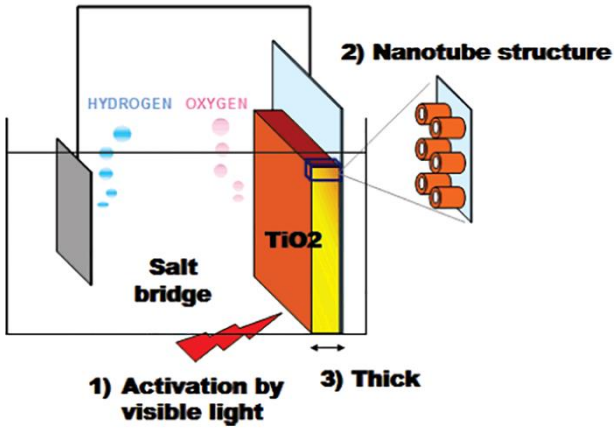

Figure 31: A schematic structure of the TiO_2 photoanode to optimise its photocatalytic activity for water splitting.

(Park *et al*., 2006).

Dye-sensitised solar cell (DSSC)

The DSSC is a relatively new class of low-cost solar cells for renewable electricity generation (Grätzel, 2001, 2005). Semiconductor sensitized solar cells have attracted growing interests, starting from quite low (4–5 percent) conversion efficiencies (Mora-Sero and Bisquert, 2010). Nanotechnology and nanoscience are believed to revolutionise the industry shortly and will have a significant economic impact allowing a considerable cost reduction of the photovoltaic energy, by both increasing efficiencies, and reducing the cost of the devices.

In 1991, nanofilm titania as an efficient dye-sensitised solar cell (DSSC) was reported by O'regan and Graetzel (O'regan and Gratzel, 1991). TiO_2 nanoparticles was used in the dye sensitised solar cell, which is based on solar energy by employing

sensitisers adsorbed on the surface of n-type semiconductor metal oxide (Bai *et al*., 2008). Moreover, TiO_2 films based DSSCs which use Ruthenium sensitisers offer power conversion efficiency of only 9.57-11.18 percent, and primarily absorb light in the region of 350-700 nm (Nazeeruddin *et al*., 2005).

Although most of the reported works on DSSCs are based on TiO_2 thin films, various nanostructured TiO_2 have also been used for DSSC fabrication. Nanocrystalline anatase TiO_2 is usually used for DSSCs and various modifications have been carried out on other TiO_2 phases to construct an energy efficient photovoltaic device (Huang *et al*., 1997).

TiO_2 nanotubes have been examined for being used as an electrode for dye-sensitised solar cells (DSSC). The potential advantage of the TiO_2 nanotubes compared to TiO_2 nanopowders is realised by exploiting the phenomenon of improved adsorption of the positively charged dyes from aqueous solution onto the surface of negatively charged TiO_2 nanotubes (Lee *et al*., 2008). The other advantage of the nanotubes is the elongated structures of these semiconductors, which can improve the electron transport and the charge collection efficiency (Bavykin and Walsh, 2010).

2.6.3 Sensing Application

Air contamination by several varieties of pollutants is a consequence of human activity. An extensive research is necessary for designing and fabrication of more efficient gas sensing systems that can detect pollutants contained in the air. Many metal oxide semiconductors such as SnO_2, TiO_2, ZnO, and so on have been used due to the fact that these are the most common ceramics used for gas sensor application. To be able to control various air pollutants, sensors must be very sensitive, selective and reliable. Below 250 °C, SiO_2–based sensors are widely used as gas-sensitive resistors because of their good sensitivity and selectivity. However, more than 250 °C, TiO_2–based sensors have been reported to become the preferred material for high temperature gas sensors because of their good sensitivity and stability (Zheng *et al*., 2008).

2.6.4 Coatings

TiO_2 is the most important white pigment used in the coatings industry as it effectively scatters visible light, brightness and opacity, and thereby imparts whiteness when incorporated into a coating. Table 5 shows the refractive indices for anatase, rutile and other pigments. Anatase and rutile, have the two highest refractive indices with 2.55 and 2.73 respectively. Rutile pigments scatter light more efficiently, and are more stable and durable manner than anatase pigments do.

Table 6: Refractive Indices (R.I.) for some Pigments.

(www.chemours.com)

Pigments	Refractive Indices (R.I)
Diatomaceous earth	1.45
Silica	1.45–1.49
Calcium carbonate	1.63
Barytes	1.64
Clay	1.65
Magnesium silicate	1.65
Lithopone	1.84
Zinc oxide	2.02
Antimony oxide	2.09–2.29
Zinc sulfide	2.37
Anatase	2.55
Rutile	2.73

2.6.5 Drug Delivery and Bio-Applications

The nanostructured TiO_2 has recently been studied as a possible element in amperometric bio-sensors due to its high surface area and affinity towards positively charged ions in aqueous solutions (Bavykin and Walsh, 2010). The use of TiO_2 nanotubes as capsules for drug delivery and controlled release could be developed based on a combination of several nanotubes properties. The high surface area and

large pore volume of the TiO_2 nanotubes provide an increased load capacity required for drug storage. It can also be potentially beneficial in drug delivery to the targeted tissue. Moreover, TiO_2 nanowires can be used as bioscaffolds for cell cultures, providing enough rigidity and a large macropods structure suitable for cell's growth and nutrition (Dong *et al*., 2007).

A co-adsorption of horseradish peroxidase with thionines on anodic TiO_2 nanotubes for biosensor design has been investigated. The TiO_2 nanotube provides excellent matrices for the coadsorption of horseradish peroxidase (HRP) and thionines, where the adsorbed HRP effectively retains its bioactivity on these TiO_2 nanotube arrays (Liu and Chen, 2005). Moreover, the titanium dioxide thin film has shown an ability to decompose organic compounds including Escherichia coli (E. coli) cells in water treatments (Sunada *et al*., 2003; Sunada *et al*., 1998).

3 Publications Forming Part of the Thesis

3.1 Phase Transformations and Crystallization Kinetics in Electrospun TiO_2 Nanofibers in Air and Argon Atmospheres

---

ALBETRAN, H., HAROOSH, H., DONG, Y., PRIDA, V. M., O'Connor, B. H., & LOW, I. M. 2014. Phase Transformations and Crystallization Kinetics in Electrospun TiO_2 Nanofibers in Air and Argon Atmospheres. *Applied Physics A*, 116, 161–169.

Appl. Phys. A (2014) 116:161–169
DOI 10.1007/s00339-014-8246-1

Applied Physics A
Materials Science & Processing

Phase transformations and crystallization kinetics in electrospun TiO_2 nanofibers in air and argon atmospheres

H. Albetran · H. Haroosh · Y. Dong · V. M. Prida · B. H. O'Connor · I. M. Low

Received: 20 September 2013 / Accepted: 9 January 2014 / Published online: 28 January 2014

Abstract The effects of atmospheric air and argon environments on thermal-induced phase transformations in electrospun TiO_2 nanofibers have been investigated in situ using synchrotron radiation diffraction. Diffraction results showed that the as-synthesized TiO_2 nanofibers were initially amorphous, but crystallized to form anatase and rutile after thermal annealing in air or argon at elevated temperatures. The crystallization temperature of anatase was delayed by 100 °C in argon relative to in air, and the transformation of anatase into rutile occurs faster in argon atmosphere than in air due to the formation of oxygen vacancies. Non-linear strains formed in both polymorphs and the substantial elevation of rutile thermal expansion pointed to strain anisotropy in the rutile phase and the concomitant fibre breakage.

H. Albetran · B. H. O'Connor · I. M. Low (✉)
Department of Imaging and Applied Physics, Curtin University, Perth, WA 6845, Australia
e-mail: j.low@curtin.edu.au

H. Albetran
Department of Physics, College of Education, University of Dammam, Dammam 31451, Saudi Arabia

H. Haroosh
Department of Chemical Engineering, Curtin University, Perth, WA 6845, Australia

Y. Dong
Department of Mechanical Engineering, Curtin University, Perth, WA 6845, Australia

V. M. Prida
Department of Physics, University of Oviedo, Calvo Sotelo s/n, 33007 Oviedo, Spain

1 Introduction

Titanium dioxide (TiO_2) is one of the most widely studied materials due to its high photo-activity, photo-durability, mechanical robustness, low cost, and chemical and biological inertness [1–6]. Titanium dioxide has three polymorphs: anatase, brookite, and rutile [7–10]. Anatase and rutile are the two main polymorphs that exhibit different properties and thus different photocatalytic performances. They both have tetragonal crystal structures, but different space groups and atoms per unit cell (Z), space group $I4/amd$ and $Z = 4$ for anatase and $P4_2/mnm$ and $Z = 2$ for rutile [9, 11]. At room temperature, the lattice parameters of anatase are $a = b = 0.3785$ nm and $c = 0.9514$ nm, while for rutile are $a = b = 0.4594$ nm and $c = 0.29589$ nm [12]. These differences in the inter-atomic spacing and crystal structures for anatase and rutile can result in different densities and electronic band structures. Anatase is considered more photochemically active than rutile by virtue of its lower rates of electronic recombination and higher surface absorptive capacity [13]. However, recent work has indicated that a mixed-phase TiO_2 tends to make a superior photocatalyst to a single-phase TiO_2. For example, a mixed-phase sample of 70 % anatase and 30 % rutile has been found as the best photocatalyst for wastewater treatment [14]. Similarly, commercial TiO_2 photocatalyst (P-25) that contains 80 wt% anatase and 20 wt% rutile has been observed to exhibit excellent photocatalytic reactions [12].

The optimum composition in terms of the anatase and rutile levels for maximum photocatalytic performance can be achieved by thermal annealing. In general, anatase forms from amorphous TiO_2 at low temperatures which subsequently transforms to rutile at higher temperatures [15, 16]. The transformation is affected by various

conditions which include the synthesis method, the amount of impurities, temperature, calcination time and atmosphere type [15, 17]. Reaction atmospheres have been observed to have a significant influence on the thermal transformation of TiO_2 phases because oxygen defect levels and interstitial titanium ion levels are influenced by the type of atmosphere [15, 18]. The effects of air, vacuum, argon, argon–chlorine mixture, hydrogen, steam and nitrogen on the anatase-to-rutile phase transformation have been reported [18]. For TiO_2 films, the amorphous to anatase and anatase-to-rutile phase transformations were observed to occur at a lower temperature when annealed in a hydrogen atmosphere than in air or vacuum [19]. The rate of anatase-to-rutile phase transformation was found to decrease in vacuum but increase in hydrogen atmosphere due to the formation of either titanium interstitials or oxygen vacancies. Since the phase transition involves an overall shrinkage of the oxygen structure and a cooperative movement of ions, the formation of oxygen vacancies would accelerate the phase transition and vice versa for the formation of titanium interstitials [15].

Nanostructured TiO_2 with elongated morphology exhibits high surface area to volume ratio which is of great significance for increasing the decomposition rate of organic pollutants because photocatalytic reactions take place rapidly and drastically on the surface of the catalyst [14, 20]. Hitherto, various techniques have been used to synthesize nanostructured TiO_2 with various morphologies (e.g. nanowires, nanorods, nanotubes, and nanofibers). These include microemulsion, sol–gel, hydrothermal and vapour deposition [8, 21]. Elongated nanostructures are of particular importance, as long and thin nanotubes or nanofibers can provide a high specific surface area for photocatalysis [9]. Furthermore, a variety of techniques, such as self-assembly, evaporation, anodisation, and electrospinning, have been developed for fabricating one-dimensional nano-TiO_2 [1, 22, 23]. Among the fabrication methods, electrospinning is a simple and cost-effective technique applicable at industrial levels for fabricating one-dimensional nanofibers [22–25]. In this process, a solution of polymer and TiO_2 precursor is ejected through a needle in a high electric field whereby composite nanofibers of polymer and amorphous TiO_2 are formed [25–29]. To the best of our knowledge, the effect of atmospheres on the in situ crystallization of anatase and rutile in electrospun TiO_2 nanofibers has not been previously reported.

In the present work, the effect of air and argon atmosphere on the transformation of anatase into rutile and the in situ crystallization kinetics of TiO_2 nanofibers were investigated using synchrotron radiation diffraction (SRD) over the temperature range of 25–900 °C. TiO_2 nanofibers were synthesized using electrospinning and their morphology, structure and thermal expansion were characterized by scanning electron microscopy (SEM) and associated energy dispersive spectroscopy (EDS), and high-temperature SRD.

2 Experimental procedure

2.1 Material synthesis

A homogenous sol–gel precursor solution was prepared by mixing titanium isopropoxide (TIP) ($M_w = 284.22$ g/mol, 97 % purity—sourced from Sigma-Aldrich), acetic acid ($M_w = 60.05$ g/mol, 99.7 % purity—Sigma-Aldrich), and ethanol ($M_w = 46.07$ g/mol, 99.5 % purity—Sigma-Aldrich) in a fixed volume ratio of 3:1:3, respectively. The sol–gel was stirred in a capped bottle for 5 min, and then, 12 wt% of poly-vinyl pyrrolidone (PVP) ($M_w = 1{,}300{,}000$ g/mol, 100 % purity—Sigma-Aldrich) was dissolved in the solution at 40 °C for 1 h using a stirrer. To achieve complete dissolution and mixing, the sol–gel solution precursor was stirred ultrasonically for 5 min before it was loaded into a 10 ml plastic syringe with a 25-gauge stainless steel needle. An electrospinning unit (Gamma High Voltage Research, USA) with a high voltage power supply was used to provide 25 kV between the needle and a mesh collector covered by an aluminium foil at a distance of approximately 12 cm. A syringe pump (Chemyx Inc. USA) was used to control the solution flow rate at 2 ml/h during the process of electrospinning.

2.2 In situ high-temperature synchrotron radiation diffraction (SRD)

The in situ crystallization behaviour of electrospun TiO_2 nanofibers was evaluated using high-temperature SRD in air and in argon. The SRD measurements were conducted at the Powder Diffraction Beamline at the Australian Synchrotron. The specimens were mounted on an Anton Parr HTK 16 hot platinum stage and heated with an Anton Paar HTK20 furnace. The SRD data were collected at an incident angle of 3° and wavelength of 0.1126 nm.

The SRD patterns were acquired initially at ambient temperature and then in steps of 100 °C from 200 °C to 900 °C at a rate of 10 °C/min with a data acquisition time of 10 min per pattern. Each pattern was measured over the angular range $2\theta = 5°–84°$. The SRD data were analysed using Rietveld pattern fitting with the Rietica program (version 2.1) [30], to compute the relative crystalline phase abundances, and the lattice parameters of anatase and rutile at each temperature [31]. The parameters optimized in the Rietveld refinements were the pattern background, 2θ-zero, and for each phase the scale factor, lattice parameters and the peak shape parameters. The Rietveld refinements were

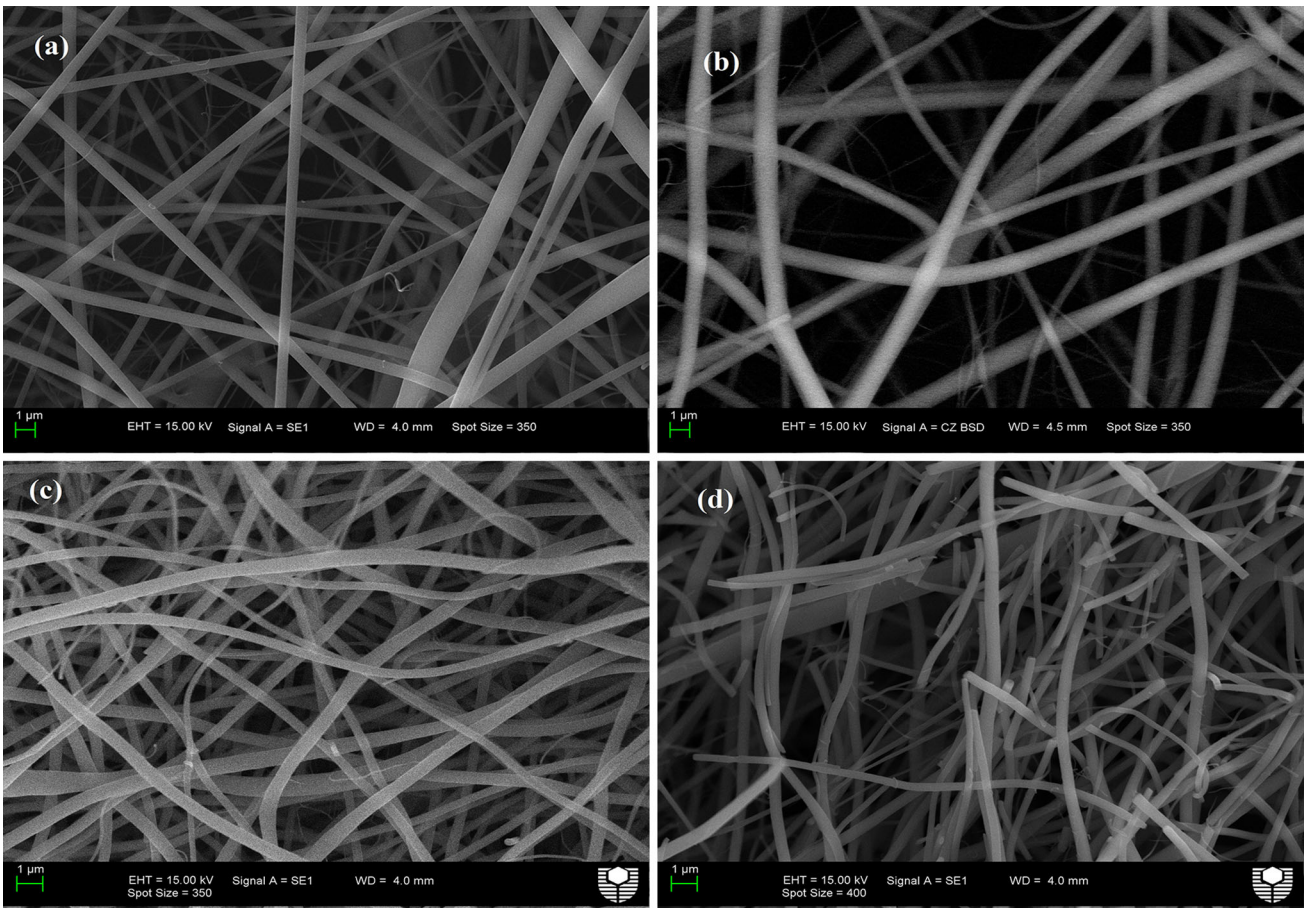

Fig. 1 SEM micrographs of as–spun TiO_2 nanofibers imaged with **a** secondary electrons **b** backscattered electrons; and with secondary electrons after cooling from 900 °C, in **c** air and **d** argon atmospheres

conducted with the crystal structures of anatase (ICSD 202242) and rutile (ICSD 64987). The Jade (version 6) program was used to perform peak broadening analyses to obtain the crystalline size (L) and the strain (ε) for each two phase as a function of temperature, using Williamson–Hall (W–H) plots [32]:

$$\beta \cos\theta = \lambda/L + 4\varepsilon \sin\theta \quad (1)$$

where λ is the X-ray wavelength, θ is the Bragg angle, and β is the integral breath of a peak. The crystallite size (L) was estimated from the y-intercept, and the strain (ε) from the slope of a linear fit to the data.

2.3 Scanning electron microscopy

The morphologies of the electrospun TiO_2 nanofibers were examined using an EVO 40XVP scanning electron microscope with an accelerating voltage of 15 kV. Prior to the microstructure observations, the samples were coated with platinum to avoid charging. The SEM images of as-spun nanofibers were taken using secondary and backscattered electrons at working distances of 4 and 4.5 mm, respectively. The samples were characterized again at the same accelerating voltage after thermal annealing in air and argon atmospheres. Associated energy dispersive X-ray spectroscopy (EDS) with an acceleration voltage of 10 kV, magnification of x606, silicon detector and zero electronic beam tilt was used to analyse the elemental compositions of the SEM-imaged materials.

3 Results and discussion

3.1 Microstructures of electrospun TiO_2 nanofibers

Figure 1 illustrates the SEM images of electrospun nanofibers using secondary and backscattered electrons, before and after thermal annealing. In the former, the nanofibers have smooth surfaces with a random distribution and annealing. The average diameter of electrospun nanofibers was 614 ± 190 nm, with the fibres being well dispersed within the PVP matrix, as shown in Figs. 1a, b.

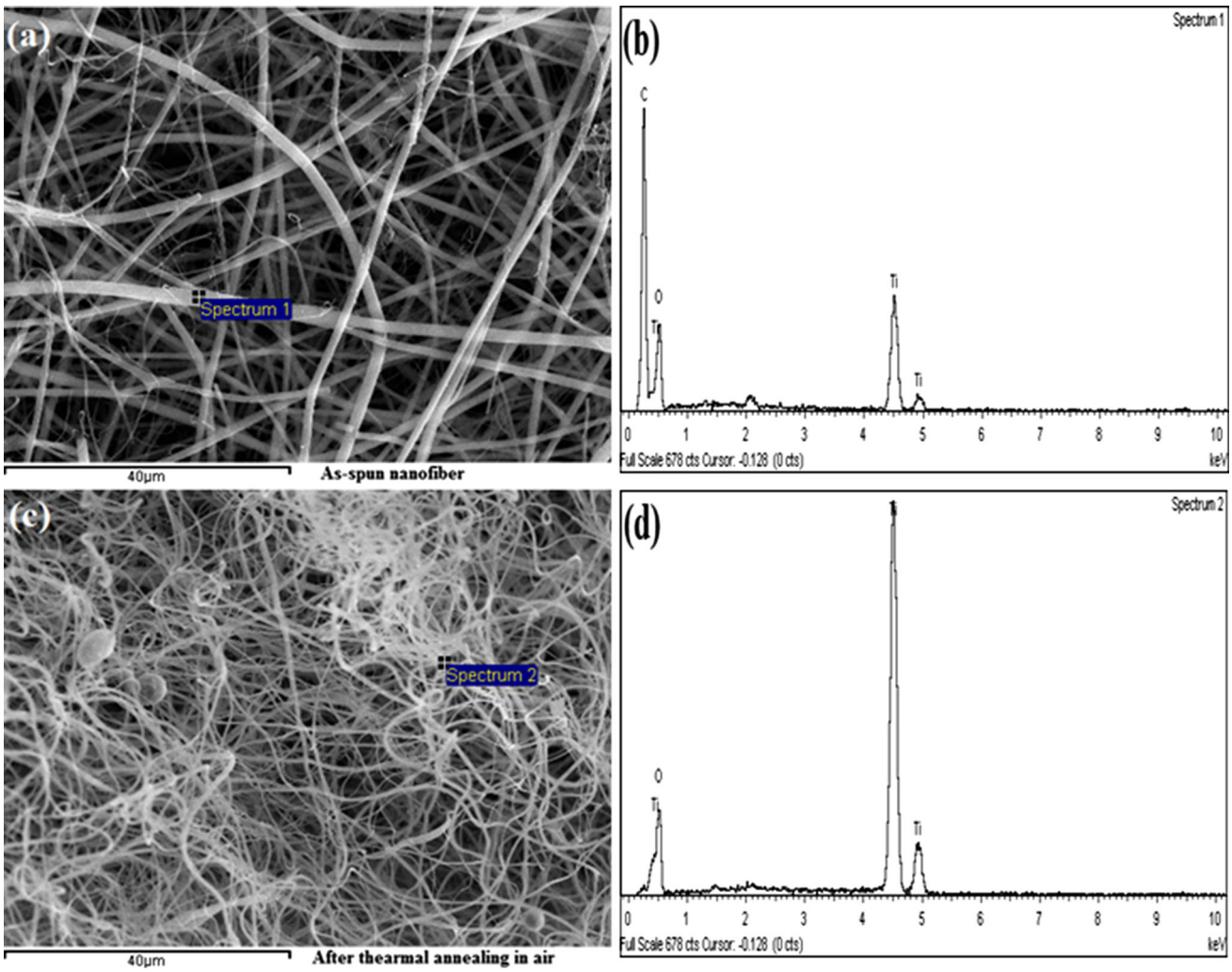

Fig. 2 **a** SEM micrograph of as-received electrospun TiO_2 nanofibers, **b** the corresponding EDS spectrum (#1); **c** SEM micrograph for electrospun TiO_2 nanofibers after cooling in air from 900 °C, and **d** the corresponding EDS spectrum (#2)

However, after thermal annealing at 900 °C, the average diameters of the nanofibers shrank by approximately 42 % in air (Fig. 1c) and 47 % in argon (Fig. 1d) compared to as-spun nanofibers, due to the loss of the organic binder during heating. The average diameters of nanofibers were 358 ± 195 nm in air and 328 ± 113 nm in argon. In argon, the nanofibers were partially broken, while in air the extent of fibre breakage was less. A probable reason for the fibre breakage could be due to the damage arising from sample handling or during the SEM examination. A more likely explanation is the thermal expansion anisotropy of rutile and the associated strains induced at elevated temperatures (see Table 2, and the thermal expansion section).

The EDS spectrum of as-spun TiO_2/PVP nanofibers in Fig. 2 b showed strong signatures for Ti, O and C, with the C content being due to the PVP polymer binder. The EDS spectrum of the nanofiber sample after thermal annealing at 900 °C (Fig. 2 d) was similar to that for the original material, other than showing the absence of the C peak due to the complete loss of the organic matrix. The same observation was made when the nanofibers were heated in argon.

3.2 Effect of environmental atmosphere on the phase transitions during thermal annealing

Figure 3 shows the effect of atmosphere on the in situ crystallization kinetics of as-synthesized TiO_2 nanofibers over the temperature range 25–900 °C, as revealed by SRD. The SRD patterns showed Pt peaks due to the Pt sample mount which were ignored in the calculations. The TiO_2/PVP nanofibers were initially amorphous as shown by the pronounced amorphous hump for the 25 °C pattern and the absence of diffraction peaks. By 200 °C the amorphous feature had largely disappeared and had gone completely by 400 °C. In air (Fig. 3a), anatase and rutile were first observed at 600 °C and 700 °C, respectively. However, in argon, both anatase and rutile were first observed at 700 °C (Fig. 3b), so that the initial crystallization of anatase was delayed by

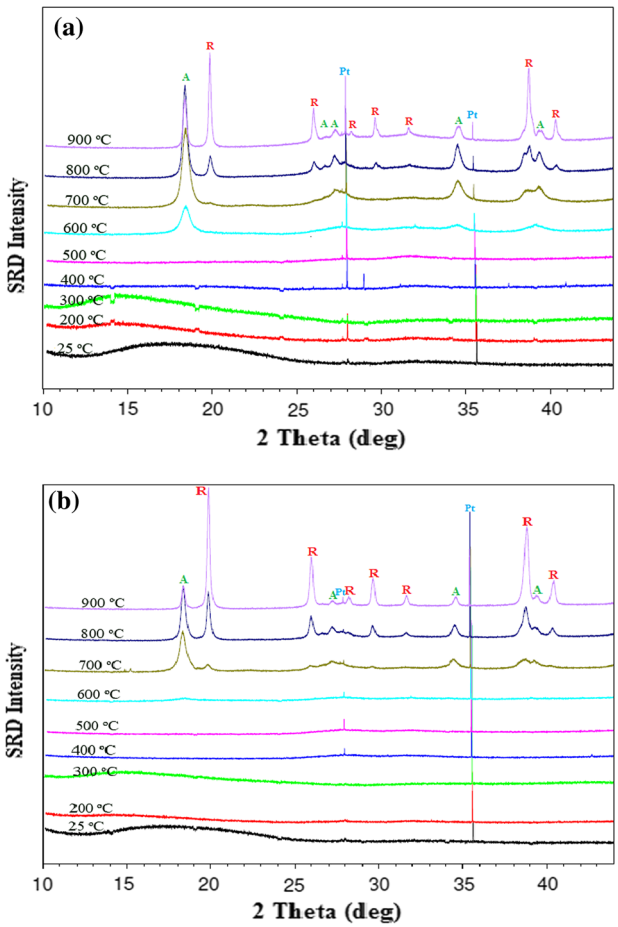

Fig. 3 In-situ SRD plots showing the effect of temperature on the crystallization behaviour of as-synthesized TiO_2 nanofibers when heated in 25–900 °C **a** in air, and **b** in argon. [Legend: anatase (A), rutile (R) and platinum (Pt)]

Table 1 Effect of atmospheres on the fraction of anatase-to-rutile transformation as a function of temperature

Temperature (°C)	Air (x)		Argon (x)	
	Spurr equation [33]	Rietveld method	Spurr equation [33]	Rietveld method
700	1.5	4.98 (10)	9.2	15.41 (28)
800	19.2	24.02 (32)	46.5	50.99 (28)
900	63.04	64.95 (60)	84.5	85.98 (49)

100 °C in argon compared with air. The reason for this delay in the formation of anatase in argon atmosphere may be attributed to the lack of oxygen. It appears that atmospheric oxygen accelerates the transformation from amorphous TiO_2 into anatase. Moreover, the partial pressure of oxygen also influences the rate of anatase-to-rutile transformation, becoming faster in argon atmosphere which has a much lower oxygen partial pressure [15]. Defects of oxygen

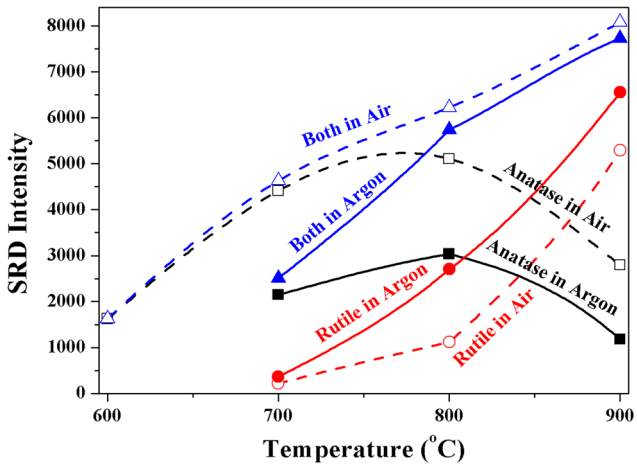

Fig. 4 The SRD intensities of the anatase (101) and rutile (110) reflections in the range 600–900 °C for TiO_2 nanofibers heated in air and argon. The vertical axis is proportional to the phase concentration for both anatase and rutile, and the sum of the anatase and rutile intensities is proportional to total crystalline titania

vacancies created in argon atmosphere by the low partial pressure of oxygen accelerate the anatase-to-rutile transformation, which involves the breaking of anatase Ti–O bonds and reforming of rutile Ti–O bonds [12, 18]. Hence, the transformation rate from anatase into rutile was faster in argon than in air atmosphere by virtue of oxygen vacancies (see Table 1).

The fraction of anatase-to-rutile transformation can be estimated using the Spurr equation [33]:

$$x = 1/[1 + 0.8(I_A/I_R)] \quad (2)$$

where I_A and I_R are the X-ray integrated intensities of anatase (101) reflection and rutile (110) reflection, respectively. Table 1 shows the fraction of anatase-to-rutile transformation as a function of temperature in air and in argon as determined using the Spurr equation and Rietveld method. It is evident that the weight fraction of rutile increased dramatically as the temperature increased by virtue of the transformation of metastable anatase into rutile at elevated temperatures. The rate of anatase-to-rutile transformation was also observed to increase faster in argon than in air. This enhanced transformation rate may be attributed to the formation of oxygen vacancies in TiO_2 annealed in argon [12]. The formation of oxygen vacancies would accelerate the phase transition since it involves an overall shrinkage of the oxygen structure and a cooperative movement of ions [15].

Figure 4 shows the intensities of anatase (101) and rutile (110) peaks over the temperature range 600–900 °C. Because the most intense peaks for both crystalline phases have virtually the same Reference Intensity Ratio, the intensity–temperature plots should be seen as 'relative concentration-temperature' plots, with the sum of the anatase and rutile peaks being proportional to the total

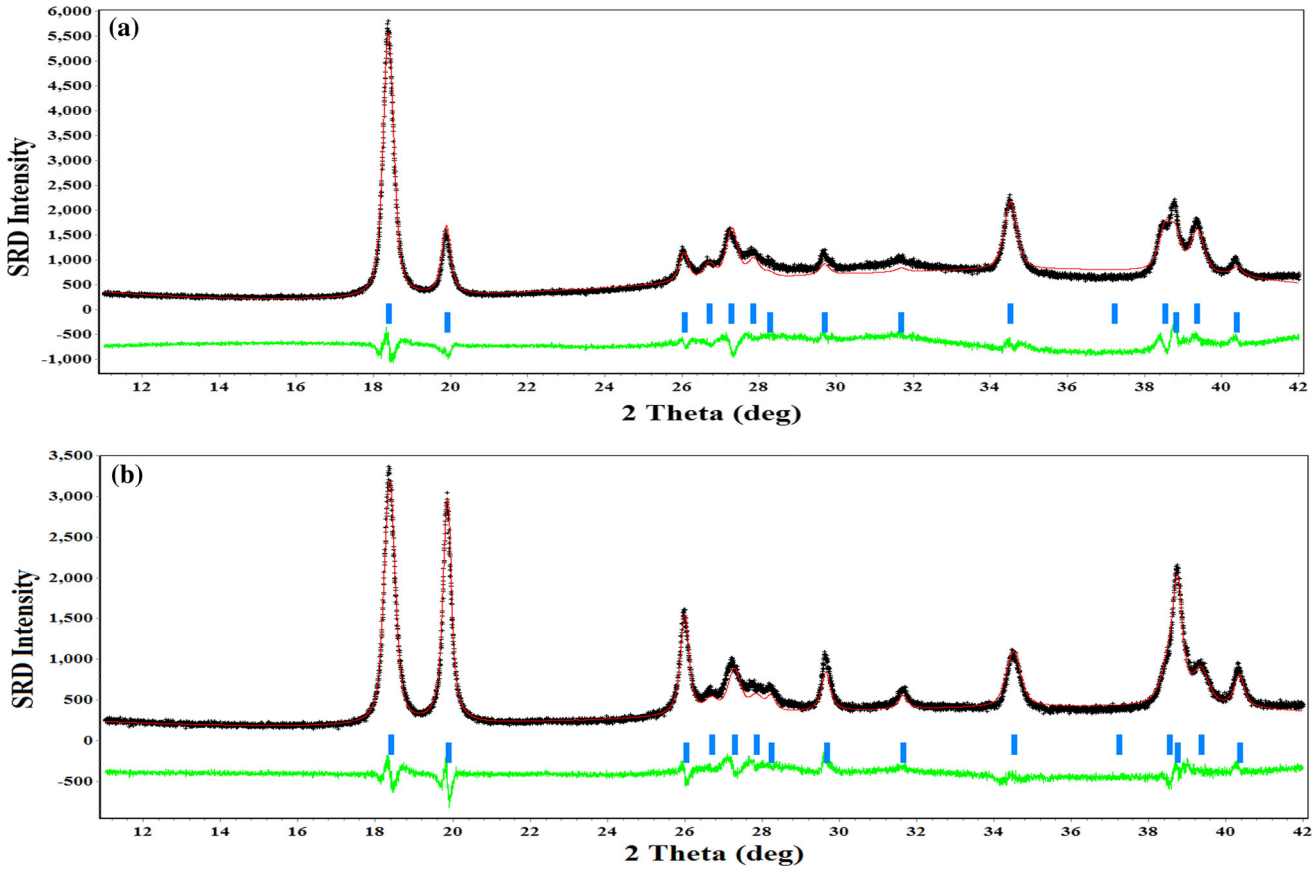

Fig. 5 SRD Rietveld difference plots for 800 °C SRD data **a** in air and **b** under argon. Measured patterns are indicated by *black crosses* and calculated patterns by *solid red lines*. The *green residual plot* shows the difference between the calculated and the measured patterns. The peak positions for anatase and rutile are indicated by the *top and bottom blue bars*, respectively

concentration of crystalline TiO_2. The formation of crystalline TiO_2 was first observed at 600 °C and increased steadily up to 900 °C, when heating in both air and argon. It is evident that the amorphous TiO_2 was not completely converted to crystalline TiO_2 by 900 °C. Figure 4 also shows the progressive growth of rutile after the formation, whereas the anatase concentration steadily reduces beyond approximately 800 °C due to transformation to rutile. Overall, Fig. 4 is consistent with the transformation of anatase into rutile becoming more likely with increases in temperature. This discussion is extended below when the results on relative amounts of anatase and rutile with temperature in Fig. 6 are considered.

Figure 5 shows the typical SRD plots from Rietveld analysis for data measured in air and argon at 800 °C. In general, the quality or goodness of fit is gauged by the values of weighted pattern R-factor (R_{wp}), the expected R-factor (R_{exp}), and the derived Bragg R-factor (R_B) [30]. In this work, values obtained for air and argon atmospheres were $R_{wp} = 13.0$ and 10.0, $R_{exp} = 3.7$ and 4.6, R_B (anatase) $= 4.6$ and 4.9, and R_B (rutile) $= 7.3$ and 4.2, respectively.

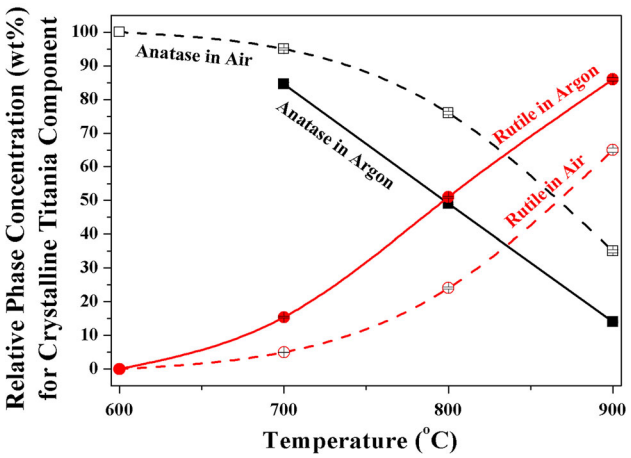

Fig. 6 Relative phase abundances of anatase and rutile for the crystalline TiO_2 component in the temperature range 600–900 °C for TiO_2 nanofibers heated in air and argon atmospheres. The phase levels represent the percentages of crystalline TiO_2 at each temperature

Figure 6 shows the variation with temperature of the relative amounts of anatase and rutile from Rietveld

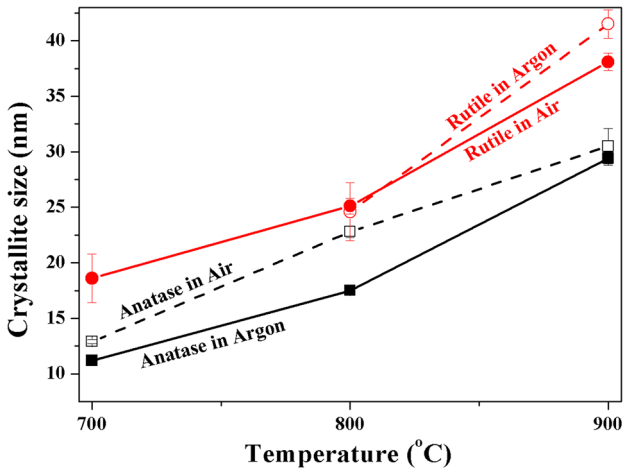

Fig. 7 Willamson–Hall plot estimates of the effect of temperature on the average crystallite size of **a** anatase and **b** rutile in TiO_2 nanofibers according to temperature

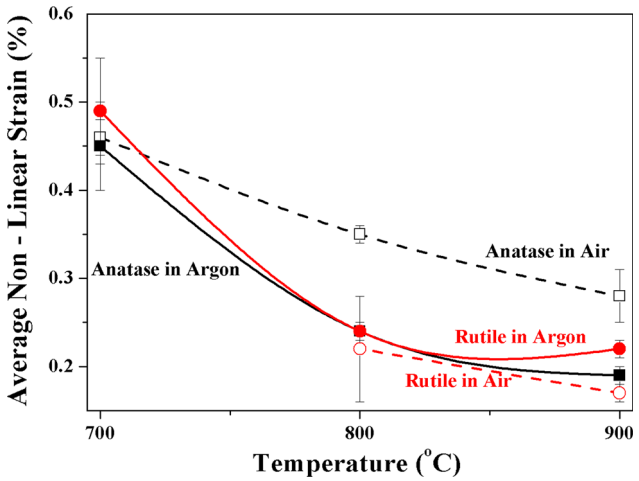

Fig. 8 Williamson–Hall plot estimates of mean strain for anatase and rutile crystallites in the range 600–900 °C for TiO_2 nanofibers heated in air and argon atmospheres

analysis, which supplements the information shown in Fig. 4. The conversion of crystalline anatase to rutile in both air and argon atmospheres is clearly indicated. The results show that the conversion is less rapid in air than in argon. At 600 °C, anatase formed in air but not yet in argon. In argon at 700 °C, anatase comprised 85 % of the crystalline TiO_2, and 95 % of the total in air. By 800 °C the abundance of anatase in crystalline TiO_2 falls to 76 % in air and 50 % in argon, and then by 900 °C to 35 % in air and to 14 % in argon. In addition, the phase content of rutile increased dramatically as the temperature increased by virtue of the transformation of metastable anatase into rutile. Rutile formed at 700 °C in both atmospheres but with different abundances. It increased from about 15 % at 700 °C to well over 85 % at 900 °C in argon atmosphere. However, in air, it increased from 5 % up to only 65 % for the same temperature range.

Figure 7 shows the effect of temperature on the growth of anatase and rutile crystallites according to atmosphere. The average crystallite size for anatase was ~13 nm at 700 °C in air and increased linearly for both atmospheres, to ~30 nm at 900 °C. The significantly larger rutile crystallite sizes were ~18 nm at 700 °C in both air and argon, but grew to ~37 nm in air and ~40 nm in argon at 900 °C. Therefore, the atmosphere had an insignificant effect on crystallite growth. The crystallite growth with temperature behaviour is attributed to the conversion of amorphous material to crystalline TiO_2 through an atomic diffusion-controlled nucleation and growth process. The gradients of the linear regressions for the plots in Fig. 5 amount to approximately 1.5–2 % volumetric growth per degree increase in temperature. This diffusion growth is orders of magnitude higher than that due to lattice thermal expansion (see Fig. 9).

The effect of temperature on the average lattice strain of both anatase and rutile for both atmospheres is shown in Fig. 8. It can be seen that the initial strain present in both phases is progressively relieved as the temperature increases. The observed strain relief is consistent with crystallite–crystalline interactions being negligible up to the maximum temperature considered in the study, at which point there is still substantial amorphous TiO_2 present. The higher strains observed for the anatase phase in air is consistent with the finding of Nicula et al. [34] who reported that the anatase phase exhibits larger strain values than rutile in titania powders over 400–850 °C.

The variations of unit-cell parameters and cell volumes for anatase and rutile with temperature are shown in Fig. 9a, b, and Fig. 10, and the corresponding linear and volumetric thermal expansion coefficients (TECs) are provided in Table 2. The unit-cell parameters and cell volume, for both phases in air and argon atmospheres increased linearly with temperature, as expected. The SRD thermal expansion data of Hummer et al. [31] measured with titania powders over the temperature range 25–300 °C, which are included in Table 2, were extrapolated to the temperatures considered in this study. It is seen that the TECs for the anatase in both air and argon compare closely with values reported for crystalline TiO_2 powder. By contrast, the rutile expansion coefficients are higher in argon, and higher again in air. There is also clear evidence for thermal expansion anisotropy in the rutile phase which points to the development of a more pronounced strain in rutile compared with anatase, and with the effect being more pronounced in argon which may explain the rougher appearance and more breakage of the nanofibers at high

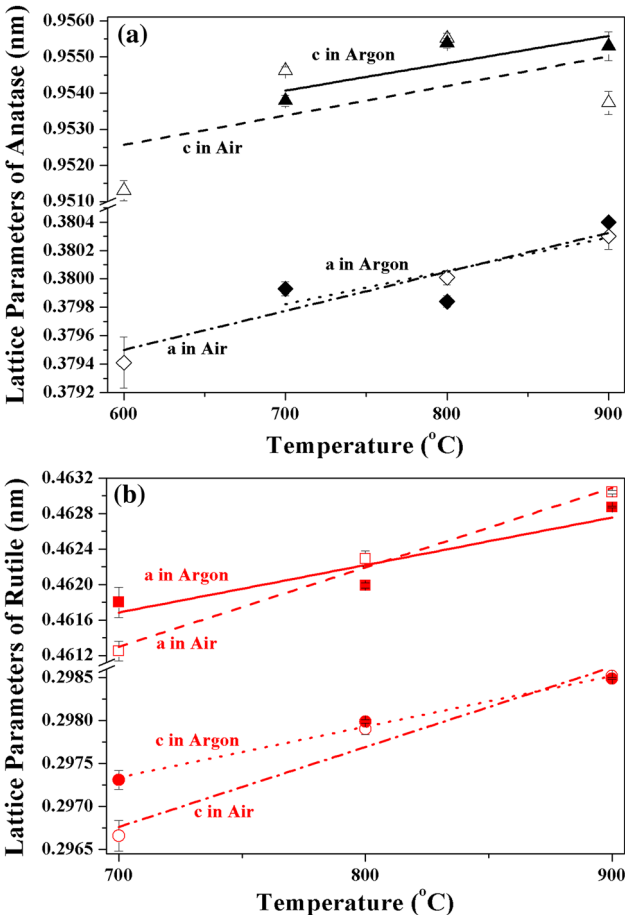

Fig. 9 Variation with temperature of the lattice parameters for anatase **a** and rutile **b** in air and argon atmospheres

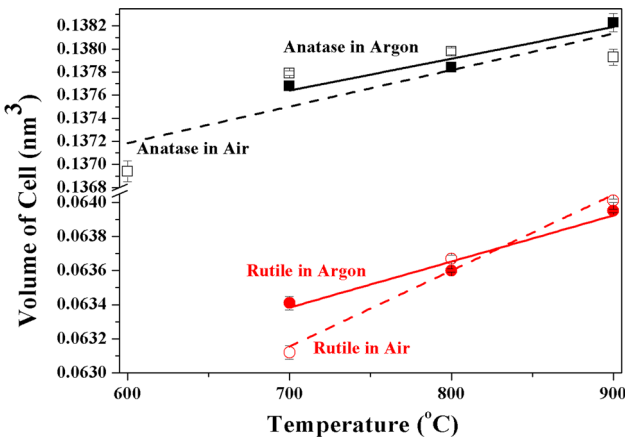

Fig. 10 Variation with temperature of the cell volume for anatase and rutile in air and argon atmospheres

temperatures compared with heating in air. In addition, for both anatase and rutile, the thermal expansion coefficients (TECs) were higher in air than in argon atmospheres due to the formation of oxygen vacancies in argon atmosphere. However, the linear expansion coefficient ratio of α_c to α_a was ~9 % higher in argon than in air, which could be the main reason for the embrittlement of nanofibers. Furthermore, it should be noted that literature equations of anatase and rutile parameters have hitherto been determined at relatively low temperatures, from room temperature to just over 300 °C using anatase and rutile TiO_2 powders, while the present study examined TiO_2 nanofibers at higher temperatures.

Table 2 Linear (α_a, α_c) and volumetric (β) thermal expansion coefficients (TECs) calculated from Fig. 9 and 10 at 800 °C

	TEC × 10^{-5} (°C^{-1})		α_a	α_c	β	α_c/α_a
Atmosphere (this study)	Air	Anatase	0.72	0.86	2.29	1.19
		Rutile	1.94	3.12	6.99	1.61
	Argon	Anatase	0.62	0.79	1.99	1.27
		Rutile	1.16	1.98	4.24	1.70
Hummer et al. [31]	Powdered TiO_2 sample in air	Anatase	0.53	1.04	2.17	1.96
		Rutile	0.87	1.01	2.83	1.16

4 Conclusions

The effect of air and argon on the dynamic crystallization behaviour of electrospun TiO_2 nanofibers was investigated in situ using SRD data measured in the temperature range 25–900 °C. The electrospun TiO_2 nanofibers were initially amorphous but crystallized progressively into anatase and rutile at elevated temperatures. In air, anatase was first observed at 600 °C and rutile at 700 °C, but in argon both appeared at 700 °C. The level of crystalline TiO_2 (anatase and rutile) increased monotonically with increase in temperature, with some amorphous TiO_2 still being observed at 900 °C. The rates of anatase-to-rutile transformation were faster in argon than in air by virtue of oxygen vacancies in the former. The non-linear strain in both polymorphs reduced with temperature, with the strain of anatase in air being elevated. The substantial elevation of rutile thermal expansion pointed to strain anisotropy in the rutile phase and the concomitant fibre breakage.

Acknowledgments The authors gratefully acknowledge the Australian Synchrotron (AS122/PDFI/5075) for work supporting. The authors would like to thank Ms. E. Miller and Dr. N. Chen-Tan for assistance with the SEM work, and Ms. K. Haynes, Mr. A. Viereckl and Mr. J. Xiao Hua for laboratory assistance.

References

1. I.M. Low, H. Albetran, V.M. Prida, V. Vega, P. Manurung, M. Ionescu, J Mater Res **28**, 304 (2013)
2. P. Manurung, Y. Putri, W. Simanjuntak, I.M. Low, Ceram Int **39**, 255 (2013)

3. P. Zhang, C. Shao, X. Li, M. Zhang, X. Zhang, Y. Sun, Y. Liu, J Hazard Mater **237–238**, 331 (2012)
4. C. Yu, L. Wei, X. Li, J. Chen, Q. Fan, J. Yu, Mater Sci Eng B **178**, 344 (2013)
5. X. Pan, Y. Zhao, S. Liu, C.L. Korzeniewski, S. Wang, Z. Fan, ACS Appl Mater Interfaces **4**, 3944 (2012)
6. V.J. Babu, A.S. Nair, Z. Peining, S. Ramakrishna, Mater Lett **65**, 3064 (2011)
7. G. Liu, L. Wang, H.G. Yang, H.M. Cheng, G.Q. Lu, J Mater Chem **20**, 831 (2010)
8. S. Chuangchote, J. Jitputti, T. Sagawa, S. Yoshikawa, ACS Appl Mater Interfaces **1**, 1140 (2009)
9. D.W. Kim, N. Enomoto, Z.E. Nakagawa, K. Kawamura, J Am Ceram Soc **79**, 1095 (1996)
10. R. Liu, L.S. Qiang, W.D. Yang, H.Y. Liu, Mater Res Bull **48**, 1458 (2013)
11. W. Li, C. Ni, H. Lin, C.P. Huang, S.I. Shah, J Appl Phys **96**, 6663 (2004)
12. D.A. Hanaor, C.C. Sorrell, J Mater Sci **46**, 855 (2011)
13. S. Shang, X. Jiao, D. Chen, ACS Appl Mater Interfaces **4**, 860 (2012)
14. H. Li, W. Zhang, W. Pan, J Am Ceram Soc **94**, 3184 (2011)
15. R.D. Shannon, J.A. Pask, J Am Ceram Soc **48**, 391 (1965)
16. R.A. Eppler, J Am Ceram Soc **70**, 64 (1987)
17. Y. Iida, S. Ozaki, J Am Ceram Soc **44**, 120 (1961)
18. J.A. Gamboa, D.M. Pasquevich, J Am Ceram Soc **75**, 2934 (1992)
19. J.H. Huang, M.S. Wong, Thin Solid Films **520**, 1379 (2011)
20. J.S. Lee, T.J. Ha, M.H. Hong, H.H. Park, Thin Solid Films **529**, 98 (2013)
21. I.M. Low, B. Curtain, M. Philipps, Q.Z. Liu, M. Ionescu, J Aust Ceram Soc **48**, 198 (2012)
22. V. Vega, V.M. Prida, M.H. Velez, E. Manova, P. Aranda, E.R. Hitzky, M. Vazquez, Nanoscale Res Lett **2**, 355 (2007)
23. S. Chuangchote, J. Jitputti, T. Sagawa, S. Yoshikawa, ACS Appl Mater Interfaces **1**, 1140 (2009)
24. Z.M. Huang, Y.Z. Zhang, M. Kotaki, S. Ramakrishna, Compos Sci Technol **63**, 2223 (2003)
25. Q. Li, D.J.G. Satur, H. Kim, H.G. Kim, Mater Lett **76**, 169 (2012)
26. W. Luo, X. Hu, Y. Sun, Y. Huang, J Mater Chem **22**, 4910 (2012)
27. C. Wessel, R. Ostermann, R. Dersch, B.M. Smarsly, J Phys Chem C **115**, 362 (2011)
28. H. Li, W. Zhang, W. Pan, J Am Ceram Soc **94**, 3184 (2011)
29. P. Zhu., A.S. Nair, P. Shengjie, Y. Shengyuan, S. Ramakrishna, ACS Appl Mater Interfaces **4**, 581 (2012)
30. W.K. Pang, I.M. Low, Z.M. Sun, J Am Ceram Soc **93**, 2871 (2010)
31. D.R. Hummer, P.J. Heaney, Powder Diffr **22**, 352 (2007)
32. G.K. Williamson, W.H. Hall, Acta Metall **1**, 22 (1953)
33. R.A. Spurr, H. Myers, Anal Chem **29**, 760 (1957)
34. R. Nicula, M. Stir, C. Schick, E. Burkel, Thermo Acta **403**, 129 (2003)

3.2 Activation Energies for Phase Transformations in Electrospun Titania Nanofibers: Comparing the Influence of Air and Argon Atmospheres

---

ALBETRAN, H., O'Connor, B. H., & LOW, I. M. 2016. Activation Energies for Phase Transformations in Electrospun Titania Nanofibers: Comparing the Influence of Argon and Air Atmospheres. *Applied Physics A*, 122, 1–9.

Appl. Phys. A (2016)122:367
DOI 10.1007/s00339-016-9871-7

Applied Physics A
Materials Science & Processing

Activation energies for phase transformations in electrospun titania nanofibers: comparing the influence of argon and air atmospheres

H. Albetran[1,3] · B. H. O'Connor[1,2] · I. M. Low[1]

Received: 2 June 2015 / Accepted: 15 November 2015

Abstract This paper reports on titania absolute phase level (amorphous, anatase, and rutile forms) changes in electrospun amorphous titania nanofibers from 25 to 900 °C in air and argon atmospheres. A novel method was developed to extract absolute levels of amorphous titania and crystalline anatase and rutile from the synchrotron radiation diffraction (SRD) data. This is a sequel to a relative phase concentrations study that has been reported previously by Albetran et al. (Appl Phys A 116:161 [2014]). Determination of absolute phase levels facilitated estimation of the activation energies for the amorphous-to-anatase transformation of 45(9) kJ/mol in argon and 69(17) in air, and for the anatase-to-rutile transformation energies of 97(7) kJ/mol for argon and 129(5) for air. An activation energy estimate for amorphous-to-crystalline titania in argon of 142(21) kJ/mol, achieved using differential scanning calorimetry (DSC), is consistent with the SRD results. The differences in phase transition and activation energies when the titania nanofibers are heated in argon is attributed to the presence of substantial oxygen vacancies in anatase. Estimates of anatase and rutile oxygen site occupancies from the SRD data show that anatase has discernible oxygen vacancies in argon, which correspond to stoichiometric TiO_{2-x} with $x < 0.4$ that the anatase stoichiometry in air is TiO_2. Rutile does not have significant oxygen vacancies in either argon or air.

1 Introduction

Titanium dioxide (TiO_2), titania, is a widely studied material principally due to its high photoactivity, photo-durability, mechanical robustness, low cost, and chemical and biological inertness [1–8]. Titania properties are influenced by the mix of the amorphous titania and the two common crystal forms (anatase and rutile) in the material, due in part to differences in the crystal structures for anatase and rutile [1]. Generally, anatase crystallizes from amorphous titania at relatively low temperatures and subsequently transforms to rutile at higher temperatures [9, 10].

The transformation behavior is influenced by various conditions that include synthesis method, level of impurities, temperature, calcination time, grain size and atmosphere type and condition [11–21]. The effects of argon, vacuum, air, argon–chlorine mixture, hydrogen, steam and nitrogen on the anatase-to-rutile phase transformation have been reported [12, 22–25]. Atmosphere type and condition may induce changes in the titania crystal structure site occupancies and/or interstitial effects which may in principle influence the diffraction data as measured in this study.

A paper of particular significance for the present study is the mini-review by Pan et al. [26], which describes the formation of oxygen vacancies in titania in an inert environment and the subsequent elimination of these vacancies in the presence of oxygen. Thus, determining oxygen site occupancies from titania diffraction data should indicate the influence of oxygen vacancies on phase evolution.

✉ I. M. Low
j.low@curtin.edu.au

[1] Department of Imaging and Applied Physics, Curtin University, Perth, WA 6845, Australia

[2] John de Laeter Centre, Curtin University, GPO Box U1987, Perth, WA 6845, Australia

[3] Department of Basic Sciences, College of Education, University of Dammam, P. O. Box 2375, Dammam 31451, Saudi Arabia

Published online: 14 March 2016

Nanostructured titania with elongated morphology exhibits high surface area-to-volume ratios which has significance in the use of titania as a catalyst in decomposing organic pollutants because photocatalytic reactions take place more readily on the surface of the catalyst [27]. Various techniques have been used to synthesize nanostructured titania with different morphologies (e.g., nanowires, nanorods, nanotubes, and nanofibers). These include solvothermal, sol–gel, evaporation, and chemical vapor deposition [28–30].

A variety of techniques, such as self-assembly, hydrothermal treatment, anodization, and electrospinning, have been developed for fabricating one-dimensional nanotitania [31–33]. Among these methods, electrospinning is a simple and cost-effective technique applicable at an industrial level [34, 35]. In this process, a solution of polymer and titania precursor is ejected through a needle in a high electric field whereby composite nanofibers of polymer and amorphous titania are formed [34, 35]. To the best of our knowledge, the effect of atmospheres on the in situ crystallization of anatase and rutile in electrospun titania nanofibers has not been previously reported other than in the preliminary paper published by the authors (Albetran et al. [1]).

The present study of the SRD data reported earlier advances the preliminary results by (1) quantifying how the absolute phase levels in electrospun nanofibers change with temperature according to the controlling environment for calcination (argon versus air), as the material is heated non-isothermally; and also (2) determining the activation energy levels for the transformations. A novel method has been developed to extract the absolute levels of amorphous titania and crystalline anatase and rutile from the SRD data. Determination of SRD absolute phase levels has facilitated estimation of the activation energies for the amorphous-to-anatase phase transformations and for anatase-to-rutile, in both argon and air atmospheres. The SRD results for heating in argon have been explored further using DSC data measured over the same temperature range as used for the SRD data. Extracting oxygen site occupancy values from the SRD data has been carried out to assess the extent of non-stoichiometry effects in the titania nanofibers as they are calcined in the two atmospheres considered in the study, and lattice parameter data have also been examined. Imaging by FESEM and TEM has been conducted to support the SRD and DSC data interpretations.

2 Experimental procedures

2.1 Synthesis of electrospun titania nanofibers

Details of the electrospinning technique are given in the preliminary study by the authors [1]. In summary, a sol–gel solution was prepared by mixing titanium (IV) isopropoxide (as a titania precursor) and acetic acid, with ethanol being used as a solvent and then dissolved with PVP polymer. The titania sol–gel was stirred before being loaded into a plastic syringe for production of the nanofibers by electrospinning.

2.2 In situ synchrotron radiation diffraction (SRD) calcination measurements and data analysis

A detailed account of the SRD data acquisition is given in Albetran et al. [1]. In summary, measurements were conducted at the Australian Synchrotron using the powder diffraction beamline, with specimens being heated, in turn, in argon and air atmospheres at atmospheric pressure. The flow rate of argon was 10 ml/min, and the in-air measurements were performed within ambient air. The SRD data were collected over a 2θ range of 5°–84° at a wavelength of 0.1126 nm and with a fixed incident beam/sample angle of 3°. The patterns were acquired at ambient temperature and then in steps of 100 °C, from 200 to 900 °C, at 10 °C/min, using a data collection time of 2 min per pattern (Fig. 1a).

The absolute levels of amorphous titania and crystalline anatase and rutile at each temperature were extracted from the SRD data using (1) the relative phase levels of anatase and rutile from Rietveld analysis (see Ref. [1]) and (2) the temperature dependence of the SRD pattern background to obtain the absolute levels of amorphous titania. In relation to (2), the SRD background–temperature plots (see Fig. 3 of Results section) were analyzed by assuming that the background $B(T)$ at temperature T is given by a component B_A (T) due to amorphous scatter plus a second component B_S attributed to atomic X-ray scatter (Compton and Rayleigh). On this basis, the weight percentage of amorphous titania ($wt_{Am}\%$) is:

$$wt_{Am}\% = \frac{B(T) - B_f}{B_o - B_f} \quad (1)$$

where $B(T)$ is the background intensity at temperature T, B_o is the background intensity prior to the onset of the amorphous-to-crystalline titania transformation, and B_f is the projected background intensity when amorphous titania has transformed completely to crystalline titania. The background values were taken at $2\theta = 17°$, with the background levels for the SRD patterns at 600 °C for argon-immersed titania and 500 °C for air-immersed titania being used as the initial background intensity B_o, corresponding to 100 % amorphous titania. The final value for the background intensity B_f for the two atmospheres was estimated by fitting the background versus temperature data with the function:

$$B(T) = B_f + ae^{-bT} \quad (2)$$

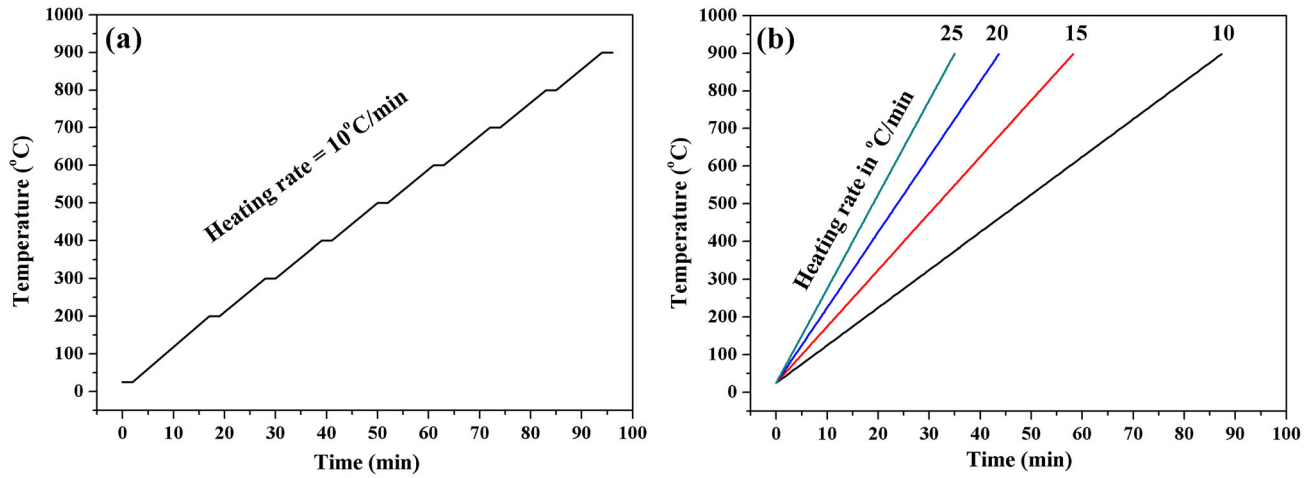

Fig. 1 **a** SRD hearing protocol. Plateaus indicate the 2-min periods during which SRD data were acquired. **b** DSC heating protocols for different heating rates

The final background intensity (B_f) estimates were 75 and 0 counts, and the amorphous transformation rates, b, were 0.0047 and 0.0026 °C^{-1} for the argon and air results, respectively.

The phase composition results from an initial Rietveld analysis of the SRD data were reported in the preliminary publication (Albetran et al. [1]) which provided the relative concentrations of anatase and rutile. These were combined with the amorphous titania concentrations from this study to give absolute anatase and rutile concentrations according to:

$$\mathrm{wt_{am}}\% + \mathrm{wt_{anatase}}\% + \mathrm{wt_{rutile}}\% = 100\,\% \quad (3)$$

Rietveld analysis of the SRD data was also used to estimate (1) the oxygen site occupancies for the anatase and rutile crystalline phases and (2) the anatase and rutile lattice parameters in order to assess conclusions regarding oxygen vacancies which are drawn from the activation energy results. The oxygen site occupancies and lattice parameters for anatase and rutile in argon and air from 700 to 900 °C were determined using TOPAS program (Bruker AXS, version 4.2).

2.3 Thermal analysis experiments

Thermal analysis calcination measurements (TGA, DTA and DSC) were made for the materials in argon, using a TGA/DSC Mettler Toledo machine. The total argon flow rate was 25 ml/min, with 20 ml/min protective argon gas flowing through the machine and a background argon flow rate of 5 ml/min. DSC measurements were made non-isothermally from 25 to 900 °C using heating rates of 10, 15, 20 and 25 °C/min (Fig. 1b). *Ca.* 25 mg of sample was held in a 150 µl alumina crucible for each heating rate. For safety reasons, thermal analysis measurements could not be conducted in air.

2.4 Crystallization activation energies

Activation energies were estimated for the amorphous-to-anatase and anatase-to-rutile transformations using the SRD phase analysis results, according to the procedure described by Matusita et al. [36], the equation used being [37]:

$$\ln[-\ln(1-\mathrm{wt})] = -1.052E/RT + \mathrm{constant} \quad (4)$$

where wt is the weight fraction of the transformed material, R is the gas constant (8.3145 J/kmol), T is the temperature (K), and E is the activation energy (kJ/mol). Thus, a plot of $\ln[-\ln(1-\mathrm{wt})]$ versus $1/T$ is expected to be linear, and the activation energy can be determined from the gradient of a linear regression fit. The combined weight fraction for anatase plus rutile at each temperature was used to calculate the activation energy for amorphous-to-anatase transformation on the basis that anatase crystallizes from amorphous titania and transforms to rutile.

Activation energies were also calculated using a modified version of the Arrhenius equation:

$$\ln \mathrm{wt} = -E/RT + \ln \mathrm{wt}_o \quad (5)$$

where wt is the weight fraction of the transformed phase(s), and wt_o is the initial weight fraction.

The non-isothermal DSC data collected at different heating rates were used to determine the activation energies for the amorphous–crystalline transformation according to the modified Avrami equation [38]:

$$\ln\left(T_p^2/\alpha\right) = E/RT_p + \ln(E/R) - \ln v \quad (6)$$

where T_p represents the DSC peak temperature (K), α is the heating rate (K/s), and v is a frequency factor. A plot of $\ln(T_p^2/\alpha)$ versus $1/T_p$ should yield a straight line for data measured at different heating rates, which allows for the calculation of activation energy from the gradient.

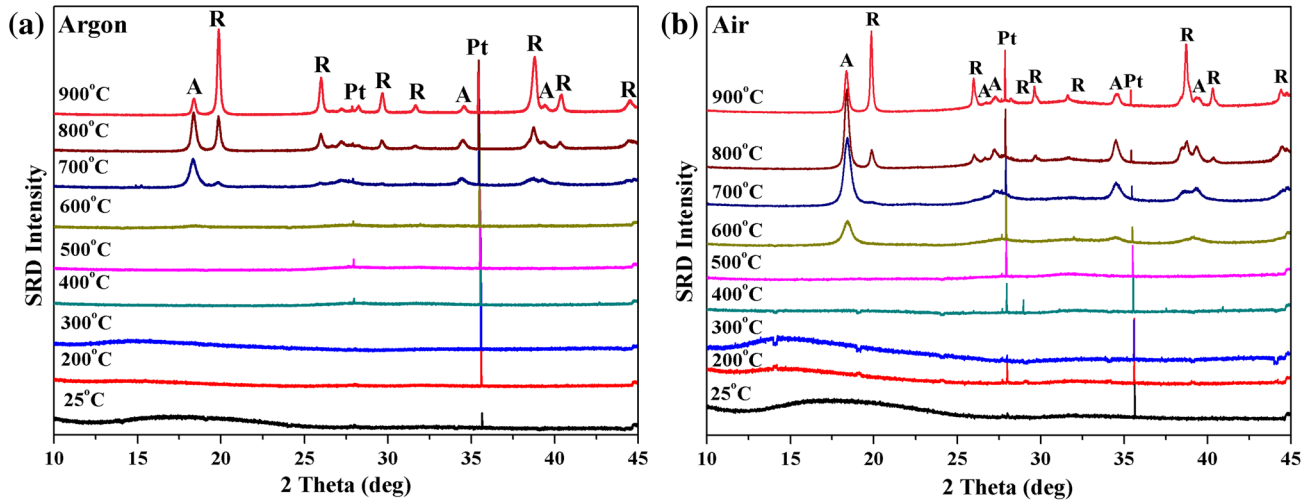

Fig. 2 Stacked SRD plots for electrospun titania nanofiber material when heated in argon and in air, from 25 to 900 °C (*A* anatase, *R* rutile, *Pt* platinum). Plots taken from Albetran et al. [1]

2.5 Microstructural imaging

Initial SEM imaging results reported in the preliminary publication (Albetran et al. [1]) were extended using TEM and FESEM to provide higher magnification and resolution. TEM measurements were carried out at the University of Western Australia using a JEPL 3000F instrument operating at 300 kV and fitted with a Gatan 10 M pixel charge-coupled device camera. After the in situ high-temperature SRD measurements in argon at 900 °C, a TEM sample was prepared for imaging at room temperature. Sample preparation involved grinding a small piece of nanofiber material (~5 mg) and then dispersing in ethanol. Two drops of the suspension were mounted onto a TEM copper grid and allowed to dry before imaging.

FESEM imaging was conducted at Curtin University after the TGA/DSC experiments, using a field emission scanning electron microscopy (ZEISS, NEON, 40EsB, FESEM). The samples were coated with a 3 nm layer of platinum prior to imaging to avoid charging.

3 Results and discussion

3.1 Phase evolution results from the SRD and DSC experiments

Figure 2 shows the stacked SRD plots measured in both argon and air over the temperature range 25–900 °C, noting that the peaks at ~27.7° and 35.6° are due to the Pt heating holder, see preliminary paper by Albetran et al. [1]. Expanded views of the plots over the 2θ range 15.5°–21°, which were used to determine the absolute levels of amorphous titania, are shown in Fig. 3. Figure 4 shows the variation in absolute phase concentrations with temperature for the argon and air atmospheres. To interpret the SRD phase evolution results, it is useful to also consider the anatase and rutile oxygen site occupancies reported in Table 1, and the phase transformation activation energies reported in Table 2. The following comments are made on the SRD phase kinetics results.

The phase composition results are consistent with there being a sequential transformation of amorphous phase to anatase and then anatase to rutile. The titania nanofibers are initially amorphous in both argon and air, as shown by the pronounced amorphous humps in the SRD patterns from 25 to 300 °C. By 400 °C, the amorphous humps have disappeared due to the loss of solvent and PVP polymer which is consistent with the TGA results in Fig. 5a.

Heating the fibers in air leads to initial crystallization of anatase from the amorphous titania matrix at a lower temperature in air (500–600 °C) than in argon (600–700 °C), and the higher concentration of anatase relative to rutile in the range 600–700 °C is more pronounced in air. This observation points to the influence that oxygen from air has in accelerating the transformation of amorphous titania to anatase. The higher concentration of anatase in air continues up to 900 °C. The site occupancies in Table 1 are consistent with (1) anatase being oxygen-deficient when forming in argon, but not when forming in air; (2) the oxygen deficiency being maintained over the observed temperature range, up to 900 °C in argon; (3) rutile being oxygen deficient in argon only below 800 °C, and not at all in air. The anatase stoichiometry in argon corresponds to TiO_{2-x}, with $x < 0.4$. It is evident from Pan et al. [26] and from the results reported here that the stoichiometry of amorphous titania in argon is TiO_{2-x} due to the formation of oxygen vacancies, but not when heated in air.

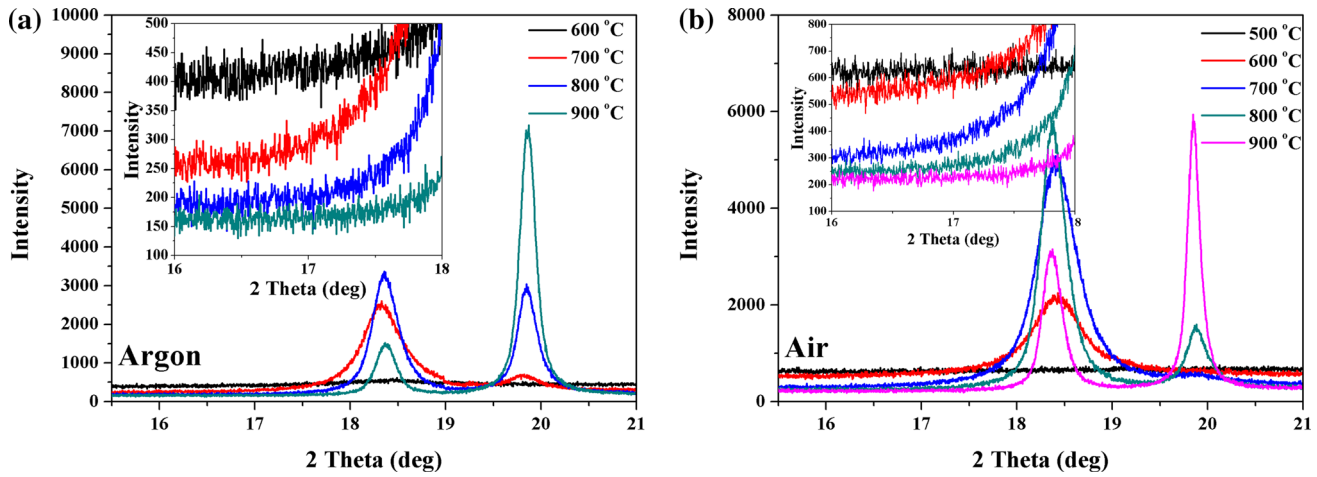

Fig. 3 Portions of SRD plots showing near-background data when nanofiber material was heated in argon and in air

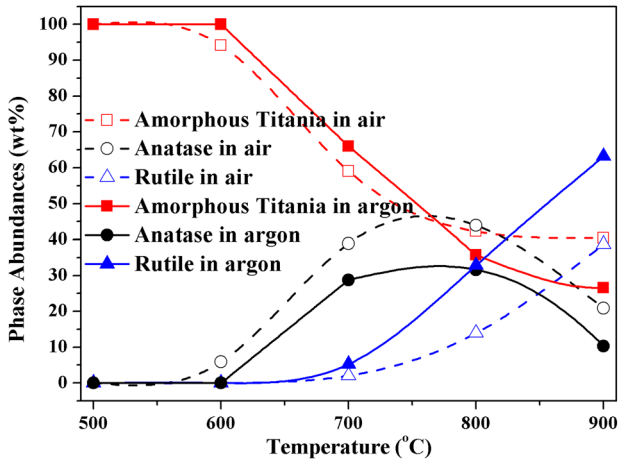

Fig. 4 Phase abundances of amorphous titania, anatase and rutile from the SRD data in argon and in air for the range 500–900 °C. Results for air are taken from Albetran et al. [1]

Table 1 Oxygen site occupancies for anatase and rutile, from Rietveld analysis of SRD data

Temperature (°C)	Anatase		Rutile	
	Argon	Air	Argon	Air
700	0.9	1.0	0.8	(Rutile not detected)
800	0.8	1.0	1.1	1.1
900	0.8	0.9	1.1	1.1

The uncertainty for each value of site occupancy was estimated to be ±0.1

The influence of atmosphere on the anatase-to-rutile transformation contrasts with that for amorphous-to-anatase in that growth in the concentration of rutile in air is retarded relative to that in argon. The evidence for the formation of oxygen vacancies in anatase under argon was obtained from the oxygen site occupancies from Rietveld analysis (Table 1). This observation is consistent with the work of Morgan and Watson [39], in which oxygen vacancy formation was found to be more favorable in anatase than in rutile in an oxygen-deficient atmosphere. In air, the excess of oxygen results in transformation from anatase-to-rutile with the TiO_2 having fully occupied oxygen sites. Thus, the oxygen site occupancy data in Table 1 suggest that the anatase-to-rutile transformation in argon and air involve:

$$\mathrm{Anatase}(\mathrm{TiO}_{2-x}) \xrightarrow{\mathrm{Argon}} \mathrm{Rutile}(\mathrm{TiO}_2)$$

$$\mathrm{Anatase}(\mathrm{TiO}_2) \xrightarrow{\mathrm{Air}} \mathrm{Rutile}(\mathrm{TiO}_2)$$

The presence of oxygen vacancies in anatase makes the anatase-to-rutile transformation in argon more efficient than in air because the transformation is reconstructive rather than displacive, thus involving the breaking of anatase Ti–O bonds followed by reforming of bonds in rutile. It is plausible from Hanaor and Sorrell [40] that a reductive atmosphere relative to air would increase the oxygen vacancy concentration in the anatase structure at elevated temperature, which is expected to enhance the anatase-to-rutile transformation.

An attempt was made to use the temperature dependence of the lattice parameters to obtain further evidence for the presence of oxygen vacancies. However, it was found that the low accuracy of the lattice parameters (ca. 0.02–0.05 %) would have obscured any evidence of vacancy-induced lattice changes.

Also noted from Fig. 4 is that by 900 °C, the fibers are predominantly crystalline, with the amorphous levels in argon and air being 28 % in argon and 40 % in air. The crystalline character of the fibers is shown clearly in the FESEM micrographs in Fig. 8a.

Table 2 The average activation energies (kJ/mol) for non-isothermal SRD data analysis in argon and air using the Arrhenius, and Matusita et al. equations (Fig. 7), and non-isothermal argon DSC

Titania format	Atmosphere	Measurements	References	Amorphous-to-anatase	Anatase-to-rutile
Nanofiber	Argon	SRD	This study	45(9)	97(7)
Nanofiber	Argon	DSC	This study	142(21)[a]	
Nanofiber	Air	SRD	This study	69(17)	129(5)
Nanotubes	Oxygen	DSC	[25]		264
Powder	Air	DSC	[41]		213
Membranes	Air	DSC	[42, 43]		213, 147

Standard deviations in parentheses

[a] The combined activation energy for amorphous-to-anatase and anatase-to-rutile

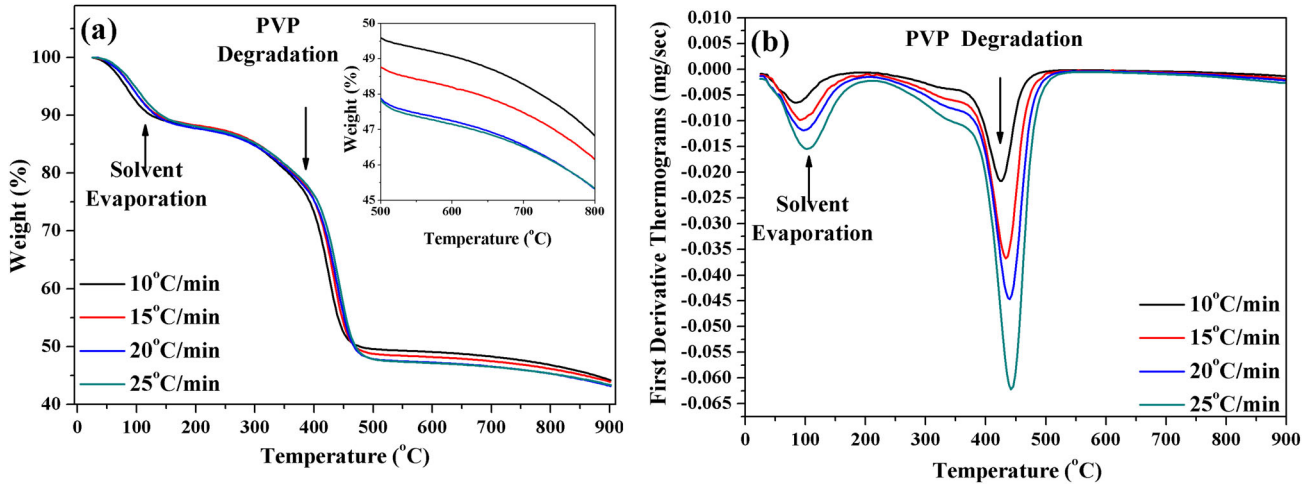

Fig. 5 **a** Thermogravimetric analysis (TGA), and **b** differential thermal analysis (DTA) results for nanofiber material heated in argon

The thermal analysis results are consistent with those from the SRD calcination experiments. Figure 5a shows the TGA weight loss data for heating in argon. The TGA curves have three distinct stages. From room temperature to ~150 °C, a ~12 % weight loss occurs due to the loss of acetic acid and ethanol. The second weight loss, ~40 %, which occurs from ~150 to 450 °C, is attributed to PVP decomposition. The DTA results in Fig. 5b show the maximum decomposition temperature (T_{max}) for solvent loss at ~100 and 450 °C for the PVP polymer loss, with the peak temperatures being 424, 433, 440, and 442 °C for 10, 15, 20, and 25 °C/min, respectively. The trend in peak temperature indicates that the thermal decomposition of PVP is endothermic. The peak temperature obtained from the DSC plots is the temperature at which the maximum decomposition rate is highest, and depends on the heating rate.

The weight loss of ~5 % between 500 and 900 °C which is attributed to the loss of oxygen from the amorphous titania to the argon atmosphere while anatase (TiO_{2-x}) is forming. The decrease in weight loss is consistent with the loss of oxygen from amorphous titania increasing with heating rate, which is also indicated by the oxygen site occupancy data in Table 1.

Figure 6a shows the DSC plots for electrospun titania nanofibers in argon at different heating rates. The DSC peak at ~700 °C is attributed to titania crystallization. From the argon SRD plots (Fig. 3), anatase and rutile crystalline phases existed simultaneously at 700 °C. Thus, the anatase and rutile crystalline phases have overlapping DSC peaks at ~700 °C, which shift slightly to a higher temperature with an increase in heating rate from 10 to 25 °C/min.

3.2 Phase transformation activation energies

The activation energy plot for the argon DSC data in Fig. 6b provided an activation energy of 142(21) kJ/mol corresponding to the transformations amorphous-to-anatase and anatase-to-rutile, noting that the DSC plots do not resolve the apparently separate crystallization events for the formation of anatase and rutile.

The linear regressions used to obtain activation energies from the argon and air SRD data are shown in Fig. 7,

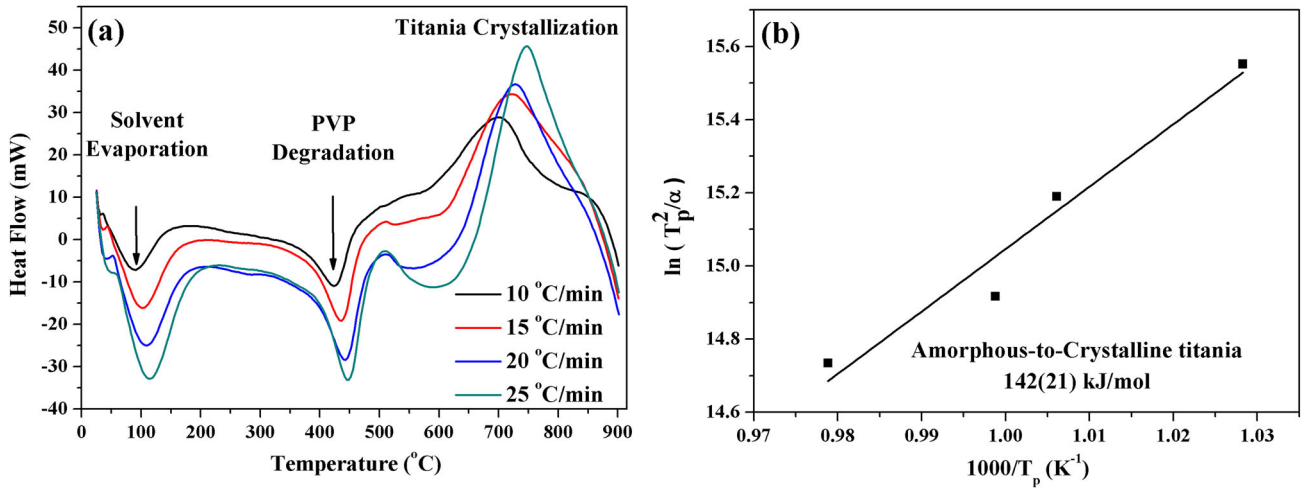

Fig. 6 **a** DSC thermoanalytical technique for the material heated in argon at different heating rates, and **b** modified Avrami plot $\ln(T_p^2/\alpha)$ versus $1000/T_p$

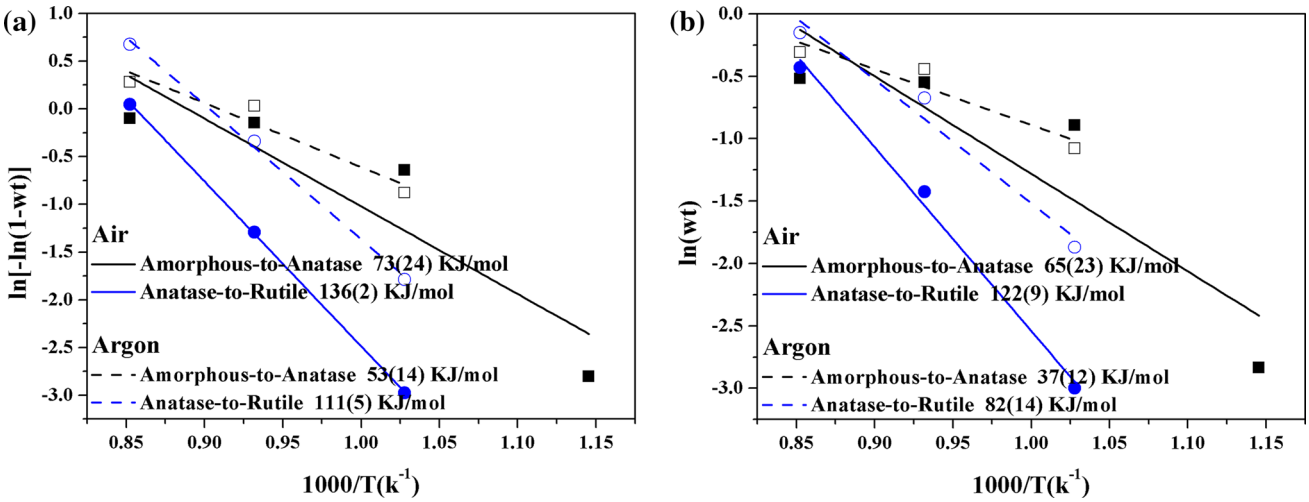

Fig. 7 SRD data plots of ln [−ln (1 − wt)] versus 1000/*T* according to Matusita et al., and ln (wt) versus 1000/*T* using the Arrhenius equation for material heated in argon and air

noting that the assumed sequential titania transformations are amorphous-to-anatase and then anatase-to-rutile. Table 2 shows the estimated activation energies for the titania transformations in argon and air, and compares these with literature values for different titania forms and atmosphere. The average estimated activation energies in argon from this study are marginally lower than in air: the average estimated activation energies for the amorphous-to-anatase transformation being 45(9) kJ/mol in argon and 69(17) kJ/mol in air; and the mean value for the anatase-to-rutile transformation being 97(7) kJ/mol in argon and 129(5) kJ/mol in air. These small differences are consistent with the phase composition results and the oxygen site occupancies.

The activation energy plot for the argon DSC data is close to the sum of the SRD activation energies for the amorphous-to-anatase and anatase-to-rutile transformations. The amorphous-to-anatase transformation is evident from the titania crystallization DSC peaks, whereas the anatase-to-rutile transformation is visible from the distinct narrowing, sharpening, and increase in heat flow with increasing heating rates. The effect of heating rate on anatase-to-rutile transformations is visible from the overlapping (anatase and rutile) peaks, which increases with increasing heating rate [14]. The argon flow rate in the DSC process was 25 ml/min, whereas the argon flow rate for the SRD experiment was 10 ml/min, which is another factor that affects the phase transformation and activation energy.

Comparison of the SRD anatase-to-rutile activation energies for the electrospun titania nanofibers reported here are lower than the values of activation energy reported in literature such as 264 kJ/mol for nanotubes [25], 213 kJ/mol for powder [41], and 213 and 147 kJ/mol for membranes [42, 43]. The difference in activation energy is attributed to various conditions that include the particle size, impurities level, calcination method (isothermal and non-isothermal), equation used, and atmosphere type and condition [12, 13, 17, 18, 42].

3.3 Microstructure imaging

In addition to the electron microscopy results discussed here, it is noted that the color of the titania nanofibers changed from white to gray after calcining in argon (optical image not shown here). This color change is attributed to oxygen loss from the titania to form oxygen vacancies [19, 23].

Table 3 shows the fiber diameter sizes from the preliminary study and from this investigation. The total number of fiber measurements was 40 for each entry in the table. The sol–gel and electrospinning parameters, including titanium isopropoxide (TiP) concentration, flow rate, needle tip-to-collector distance, and applied voltage affect the diameter and variation in titania nanofiber size [44].

Figure 8a shows the secondary electron FESEM images recorded after heating at 25 °C/min from 25 to 900 °C in argon for the TGA/DSC measurements. The nanofibers have developed highly uneven surfaces, which are clearly due to the formation of anatase and rutile grains. The average FESEM nanofiber diameter and size range was found to be 381 ± 150 nm, and the average grain size is 85 ± 18 nm.

Figure 8b shows typical TEM photographs of the nanofibers after cooling to room temperature from 900 °C in argon following the SRD analysis with a heating rate of 10 °C/min. The surface of the fibers imaged by TEM appears to be smoother at low resolution than those from FESEM, but clear evidence for the development of granularity is seen in the higher-resolution images. The average diameter fibers and size range from the TEM images was 185 ± 92 nm, and the average grain size is 32 ± 24 nm which are not significantly less than the values from FESEM imaging. The variation in grain size from FESEM and TEM provides additional evidence of the effect of heating rate on the formation of titania crystals. The crystallite size increases with increasing heat rate [14], which indicates that the higher heating rate from FESEM compared with TEM can promote grain growth in crystalline titania.

Table 3 Fiber diameters (nm) from electron microscopy after calcining to 900 °C and then cooling to room temperature

EM imaging method	Reference	Argon	Air
SEM	Albetran et al. [1]	328 ± 113	358 ± 195
FESEM	This study	381 ± 150	Not measured
TEM	This study	185 ± 92	Not measured

The ± symbol refers to the size range for the size assessment. The number of measurements for each entry was 40

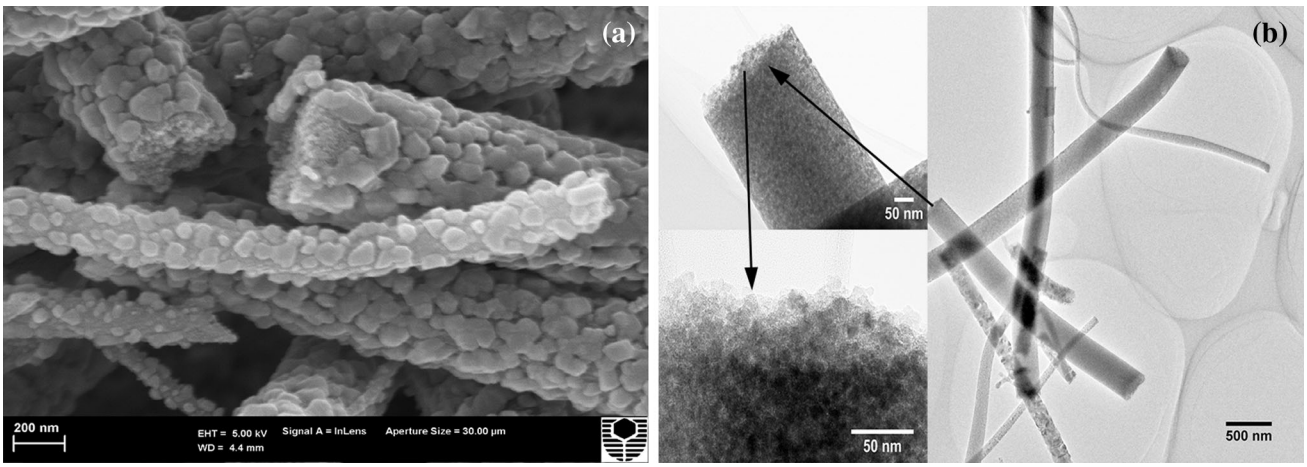

Fig. 8 **a** FESEM image following the TGA/DSC experiment in argon, and **b** TEM images following the SRD experiment in argon

4 Conclusions

The following principal conclusions were drawn from the study:

- The results point to the effect of the surrounding atmospheric environment in influencing the phase kinetics. Heating in argon causes some loss of oxygen from the initially amorphous fibers, resulting in a fiber non-stoichiometry TiO_{2-x} $(x < 0.4)$ on crystallizing from the amorphous matrix in argon. The stoichiometry TiO_2 is found for anatase in air and for rutile in both argon and air.
- The phase analysis results show that the concentration of anatase in air exceeds that observed in argon, whereas the concentration of rutile in air is substantially less that seen in argon. These differences are attributed to a faster anatase-to-rutile transformation when the samples are heated in argon compared with air due to oxygen vacancies. The phase analysis results also show that the fibers become mainly crystalline after heating to 900 °C in either argon or air, and this finding is supported by FESEM and TEM imaging.
- The estimated activation energy data are consistent with the phase composition and site occupancy data. The formation of oxygen vacancies in the anatase structure is thought to promote the anatase-to-rutile transformation in argon.

Acknowledgments The SRD work is supported financially by the Australian Synchrotron (Powder Diffraction Beamline) (AS122/PDFI/5075). The authors thank Dr. J. Kimpton at the Australian Synchrotron for guidance on use of the instrumentation at the Powder Diffraction Beamline; and at Curtin University to Dr. Y. Dong for the use of his electrospinning equipment, to Ms. E. Miller for assistance with FESEM, to Dr. X. Wang for assistance with TEM, and to Prof. M. Tade, Ms. K. Haynes, and Mr. A. Chan for TGA support.

References

1. H. Albetran, H. Haroosh, Y. Dong, V.M. Prida, B.H. O'Connor, I.M. Low, Appl. Phys. A **116**, 161 (2014)
2. H.C. Liang, X.Z. Li, J. Hazard. Mater. **162**, 1415 (2009)
3. J. Nowotny, T. Bak, M.K. Nowotny, L.R. Sheppard, J. Phys. Chem. B **110**, 18492 (2006)
4. P. Jantawasu, T. Sreethawong, S. Chavadej, Chem. Eng. J. **155**, 223 (2009)
5. P. Mishra, P.K. Shukla, A.K. Singh, O.N. Srivastava, Int. J. Hydrogen Energy **28**, 1089 (2003)
6. C. Xu, R. Killmeyer, M.L. Gray, S.U.M. Khan, Electrochem. Commun. **8**, 1650 (2006)
7. D. Wu, M. Long, ACS Appl. Mater. Interfaces **3**, 4770 (2011)
8. J.H. Park, S. Kim, A.J. Bard, Nano Lett. **6**, 24 (2006)
9. I.M. Low, H. Albetran, V.D.L. Prida, P. Manurung, M. Ionescu, Dev. Strateg. Mater. Comput. Des. **III**, 149 (2012)
10. I.M. Low, B. Curtain, M. Philipps, Z.Q. Liu, M. Ionescu, J. Aust. Ceram. Soc. **48**, 198 (2012)
11. D. Fang, Z. Luob, K. Huanga, D.C. Lagoudas, Appl. Surf. Sci. **257**, 6451 (2011)
12. F. Gennari, D. Pasquevich, J. Mater. Sci. **33**, 1571 (1998)
13. H. Zhang, J.F. Banfield, Chem. Mater. **17**, 3421 (2005)
14. R. Liu, L.S. Qiang, W.D. Yang, H.Y. Liu, Mater. Res. Bull. **48**, 1458 (2013)
15. K. Okada, N. Yamamoto, Y. Kameshima, A. Yasumori, K.J.D. MacKenzie, J. Am. Ceram. Soc. **84**, 1591 (2001)
16. X.Z. Ding, X.H. Liu, Y.Z. He, J. Mater. Sci. Lett. **15**, 1789 (1996)
17. M. Barakat, G. Hayes, S.I. Shah, J. Nanosci. Nanotechnol. **5**, 759 (2005)
18. H. Zhang, J.F. Banfield, J. Mater. Res. **15**, 437 (2000)
19. R.D. Shannon, J.A. Pask, J. Am. Ceram. Soc. **48**, 391 (1965)
20. R.A. Eppler, J. Am. Ceram. Soc. **70**, 64 (1987)
21. M.K. Akhtar, S.E. Pratsinis, S.V. Mastrangelo, J. Am. Ceram. Soc. **75**, 3408 (1992)
22. J.H. Huang, M.S. Wong, Thin Solid Films **520**, 1379 (2011)
23. J.A. Gamboa, D.M. Pasquevich, J. Am. Ceram. Soc. **75**, 2934 (1992)
24. R. Plugaru, A. Cremades, J. Piqueras, J. Phys. Condens. Matter **16**, 261 (2004)
25. O.K. Varghese, D. Gong, M. Paulose, C.A. Grimes, E.C. Dickey, J. Mater. Res. **18**, 156 (2003)
26. X. Pan, M.Q. Yang, X. Fu, N. Zhang, Y.J. Xu, Nanoscale **5**, 3601 (2013)
27. I.M. Low, H. Albetran, V.M. Prida, V. Vega, P. Manurung, M. Ionescu, J. Mater. Res. **28**, 304 (2013)
28. X. Pan, Y. Zhao, S. Liu, C.L. Korzeniewski, S. Wang, Z. Fan, ACS Appl. Mater. Interfaces **4**, 3944 (2012)
29. B.C. Kang, S.B. Lee, J.H. Boo, Surf. Coat. Technol. **131**, 88 (2000)
30. S. Shang, X. Jiao, D. Chen, ACS Appl. Mater. Interfaces **4**, 860 (2012)
31. I.M. Low, F.K. Yam, W.K. Pang, Mater. Lett. **87**, 150 (2012)
32. S.W. Hsu, T.S. Yang, T.K. Chen, M.S. Wong, Thin Solid Films **515**, 3521 (2007)
33. F. Dong, W. Zhao, Z. Wu, Nanotechnology **19**, 365607 (2008)
34. J.Y. Park, J.J. Yun, C.H. Hwang, I.H. Lee, Mater. Lett. **64**, 2692 (2010)
35. Q. Li, D.J.G. Satur, H. Kim, H.G. Kim, Mater. Lett. **76**, 169 (2012)
36. K. Matusita, T. Komatsu, R. Yokota, J. Mater. Sci. **19**, 291 (1984)
37. H. Albetran, V.M. Prida, B.H. O'Connor, I.M. Low, Appl. Phys. A **120**, 623 (2015)
38. N.P. Bansal, R.H. Doremus, A.J. Bruce, C.T. Moynihan, J. Am. Ceram. Soc. **66**, 233 (1983)
39. B.J. Morgan, G.W. Watson, J. Phys. Chem. C **114**, 2321 (2010)
40. D.A. Hanaor, C.C. Sorrell, J. Mater. Sci. **46**, 855 (2011)
41. K.N. Kumar, J. Engell, J. Kumar, K. Keizer, T. Okubo, M. Sadakata, J. Mater. Sci. Lett. **14**, 1784 (1995)
42. K.N.P. Kumar, K. Keizer, A.J. Burggraaf, J. Mater. Chem. **3**, 917 (1993)
43. K.N.P. Kumar, K. Keizer, A.J. Burggraaf, J. Mater. Chem. **3**, 1141 (1993)
44. H. Albetran, Y. Dong, I.M. Low, J. Asian Ceram. Soc. JASCER **161**, 292 (2015)

3.3 Effect of Vanadium Ion Implantation on the Crystallization Kinetics and Phase transformation of Electrospun TiO_2 Nanofibers

---

ALBETRAN, H., O'Connor, B. H., PRIDA, V. M., & LOW, I. M. 2015. Effect of Vanadium Ion Implantation on the Crystallization Kinetics and Phase Transformation of Electrospun TiO_2 Nanofibers. *Applied Physics A*, 120, 623–634.

Appl. Phys. A (2015) 120:623–634
DOI 10.1007/s00339-015-9227-8

Applied Physics A
Materials Science & Processing

Effect of vanadium ion implantation on the crystallization kinetics and phase transformation of electrospun TiO_2 nanofibers

H. Albetran[1,2] · B. H. O'Connor[1,3] · V. M. Prida[4] · I. M. Low[1]

Received: 16 February 2015 / Accepted: 8 May 2015 / Published online: 20 May 2015

Abstract The influence of V ion implantation on the thermal response of electrospun amorphous TiO_2 nanofibers was studied with reference to structural phase transformation behavior, using in situ synchrotron radiation diffraction (SRD) measurements from room temperature to 1000 °C. Analysis of the SRD data provided activation energies for amorphous-to-crystalline TiO_2 (anatase and rutile) and anatase-to-rutile transformations, and also assessments of the influence of V ion implantation on microstructure development during calcination using estimates of crystallite size and microstrain. Non-implanted nanofibers were initially amorphous, with crystalline anatase first appearing at 600 °C, followed by rutile at 700 °C. The corresponding activation energies were 69(17) kJ/mol for the amorphous-to-crystalline TiO_2 transformation and 129(5) kJ/mol for the anatase-to-rutile transformation. V ion implantation resulted in a lowering of the temperature at which each crystalline phase first appeared, with both phases being initially observed at 500 °C and with the anatase-to-rutile transformation being accelerated relative to the non-implanted sample. The effect of V ion implantation is seen through the substantial reduction in activation energies, which are 25(3) kJ/mol for amorphous-to-crystalline TiO_2 and 16(3) kJ/mol for anatase-to-rutile transformations.

✉ I. M. Low
j.low@curtin.edu.au

[1] Department of Imaging and Applied Physics, Curtin University, Perth, WA 6845, Australia

[2] Department of Basic Sciences, College of Education, University of Dammam, P. O. Box 2375, Dammam 31451, Saudi Arabia

[3] John de Laeter Centre, Curtin University, GPO Box U1987, Perth, WA 6845, Australia

[4] Department of Physics, University of Oviedo, Calvo Sotelo s/n, 33007 Oviedo, Spain

1 Introduction

The photocatalytic activity of titania (TiO_2) has become well known over the last three decades, and numerous investigations have been conducted to improve the efficiency of photocatalysis [1, 2]. TiO_2 is an excellent photocatalyst and a competitive candidate for many photocatalytic applications. These applications depend on the morphology, particle size, crystallinity and phase composition of the photocatalyst [1]. The main attractions of using TiO_2 as a photocatalyst are its high photoactivity, photodurability, non-toxicity, high oxidizing power, high chemical stability, mechanical robustness and relatively low cost [3–5].

TiO_2 has three polymorphs, namely anatase, rutile and brookite [6–8]. The anatase polymorph generally has higher photoactivity than the other polymorphs, but mixtures of anatase and rutile have been generally reported to exhibit superior photoactivity than either anatase or rutile alone [9–11]. However, Chuangchote et al. [12] claimed that TiO_2 nanofiber photocatalysts reported lower activity when both rutile and anatase phases were present.

TiO_2 is an n-type semiconductor with a 3.0–3.2 eV band gap (E_g) [13–15]. It is activated by UV irradiation, about 4 % of natural solar light, which is one of the major factors limiting the efficiency of the TiO_2 photocatalysis [2, 16]. Considerable effort has been taken over the last two decades to develop modified TiO_2 that becomes active under visible light irradiation [2, 17–20]. Both metal doping and non-metal doping of TiO_2 are cost-effective methods for narrowing its band gap. Visible light photoactivity of metal- and non-metal-doped TiO_2 can be achieved by

creating a new energy level between the conduction band and the valence band [16].

Various methodologies have been proposed for doping titanium dioxide, including ion-assisted sputtering, hydrothermal, sol–gel and ion implantation [2, 21]. Metal ion implantation using an accelerated metal ion beam has been applied to modify the electronic structure of the TiO_2 semiconductor [19–23]. Depending on the type and amount of metal used, metallic ion implantation can improve the electronic properties of TiO_2 photocatalysts by extending the absorption range up to the visible light region [19–23].

The presence of foreign ions can affect on the kinetics of the anatase-to-rutile transformation at elevated temperatures, which is considered in this study. In general, ions that increase the oxygen vacancy concentration will enhance the phase transition. By contrast, ions that increase the concentration of interstitial titanium will tend to inhibit the transformation [1, 7].

Nanostructured TiO_2 with various morphologies (e.g., nanopowders [9], nanoparticles [24], nanosquares [2], nanowires [25], thin films [20, 26], nanorods [25], nanosheets [15], nanotubes [19, 25, 27] and nanofibers [12, 28–30]) can provide a large specific surface area for increasing the photodegradation rate since photocatalytic reactions mainly take place on the surface of the TiO_2 photocatalyst [15, 26, 28]. Various techniques such as anodization, evaporation, self-assembly and electrospinning have been used to synthesize nanostructured TiO_2 [29]. Among these techniques, TiO_2-based nanofibers fabricated by electrospinning are of much interest as it is a simple, straightforward and cost-effective technique that can be used at the industrial level. This technique employs a sol–gel solution of the polymer and a solvent, and the amorphous TiO_2 precursor is ejected through a needle under a strong electric field [12]. Using the sol–gel method, highly photocatalytic electrospun TiO_2 nanofibers doped with V have been synthesized by Zhang et al. [31]. However, the use of ion implantation to dope electrospun TiO_2 nanofibers with V ions has yet to be attempted.

For this study, TiO_2 nanofibers were prepared from titanium isopropoxide (TIP) sol–gel precursors, synthesized using electrospinning, and then doped with V ions using ion implantation. The effects of V ion implantation on crystallization kinetics, phase transformations and activation energies of electrospun TiO_2 nanofibers were investigated using in situ high-temperature synchrotron radiation diffraction (SRD) over the temperature range of 25–1000 °C. The electrospun TiO_2 nanofibers were characterized by means of scanning electron microscopy (SEM), energy dispersive X-ray spectroscopy (EDS), high-resolution transmission electron microscopy (HR-TEM) and X-ray photoelectron spectroscopy (XPS). This paper reports the first attempt at preparing V ion-implanted electrospun TiO_2 nanofibers and focuses on the TiO_2 phase transformation and crystallization kinetics.

2 Experimental procedures

2.1 Fabrication of electrospun TiO_2 nanofibers

A TiO_2 solution was prepared from TIP ($M_W = 284.22$ g/mol, 97 % purity) precursors by mixing 6 ml of TIP with 8 ml of a mixed solvent comprising acetic acid (33.3 wt%) and ethanol (66.6 wt%). Then, 1.8 g of polyvinyl pyrrolidone (PVP, $M_W = 1{,}300{,}000$ g/mol, 100 %) was dissolved, followed by continuous stirring for 60 min at 40 °C. The TiO_2 solution was then ultrasonically stirred for 5 min to achieve complete dissolution and mixing.

The TiO_2 solution was loaded into a 10 ml plastic syringe with a stainless steel needle of 0.514 mm diameter. The distance between the tip of the syringe needle and the collector was fixed at 12 cm, and the flow rate of the TiO_2 solution was 2 ml/h. A voltage of 25 kV was applied between the needle and aluminum collector, which was covered by an aluminum foil to collect the prepared fibers.

2.2 Ion implantation

The synthesized TiO_2 nanofiber material was cut into 14 mm × 14 mm squares, which were then implanted with V ions using the MEVVA ion implanter at the Australian Nuclear Science and Technology Organisation (ANSTO). During implantation, the samples were doped by exposing a flux of V ions directed perpendicular to the sample surface. The average implantation energy of V ions produced was 25 keV, and the penetration depth of V peak in the TiO_2 fibers was close to the stopping and range of ions in matter (SRIM) prediction of 70 nm based on these implantation parameters. The near-surface composition depth profiling of V ion-implanted TiO_2 nanofibers was measured by RBS using He^{+1} ions at 2 MeV, and the implanted dose was $\sim 4 \times 10^{15}$ ions/cm^2.

2.3 Characterization of the materials

2.3.1 Scanning electron microscopy (SEM)

The morphology of TiO_2 nanofibers was examined using SEM (EVO, 40XVP). The samples were coated with platinum to avoid charging, and images were taken using secondary electrons. EDS at an acceleration voltage of 10 kV was used to qualitatively analyze the elemental compositions.

2.3.2 High-resolution transmission electron microscopy (HR-TEM)

A small piece of implanted nanofiber material was ground and suspended with ethanol. Two drops of suspension were mounted onto carbon-coated copper grids for TEM imaging. HR-TEM was carried out with a JEOL 3000F TEM operating at 300 kV and fitted with a Gatan Orius 10-MP CCD camera.

2.3.3 X-ray photoelectron spectroscopy (XPS)

XPS analyses were performed using a Phoibos 100 MCD5 system (SPECS Nanotechnology, Delft, the Netherlands). The X-ray source was MgKα (1253.6 eV) radiation operating at 200 W. The operating pressure of the spectrometer was 1×10^{-9} mbar, and the analyzed area was ~500 μm in diameter. XPS measurements were carried out in two stages. First, a survey spectrum was measured from 1200 to 0 eV using an energy pass of 90 eV and an energy step of 1 eV to obtain a global measurement. Then, high-resolution spectra were acquired with an energy pass of 30 eV and an energy step of 0.1 eV for more detailed analysis.

2.4 In situ high-temperature synchrotron radiation diffraction (SRD)

2.4.1 SRD data acquisition and Rietveld analysis

The in situ crystallization behavior of non-implanted and V ion-implanted nanofibers was evaluated using the powder diffraction beamline at the Australian Synchrotron using non-isothermal SRD. The specimens were mounted and heated in air using an Anton Parr HTK 16 hot platinum stage. The SRD data were acquired at a grazing incidence angle of 3° and with a wavelength of 0.1126 nm and recorded using a Mythen II microstrip X-ray detector.

The SRD patterns were initially acquired at ambient temperature and then in steps of 100 from 200 to 900, or 1000 °C, with a ramping rate of 10 °C/min and data acquisition time of 2 min per SRD pattern. Each pattern was measured over the angular range between $5° \leq 2\theta \leq 84°$.

The SRD patterns were analyzed by Rietveld pattern-fitting using the *Rietica* program (version 2.1), with the goodness of fit being gauged by the values of the weighted pattern *R*-factor (R_{wp}), the expected *R*-factor (R_{exp}) and the derived Bragg *R*-factors (R_B) [32]. To compute the relative crystalline phase abundances for anatase and rutile, and also the lattice parameters at each temperature, the parameters optimized in the Rietveld refinements were the pattern background, 2θ-zero, and, for each phase, the scale factor, lattice parameters and peak shape parameters. The Rietveld refinements were conducted with the crystal structures of anatase (ICSD 202242) and rutile (ICSD 64987). The TiO_2 Rietveld phase abundance ratios were determined and then independently by line ratio analysis according to the Spurr and Myers equations [33], which provided very similar results [34].

2.4.2 Analysis of absolute phase compositions

Rietveld analysis provided only the relative levels of anatase and rutile. In order to determine absolute levels for the amorphous and crystalline components, a novel technique was developed using the temperature dependence of the SRD pattern background levels. The background-temperature plots were analyzed by assuming that the background $B(T)$ at temperature T is given by a component $B_A(T)$ due to amorphous scatter and a secondary component B_S attributed to atomic X-ray scatter (Compton and Rayleigh). On this basis, the weight percentage of amorphous TiO_2 ($wt_{Am}\%$) was calculated using:

$$wt_{Am}\% = \frac{B(T) - B_f}{B_o - B_f} \quad (1)$$

where $B(T)$ is the background intensity at temperature T, B_o is the background intensity prior to the onset of the amorphous-to-crystalline TiO_2 transformation and B_f is the estimated background intensity when amorphous TiO_2 has been completely transformed into crystalline TiO_2. Further details are given in Sect. 3.

2.4.3 Estimation of activation energies

The SRD results were used to examine the crystallization kinetics of TiO_2 with the equation of Matusita et al. [35] for non-isothermal heating conditions:

$$\ln[-\ln(1-x)] = -n\ln\alpha - 1.052\,mE/RT + \text{constant} \quad (2)$$

where x is the volume fraction of transformed material; n is a numerical factor depending on the nucleation process, where $n = m + 1$, with $m = 1, 2, 3$ being the number of dimensional growth; α is the constant heating rate; R is the ideal gas constant = 8.3145 J/Kmol; T is the temperature in Kelvin; and E is the activation energy in kJ/mol.

To obtain the activation energies of amorphous-to-crystalline TiO_2 (anatase and rutile) transformation or anatase-to-rutile transformation at a heating rate of 10 °C/min, the weight percentages (wt) of crystalline TiO_2 or rutile were used rather than the volume fractions because anatase and rutile have almost the same density, and $m = 1$ for one dimensional nanofibers [35].

Equation 2 is written as:

$$\ln[-\ln(1-\text{wt})] = -1.052\,E/RT + \text{constant} \quad (3)$$

A plot of ln [–ln (1–wt)] for crystalline TiO_2 (total of anatase and rutile) or rutile against $1/T$ is expected to be linear, and the activation energy for each transformation can be estimated from the gradient. The activation energies were also calculated using a modified version of the Arrhenius equation:

$$\ln \mathrm{wt} = -E/RT + \ln \mathrm{wt_o} \quad (4)$$

where wt is the weight percentage of the transformed phase(s) (crystalline TiO_2 or rutile) and $\mathrm{wt_o}$ is the initial weight percentage.

2.5 Estimation of crystallite size and strain

The average crystallite size (L) and the rms microstrain (ε) for each phase at each temperature were estimated using Williamson–Hall (W–H) plots [36]:

$$\beta \cos\theta = \lambda/L + 4\varepsilon \sin\theta \quad (5)$$

where λ is the X-ray wavelength, θ is the Bragg angle and β is the integral breath of each peak. Care was taken to confine the peaks used in the analysis to well-defined peaks with minimal peak overlap. The five peaks used for the rutile plots were 110 ($2\theta = 19.91°$), 011 (26.07°), 111 (29.74°), 120 (31.72°) and 220 (40.44°). Only two peaks could be used for the anatase plots: 011 (18.41°) and 020 (34.52°). The integral widths were determined using the program X'Pert HighScore Plus (version 3.0).

The integral widths were large (in the $\Delta 2\theta$ range 0.18°–0.43° for rutile and 0.26°–1.08° for anatase) compared with the broadening due to the instrument. Instrument broadening corrections were applied according to the optics of the SRD instrument. According to Eq. 6, a near-parallel beam is incident on the sample and then diffracted by the sample [37, 38]:

$$\mathrm{FWHM}(^\circ) = \left[\varphi_V^2 \left(\frac{2\tan\theta}{\tan\theta_m} - 1\right)^2 + \delta^2\right]^{1/2} \quad (6)$$

where φ_V is a vertical divergence of the incident beam = 0.02°, θ is the Bragg angle for the SRD line, θ_m is the Bragg angle for the Si (111) double-crystal monochromator = 10.3435° and δ is the divergence angle for the diffracted beam, which is calculated using:

$$\delta = \frac{\left(d_S^2 + d_{IP}^2\right)^{1/2}}{R} \quad (7)$$

where d_S is width of the incident beam at the specimen, in the direction of the incident beam = 0.2 mm, d_{IP} is the spatial resolution of the imaging plate = 0.053 mm and angular resolution = 0.004° for the MYTHEN detector and R is the radius of the instrument, or the specimen-to-detector distance = 760 mm. On this basis, the instrument width was 0.020° for the data used for W–H plots.

3 Results and discussion

3.1 Microstructures of electrospun TiO_2 nanofibers

A typical SEM image of the as-prepared TiO_2/PVP nanofibers before thermal treatment is shown in Fig. 1a. The diameters of the electrospun nanofibers from the SEM images were measured by ImageJ® software (version 1.48e) developed by the National Institutes of Health (NIH), USA. The randomly oriented TiO_2/PVP composite nanofibers had smooth surfaces. The corresponding mean diameter and standard deviation for 40 nanofibers were 665 ± 330 nm.

After the in situ high-temperature SRD measurements at 900 °C for non-implanted material and at 1000 °C for the V-implanted material, the morphologies of the nanofibers were re-examined after cooling to room temperature, using the same SEM conditions. Figure 1b, c shows the SEM images of non-implanted and V-implanted materials, respectively. The mean diameters and standard deviation for 40 nanofibers after thermal treatment were much smaller, being 351 ± 145 nm for non-implanted and 358 ± 155 nm for V-implanted nanofibers. It should be noted that the mean diameters of non-implanted and V-implanted nanofibers are about the same within the error or scatter of the standard deviation. The average diameters of thermally treated nanofibers were much smaller than those observed for the as-prepared TiO_2/PVP nanofibers, representing diametric shrinkage of ~47 % in non-implanted nanofibers and ~46 % in the implanted nanofibers. The shrinkage is attributed to the evaporation of the solvents and loss of the PVP polymer and TIP during thermal treatment.

Qualitative and quantitative EDS analyses were carried out using Oxford Instruments INCA (version 5.05) software. EDS was collected from a small point. Figure 2a gives an EDS spectrum for the as-prepared TiO_2/PVP material, showing strong signatures for Ti, O and C, with the C content being due to the PVP binder. The quantitative EDS analysis is approximated for electrospun nanofibers because the EDS has a large interaction volume, which can be greater than the fiber diameter size. The quantitative EDS analysis for as-prepared TiO_2/PVP indicated 42.48 C k, 38.38 O k and 19.13 % Ti k. Figure 2b shows an EDS spectrum for V-implanted nanofibers after cooling from 1000 °C, which was essentially the same for non-implanted electrospun TiO_2 nanofibers after cooling from 900 °C. The absence of the C peak in Fig. 2b indicates the complete loss of organic material. The quantitative EDS

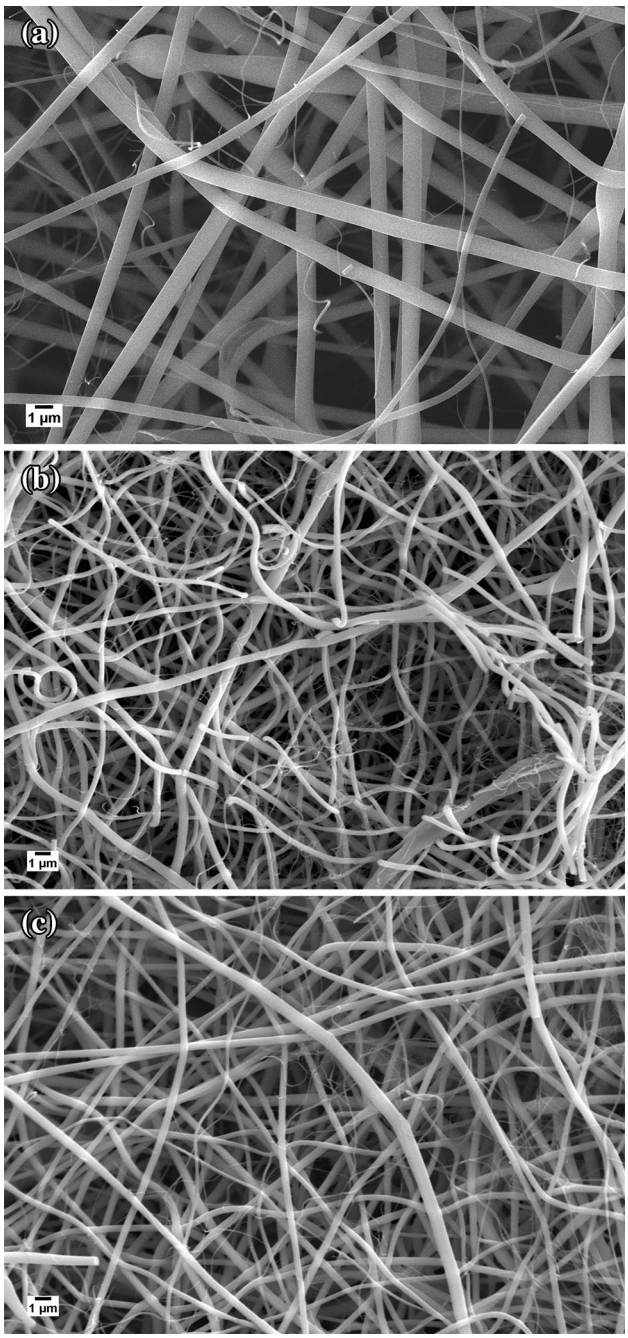

Fig. 1 SEM micrographs of **a** electrospun TiO_2 nanofibers prior to heating; **b** after thermal treatment at 900 °C and cooling to room temperature; **c** after V ion implantation and thermal treatment at 1000 °C and cooling to room temperature

analysis of V ion-implanted nanofiber indicated 66.18 O K_α and 33.82 % Ti K_α, thus confirming the presence of TiO_2 in the material. The V K_β signature (5.43 keV) was not detected for the ion-implanted material due to the low V concentration, noting also that Ti K_β peak (4.93 keV) and V K_α peak (4.95 keV) have overlapping EDS peaks.

3.2 HR-TEM imaging of calcined TiO_2 nanofibers

Figure 3a shows a typical TEM image of V-implanted material after thermal treatment at 1000 °C. The diameters of nanofibers are in agreement with the values obtained from SEM analysis (Fig. 1b). The presence of V ions is not obvious from the image because the atomic numbers for ^{22}Ti and ^{23}V are very similar. Figure 3b and c shows polycrystalline rutile composed of randomly oriented crystallites.

3.3 X-ray photoelectron spectroscopy

Figure 4 illustrates the XPS spectra of the non-implanted and V-implanted material at room temperature after the in situ SRD measurements. O, Ti, N and C features are observed, according to the photoelectron peaks at binding energies of 532, 461, 399 and 284 eV, respectively. The peak located at 284 eV corresponds to residual carbon from the adventitious hydrocarbon coming from the XPS instrument, and the N_{1s} peak is attributed to impurities in the XPS equipment. The appearance of Ti and O for the non-implanted material (Fig. 4a) is that expected for TiO_2. There are two spin orbital components for Ti, where $Ti_{2p1/2}$ is located at 461 and $Ti_{2p3/2}$ at 455 eV. The splitting between them is ~6 eV, indicating the presence of Ti^{4+} ions in the non-implanted TiO_2 [3]. The XPS plot for the implanted material in Fig. 4b clearly shows the O_{1s} feature, as in the corresponding peak for the non-implanted sample. However, the twin Ti_{2p} peaks are barely seen for the implanted material, which is attributed to a substantial reduction in Ti^{4+} concentration through V ion implantation. The Ti_{2p} spectrum in Fig. 4c, collected over a longer period, shows that there remain some Ti^{4+} ions in the implanted material but much less than the concentration seen in the non-implanted material. Figure 4d shows the XPS spectrum in the vicinity of the V_{2p} position for the V-implanted material. It is further evident from Fig. 4c and d that V ion implantation has substantially diminished the Ti^{4+} concentration. In addition, it is seen from Fig. 4d that the V concentration is insufficient to unambiguously observe a V_{2p} peak.

XPS quantitative analysis, which is usually performed in the low-resolution mode, cannot provide evidence of the presence of V in the ion-implanted sample because XPS peaks that originate from elements with low concentration are not clearly visible. V was detected using high-resolution XPS, but this technique is applied mainly for qualitative analysis rather than for quantitative analysis. The V_{2p} line spectrum of V appears at ~513 eV. If we assume that the inelastic mean free path (IMFP) of scattered electrons for V is ~1.25 nm, then a mean depth of analysis of approximately 3.75 nm is obtained.

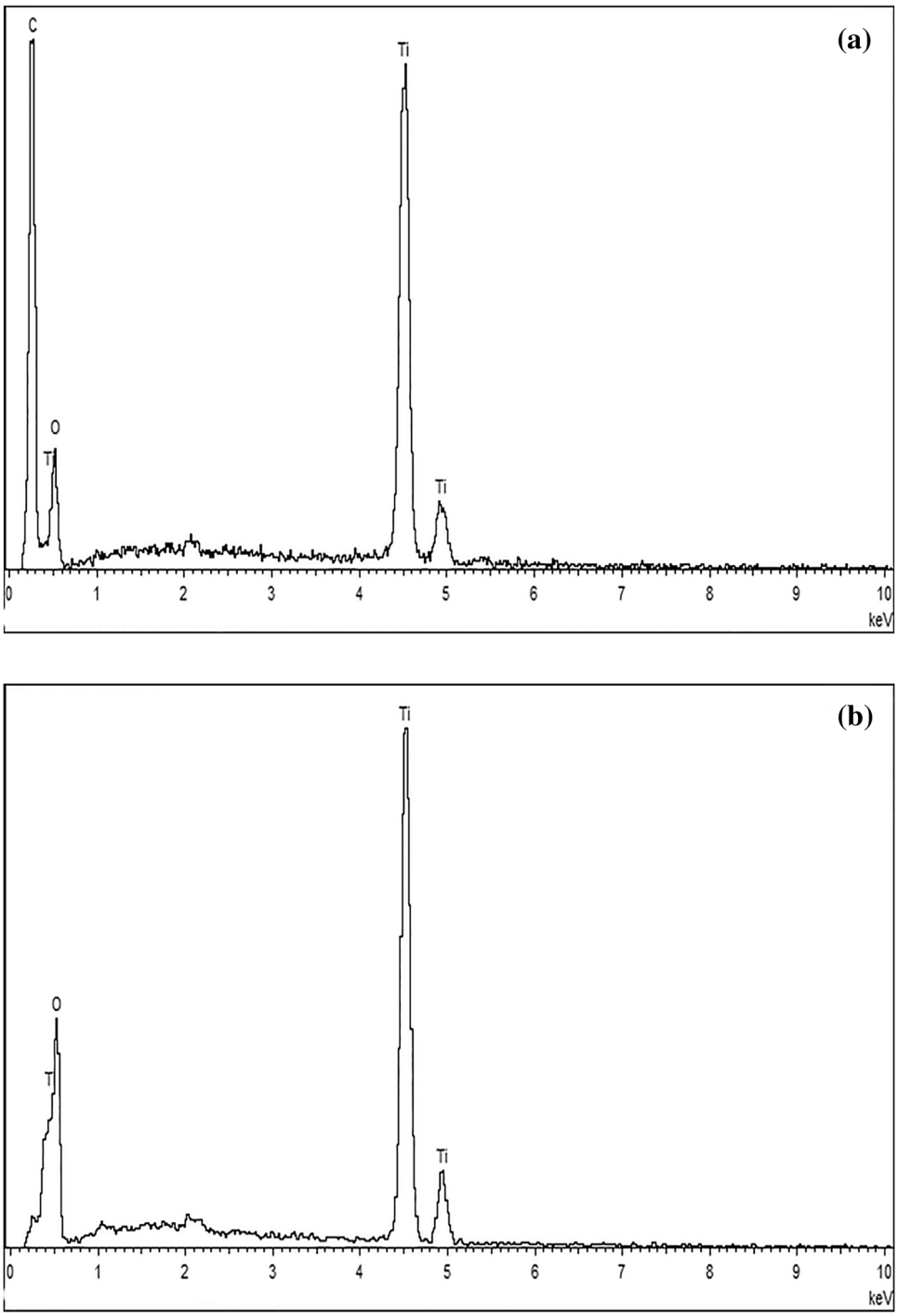

Fig. 2 EDS spectra of **a** electrospun TiO_2 nanofibers prior to heating; **b** after V ion implantation and cooling to room temperature from 1000 °C

The RBS results in Fig. 5 show the elemental concentration versus depth for the V-implanted TiO_2 fibers. A maximum V concentration of 4 at.% has been implanted in TiO_2 fibers down to a depth of about 400 monolayers or 70 nm from SRIM prediction.

3.4 Effect of ion implantation on phase transitions

Figure 6 illustrates stacked SRD plots for the non-implanted and V-implanted materials over the temperature range of 25–900 °C. The Pt peaks in the SRD patterns

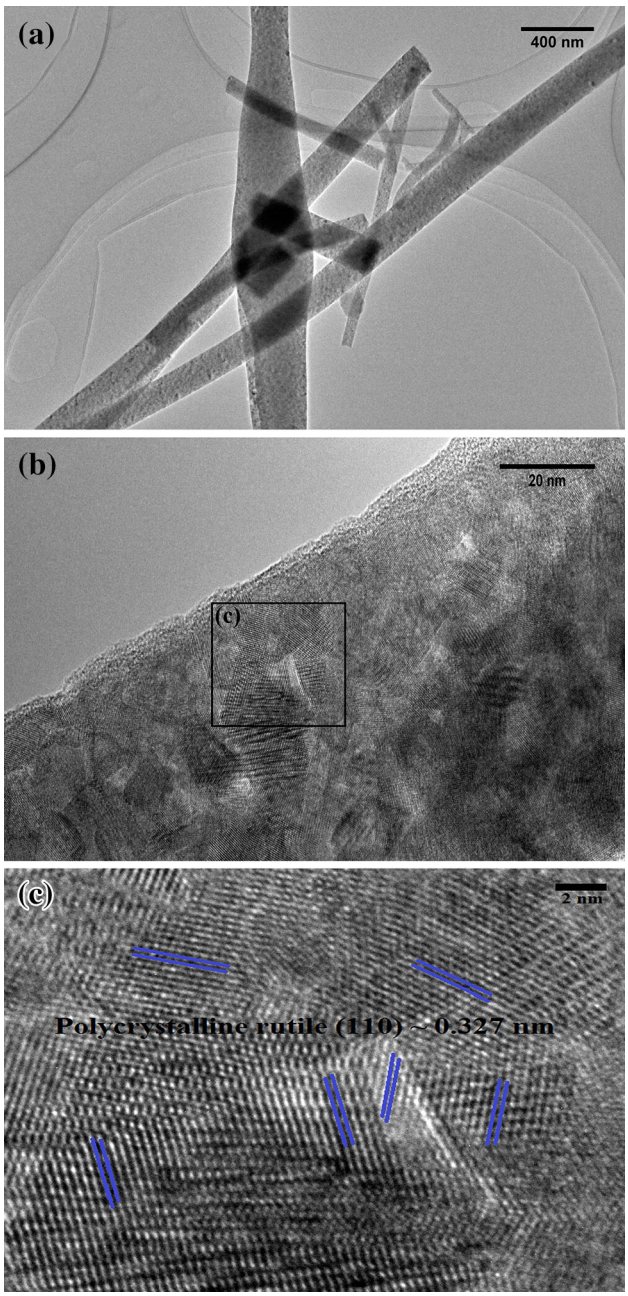

Fig. 3 TEM images of V ions implanted electrospun TiO_2 nanofibers after the high-temperature SRD experiment, followed by cooling to room temperature from 1000 °C **a** low-resolution image, **b**, **c** lattice-resolved HR-TEM images which show the existence of polycrystalline rutile material, with the d-spacing between adjacent (110) with lattice planes being ~0.327 nm

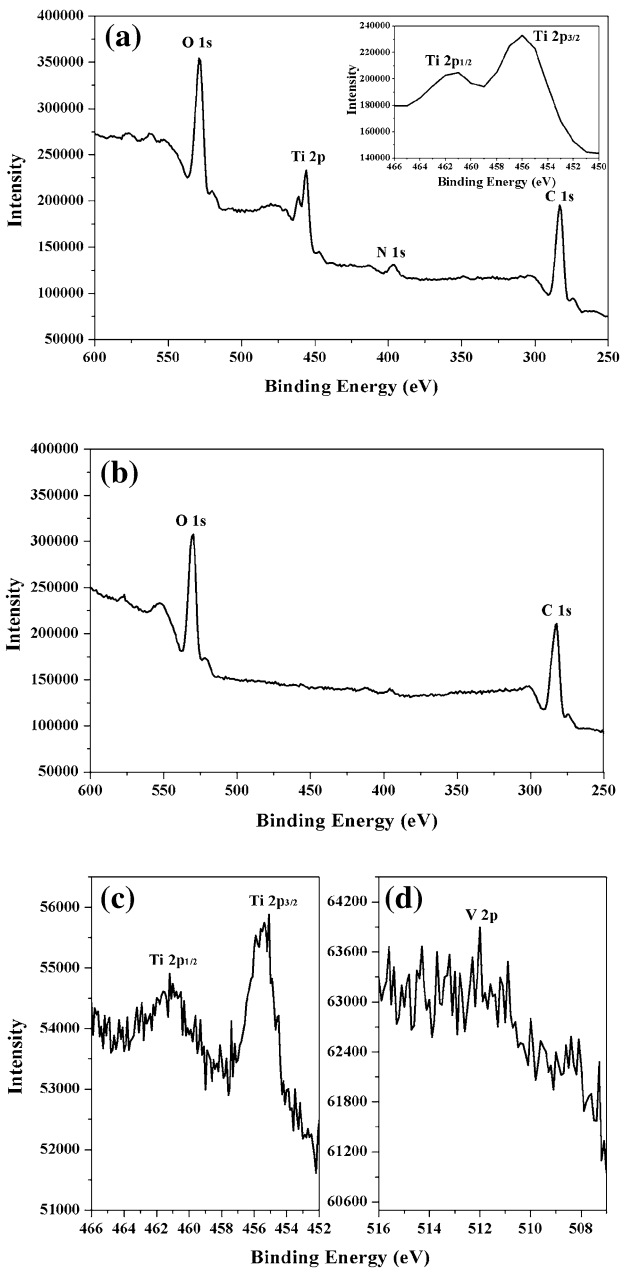

Fig. 4 XPS spectra of **a** non-implanted electrospun TiO_2 nanofibers after thermal treatment at 900 °C, **b** V ion-implanted material after thermal treatment at 1000 °C, and high-resolution spectra for the implanted material showing the spectra for **c** Ti_{2p} and **d** V_{2p}

come from the platinum holder. The SRD patterns for both the non-implanted and implanted samples exhibit prominent "amorphous" humps for the range between 25 and 300 °C, which disappear at 400 °C. This behavior is attributed to amorphous PVP and other organic substances evaporating completely by 400 °C, which was very similar to the interpretation of TGA spectra for TIP/PVP nanofibers from room temperature to 400 °C by Park and his coworkers [29, 30]. The SRD patterns for both non-implanted and V ion-implanted materials indicate the presence of anatase and rutile crystalline phases at elevated temperatures, which are TiO_2 phases and contain Ti and O elements. This confirms the signatures for Ti and O elements in the EDS and XPS results.

The TiO_2 was initially amorphous but then partly crystallized to form anatase and rutile at elevated temperatures.

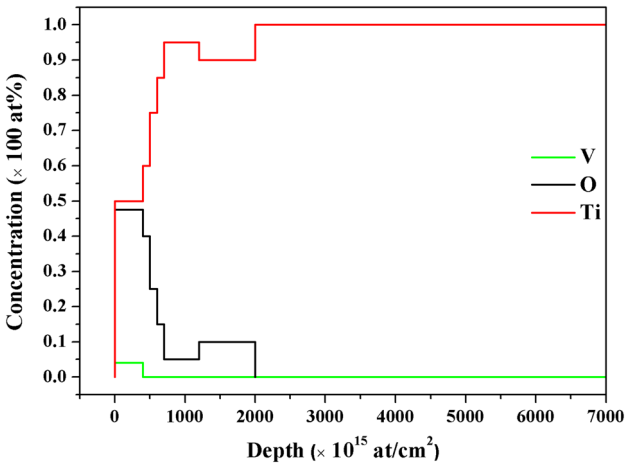

Fig. 5 Composition depth profiles in V-implanted TiO_2 nanofibers

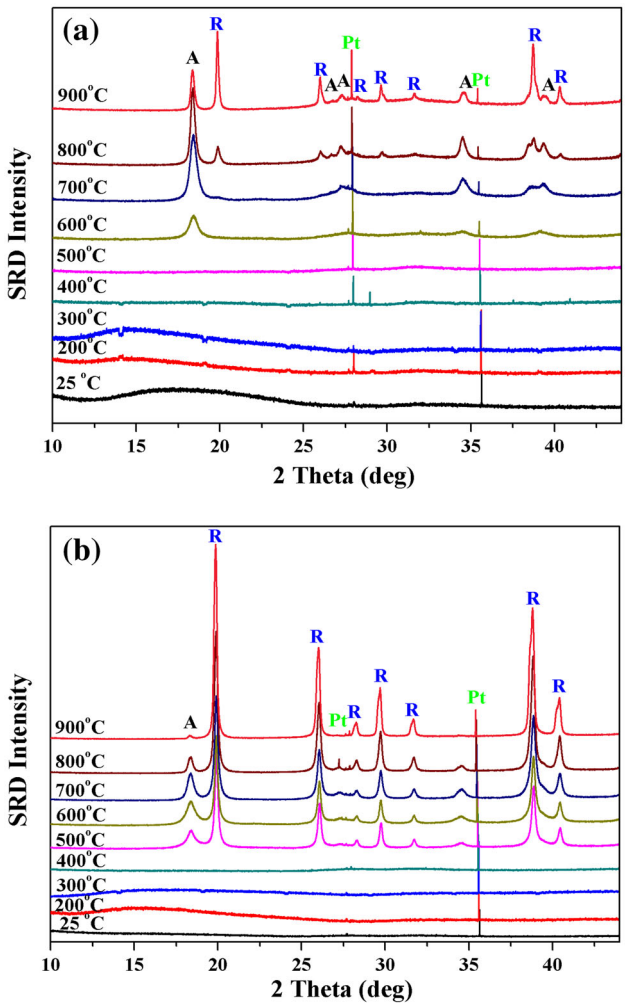

Fig. 6 Stacked SRD plots for the temperature range 25–900 °C of **a** non-implanted material and **b** after V ion implantation. [Legend: anatase (*A*), rutile (*R*) and platinum holder peaks (Pt_t)]

In the non-implanted material (Fig. 6a), anatase and rutile were first observed at 600 and 700 °C, respectively; whereas in V-implanted material (Fig. 6b), anatase and rutile were first observed at 500 °C, which is 100 °C lower for anatase and 200 °C lower for rutile than observed in the non-implanted material. These results are consistent with previously reported observations of non-implanted and Cr ion-implanted anodized TiO_2 nanotubes whereby Cr ion implantation lowered the crystallization temperature of anatase from 600 to 400 °C and rutile from 600 to 500 °C [14]. The observations are consistent with V ions entering the TiO_2 crystal structure [39], through the implanted ions occupying the Ti sub-lattice substitutionally, rather than interstitial positions. The presence of interstitial ions inhibits the anatase-to-rutile transformation; however, substitutional ions may inhibit or accelerate the phase transformation depending on the substitutional ion types [7]. The relative ease by which anatase transforms to rutile in the V-implanted material appears to be due to the relatively small radius of the V ions (0.058 nm), which partly replace the Ti ions (0.061 nm), thus causing some relaxation of the Ti bonding environment through lessening of structural rigidity. This behavior of easy rearrangement of the atoms in the anatase and rutile lattices has also been reported with respect to their influence on oxygen vacancies when electrospun TiO_2 nanofibers were heated in an argon atmosphere [34].

Figure 7 shows typical SRD Rietveld residual plots for data measured in non-implanted and V ion-implanted electrospun TiO_2 nanofibers at 800 °C. In non-implanted material, $R_{wp} = 13.0$, $R_{exp} = 3.7$, R_B (anatase) = 4.6 and R_B (rutile) = 7.3 %, and for the implanted material, $R_{wp} = 13.6$, $R_{exp} = 3.1$, R_B (anatase) = 5.9 and R_B (rutile) = 5.8 %. The goodness-of-fit (GOF) values are 12.2 for non-implanted and 19.2 for implanted nanofibers, which are acceptable refinements given the focus of the data analysis.

The absolute weight percentages of amorphous TiO_2 have been determined using the background intensities of SRD patterns at 17° (see Sect. 2.4). The background levels for the SRD patterns at 500 °C for non-implanted TiO_2 and 400 °C for V ion-implanted TiO_2 were used as the initial background intensity B_o, corresponding to 100 % amorphous TiO_2 and 0 % crystalline TiO_2. The background intensities were corrected for minor variations in incident beam intensity during data collection. The SRD background level decreased with temperature due to the amorphous-to-crystalline TiO_2 transformation.

The value of final background intensity B_f and then the wt_{Am}% for both non-implanted and V ion-implanted TiO_2 (Fig. 8) were estimated by fitting the plots of the intensities of the backgrounds versus temperature data using the function:

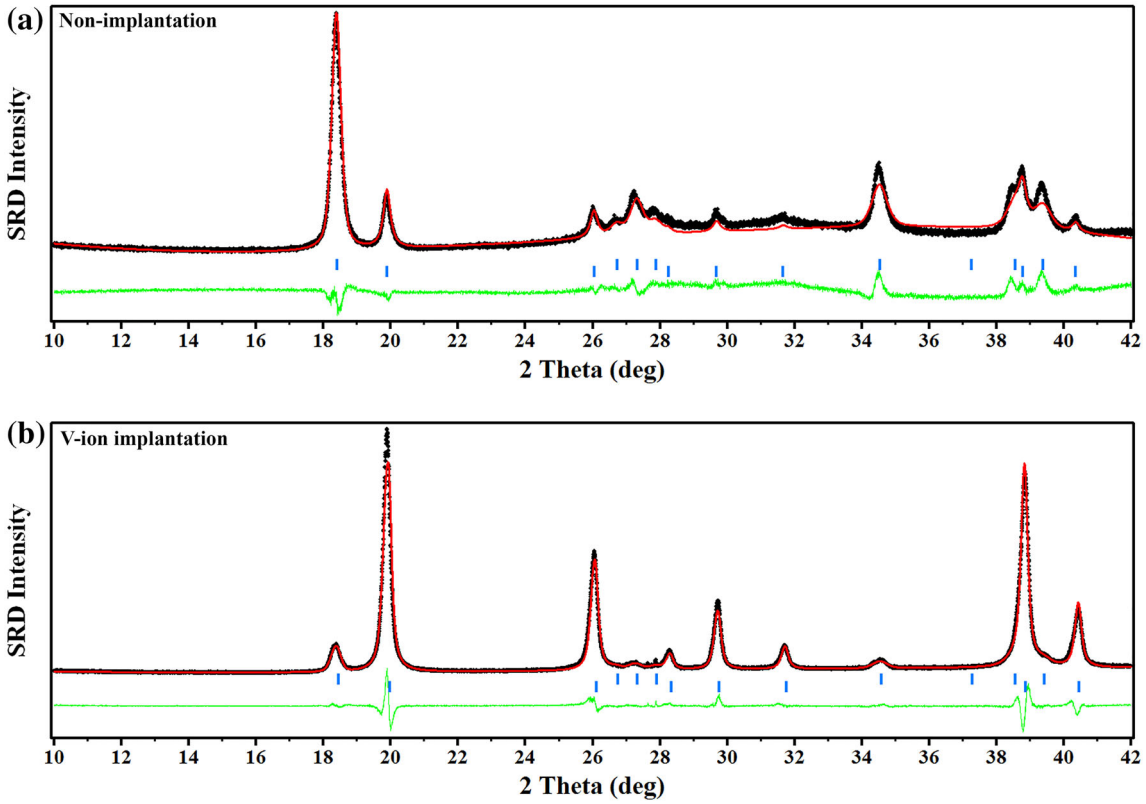

Fig. 7 SRD Rietveld difference plots for data measured in non-implanted and V ion-implanted material at 800 °C. Measured patterns are indicated by *black crosses* and calculated patterns by *solid red lines*. The *green residual plot* shows the difference between the calculated and the measured patterns. The peak positions for anatase and rutile are indicated by the *top* and *bottom blue bars*, respectively

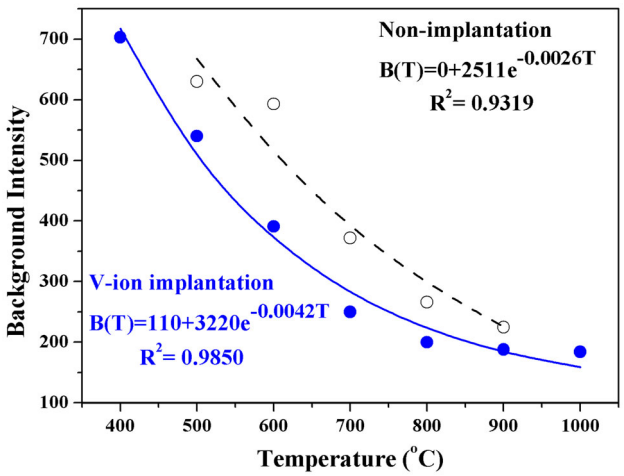

Fig. 8 Variation with temperature of the SRD background intensity for the non-implanted and implanted material as fitted with exponential functions

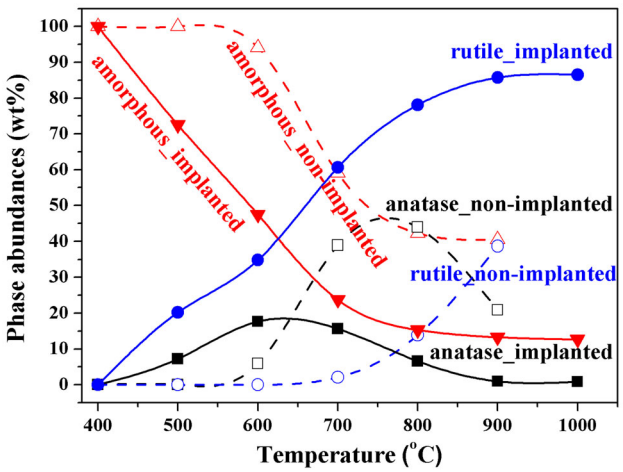

Fig. 9 Phase abundances of amorphous TiO_2, anatase and rutile in the temperature range 400–1000 °C for non-implanted and V ion-implanted material

$$B(T) = B_f + ae^{-bT} \quad (6)$$

The final background intensity (B_f) estimates were 0 and 110 counts, and the amorphous transformation rates (b) were −0.0026 and −0.0042 $°C^{-1}$ for non-implanted and ion-implanted material, respectively.

Figure 9 shows the influence of V ion implantation on the temperature dependence of the levels of amorphous TiO_2, crystalline anatase and crystalline rutile. It is evident from the plots that implantation accelerates the transformations for amorphous material to anatase and for anatase

to rutile also. In non-implanted nanofibers, only 6 % of amorphous TiO_2 had transformed to anatase crystalline phase by 600 °C, whereas ~48 % of the amorphous material had transformed in the implanted material at this temperature. The temperature dependence of the anatase and rutile concentrations further underlines the influence of implantation in accelerating the anatase-to-rutile transformation. These results are consistent with there being sequential transformation of amorphous to anatase and then anatase to rutile. In non-implanted material, anatase first appears by 600 °C and its concentration then peaks (ca. 46 % by weight) at 750 °C; the formation of rutile from anatase is first seen by 700 °C and has increased to ca. 39 % at 900 °C. Formation of anatase and then rutile occurs much more readily in the implanted material, with the anatase concentration peaking (ca. 18 % by weight) only at 625 °C. The rapid formation of the rutile phase after V ion implantation is evident, and by 1000 °C, the implanted material is principally rutile (ca. 87 % by weight).

3.5 Crystallization kinetics modeling

Table 1 shows the average activation energies for the amorphous-to-crystalline TiO_2 (anatase plus rutile) and anatase-to-rutile transformations for non-implanted and implanted material, using Arrhenius and Matusita et al. equations (Fig. 10). For non-implanted material, the activation energy for the amorphous-to-crystalline TiO_2 transformation was determined to be 69(17) kJ/mol, and anatase-to-rutile transformation was 129(3) kJ/mol. The estimated activation energy for anatase-to-rutile transformation is substantially lower than reported for other pure TiO_2 samples, e.g., 264 kJ/mol for TiO_2 nanotubes, 213 kJ/mol for TiO_2 powder and 213 kJ/mol for TiO_2 membrane [40–42]. For V ion implantation, the apparent activation energies had reduced substantially, being only 25(3) kJ/mol for the amorphous-to-crystalline TiO_2 transformation and 16(3) for the anatase-to-rutile transformation. Thus, V implantation substantially lowered the activation energies for the amorphous-to-crystalline TiO_2 and anatase-to-rutile transformations. This is consistent with reports in the literature that the presence of impure ions and the ion concentration can affect the activation energy for TiO_2 transformations [41, 42].

3.6 Microstructure development

W–H analysis provided crystallite size and non-linear strain estimates. The plots of crystallite size versus

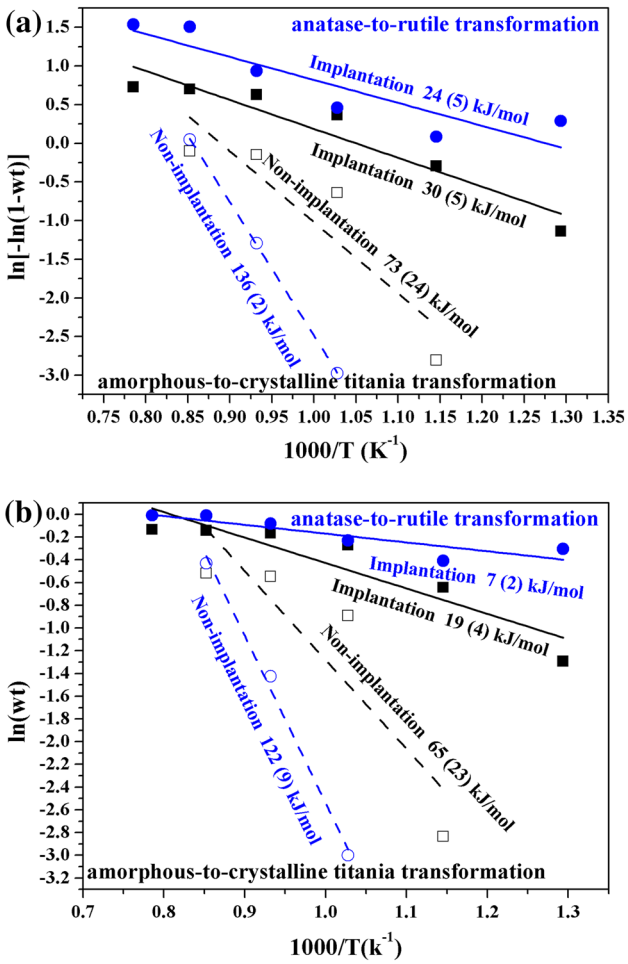

Fig. 10 Estimated values of non-isothermal activation energies for amorphous-to-crystalline TiO_2 and anatase-to-rutile transformations were calculated from the corresponding slopes of **a** variation of ln [–ln (1–wt)] against reciprocal temperature 1/*T* using Matusita et al.; **b** variation of ln (wt) against reciprocal temperature 1/*T* using the Arrhenius equation

Table 1 Phase transformation activation energies (kJ/mol) for non-implanted and V ion-implanted materials from non-isothermal SRD data analyses using the Arrhenius and Matusita et al. equations

	Amorphous-to-crystalline TiO_2			Anatase-to-rutile		
	Arrhenius equation	Matusita et al.	Average	Arrhenius equation	Matusita et al.	Average
Non-implanted	65 (23)	73 (24)	69 (17)	122 (9)	136 (2)	129 (5)
V ion-implanted	19 (4)	30 (5)	25 (3)	7 (2)	24 (5)	16 (3)

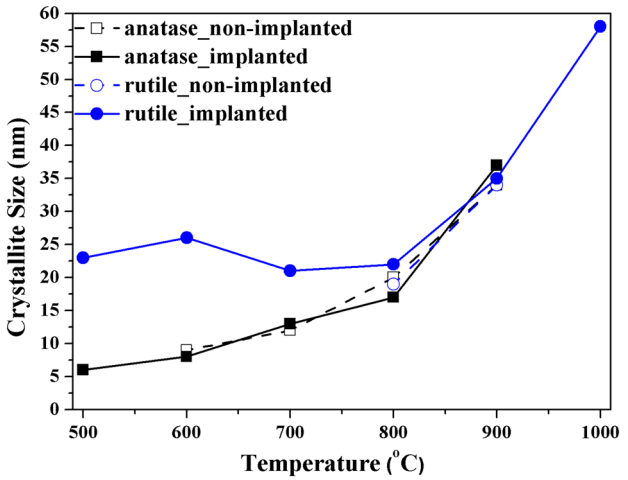

Fig. 11 Williamson–Hall plot estimates of the effect of ion implantation on the average crystallite size for the anatase and rutile crystalline phases over the temperature range of 500–1000 °C for non-implanted and V ion-implanted material

temperature are given in Fig. 11, and the nonlinear strain estimates using SRD integral breadth measurements are provided in Table 2. Both crystallite size and strain contribute substantially to line broadening. The crystallite size results show that the anatase and rutile crystalline phases for the non-implanted material are in the nanoscale range of 9–34 nm for the temperatures considered. The plots for anatase show that implantation does not have a discernible influence on the temperature dependence of crystalline anatase growth following nucleation from the amorphous phase. The temperature dependence of the rutile crystallite size, and therefore the grain growth, is very similar to that for anatase from 800 °C, with there being no indication of rutile crystallite growth below 800 °C. Comparing the SRD size results with the TEM images in Fig. 3 for the implanted material heated to 1000 °C, the detail within the fiber microstructure in Fig. 3a points to there being rutile grains in the vicinity of 30–50 nm, which is consistent with the SRD size estimate of 58 nm in Table 2. The estimate here of grain growth rate with temperature points to grain growth being driven by crystallization of material onto existing grains from the surrounding amorphous TiO_2 material as the temperature is raised.

The strain estimates show (1) substantially higher nonlinear strain in anatase (ca. 0.3 %) than in rutile (ca. 0.1 %) for both non-implanted and V-implanted materials, but (2) no increase in strain for both phases in the implanted material at elevated temperatures. The greater strains observed for anatase are consistent with the findings of Nicula et al. [43], who reported that anatase exhibits larger strain values than rutile in TiO_2 powders from 400 to 850 °C.

Table 2 Nonlinear strain estimates from Williamson–Hall plots, using SRD integral breadth measurements

Temperature (°C)	Nonlinear strain (%)			
	Non-implanted		Implanted	
	Anatase	Rutile	Anatase	Rutile
500			<0.35	0.07
600	0.51		0.39	0.15
700	0.27		0.24	0.11
800	0.23	0.09	0.10	0.07
900	0.32	0.09	0.29	0.17
1000				0.21
Mean	0.33	0.09	0.26	0.13

4 Conclusions

The effect of V ion implantation on the crystallization of electrospun amorphous TiO_2 nanofibers was investigated using in situ high-temperature SRD. The SRD results were used to study the crystallization kinetics in terms of the influence of implantation on the activation energies for the amorphous-to-crystalline TiO_2 and anatase-to-rutile transformations.

The following principal conclusions were drawn from the study:

- The anatase crystalline phase was first observed at 600 and rutile at 700 °C for non-implanted TiO_2, whereas anatase and rutile were both initially observed at 500 °C for V-implanted TiO_2.
- The temperature dependence of both the amorphous-to-crystalline TiO_2 and anatase-to-rutile transformations was much more pronounced in V-implanted material, with the composition of the implanted material predominantly comprising crystalline rutile by 1000 °C.
- The average activation energies for the amorphous-to-crystalline TiO_2 transformation decreased from 69(17) to 25(3) kJ/mol following implantation and from 129(5) to 16(3) kJ/mol for the anatase-to-rutile transformation.
- XPS analysis showed that the concentration of Ti^{4+} ions in TiO_2 is substantially reduced by implantation, which appears to account for the relative ease for the transformations in the implanted material.
- The crystallite sizes for both anatase and rutile for non-implanted and anatase for V ion-implanted electrospun TiO_2 nanofibers increased steadily with the temperature, indicating that grain growth is driven by crystallization of material onto existing grains from the surrounding amorphous TiO_2 as the temperature is elevated, rather than unit cell expansion.

- The strain estimates show substantially higher nonlinear strain in anatase than in rutile for both non-implanted and implanted material. There is no discernible increase in strain in the implanted material at elevated temperatures for either phase.

It was concluded that V ion implantation had lowered the crystallization temperatures due to substitution of relatively small V ions for Ti in the TiO_2 crystal structure. Implantation of V ions is responsible for the dramatic reductions in activation energies.

Acknowledgments The authors acknowledge financial support from the Australian Synchrotron (Powder Diffraction Beamline, AS122/PDFI/5075) and the Australian Institute of Nuclear Science and Engineering (ALNGRA11135). H. Albetran is grateful to the College of Education, University of Dammam, for the financial support in the form of a Ph.D. scholarship. Spanish MINECO grants under projects MAT2010-20798-C05-04 and MAT2013-48054-C2-2-R are also gratefully acknowledged. Scientific support from the XPS laboratory of the University of Oviedo SCTs is recognized. The authors would like to thank Dr. Y. Dong for allowing the use his electrospun machine, Ms. E. Miller for assistance with the SEM imaging, Dr. X. Wang for assistance with TEM, Dr. J. Kimpton at the Australian Synchrotron for advising on instrumentation at Powder Diffraction Beamline and Dr. M. Ionescu of ANSTO for helpful assistance with ion implantation and SRIM simulation of RBS data.

References

1. D.A. Hanaor, C.C. Sorrell, J. Mater. Sci. **46**, 855 (2011)
2. C. Yu, L. Wei, X. Li, J. Chen, Q. Fan, J. Yu, Mater. Sci. Eng. B **178**, 344 (2013)
3. P. Zhang, C. Shao, X. Li, M. Zhang, X. Zhang, Y. Sun, Y. Liu, J. Hazard. Mater. **237–238**, 331 (2012)
4. Q. Li, D.J.G. Satur, H. Kim, H.G. Kim, Mater. Lett. **76**, 169 (2012)
5. J.H. Huang, M.S. Wong, Thin Solid Films **520**, 1379 (2011)
6. P. Manurung, Y. Putri, W. Simanjuntak, I.M. Low, Ceram. Int. **39**, 255 (2013)
7. R.D. Shannon, J.A. Pask, J. Am. Ceram. Soc. **48**, 391 (1965)
8. D.W. Kim, N. Enomoto, Z. Nakagawa, K. Kawamura, J. Am. Ceram. Soc. **79**, 1095 (1996)
9. A. Natoli, A. Cabeza, A.G. Torre, M.A. Aranda, I. Santacruz, J. Am. Ceram. Soc. **95**, 502 (2012)
10. S. Kment, P. Kluson, V. Stranak, P. Virostko, J. Krysa, M. Cada, J. Pracharova, M. Kohout, M. Morozova, P. Adamek, Z. Hubicka, Electrochim. Acta **54**, 3352 (2009)
11. H. Li, W. Zhang, W. Pan, J. Am. Ceram. Soc. **94**, 3184 (2011)
12. S. Chuangchote, J. Jitputti, T. Sagawa, S. Yoshikawa, ACS Appl. Mater. Interfaces **1**, 1140 (2009)
13. S. Shang, X. Jiao, D. Chen, ACS Appl. Mater. Interfaces **4**, 860 (2012)
14. I.M. Low, H. Albetran, V.M. Prida, V. Vega, P. Manurung, M. Ionescu, J. Mater. Res. **28**, 304 (2013)
15. J. Liu, E.J. Nichols, J. Howe, S.T. Misture, J. Mater. Res. **28**, 424 (2013)
16. V.J. Babu, A.S. Nair, Z. Peining, S. Ramakrishna, Mater. Lett. **65**, 3064 (2011)
17. R. Asahi, T. Morikawa, T. Ohwaki, K. Aoki, Y. Taga, Science **293**, 269 (2001)
18. S.U. Khan, M. Al-Shahry, W.B. Ingler, Science **297**, 2243 (2002)
19. A. Ghicov, J.M. Macak, H. Tsuchiya, J. Kunze, V. Haeublein, L. Frey, P. Schmuki, Nano Lett. **6**, 1080 (2006)
20. M. Takeuchi, H. Yamashita, M. Matsuoka, M. Anpo, T. Hirao, N. Itoh, N. Iwamoto, Catal. Lett. **67**, 135 (2000)
21. H. Yamashita, M. Harada, J. Misaka, M. Takeuchi, B. Neppolian, M. Anpo, Catal. Today **84**, 191 (2003)
22. H. Yamashita, M. Harada, J. Misaka, M. Takeuchi, K. Ikeue, M. Anpo, J. Photochem. Photobiol. A Chem. **148**, 257 (2002)
23. G. Impellizzeri, V. Scuderi, L. Romano, P.M. Sberna, E. Arcadipane, R. Sanz, M. Scuderi, G. Nicotra, M. Bayle, R. Carles, F. Simone, V. Privitera, J. Appl. Phys. **116**, 173507 (2014)
24. C. Wessel, R. Ostermann, R. Dersch, B.M. Smarsly, J. Phys. Chem. C **115**, 362 (2011)
25. I.M. Low, B. Curtain, M. Philipps, Q.Z. Liu, M. Ionescu, J. Aust. Ceram. Soc. **48**, 198 (2012)
26. J.S. Lee, T.J. Ha, M.H. Hong, H.H. Park, Thin Solid Films **529**, 98 (2013)
27. R. Liu, L.S. Qiang, W.D. Yang, H.Y. Liu, Mater. Res. Bull. **48**, 1458 (2013)
28. W. Luo, X. Hu, Y. Sun, Y. Huang, J. Mater. Chem. **22**, 4910 (2012)
29. J.Y. Park, S.S. Kim, Met. Mater. Int. **15**, 95 (2009)
30. J.Y. Park, J.J. Yun, C.H. Hwang, I.H. Lee, Mater. Lett. **64**, 2692 (2010)
31. Z. Zhang, C. Shao, L. Zhang, X. Li, Y. Liu, J. Colloid Interface Sci. **351**, 57 (2010)
32. W.K. Pang, I.M. Low, J. Am. Ceram. Soc. **93**, 2871 (2010)
33. R.A. Spurr, H. Myers, Anal. Chem. **29**, 760 (1957)
34. H. Albetran, H. Haroosh, Y. Dong, V.M. Prida, B.H. O'Connor, I.M. Low, Appl. Phys. A **116**, 161 (2014)
35. K. Matusita, T. Komatsu, R. Yokota, J. Mater. Sci. **19**, 291 (1984)
36. G.K. Williamson, W.H. Hall, Acta Metall. **1**, 22 (1953)
37. B.H. O'Connor, A.V. Riessen, J. Carter, G.R. Burton, D.J. Cookson, R.F. Garrett, J. Am. Ceram. Soc. **80**, 1373 (1997)
38. D.E. Cox, B.H. Toby, M.M. Eddy, Aust. J. Phys. **41**, 117 (1988)
39. G.C. Bond, A.J. Sarkany, G.D. Parfitt, J Catal. **57**, 476 (1979)
40. O.K. Varghese, D. Gong, M. Paulose, C.A. Grimes, E.C. Dickey, J. Mater. Res. **18**, 156 (2003)
41. K.N.P. Kumar, J. Engell, J. Kumar, K. Keizer, T. Okubo, M. Sadakata, J. Mater. Sci. Lett. **14**, 1784 (1995)
42. K.N.P. Kumar, K. Keizer, A.J. Burggraaf, J. Mater. Chem. **3**, 917 (1993)
43. R. Nicula, M. Stir, C. Schick, E. Burkel, Thermochim. Acta **403**, 129 (2003)

3.4 Effect of Calcination on Band Gaps for Electrospun Titania Nanofibers Heated in Air–Argon Mixtures

---

ALBETRAN, H., O'Connor, B. H., & LOW, I. M. 2016. Effect of Calcination on Band Gaps for Electrospun Titania Nanofibers Heated in Air–Argon Mixtures. *Materials & Design*, 92, 480–485.

Materials and Design 92 (2016) 480–485

Contents lists available at ScienceDirect

Materials and Design

journal homepage: www.elsevier.com/locate/matdes

Effect of calcination on band gaps for electrospun titania nanofibers heated in air–argon mixtures

H. Albetran [a,b], B.H. O'Connor [a,c], I.M. Low [a,*]

[a] Department of Imaging & Applied Physics, Curtin University, GPO Box U1987, Perth, WA 6845, Australia
[b] Department of Basic Sciences, College of Education, University of Dammam, PO Box 2375, Dammam 31451, Saudi Arabia
[c] John de Laeter Centre, Curtin University, GPO Box U1987, Perth, WA 6845, Australia

ARTICLE INFO

Article history:
Received 10 August 2015
Received in revised form 7 December 2015
Accepted 11 December 2015
Available online 12 December 2015

Keywords:
Titania nanofibers
Electrospinning
Oxygen vacancies
Band gap
Photocatalysis

ABSTRACT

The relationship between the band gap in electrospun titania nanofibers at ambient temperature and the nature of the air–argon atmosphere in which the material has been heated non-isothermally to 900 °C was investigated by ultraviolet–visible absorption spectrometry at room temperature. The results for heating in different selected air–argon mixtures show that the UV-region band gap found in unheated as-spun amorphous nanofibers, 3.33 eV, may be shifted well into the visible region by calcining in the different air–argon mixtures. The band gap value found for heating in air, 3.09 eV, reduces systematically when the material is heated in an air–argon mixture, with the gap in pure argon being 2.18 eV. The progressive lowering of the band gap is attributed to the development of crystallinity in the fibers as the material is calcined and the associated development of oxygen vacancies when heated in argon, and therefore to the formation of defect states below the conduction band.

1. Introduction

Titanium dioxide (TiO_2) or titania has received much attention as a photocatalytic and photovoltaic semiconductor because it is relatively inexpensive, eco-friendly and has long-term photostability [1–2]. It is a wide band gap semiconductor ceramic with an optical band gap for amorphous titania being in the range 3.30–3.5 eV [3]. This value decreases for two common crystalline titania forms: crystalline anatase (~3.20 eV), and crystalline rutile (~3.02 eV) [4,5].

Although rutile has a smaller band gap than crystalline anatase, the latter is most favored because it has a higher photoactivity than crystalline rutile, whereas a mixture of crystalline anatase and rutile has been reported to exhibit superior photocatalytic ability [6–8]. Thus, many studies have been conducted on the photocatalytic activity of crystalline titania because crystallinity is an important parameter that influences band gap narrowing in titania. Titania powder which is used as a commercial photocatalytic material (Degussa, P25), may include small amounts of amorphous phase, a minor quantity of crystalline rutile, and more than 70% crystalline anatase [9]. Some studies have focused on photocatalytic activities and the band gap for amorphous titania or a mixture of amorphous and crystalline titania [3].

An optimum combination of titania phases with lower band gap can be synthesized by thermal treatment of amorphous titania, which transforms to crystalline anatase at relatively low temperature, and then the crystalline anatase transforms to crystalline rutile at higher temperature. The amorphous-to-crystalline transformation of electrospun titania nanofibers has been studied by the authors from room temperature to 900 °C in 100% air and 100% argon atmospheres [10]. After thermal treatment, a sample heated in 100% argon contains more crystalline content (anatase and rutile) than that heated in 100% air due to the influence of oxygen vacancies created under argon. To the best of the author's knowledge, the effect of degree of crystallinity on the titania band gap for a mixture of amorphous and crystalline titania has not been reported previously.

When chemically pure, titania must be exposed to ultraviolet (UV) radiation to become photo-active. Various treatments, such as an organic dye attachment, hydrogen plasma reduction, and extrinsic chemical doping [11,12], have been investigated to reduce the band gap of titania in order to achieve photocatalytic activity under visible light (1.77–3.10 eV).

Impurity doping with various anions and cations has been used to create oxygen vacancies and thus modify the electronic structure to achieve visible light absorption [13–19]. A major disadvantage with chemical doping, however, is that dopant chemicals may be corrosive and pollute the environment (*i.e.*, secondary pollution). A reduction of the band gap without chemical doping is, therefore, an attractive proposition.

The introduction of oxygen vacancies can result in Ti^{3+} states which may be used as intrinsic donors to narrow the band gap of titania such that they can act as n-type donors. The introduction of oxygen vacancy defects into non-doped titania can influence the photocatalytic behavior

* Corresponding author.
E-mail address: j.low@curtin.edu.au (I.M. Low).

http://dx.doi.org/10.1016/j.matdes.2015.12.044
0264-1275/

significantly. Here the defects act as recombination centers for photo-induced electron–hole pairs, thereby reducing the band gap and enabling photoactivity under visible light [20]. Oxygen vacancies have been created by annealing titania in hydrogen, argon, or in a vacuum [20–22]. The oxygen vacancy concentration increases with increase in calcination temperature in these atmospheres, whereas it remains constant in air.

Using titania in an electrospun nanofiber form is attractive for photocatalysis applications since titania nanofibers have a high ratio of surface area to volume, which increase the decomposition rate of air and water pollutants and this allows for photocatalytic reactions to occur more rapidly on the photocatalyst surface [23–30].

In this work, a novel strategy was used to create oxygen vacancies in a mixture of amorphous titania, crystalline anatase, and crystalline rutile in electrospun titania nanofibers to narrow the band gap. Amorphous titania nanofibers were synthesized by electrospinning, and their morphology and band gap were characterized before and after calcination in air–argon mixtures, using field emission scanning electron microscopy (FESEM), energy dispersive spectroscopy (EDS) and UV–visible spectrometry.

2. Experimental procedures

2.1. Electrospun titania nanofiber synthesis

Electrospun titania nanofibers were synthesized by a combination of sol–gel and electrospinning methods. A titania sol–gel solution was prepared by mixing titanium isopropoxide (IV), ethanol, and acetic acid in a fixed volume ratio of 3:3:1, and then 12 wt.% polyvinylpyrrolidone (PVP) was dissolved in the solution. The titania sol–gel solution precursor was stirred ultrasonically before being loaded into a 10 ml plastic syringe with a 25-G stainless steel needle in the electrospinning experiment. The voltage setting was controlled using a high voltage power supply to maintain 25 kV between the needle tip and an aluminum collector at 12 cm. A syringe pump was used to control the titania sol–gel solution flow rate at 2 ml/h during the electrospinning process [25].

2.2. Heating protocol

Electrospun titania nanofibers were heated non-isothermally from 25 to 900 °C, at 10 °C/min in air–argon mixtures using a TGA/DSC Mettler Toledo machine. The thermal experiments were conducted using 150 μl alumina crucibles loaded with ~25 mg of sample. Protective argon gas flowed through the machine at 20 ml/min, with the flow rates of air or argon varied as required. Samples were heated in 50% air–50% argon, 25% air–75% argon, and 100% argon mixtures. The calculation of percentage air to argon included the protective argon gas. Because of safety considerations, mixtures of 25% argon–75% air and 100% air could not be used in the Mettler Toledo machine. Instead, samples were heated in 100% air using a furnace with the same non-isothermal heating conditions, also from room temperature to 900 °C at 10 °C/min.

2.3. In-situ high-temperature synchrotron radiation diffraction (SRD)

The *in-situ* crystallization behavior of electrospun titania nanofibers was estimated using non-isothermal high-temperature SRD in 100% air and 100% argon from 25 to 900 °C, at 10 °C/min. SRD data were collected at the Australian Synchrotron using the Powder Diffraction Beamline using an Anton Parr HTK 16 hot platinum stage, at a wavelength of 0.1126 nm and with a fixed incident beam-sample angle of 3°, for $5° \le 2\theta \le 84°$. The SRD patterns were acquired using a data collection time of 2 min per pattern, at ambient temperature and then in steps of 100 °C, from 200 °C to 900 °C [25].

The relative phase levels of crystalline anatase and rutile in 100% air and 100% argon were determined from Rietveld analysis using the TOPAS program (Bruker AXS, Version 4.2). Rietveld analysis of the SRD data was also used to estimate oxygen site occupancies for the crystalline anatase and rutile phases.

2.4. Microstructural imaging

The structure and morphology of electrospun titania nanofibers prior and following calcination in 100% air and 100% argon were studied by field emission scanning electron microscopy (FESEM, Zeiss, Neon, 40EsB, Germany). The samples were coated with a 3 nm layer of platinum before FESEM imaging to avoid charging. The elemental sample composition was determined by energy dispersive X-ray spectroscopy (EDS).

2.5. Band gap

Band gap assessments were made from absorption spectra recorded using a V-670 UV–visible spectrometer (Jasco, Japan). The main instrument settings were: absorbance photometric mode, a wavelength range from 200 to 750 nm, and a 200 nm/min scanning speed. The sample band gap (E_g) was calculated from:

$$E_g = hC/\lambda$$

where h is Planck's constant (6.626×10^{-34} J·s), C is the speed of light (3×10^8 m/s), and λ is the extrapolated wavelength (nm) at which the absorbance value reaches the instrument limit.

3. Results and discussion

3.1. Microstructure imaging

Fig. 1 shows secondary electron FESEM images of electrospun titania nanofibers recorded at ambient temperature: (a) as-electrospun prior to heating, and after non-isothermal thermal processing from 25 to 900 °C at 10 °C/min in (b) 100% air and (c) 100% argon atmospheres. The heated nanofibers have uneven surfaces compared with the as-spun amorphous fibers because of the development of crystalline grains of anatase and rutile [25]. Table 1 shows that the crystalline grains were larger in 100% argon than in 100% air, which is consistent with oxygen vacancies created in argon at elevated temperature affecting titania grain growth positively because of enhanced solid state diffusion. Atomic diffusion or the cooperative rearrangement of titania atoms and grain boundary movement during titania phase transformations occurs more easily in 100% argon than in 100% air because of the higher mobility of titania atoms in the presence of oxygen vacancies. This can lead to higher grain growth and larger titania grains [31,32].

The EDS spectrum of the nanofiber sample was recorded after thermal treatment in 100% argon (Fig. 2). The spectrum is similar to that for as-spun nanofiber (not shown here) besides an absence of the C peak from loss of organic substance and PVP polymer. The EDS spectrum shows strong Ti and O signatures and a weak Pt signature from the platinum coating on the sample, which are essentially the same when the sample was heated in 100% air. The complete loss of organic material and PVP polymer from the electrospun titania nanofibers occurred at ~450 °C, see our preliminary results from *in-situ* high temperature synchrotron radiation diffraction (SRD) (see Fig. 4) and thermal gravimetric analysis (TGA) [10]. The titania nanofibers were initially amorphous by the pronounced amorphous humps in the SRD patterns for 100% air and 100% argon, but these humps disappeared by 400 °C. The TGA results showed that the loss of organic material (ethanol and acetic acid) occurred from room temperature to ~150 °C, and the PVP polymer decomposition occurred from ~150 to 450 °C.

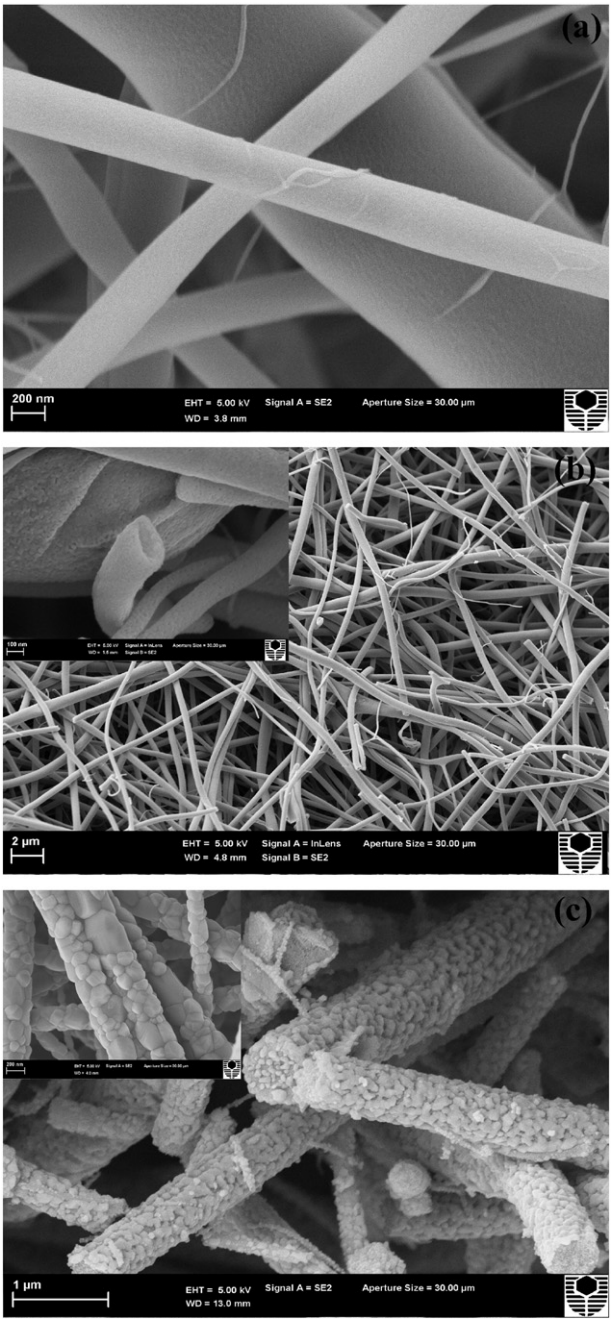

Fig. 1. Secondary electron FESEM micrographs of electrospun titania nanofibers recorded at ambient temperature: (a) as-electrospun prior to heating, and after non-isothermal heating from 25 °C to 900 °C at 10 °C/min (b) in 100% air, and (c) in 100% argon atmospheres.

Table 1
Nanofiber and grain size measurements. The ± symbol refers to the size range for size assessment. The number of measurements for each entry was 40.

Calcination conditions	Nanofiber size (nm)	Grain size (nm)
As-spun (not calcined)	665 ± 330	Amorphous
100% air	351 ± 145	21 ± 5
100% argon	328 ± 113	118 ± 49

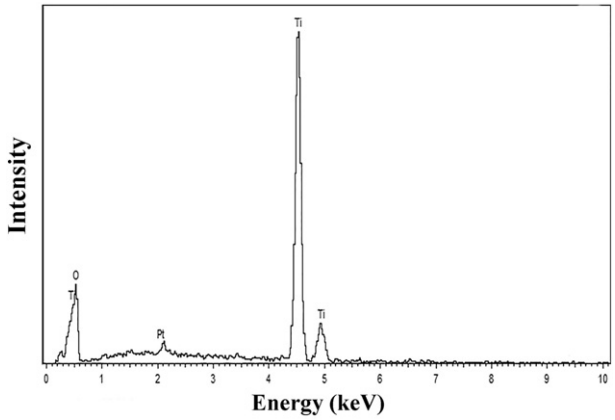

Fig. 2. EDS spectrum of electrospun titania nanofibers recorded at ambient temperature after heating from 25 °C to 900 °C at 10 °C/min in 100% argon.

3.2. Influence of calcining atmosphere on titania color

Fig. 3 shows the progressive color change in titania from white after thermal treatment in 100% air to progressively darker shades of gray after thermal treatment in air–argon compositions from 100% air to 100% argon. This color change is attributed to oxygen loss from the titania to form oxygen vacancy defects, and the color intensification is considered to result from an increase in oxygen vacancy concentration with increasing argon concentration. A similar color change effect has been reported by Gamboa and Pasquevich [33] in a calcining experiment in which the effect of low levels of chlorine addition to air and argon was studied. This color change was attributed to the formation of oxygen vacancies when heating in argon.

3.3. Phase composition results from the SRD

Fig. 4 shows the stacked SRD plots measured in 100% air and 100% argon over the temperature range 25–900 °C, and noting that the peaks at ~27.7° and 35.6° occur because of the Pt heating holder. Table 2 shows the variation in absolute phase concentrations following SRD for the 100% argon and 100% air atmospheres. The presence of oxygen vacancies makes the anatase-to-rutile transformation in 100% argon more efficient than in 100% air because some relaxation of the Ti binding environment occurs. Details of absolute levels of amorphous titania and crystalline anatase and rutile at each temperature extracted

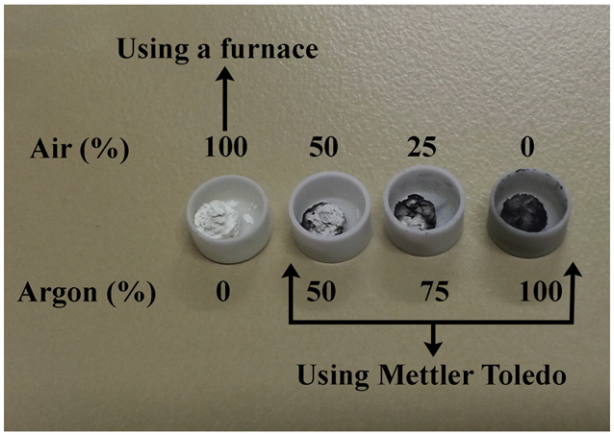

Fig. 3. Color changes in electrospun titania nanofibrous material observed at room temperature following non-isothermal heating from 25 °C to 900 °C at 10 °C/min in argon–air mixtures.

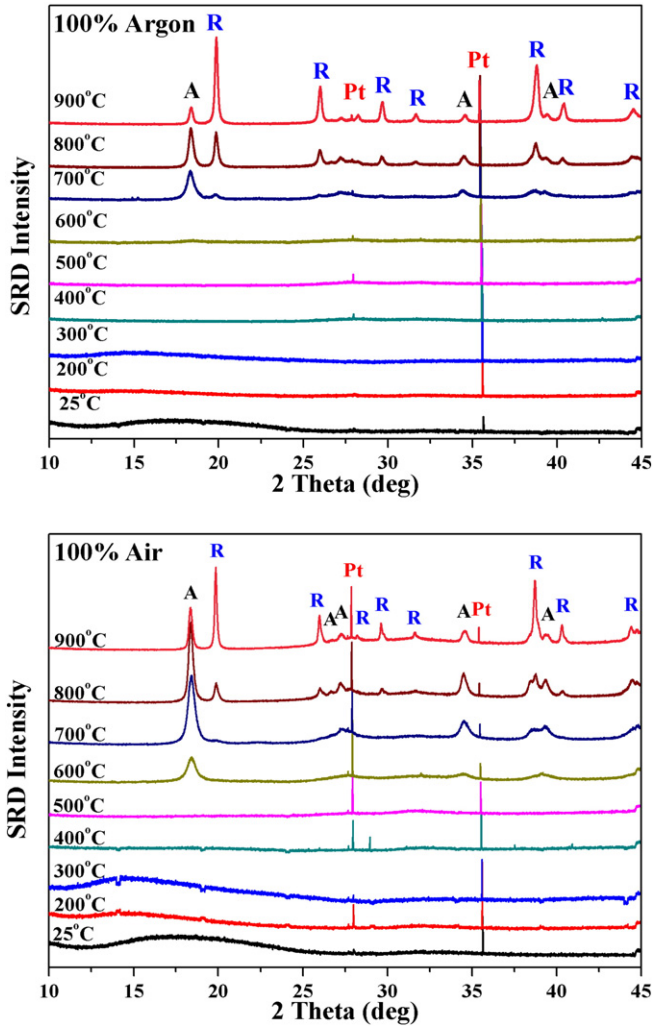

Fig. 4. UV–visible spectra for as-electrospun titania nanofibrous material after non-isothermal heating from 25 °C to 900 °C at 10 °C/min in 100% air, 50% air–50% argon, 25% air–75% argon and 100% argon, and then cooling to room temperature.

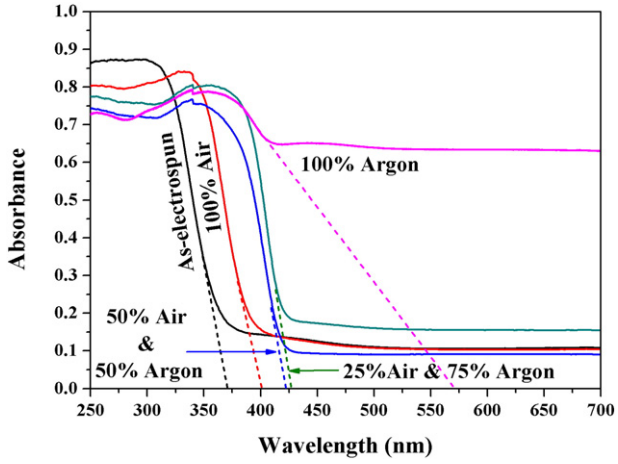

Fig. 5. Band gap values of as-electrospun titania nanofibrous material, extracted from UV–visible spectra in Fig. 4. Band gaps in eV at room temperature following non-isothermal heating from 25 °C to 900 °C at 10 °C/min in air–argon mixtures, and then cooling to room temperature.

from the SRD data are given in the preliminary novel study by the authors [10].

3.4. UV–visible spectral analysis results

Fig. 5 compares the UV–visible diffuse reflectance spectra of non-calcined as-electrospun nanofibers with those after thermal treatment in the argon–air mixtures followed by cooling to room temperature. The absorption thresholds, band gap, and absorbance were determined from an absorbance *versus* wavelength graph. The absorbance plots for unheated fibers, and those after heating in 100%, 50% air and 25% air are similar in form. The absorbance falls from ~0.7–0.8 to ~0.1–0.2 with all showing the expected precipitous drop in absorbance when the photon energy exceeds the band energy gap. A systematic red-shift occurs as the level of argon increases which is consistent with the development of oxygen vacancy levels within the band gap. The red-shift seen here resembles that reported by various authors such as Buha [34] who reported titania thin-film absorbance spectra with different levels of carbon doping, in which an increase in C-doping level increased the magnitude of absorption across the entire visible range. A similar substantial red-shift in absorption of Ag-doped titania nanosquares and Fe-doped titania nanoparticles was observed under visible light irradiation [15,17].

The absorbance–wavelength plot for the sample heated in 100% argon is substantially different from those for the other samples discussed above, with there being a reduced absorbance range, from *ca.* 0.80 to 0.65, across the wavelength band investigated. This effect is consistent with accounts in the literature that the development of substantial oxygen vacancy defects is responsible for such changes in optical properties. The absorbance change resembles that for C-doped titania thin films for with the absorbance fell from 0.7 to 0.5 over the range 300 nm to 800 nm [34]. Following the present study, the measurement of additional absorbance spectra would be required for argon contents of between 75% and 100% to reveal the underlying band structure.

3.5. Influence of calcining atmosphere on band-gap structure

Fig. 6 shows a plot of band gap *versus* argon content corresponding to the absorbance spectra in Fig. 5, and Table 2 lists the band gap values for each sample type, and also specifies the sample phase compositions [10,25,30]. Table 3 compares band gap results from this study with literature data for titania materials with different forms, mixtures and atmospheric treatment.

The effect on band gap for the as-produced amorphous fiber sample through calcining in 100% air was to reduce it from the amorphous value of 3.33 eV to 3.09 eV, *i.e.*, from within the UV to the visible region. As earlier work on the same sample has indicated that the development of vacancies on heating in air is minimal, the reduction to 3.09 eV is

Table 2
Phase compositions and band gaps for titania nanofibers at room temperature after calcining to 900 °C in 100% air, 100% argon, and air–argon mixtures.

Calcination conditions	Amorphous (%)	Anatase (%)	Rutile (%)	Crystallinity (%)	Band gap (eV)
As-spun (not calcined)	100	0	0	0	3.33
100% air	40.5	20.9	38.6	59.5	3.09
50% air–50% argon	NA[a]	NA[a]	NA[a]	NA[a]	2.94
25% air–75% argon	NA[a]	NA[a]	NA[a]	NA[a]	2.91
100% argon	26.6	10.3	63.1	73.4	2.18

[a] Not available.

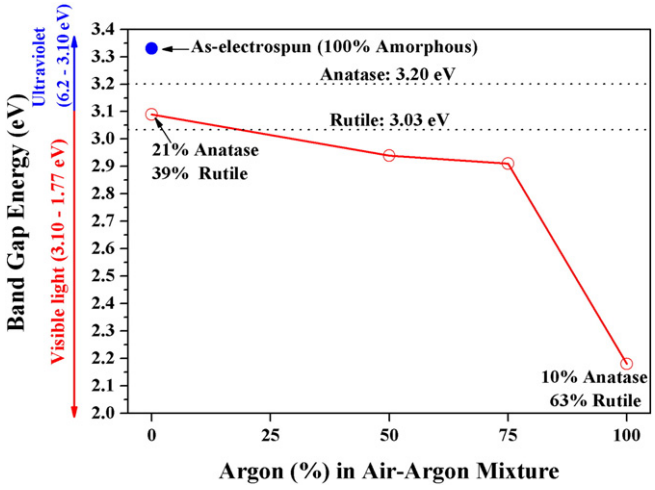

Fig. 6. Stacked SRD plots for electrospun titania nanofibers material when heated in 100% air and in 100% argon, from 25 to 900 °C [A: anatase, R: rutile, Pt: platinum]. Plots taken from Albetran et al. [25].

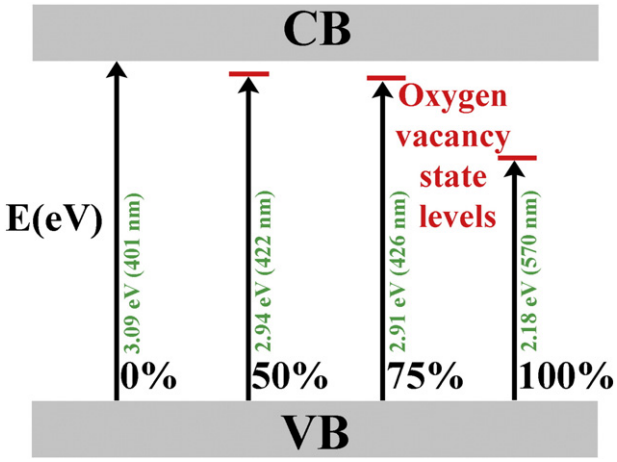

Fig. 7. Band gap states and the assumed influence of oxygen vacancies with change in air–argon mix. Argon (%) in air–argon mixtures [legend: CB = conduction band, VB = valence band].

attributed entirely to the development of crystallinity in the fibers — noting the phase levels of about 21% anatase and 39% rutile on calcining amorphous material in 100% air [10]. It is noted that the measured gap value 3.09 eV agrees with the concentration-weighted gap for the two phases: 3.20 eV for pure anatase [5] and 3.03 eV for pure rutile [4,5]. This appears to be consistent with literature reports of band gaps for mixtures of anatase and rutile [5].

Two factors appear to drive the further reduction in band gap as argon is introduced: (i) changes in the titania phase mix, and (ii) the progressive development of oxygen vacancies. The measured gap of 2.18 eV for heating in 100% argon is related to the titania phase composition (10% anatase and 63% rutile) for which the concentration-weighted gap would be 3.05 eV which is ~0.87 eV greater than the measured gap of 2.18 eV. The 0.87 eV difference is attributed to oxygen vacancy development. The presence of oxygen vacancies provides more surface active sites and allows for a larger charge carrier density. This is consistent with the electronic structure of titania material being changed by an absent oxygen atom, resulting in the localization of one or two electrons in an oxygen state. The formation of oxygen vacancies results in the formation of unpaired electrons or Ti^{3+} centers, which form oxygen vacancy states below the conduction band and act as n-type donors [35,36].

The development of oxygen vacancies as the concentration of argon increases was discussed by the authors [10] in terms of non-stoichiometric effects of titania heated in 100% argon. Oxygen is lost when the sample is heated in argon due to the formation of non-stoichiometric anatase (TiO_{2-x}). This is consistent with the work of Andersson et al. who investigated the composition range of argon-annealed $TiO_{1.9-2}$ using X-ray powder diffraction [37].

Fig. 7 shows a schematic depicting the assumed band gap states and the apparent influence of oxygen vacancies after calcining to 900 °C and cooling to room temperature in air–argon mixtures. The introduction of oxygen vacancies in titania results with a presence of localized new oxygen vacancy states existing between the valence (VB) and conduction (CB) bands in the titania band structure. Electrons may be excited from VB to the oxygen vacancy states even under visible light. As the argon level increases from 25% to 100%, the effective energy gap red-shifts systematically and the sample becomes active in visible light, with the band gap narrowing significantly to 2.94, 2.91, and then 2.18 eV for 50% air–50% argon, 25% air–75% argon, and 100% argon, respectively. Thus, the combined influence of crystallinity development and oxygen vacancy formation have extended the light excitation of electrospun titania nanofibers from the UV to well into the visible light range. This has been achieved without chemical doping. Finally, a comparison of band gap results, as shown in Table 3, indicates that the current band gap

Table 3
Comparison of band gap results from present study with data from literature for titania materials.

Study	Titania nano-material	Treatment	Band gap (eV)	Am:A:R	Comment
This study	Fiber	As-spun	3.33	100:0:0	
		100% air	3.09	40:21:39	
		100% argon	2.18	27:10:63	Presence of oxygen vacancies
Potlog et al. [1]	Films	vacuum	3.34	0:62:38	
		100% H_2	3.22	0:100:0	
Tang et al. [4]	Films	Argon & O_2	3.20	0:100:0	
			3.00	0:0:100	
Chen et al. [38]	Powder	100% air	3.15	0:100:0	
Rosseler et al. [39]	Sol–gel promoted template	100% air	3.02	0:50:50	TiO_2–polyoxyethylene cetylether
			2.99	0:40:60	TiO_2–CTAB
			2.97	0:30:70	TiO_2–polyvinyl alcohol
			2.94	0:5:95	TiO_2–polyethylene glycol
Reyes-Coronado et al. [40]	Particles	100% air	3.21	0:100:0	
			3.00	0:0:100	

Am: amorphous, A: anatase, and R: rutile.

results are consistent with other data for nano-titania materials reported in the literature.

4. Conclusions

This paper focuses on the use of heat treatment of amorphous titania nanofibers, rather than chemical doping, to develop titania photocatalysts that are photoactive in visible light. The results have significance for the development of waste treatment technologies using photocatalytic titania nanofibers which may function in the visible light. The results for heating in different selected air–argon mixtures show that the UV-region band gap found in as-electrospun amorphous nanofibers, 3.33 eV, shifted well into the visible region by calcining in air, argon and argon–air mixtures. The band gap value observed for heating in air, 3.09 eV, reduces systematically when the material is heated in an air–argon mixture, with the gap for heating in 100% argon being 2.18 eV. The progressive lowering of the band gap is attributed to the development of crystallinity in the fibers as the material is calcined and the associated development of oxygen vacancies when heated in argon.

The narrowed band gap is attributed to the heterostructure titania phases (anatase and rutile) and the formation of oxygen vacancies, which creates a state below the conduction band. Increasing the percentage of argon in the air–argon mixtures reduce the state to below the titania conduction band, which thus increases the oxygen vacancy concentration, and the subsequent band gap narrowing.

Acknowledgments

The authors thank the following Curtin University colleagues: Dr. Y. Dong of Mechanical Engineering for access to the electrospinning equipment; Ms. E. Miller of the John de Laeter Centre for assistance with electron microscopy; and Prof. M. Tade, Ms. K. Haynes, and Mr. A. Chan of Chemical Engineering for access to the TGA/DSC Mettler Toledo and UV–visible spectrometer instruments.

References

[1] T. Potlog, P. Dumitriu, M. Dobromir, A. Manole, D. Luca, Nb-doped TiO_2 thin films for photovoltaic applications, Mater. Des. 85 (2015) 558–563.
[2] D. Wu, M. Long, Realizing visible-light-induced self-cleaning property of cotton through coating N-TiO_2 film and loading AgI particles, ACS Appl. Mater. Interfaces 3 (2011) 4770–4774.
[3] K. Eufinger, D. Poelman, H. Poelman, R.D. Gryse, G.B. Marin, Photocatalytic activity of dc magnetron sputter deposited amorphous TiO_2 thin films, Appl. Surf. Sci. 254 (2007) 148–152.
[4] H. Tang, K. Prasad, R. Sanjines, P.E. Schmid, F. Levy, Electrical and optical properties of TiO_2 anatase thin films, J. Appl. Phys. 75 (1994) 2042–2047.
[5] D.O. Scanlon, C.W. Dunnill, J. Buckeridge, S.A. Shevlin, A.J. Logsdail, S.M. Woodley, C.R. Catlow, M.J. Powell, R.G. Palgrave, I.P. Parkin, G.W. Watson, T.W. Keal, P. Sherwood, A. Walsh, A.A. Sokol, Band alignment of rutile and anatase TiO_2, Nat. Mater. 12 (2013) 798–801.
[6] A. Natoli, A. Cabeza, A.G. Torre, M.A. Aranda, I. Santacruz, Colloidal processing of macroporous TiO_2 materials for photocatalytic water treatment, J. Am. Ceram. Soc. 95 (2012) 502–508.
[7] S. Kment, P. Kluson, V. Stranak, P. Virostko, J. Krysa, M. Cada, J. Pracharova, M. Kohout, M. Morozova, P. Adamek, Z. Hubicka, Photo-induced electrochemical functionality of the TiO_2 nanoscale films, Electrochim. Acta 54 (2009) 3352–3359.
[8] H. Li, W. Zhang, W. Pan, Enhanced photocatalytic activity of electrospun TiO_2 nanofibers with optimal anatase/rutile ratio, J. Am. Ceram. Soc. 94 (2011) 3184–3187.
[9] B. Ohtani, O.O. Mahaney, D. Li, R. Abe, What is degussa (evonik) P25? crystalline composition analysis, reconstruction from isolated pure particles and photocatalytic activity test, J. Photochem. Photobiol. A Chem. 216 (2010) 179–182.
[10] H. Albetran, B. H. O'Connor, I. M. Low, Activation energies for phase transformations in electrospun titania nanofibers: comparing the influence of argon and air atmospheres, Appl. Phys. A Mater. Sci. Process. APYA-15-00895R1. (in press).
[11] S.W. Hsu, T.S. Yang, T.K. Chen, M.S. Wong, Ion-assisted electron-beam evaporation of carbon-doped titanium oxide films as visible-light photocatalyst, Thin Solid Films 515 (2007) 3521–3526.
[12] J. Yi, X. Yuan, H. Wang, H. Yu, F. Peng, Preparation of $Bi_2Ti_2O_7/TiO_2$ nanocomposites and their photocatalytic performance under visible light irradiation, Mater. Des. 86 (2015) 152–155.
[13] V.J. Babu, A.S. Nair, Z. Peining, S. Ramakrishna, Synthesis and characterization of rice grains like nitrogen-doped TiO_2 nanostructures by electrospinning–photocatalysis, Mater. Lett. 65 (2011) 3064–3068.
[14] A. Ghicov, J.M. Macak, H. Tsuchiya, J. Kunze, V. Haeublein, L. Frey, P. Schmuki, Ion implantation and annealing for an efficient N-doping of TiO_2 nanotubes, Nano Lett. 6 (2006) 1080–1082.
[15] C. Yu, L. Wei, X. Li, J. Chen, Q. Fan, J.C. Yu, Synthesis and characterization of Ag/TiO_2-B nanosquares with high photocatalytic activity under visible light irradiation, Mater. Sci. Eng. B 178 (2013) 344–348.
[16] M. Takeuchi, H. Yamashita, M. Matsuoka, M. Anpo, T. Hirao, N. Itoh, N. Iwamoto, Photocatalytic decomposition of NO under visible light irradiation on the Cr-ion-implanted TiO_2 thin film photocatalyst, Catal. Lett. 67 (2000) 135–137.
[17] S.K. Patel, S. Kurian, N.S. Gajbhiye, Room-temperature ferromagnetism of Fe-doped TiO_2 nanoparticles driven by oxygen vacancy, Mater. Res. Bull. 48 (2013) 655–660.
[18] D. Li, N. Ohashi, S. Hishita, T. Kolodiazhnyi, H. Haneda, Origin of visible-light-driven photocatalysis: a comparative study on N/F-doped and N–F-codoped TiO_2 powders by means of experimental characterizations and theoretical calculations, J. Solid State Chem. 178 (2005) 3293–3302.
[19] R.P. Antony, T. Mathews, P.K. Ajikumar, D.N. Krishna, S. Dash, A.K. Tyagi, Electrochemically synthesized visible light absorbing vertically aligned N-doped TiO_2 nanotube array films, Mater. Res. Bull. 4 (2012) 4491–4497.
[20] J.H. Huang, M.S. Wong, Structures and properties of titania thin films annealed under different atmosphere, Thin Solid Films 520 (2011) 1379–1384.
[21] A. Ghicov, H. Tsuchiya, J.M. Macak, P. Schmuki, Annealing effects on the photoresponse of TiO_2 nanotubes, Phys. Status Solidi A 203 (2006) 28–30.
[22] Q. Wu, R.V. Krol, Selective photoreduction of nitric oxide to nitrogen by nanostructured TiO_2 photocatalysts: role of oxygen vacancies and iron dopant, J. Am. Chem. Soc. 134 (2012) 9369–9375.
[23] J.Y. Park, J.J. Yun, C.H. Hwang, I.H. Lee, Influence of silver doping on the phase transformation and crystallite growth of electrospun TiO_2 nanofibers, Mater. Lett. 64 (2010) 2692–2695.
[24] I.M. Low, F.K. Yam, W.K. Pang, In-situ diffraction studies on the crystallization and crystal growth in anodized TiO_2 nanofibres, Mater. Lett. 87 (2012) 150–152.
[25] H. Albetran, H. Haroosh, Y. Dong, V.M. Prida, B.H. O'Connor, I.M. Low, Phase transformations and crystallization kinetics in electrospun TiO_2 nanofibers in air and argon atmospheres, Appl. Phys. A Mater. Sci. Process. 116 (2014) 161–169.
[26] Q. Li, D.J.G. Satur, H. Kim, H.G. Kim, Preparation of sol–gel modified electrospun TiO_2 nanofibers for improved photocatalytic decomposition of ethylene, Mater. Lett. 76 (2012) 169–172.
[27] H. Li, W. Zhang, B. Li, W. Pan, Diameter-dependent photocatalytic activity of electrospun TiO_2 nanofiber, J. Am. Ceram. Soc. 93 (2010) 2503–2506.
[28] S. Chuangchote, J. Jitputti, T. Sagawa, S. Yoshikawa, Photocatalytic activity for hydrogen evolution of electrospun TiO_2 nanofibers, ACS Appl. Mater. Interfaces 1 (2009) 1140–1143.
[29] R. Chandrasekar, L. Zhang, J.Y. Howe, N.E. Hedin, Y. Zhang, H. Fong, Fabrication and characterization of electrospun titania nanofibers, J. Mater. Sci. 44 (2009) 1198–1205.
[30] H. Albetran, B.H. O'Connor, I.M. Low, Effect of vanadium ion implantation on the crystallization kinetics and phase transformation of electrospun TiO_2 nanofibers, Appl. Phys. A Mater. Sci. Process. 120 (2015) 623–634.
[31] Y. Iida, S. Ozaki, Grain growth and phase transformation of titanium oxide during calcination, J. Am. Ceram. Soc. 44 (1961) 120–127.
[32] X. Ding, X. Liu, Correlation between anatase-to-rutile transformation and grain growth in nanocrystalline titania powders, J. Mater. Res. 13 (1998) 2556–2559.
[33] J.A. Gamboa, D.M. Pasquevich, Effect of chlorine atmosphere on the anatase–rutile transformation, J. Am. Ceram. Soc. 75 (1992) 2934–2938.
[34] J. Buha, Solar absorption and microstructure of C-doped and H-co-doped TiO_2 thin films, J. Phys. D. Appl. Phys. 45 (2012) 385305.
[35] I. Nakamura, N. Negishi, S. Kutsuna, T. Ihara, S. Sugihara, K. Takeuchi, Role of oxygen vacancy in the plasma-treated TiO_2 photocatalyst with visible light activity for NO removal, J. Mol. Catal. A Chem. 161 (2000) 205–212.
[36] H. Seo, L.R. Baker, A. Hervier, J. Kim, J. Whitten, G.A. Somorjai, Generation of highly n-type titanium oxide using plasma fluorine insertion, Nano Lett. 11 (2010) 751–756.
[37] S. Andersson, B. Collen, U. Kuylenstierna, A. Magneli, Phase analysis studies on the titanium–oxygen system, Acta Chem. Scand. 11 (1957) 1641–1652.
[38] D. Chen, Z. Jiang, J. Geng, Q. Wang, D. Yang, Carbon and nitrogen Co-doped TiO_2 with enhanced visible-light photocatalytic activity, Ind. Eng. Chem. Res. 46 (2007) 2741–2746.
[39] O. Rosseler, M.V. Shankar, M.K. Du, L. Schmidlin, N. Keller, V. Keller, Solar light photocatalytic hydrogen production from water over Pt and Au/TiO_2 (anatase/rutile) photocatalysts: influence of noble metal and porogen promotion, J. Catal. 269 (2010) 179–190.
[40] D. Reyes-Coronado, G. Rodriguez-Gattorno, M.E. Espinosa-Pesqueira, C. Cab, R. de Coss, G. Oskam, Phase-pure TiO_2 nanoparticles: anatase, brookite and rutile, Nanotechnology 19 (2008) 145605.

Corrigendum sheet

This corrigendum sheet lists the errors on page proofs that were not corrected by Elsevier and their corrections for "**ALBETRAN, H.,** O'Connor, B. H., & LOW, I. M. 2016. Effect of Calcination on Band Gaps for Electrospun Titania Nanofibers Heated in Air–Argon Mixtures. *Materials & Design*, 92, 480–485."

Page	Error	Correction
283, Caption for Figure 4	UV–visible spectra for as-electrospun titania nanofibrous material after non-isothermal heating from 25 °C to 900 °C at 10 °C/min in 100% air, 50% air–50% argon, 25% air–75% argon and 100% argon, and then cooling to room temperature.	Stacked SRD plots for electrospun titania nanofibers material when heated in 100% air and in 100% argon, from 25 to 900 °C [A: anatase, R: rutile, Pt: platinum]. Plots taken from Albetran *et al*. [25].
283, Caption for Figure 5	Band gap values of as-electrospun titania nanofibrous material, extracted from UV–visible spectra in Fig. 4. Band gaps in eV at room temperature following non-isothermal heating from 25 °C to 900 °C at 10 °C/min in air–argon mixtures, and then cooling to room temperature.	UV–visible spectra for as-electrospun titania nanofibrous material after non-isothermal heating from 25 °C to 900 °C at 10 °C/min in 100% air, 50% air–50% argon, 25% air–75% argon and 100% argon, and then cooling to room temperature
284, Caption for Figure 6	Stacked SRD plots for electrospun titania nanofibers material when heated in 100% air and in 100% argon, from 25 to 900 °C [A: anatase, R: rutile, Pt: platinum]. Plots taken from Albetran *et al*. [25].	Band gap values of as-electrospun titania nanofibrous material, extracted from UV–visible spectra in Fig. 5. Band gaps in eV at room temperature following non-isothermal heating from 25 °C to 900 °C at 10 °C/min in air–argon mixtures, and then cooling to room temperature.
282, Section 3.3, line 2	"and noting"	"noting"
282, Section 3.3, line 8	"binding"	"bonding"
283, Section 3.3, line 10	"novel"	Delete "novel"

3.5 Characterization and Optimization of Electrospun TiO_2/PVP Nanofibers Using Taguchi Design of Experiment Method

---

ALBETRAN, H., DONG, Y. & LOW, I. M. 2015. Characterization and Optimization of Electrospun TiO_2/PVP Nanofibers Using Taguchi Design of Experiment Method. *Journal of Asian Ceramic Societies*, 3, 292–300.

Journal of Asian Ceramic Societies 3 (2015) 292–300

HOSTED BY

Contents lists available at ScienceDirect

Journal of Asian Ceramic Societies

journal homepage: www.elsevier.com/locate/jascer

Characterization and optimization of electrospun TiO_2/PVP nanofibers using Taguchi design of experiment method

H. Albetran[a,b], Y. Dong[c], I.M. Low[a,*]

[a] Department of Imaging and Applied Physics, Curtin University, Perth, WA 6845, Australia
[b] Department of Basic Sciences, College of Education, University of Dammam, Dammam 31451, Saudi Arabia
[c] Department of Mechanical Engineering, Curtin University, Perth, WA 6845, Australia

ARTICLE INFO

Article history:
Received 3 March 2015
Received in revised form 1 May 2015
Accepted 5 May 2015
Available online 23 May 2015

Keywords:
Taguchi method
TiO_2/PVP nanocomposites
Electrospun nanofibers

ABSTRACT

TiO_2 nanofibers were prepared within polyvinylpyrrolidone (PVP) polymer using a combination of sol–gel and electrospinning techniques. Based on a Taguchi design of experiment (DoE) method, the effects of sol–gel and electrospinning on the TiO_2/PVP nanofibers' diameter, including titanium isopropoxide (TiP) concentration, flow rate, needle tip-to-collector distance, and applied voltage were evaluated. The analysis of DoE experiments for nanofiber diameters demonstrated that TiP concentration was the most significant factor. An optimum combination to obtain smallest diameters was also determined with a minimum variation for electrospun TiO_2/PVP nanofibers. The optimum combination was determined to be a 60% TiP concentration, at a flow rate of 1 ml/h, with the needle tip-to-collector distance at 11 cm (position *a*), and the applied voltage of 18 kV. This combination was further validated by conducting a confirmation experiment that used two different needles to study the effect of needle size. The average nanofiber diameter was approximately the same for both needle sizes in good accordance with the optimum condition estimated by the Taguchi DoE method.

1. Introduction

The electrospinning technique has attracted considerable attention as a relatively new, cheap and simple synthesis method for one-dimensional nanostructures [1–4]. The unique nanofibers prepared by electrospinning generally exhibit high surface area-to-volume ratios, high porosity, nanosized effects, and excellent mechanical strength [5]. They have been suggested for many applications, such as membrane separation, drug delivery, protective clothing, wound dressings, filtration, tissue engineering, and electronics [6–9].

Titanium dioxide (TiO_2), also known as titania, has emerged as a promising photocatalyst in the current market. It has the advantages of being photocatalytically stable, reasonably inexpensive, and relatively easy to produce and use. It is a human and environmentally friendly photocatalyst used to treat polluted air and water, and to split water to generate hydrogen [10]. A high surface area-to-volume ratio (SA/vol) of electrospun nanofibers can significantly improve the photocatalytic performance of TiO_2 because of small fiber size, and the high SA/vol provides further means for quick charge transfer to the dynamics of hole–electron (e^-/h^+) recombination on a large specific surface area of TiO_2 nanofibers [6,11].

TiO_2 nanofibers can be synthesized by combining electrospinning with a TiO_2 sol–gel technique [2,3,11–14]. The components of the electrospun experiment to synthesize TiO_2 nanofibers comprise a syringe pump, a syringe with a conductive needle, a high voltage supply, a conductive collector, copper wires, and a sol–gel of polymer (binder), and a TiO_2 precursor [4]. In general, electrospun nanofiber diameters depend primarily on three processing parameter sets [15] mentioned below.

The first set of adjusted parameters involved in the sol–gel solution include electrical conductivity, viscosity, surface tension, polymer concentration, and molecular weight. They are related to one another, and these relationships have important influences on electrospun nanofiber diameters [16]. The viscosity of the TiO_2 solution depends on the molecular weight and concentration of the material solution, such as polymer, solvent, and TiO_2 sources. The polymer concentration is one of the most significant factors in controlling beads and fiber diameters [16–18]. The TiO_2 fiber diameter

* Corresponding author. Tel.: +61 8 9266 7544; fax: +61 8 9266 2377.
E-mail address: j.low@curtin.edu.au (I.M. Low).
Peer review under responsibility of The Ceramic Society of Japan and the Korean Ceramic Society.

http://dx.doi.org/10.1016/j.jascer.2015.05.001

increases with a higher TiO_2 concentration in a precursor solution [12,19].

Electrospinning conditions are the second set of parameters, which consist of applied voltage, flow rate, needle size, and needle tip-to-collector distance [16]. Optimally applied voltage is a significant factor to affect fiber diameters [17,19–21]. High applied voltage (i.e., strong electrical repulsive forces) reduces the nanofiber diameter, resulting in highly stretched and elongated fibers [20]. Flow rate plays one of the most important roles in determining the fiber diameter and bead formation, because it determines the amount of sol–gel solution available to be stretched into nanofibers [16,19,20]. During the electrospinning process, the shape and size of the needle tip affect the formation of Taylor cone and nanofiber oscillation [22]. Ksapabutr et al. [22] claimed that a sawtooth needle shape allowed for Taylor cones of greater length than standard and flat counterparts. A needle tip-to-collector distance with the sufficient field gradient produces fibers with less bead defects, but the more considerable distance increases the nanofiber diameter owing to subsequent decreases in the electric field gradient [17]. Applied high voltage setting, a large needle tip-to-collector distance, a comparatively low concentration of polymer solutions and a low flow rate reduce the variation in product quality of electrospun fiber mats with a minimum number of experiments [17]. It is clear that the relationship between electrospun variables and associated fibrous structures is still not well understood to achieve ultrafine bead-free nanofibers with good dimensional stability.

Aspects of the atmospheric environment, such as humidity, pressure, and temperature, belong to the last set of parameters. The average nanofiber diameter decreases with increasing atmospheric temperature and decreasing atmospheric humidity [23].

Electrospun TiO_2/PVP nanofibers were synthesized using different titanium oxide precursors with a constant flow rate, needle tip-to-collector distance, and applied voltage in most electrospun experiments [2,8,28–31]. The fibers have a smooth and uniform surface with a random orientation, and the average fiber diameters range from 132 to 2280 nm [24–27]. Kumar and co-worker used a different applied voltage and flow rate with a constant needle-to-collector distance. At ~10 cm, the average diameter of the as-spun TiO_2/PVP nanofiber was 450 nm at 10 kV and 1 ml/h, 262 nm at 20 kV and 1 ml/h, and 145 nm at 20 kV and 0.5 ml/h [20].

The Taguchi method for robust experimental design is a useful engineering approach to select the optimal levels of processing parameters with the minimal sensitivity to different causes of variations. Furthermore, such a method can also elucidate the effects of a large and complex number of factors on an individual and interactive basis. In general, two essential tools are required, namely an orthogonal array (OA) to simultaneously accommodate several experimental design factors, and signal to noise ratio (S/N) to measure the most robust set of operating conditions from variations within the results [17,28–31].

In this study, TiO_2 nanofibers were fabricated with PVP polymer as precursor using both sol–gel and electrospinning techniques. An optimum combination of parameters obtained from TiP concentration, flow rate, needle tip-collector distance, and applied voltage in response to minimizing diameter size and its variation for TiO_2/PVP nanofibers was determined by means of the Taguchi DoE method. Such an optimum condition was further implemented to explore the effect of needle size on fiber diameters accordingly.

2. Experimental procedure

2.1. Materials

Titanium isopropoxide (TiP) (M_W = 284.22 g/mol, 97% purity), polyvinylpyrrolidone (PVP) (M_W = 1,300,000 g/mol, 100% purity),

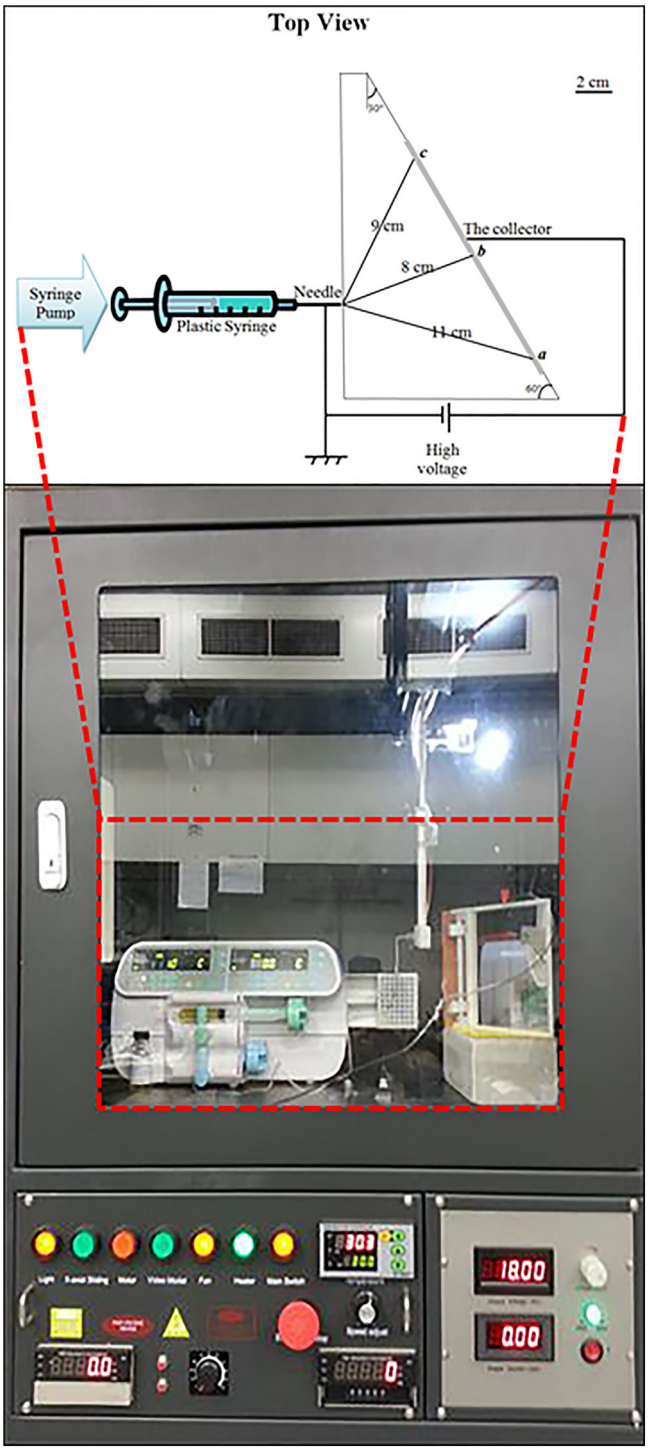

Fig. 1. Schematic diagram of electrospinning process with a slope collector.

acetic acid (M_W = 60.05 g/mol, 99.7% purity) and ethanol (M_W = 46.07 g/mol, 99.5% purity) were all purchased from Sigma–Aldrich, Inc., NSW, Australia.

2.2. Preparation of TiO_2/PVP sol–gel

TiO_2/PVP solutions were prepared by mixing 40 wt%, 50 wt% or 60 wt% TiP with a constant mixed solvent, which comprised 2.098 g acetic acid and 4.734 g ethanol (1:3 volume ratio) with 2.05 g PVP polymer inside a glass bottle. The solutions were subsequently subjected to magnetic stirring for 120 min at 80 °C. The viscosity of

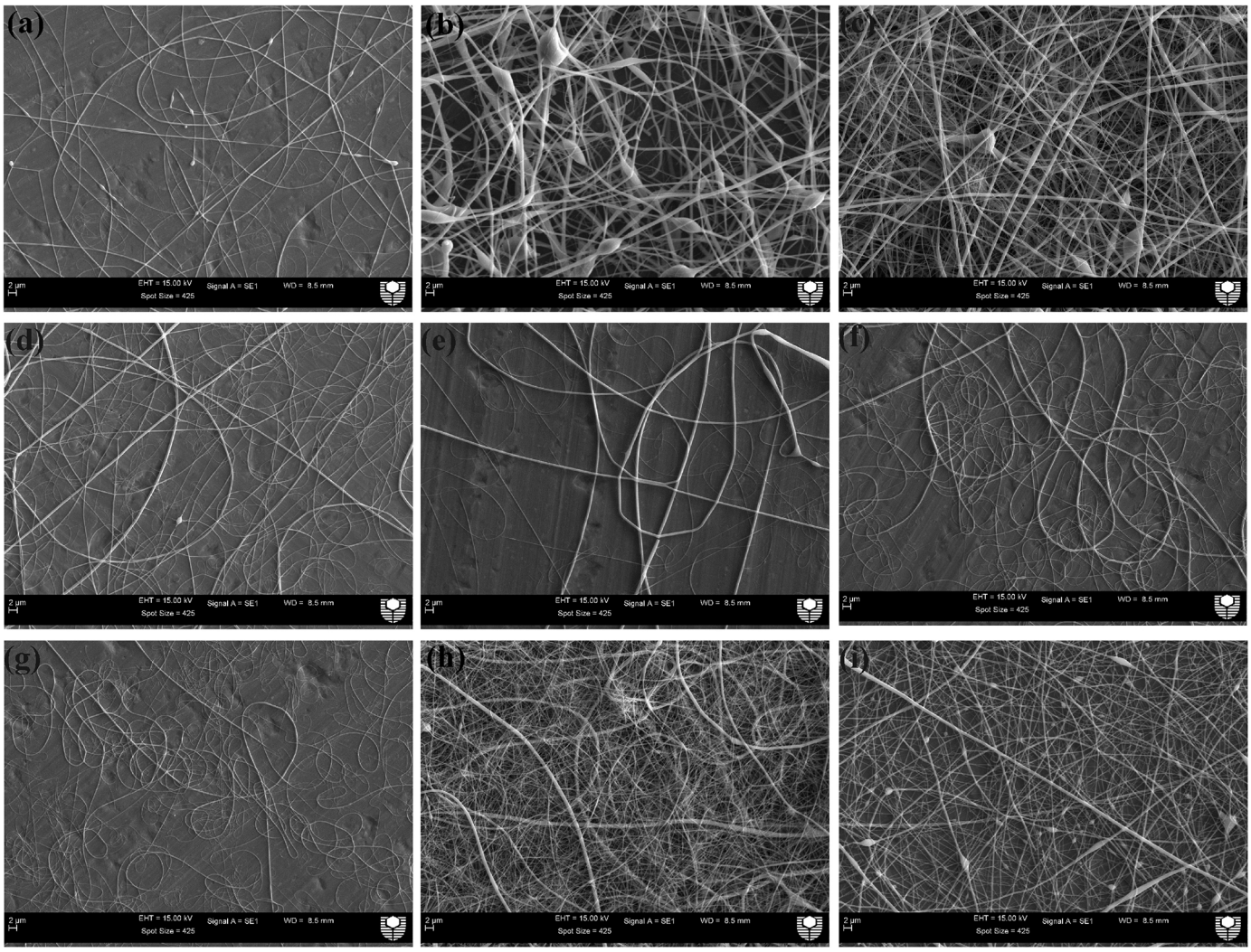

Fig. 2. SEM micrographs of electrospun TiO_2/PVP nanofibers used in DoE study: (a) T1, (b) T2, (c) T3, (d) T4, (e) T5, (f) T6, (g) T7, (h) T8, and (i) T9. All scale bars represent 2 μm.

the TiO_2/PVP solution depends on the concentration and molecular weight of PVP polymer, the solvent, and TiO_2 sources [3,12]. As the solvent and PVP were constant, the viscosities of the solutions were solely controlled by the TiP concentration (wt%). Increasing the TiP concentration (284.22 g/mol) reduces the concentration of PVP (1,300,000 g/mol), which further reduces the solution viscosity.

2.3. Electrospinning experiments

A commercial Nabond® electrospinning unit (standard type) was purchased from Nabond Technologies Co., Ltd., Shenzhen, China to fabricate electrospun fiber mats. The homogeneous solution was loaded into a 10 ml plastic syringe that was attached to a stainless steel needle with the inner diameter of approximately 0.514 mm. The needle tip-to-collector distance was varied due to a slope aluminum collector (see Fig. 1). Thus, the needle tip-to-collector distances were in range of ~11 cm for position *a*, ~8 cm for position *b*, and ~9 cm for position *c*. A syringe pump was used to control the solution flow rate at 0.5, 1, or 2 ml/h during the electrospinning process. The voltage setting was controlled by a high voltage power supply to maintain 14, 18, or 25 kV between the needle and the slope collector. The slope collector was covered

Table 1
Four factors and three levels selected in the DoE study for electrospun TiO_2/PVP nanofibers.

	Factor description	Level		
		1	2	3
A	TiP concentration (wt%)	40	50	60
B	Flow rate (ml/h)	0.5	1	2
C	Needle tip-to-collector distance (cm)	~11	~8	~9
D	Applied voltage (kV)	14	18	25

Table 2
Taguchi orthogonal array with nine trials (L_9).

Trial	Factor			
	A: TiP concentration (wt%)	B: flow rate (ml/h)	C: needle tip-to-collector distance (cm)	D: applied voltage (kV)
T1	40	0.5	a	14
T2	40	1	b	18
T3	40	2	c	25
T4	50	0.5	b	25
T5	50	1	c	14
T6	50	2	a	18
T7	60	0.5	c	18
T8	60	1	a	25
T9	60	2	b	14

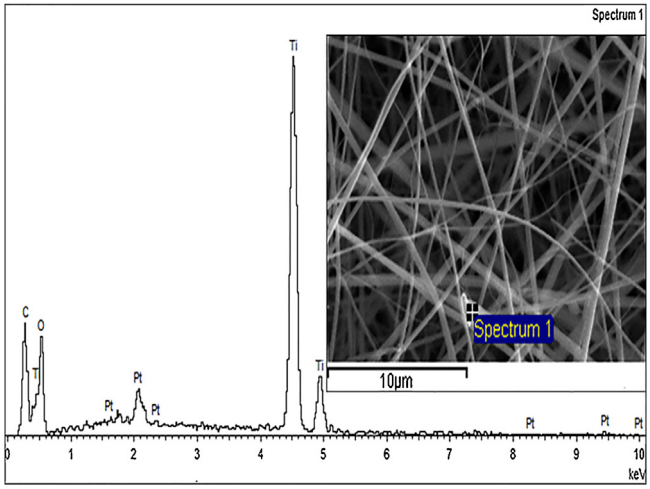

Fig. 3. EDS spectra of electrospun TiO_2/PVP nanofibers.

with an aluminum foil, and the needle tip-to-collector distance was adjusted accordingly. The electrospinning experiments were performed in a sealed environmental chamber at a constant temperature of 30 °C maintained by a lamp heater.

2.4. Taguchi DoE

Four factors of sol–gel and electrospinning parameters have been selected for this experiment, which are given by TiP concentration, flow rate, collector distance, and applied voltage at three different levels (Table 1). The full factorial experiment of 81 (3^4) trials can be completed in just 27 runs due to the slope collector, but that entails a large number of tests, which are significant in both experimental cost and time. As a result, Taguchi DoE layouts are more applicable when compared to a traditional full-factorial counterpart. This is because it reduced the number of tests to a practical level, thus significantly saving the experimental time and associated costs as opposed to the conduct of four factors individually. The L_9 DoE orthogonal array was selected with the assumption of no factorial interactions, resulting in nine trials as illustrated in Table 2.

2.5. Analysis of variance (ANOVA)

As earlier mentioned, the Taguchi DoE method replaces the full factorial experiments with only a simple orthogonal array of nine trials. To determine the significant factors, and optimum combination of factors, an analysis of variance (ANOVA) was utilized in order to offer a measure of confidence by determining and analyzing the

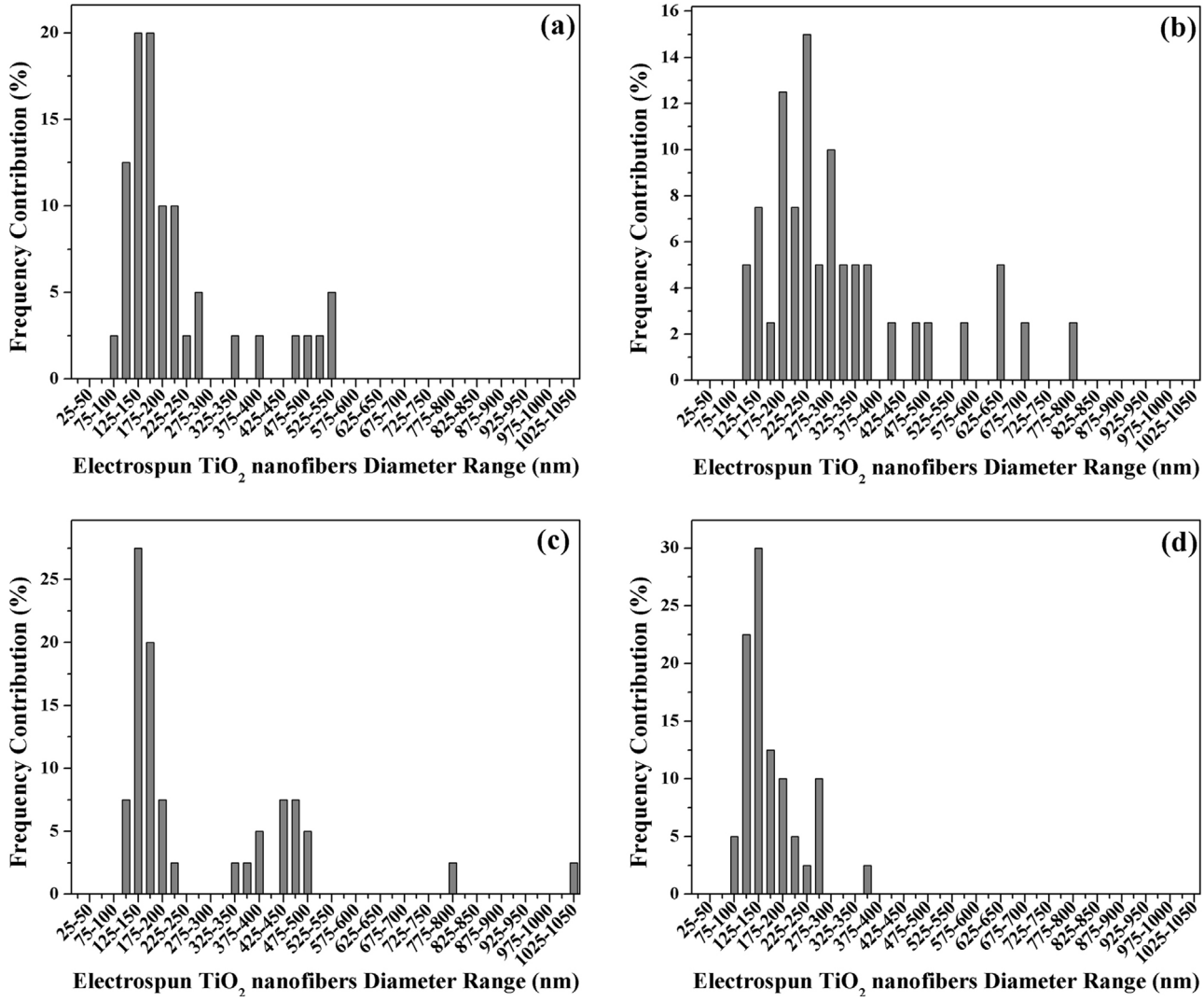

Fig. 4. Frequency contributions to electrospun TiO_2/PVP nanofibers diameter range in DoE study: (a) T1, (b) T2, (c) T3, (d) T4, (e) T5, (f) T6, (g) T7, (h) T8, and (i) T9.

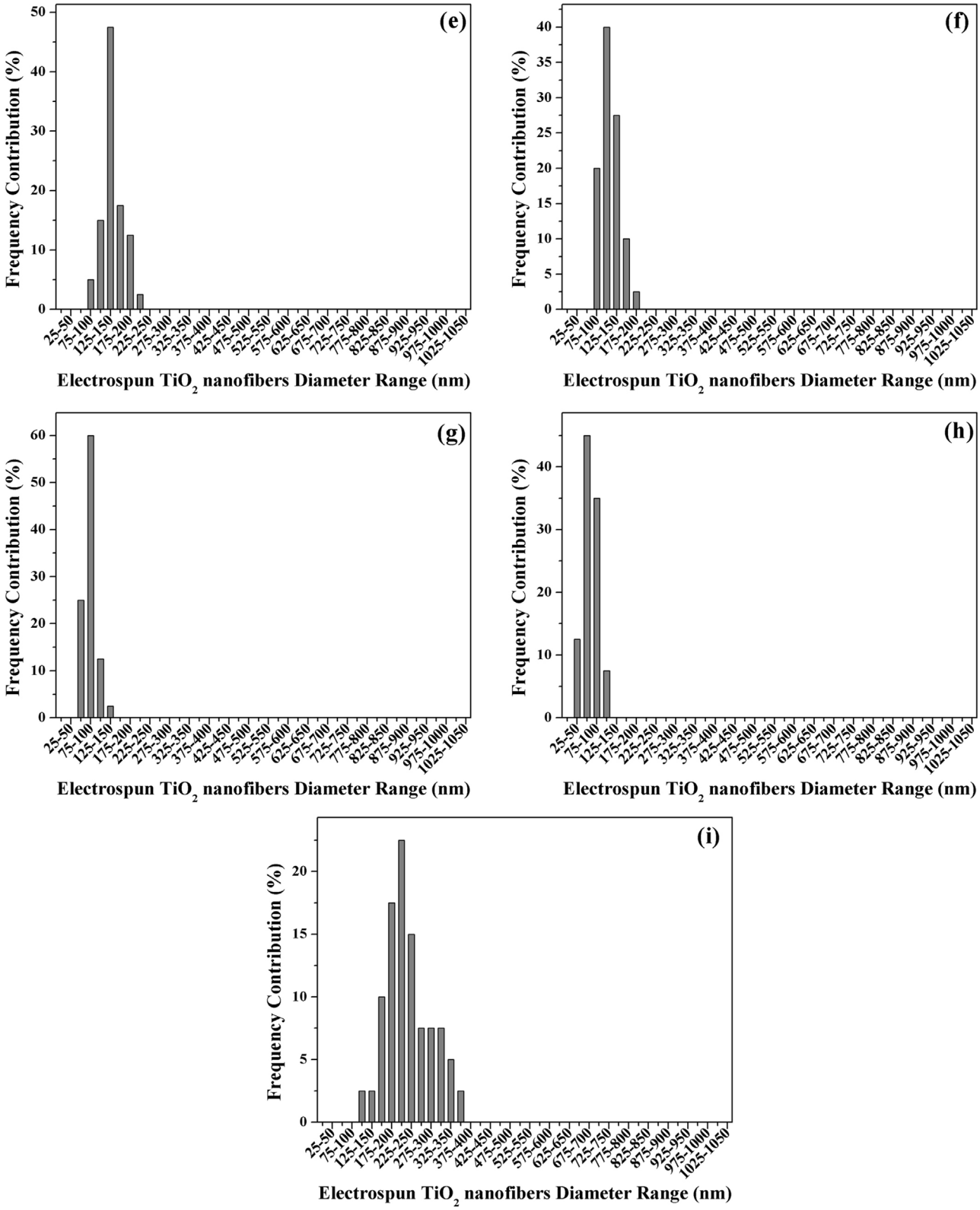

Fig. 4. (*Continued*)

data variance [31]. In the ANOVA, the total variation (S_T), the sum of squares of each factor (S_i) and the percentage contribution (%) were computed, respectively [31].

2.5.1. Total variation (S_T)

The total variation (S_T) is the sum of squares of all trial results, which is expressed in the following form:

$$S_T = \left[\sum_{i=1}^{N} \bar{Y}_i^2\right] - \left[\frac{\left(\sum_{i=1}^{N} \bar{Y}_i\right)^2}{N}\right] \quad (1)$$

where $\bar{Y}_i$ is the mean fiber diameter and N is the number of trials in Taguchi DoE study.

2.5.2. Total variance of each factor (S_i)

$$S_A = \frac{A_{40}^2}{3} + \frac{A_{50}^2}{3} + \frac{A_{60}^2}{3} - C.F \quad (2)$$

$$S_B = \frac{B_{0.5}^2}{3} + \frac{B_1^2}{3} + \frac{B_2^2}{3} - C.F \quad (3)$$

$$S_C = \frac{C_a^2}{3} + \frac{C_b^2}{3} + \frac{C_c^2}{3} - C.F \quad (4)$$

$$S_D = \frac{D_{14}^2}{3} + \frac{D_{18}^2}{3} + \frac{D_{25}^2}{3} - C.F \quad (5)$$

where S_A, S_B, S_C, and S_D are the sum squares for four factors of TiP concentration, flow rate, needle tip-to-collector distance, and applied voltage at three different levels, respectively. $C.F$ is denoted as the correction factor, which is a term similar to the $\left[\left(\sum_{i=1}^{N} \bar{Y}_i\right)^2/N\right]$ in Eq. (1) and it remains constant for all factors. The correction factor ($C.F$) is used for the calculation of all sums of squares [31].

2.5.3. Percentage contribution (%)

The percentage contribution of four factors (P_A, P_B, P_C, or P_D) is the ratio of the total variance of each factor (S_A, S_B, S_C, or S_D) to total variation (S_T) as given by:

$$P_i = \frac{S_i}{S_T} \times 100 \quad (6)$$

where i is the number of factors ($i = 4$ for this study).

2.5.4. Signal to noise ratio (S/N) of electrospun TiO_2 nanofiber diameter

A "smaller the better" characteristic formula [17,28,29,31] has been used to identify the optimum combination of factors to reduce both the fiber diameter and its variation in electrospun TiO_2/PVP nanofibers as indicated below:

$$\mathrm{S/N} = -10 \log\left(\frac{1}{n}\sum_{i=1}^{n} y_i^2\right) \quad (7)$$

where S/N is the signal-to-noise ratio, n is the number of measurements, and y is the diameter of electrospun TiO_2/PVP nanofibers. Mathematically the greater the value of S/N, the smaller the variance for electrospun TiO_2/PVP nanofibers.

3. Characterization

3.1. Scanning electron microscopy (SEM)

Electrospun TiO_2/PVP nanofibers were sputter coated with 3 nm platinum layers to be electrically conductive for reducing the surface charge issue. The surface morphologies of the samples were examined using an EVO 40XVP scanning electron microscope at an accelerating voltage of 15 kV and the magnification of 3000× with a working distance at 8.5 mm. Energy dispersive X-ray spectroscope (EDS) at an acceleration voltage of 10 kV was also used to qualitatively analyze the elemental compositions.

Table 3
Changes in nanofiber diameters of electrospun TiO_2/PVP.

Trial	Combination of factors	Average nanofiber diameter and standard deviation (nm)	S/N
T1	$A_{40}B_{0.5}C_aD_{14}$	218 ± 126	−47.99
T2	$A_{40}B_1C_bD_{18}$	305 ± 165	−50.78
T3	$A_{40}B_2C_cD_{25}$	271 ± 203	−50.56
T4	$A_{50}B_{0.5}C_bD_{25}$	162 ± 59	−44.73
T5	$A_{50}B_1C_cD_{14}$	142 ± 28	−43.21
T6	$A_{50}B_2C_aD_{18}$	118 ± 25	−41.61
T7	$A_{60}B_{0.5}C_cD_{18}$	85 ± 18	−38.81
T8	$A_{60}B_1C_aD_{25}$	70 ± 18	−37.22
T9	$A_{60}B_2C_bD_{14}$	227 ± 57	−47.37

3.2. Imaging analysis

The electrospun nanofiber diameters from the SEM images were measured by *ImageJ*® software (version 1.48e) developed by the National Institutes of Health (NIH), USA. The number of pixels over the scale bar in the SEM image was calibrated by the given length of the scale bar in the corresponding image. Subsequently, the fiber length perpendicular to the fiber axis was measured manually for each fiber. The total number of fiber measurements was 40 in each SEM image and associated average nanofiber diameters along with their standard deviations were calculated accordingly.

4. Results and discussion

4.1. Nanofiber morphology and diameter

SEM micrographs of electrospun nanofiber morphology for the L_9 DoE are illustrated in Fig. 2. The randomly oriented nanofibers had smooth surfaces along with most of large beads as typical defects except that only minor bead defects are noticed in Fig. 2e–g. Fig. 3 shows a typical EDS spectrum of the DoE study with elemental signals for Ti, O, Pt, and C, where Ti and O elements are assigned to TiO_2, as well as C and Pt elements are due to PVP polymer and the platinum coating, respectively [14].

Fig. 4 shows the frequency contribution diagrams for the DoE study in the diameter range of 25–1050 nm. The corresponding average fiber diameters and standard deviations are illustrated in Table 3. T2 in the DoE study yielded the highest average diameter (305 ± 165 nm) with the highest range of variation in diameter (125–1050 nm). The highest viscosity level of the sol–gel solution with 40% TiP concentration and the lowest needle tip-to-collector distance (position b) were the main reasons for the increased nanofiber diameter. However, nanofiber diameter decreased slightly for T1, T3, and T9, where the average diameters and the standard deviations were 218 ± 126 nm, 271 ± 203 nm, and 227 ± 57 nm, respectively. Both T1 and T3 had the same sol–gel concentrations as opposed to T2 with 40 wt% TiP, but with different electrospinning parameters. The needle tip-to-collector distance for T1 (position a) and T3 (position c) was higher than that for the T2 (position b), which was one reason for decreasing fiber diameter. Other reasons to achieve this were to reduce the flow rate or increase the applied voltage. T1 had the lowest level of flow rate (0.5 ml/h), but it also had the lowest level of the applied voltage (14 kV). T3 had the highest level of the applied voltage (25 kV), but also had the highest level of the flow rate (2 ml/h). For T9,

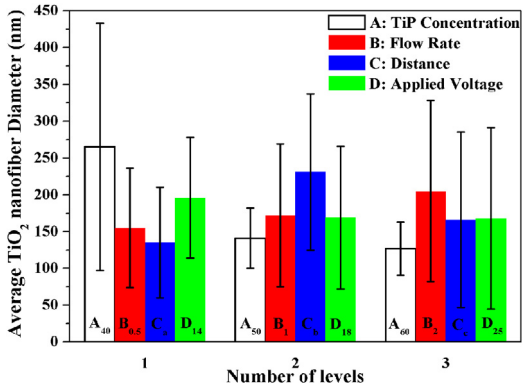

Fig. 5. The effect of TiP concentration, flow rate, needle tip-to-collector distance, and applied voltage on the average nanofiber diameter of electrospun TiO_2/PVP.

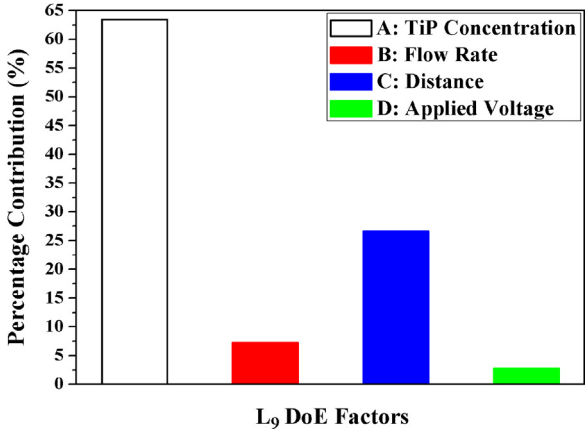

Fig. 6. ANOVA diagram for the determination of significant factors to influence electrospun TiO_2/PVP nanofiber diameters.

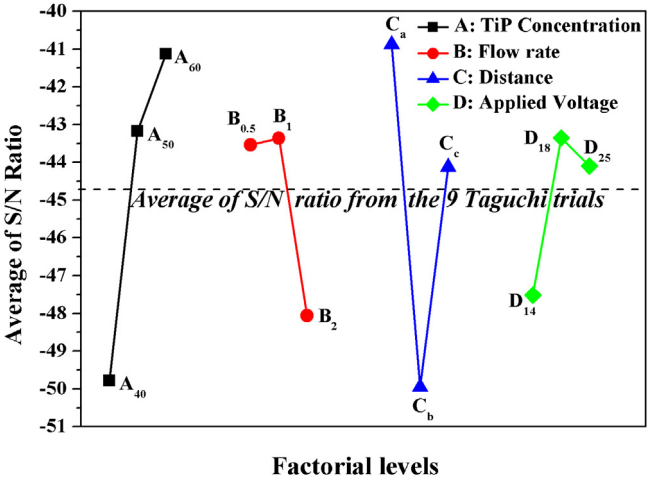

Fig. 7. Average S/N ratio diagram for the determination of the optimum combination of factors for electrospun TiO_2/PVP nanofibers with the smallest fiber diameter size and its minimum variation.

the main reason for the reduction in the diameter size was the TiP concentration of 60 wt%, despite its lowest distance (position *b*), lowest applied voltage (14 kV), and highest flow rate (2 ml/h). The TiP concentration of T4, T5, and T6 was 50 wt%, but with different combinations of electrospinning factors. Most of the diameter variation was from 75 to 275 nm, and the average diameters were under 200 nm. For both T7 and T8, the highest level of TiP concentration at 60 wt% was used. The average fiber diameters and the standard deviations were 85 ± 18 nm for T7, and 70 ± 18 for T8 due to different electrospinning conditions. Both T7 and T8 had a minimum variance of fiber diameter, where about 80% frequency contribution was detected in the fiber diameter range of 50–100 nm. Fig. 5 shows the effect of TiP concentration, flow rate, needle tip-to-collector distance, and applied voltage on the average nanofiber diameter of electrospun TiO_2/PVP. It was found that the fiber diameters decreased with increasing the TiP concentration (a decrease in viscosity due to the low concentration of PVP polymer in the TiP/PVP solution), needle tip-to-collector distance (position *a*) and applied voltage setting while decreasing the flow rate, which is in good agreement with previous literature [11,17,20]. The nanofiber diameters decreased relatively sharply from 265 nm with the 40 wt% TiP to 127 nm with 60 wt% TiP. This finding suggests that the TiP concentration is the most significant factor for achieving the small nanofiber diameter of electrospun TiO_2/PVP with the minimum variance (a further detail is included in the Taguchi analysis).

4.2. Analysis of variance (ANOVA)

The relative percentage contributions of electrospinning factors were determined using Eqs. (1)–(6). The ANOVA diagram depicted in Fig. 6 demonstrates that the effect of processing parameters on nanofiber diameters of electrospun TiO_2/PVP by the percentage contributions for selected L_9 DoE factors. The TiP concentration (factor A) was a significant variable to control the nanofiber diameter with a percentage contribution of 63.45%. This provides the further evidence that increasing the TiP concentration decreases the diameter size. The second and third most prevalent factors in minimizing nanofiber diameters were the needle tip-to-collector distance (factor C) and the flow rate (factor B) with the percentage of contributions of 26.59% and 7.23% accordingly. The applied voltage (factor D) appeared to be insignificant at 2.72% only. It is implied that the applied voltage has a trivial impact on the nanofiber diameter, which can be maintained at the workable experimental range.

4.3. Optimum combination of factors

The S/N ratios for electrospun TiO_2/PVP nanofibers were calculated using the "smaller the better" Eq. (7) for the nine Taguchi DoE study (Table 3). Since the purpose of this research work is to determine the smallest nanofiber with the minimum variance, the highest value of S/N ratio yields the optimum condition from the Taguchi DoE work [17,28,31]. As illustrated in Table 3, T8 ($A_{60}B_1C_aD_{25}$) was determined to be the best candidate for inclusion in the optimal combination, which has the maximum S/N value of −37.22 with the average nanofiber diameter and standard deviation at 70 ± 18 nm. However, T7 ($A_{60}B_{0.5}C_cD_{18}$) with the S/N value of −38.81 and the average fiber diameter and standard deviation at 85 ± 18 nm is another strong candidate. The average fiber diameter for T8 is slightly smaller than that for T7, but the fiber variance for T7 is less than that for T8, and the standard deviation is ±18 nm in both cases. In Fig. 4, 60% frequency contribution of fibers in the nanofiber diameter range from 75 to 100 nm for T7; whereas for T8, it is 45% in the diameter range of 50 to 75 nm, and 35% between 75 and 100 nm.

Therefore, the average S/N ratio was calculated to determine the best level factor for the optimum contribution to minimize the diameter and variation of electrospun TiO_2/PVP nanofibers as shown in Fig. 7. It suggests that 60 wt% TiP concentration, a flow rate of 1 ml/h, needle tip-to-collector distance (position *a*), and applied voltage of 18 kV ($A_{60}B_1C_aD_{18}$) is the optimum combination of factors to obtain small electrospun TiO_2/PVP nanofiber with the minimum variation. It is further proven that the TiP concentration and the needle tip-to-collector distance are the two most

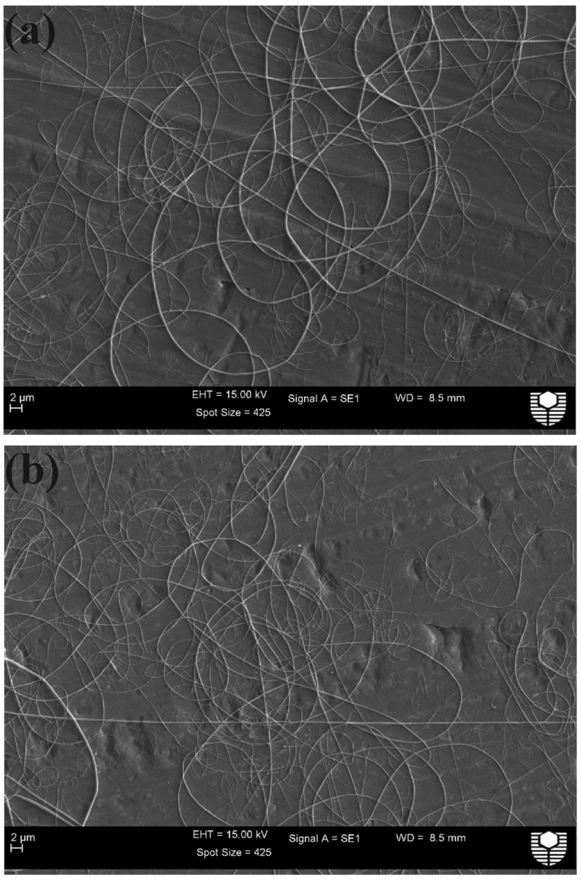

Fig. 8. SEM micrographs of the confirmation experiment for the optimum combination of factors ($A_{60}B_1C_aD_{18}$) using two different needle sizes: (a) 0.514 mm and (b) 0.819 mm. All scale bars represent 2 μm.

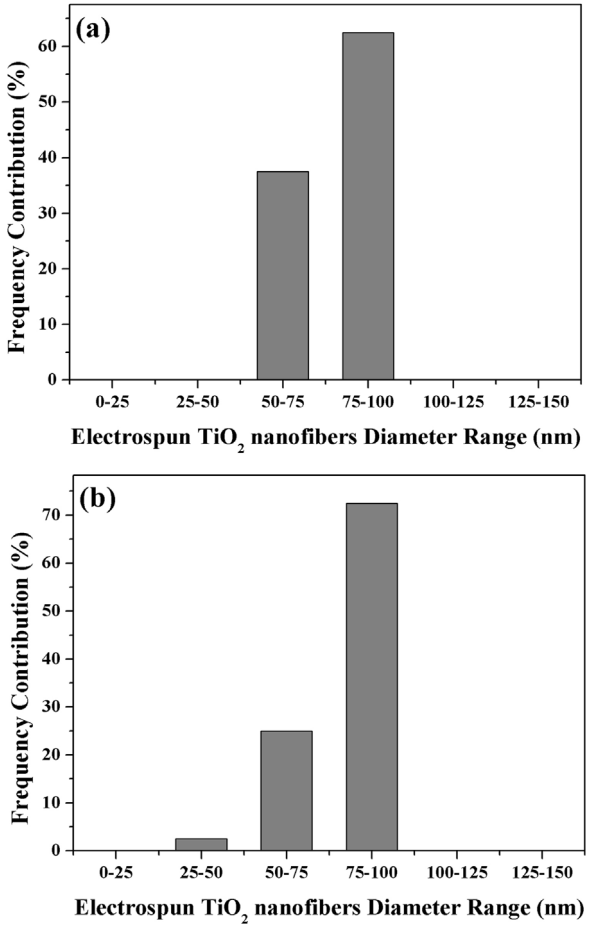

Fig. 9. Frequency contributions to electrospun TiO_2/PVP nanofibers diameter range for confirmation experiments using needle sizes of (a) 0.514 mm and (b) 0.819 mm.

significant factors; whereas the flow rate and the applied voltage appear to be relatively insignificant.

4.4. Confirmation experiment to optimum conditions

The confirmation experiment for the optimum combination of factors was subsequently carried out as a necessary and important post-step in the Taguchi DoE method [31]. The optimum combination ($A_{60}B_1C_aD_{18}$) was tested with the same needle size of 0.514 mm and a new needle size of 0.819 mm to study the effect on the nanofiber diameter of electrospun TiO_2/PVP. Fig. 8 shows the typical SEM images of confirmation experiments with both needle sizes. The randomly oriented nanofibers had smooth surfaces without beads defects in both images. The mean diameter and range are 79 ± 11 nm and 84 ± 13 nm for the confirmation experiments of the needle size of 0.514 mm, and needle size of 0.819 mm, respectively. It is clear that the needle size is a non-significant factor in the nanofiber diameter of electrospun TiO_2/PVP. The diameters of these nanofibers for both needles sizes are compared closely with the best Taguchi candidate values obtained in T7 (85 ± 18), and T8 (70 ± 18). The T8 gives the smallest nanofiber diameter, but the optimum combination ($A_{60}B_1C_aD_{18}$) gives comparatively small electrospun TiO_2/PVP nanofiber diameter with the smallest standard deviation. In Fig. 9, most the frequency contribution diagrams for both confirmation experiments are presented in the fiber diameter range of 50–100 nm with smallest standard deviations, as compared to the orthogonal array with nine trials (L_9).

5. Conclusions

An L_9 orthogonal array along with S/N ratios and ANOVA in Taguchi DoE method was used to investigate TiP concentration, flow rate, needle tip-to-collector distance, and applied voltage at three different levels on the nanofiber diameter of electrospun TiO_2/PVP. The small nanofiber diameter with the minimum variance has been found to be controlled mainly by two significant factors, namely TiP concentration, and needle tip-to-collector distance. The optimum combination of factors with the highest level of the TiP concentration, and the highest relative needle tip-to-collector distance (position *a*) was found along with a flow rate of 1 ml/h and an applied voltage setting of 18 kV ($A_{60}B_1C_aD_{18}$). The effects of the needle size on the nanofiber diameter and its variation of electrospun TiO_2/PVP were also investigated based on this optimal combination. It was determined that the needle size is a non-significant factor in the nanofiber diameter of electrospun TiO_2/PVP.

Acknowledgments

The authors wish to acknowledge Mrs. E. Miller for the technical assistance with SEM analysis. Moreover, H. Albetran is grateful to the College of Education - Dammam, University of Dammam, Saudi Arabia for the financial support in the form of a PhD Scholarship.

References

[1] P. Panda and S. Ramakrishna, J. Mater. Sci., 42, 2189–2193 (2007).

[2] J.Y. Park and S.S. Kim, Met. Mater. Int., 15, 95–99 (2009).
[3] C. Wang, Y. Tong, Z. Sun, Y. Xin, E. Yan and Z. Huang, Mater. Lett., 61, 5125–5128 (2007).
[4] W. Sigmund, J. Yuh, H. Park, V. Maneeratana, G. Pyrgiotakis, A. Daga, J. Taylor and J.C. Nino, J. Am. Ceram. Soc., 89, 395–407 (2006).
[5] Y. Dong, T. Mosaval, H.J. Haroosh, R. Umer, H. Takagi and K.T. Lau, J. Polym. Sci. Part B: Polym. Phys., 52, 618–623 (2014).
[6] H. Wu, W. Pan, D. Lin and H. Li, J. Adv. Ceram., 1, 2–23 (2012).
[7] T. Jamnongkan, R. Shirota, S.K. Sukumaran, M. Sugimoto and K. Koyama, SPE Plast. Res. Online, (2013), http://dx.doi.org/10.2417/spepro.005181
[8] J.Y. Park, J.J. Yun, C.H. Hwang and I.H. Lee, Mater. Lett., 64, 2692–2695 (2010).
[9] M. Samadi, H.A. Shivaee, M. Zanetti and A. Moshfegh, J. Mol. Catal. A: Chem., 359, 42–48 (2012).
[10] D.A. Hanaor and C.C. Sorrell, J. Mater. Sci., 46, 855–874 (2011).
[11] H. Li, W. Zhang, B. Li and W. Pan, J. Am. Ceram. Soc., 93, 2503–2506 (2010).
[12] Q. Li, D.J.G. Satur, H. Kim and H.G. Kim, Mater. Lett., 76, 169–172 (2012).
[13] C. Wessel, R. Ostermann, R. Dersch and B.M. Smarsly, J. Phys. Chem. C, 115, 362–372 (2011).
[14] H. Albetran, H. Haroosh, Y. Dong, V. Prida, B. O'Connor and I. Low, Appl. Phys. A, 116, 161–169 (2014).
[15] Z.M. Huang, Y.Z. Zhang, M. Kotaki and S. Ramakrishna, Compos. Sci. Technol., 63, 2223–2253 (2003).
[16] S.V. Fridrikh, J.H. Yu, M.P. Brenner and G.C. Rutledge, Phys. Rev. Lett., 90, 144502–144506 (2003).
[17] S. Patra, A. Easteal and D. Bhattacharyya, J. Mater. Sci., 44, 647–654 (2009).
[18] R. Inai, M. Kotaki and S. Ramakrishna, Nanotechnology, 16, 208–213 (2005).
[19] D. Li and Y. Xia, Nano Lett., 3, 555–560 (2003).
[20] A. Kumar, R. Jose, K. Fujihara, J. Wang and S. Ramakrishna, Chem. Mater., 19, 6536–6542 (2007).
[21] C.M. Wu, H.G. Chiou, S.L. Lin and J.M. Lin, J. Appl. Polym. Sci., 126, 89–97 (2012).
[22] B. Ksapabutr, T. Chalermkiti and M. Panapoy, Chiang Mai Univ. J., 4, 115–119 (2005).
[23] O. Hardick, B. Stevens and D.G. Bracewell, J. Mater. Sci., 46, 3890–3898 (2011).
[24] W.K. Son, D. Cho and W.H. Park, Nanotechnology, 17, 439–443 (2006).
[25] J.A. Park, J. Moon, S.J. Lee, S.H. Kim, T. Zyung and H.Y. Chu, Thin Solid Films, 518, 6642–6645 (2010).
[26] W. Nuansing, S. Ninmuang, W. Jarernboon, S. Maensiri and S. Seraphin, Mater. Sci. Eng. B, 131, 147–155 (2006).
[27] S. Chuangchote, J. Jitputti, T. Sagawa and S. Yoshikawa, ACS Appl. Mater. Interfaces, 1, 1140–1143 (2009).
[28] Y. Dong, T. Bickford, H.J. Haroosh, K.T. Lau and H. Takagi, Appl. Phys. A, 112, 747–757 (2013).
[29] J. Ghani, I. Choudhury and H. Hassan, J. Mater. Process. Technol., 145, 84–92 (2004).
[30] Y. Dong and D. Bhattacharyya, Composites Part A: Appl. Sci. Manuf., 39, 1177–1191 (2008).
[31] R. Ranjit, A Primer on the Taguchi Method, van Nostrand Reinhold, New York (1990).

3.6 A Comparative Study on Crystallization Behavior, Phase Stability, and Binding Energy in Pure and Cr-Doped TiO_2 Nanotubes

---

LOW, I. M., **ALBETRAN, H.,** PRIDA, V. M., VEGA, V., MANURUNG, P., & IONESCU, M. 2013. A Comparative Study on Crystallization Behavior, Phase Stability, and Binding Energy in Pure and Cr-Doped TiO_2 Nanotubes. *Journal of Materials Research*, 28, 304–312.

A comparative study on crystallization behavior, phase stability, and binding energy in pure and Cr-doped TiO_2 nanotubes

It Meng Low[a] and Hani Albetran
Department of Applied Physics, Centre for Materials Research, Curtin University, Perth, Western Australia 6845, Australia

Victor Manuel Prida and Victor Vega
Department of Physics, University of Oviedo, Calvo Sotelo s/n, 33007-Oviedo, Spain

Posman Manurung
Department of Physics, University of Lampung, Bandar Lampung 35145, Indonesia

Mihail Ionescu
Institute for Environmental Research, Australian Nuclear Science and Technology Organisation, Sydney, New South Wales 2234, Australia

(Received 7 May 2012; accepted 26 July 2012)

Use of nanostructured TiO_2 for photocatalysis is a cost-effective and sustainable technology. However, to make this an attractive viable technology will require the design of TiO_2 photocatalyst capable of harnessing the energy of visible light. One possible solution is the doping of TiO_2 to reduce its band gap. In this paper, the effect of Cr-doping by ion implantation on the in situ crystallization and phase stability of anodic TiO_2 nanotubes at elevated temperature is described. Cr-doping has dramatically reduced the fraction of anatase-to-rutile transformation and lowered the crystallization temperature of anatase from 600 to 400 °C and rutile from 600 to 500 °C. Ion beam analysis by Rutherford backscattering spectrometry has confirmed the existence of Cr ions composition gradation in doped TiO_2 nanotubes. The real doping of Ti lattices with Cr ions was evidenced by the analyses of surface compositions and chemical states of the nanotubes using x-ray photoelectron spectroscopy.

I. INTRODUCTION

Titanium dioxide (TiO_2) is a wide band gap semiconductor with energy of 3.0–3.2 eV. It is widely used in applications such as hydrogen production, gas sensors, photocatalytic activities, dye-sensitized solar cells, and photoelectrochemical cells because of its relative high efficiency and high stability.[1] However, due to its wide band gap energy, TiO_2 is active only under near-ultraviolet irradiation. Therefore, numerous studies have been carried out over the last 20 years to develop modified TiO_2 catalysts so that they are active under visible light irradiation (>400 nm). One of the most studied methods is by doping the TiO_2 materials with metal ions (Fe, Ni, Co, and Va)[2–5] or nonmetallic elements (N, S, and C).[6–15] For instance, N-doping of TiO_2 can result in visible light response by virtue of a narrowing in the band gap due to the mixing of *p* states of nitrogen with O 2*p* states. Among these doping methods, doping with transitional metals is one of the most efficient methods. Recent theoretical calculations showed that 3*d* transition metals such as Mn have good potential as a substitutional dopant for TiO_2 because of their ability to induce significant spin polarization and reduce the energy gap of rutile by forming intermediate bands with adequate curvatures and density of states.[16–18] Unlike defect states in the form of nearly straight horizontal lines within the energy gap, these curvy intermediate bands can act as stepping-stones to relay valence electrons to the conduction band.[16,17] As a result, the optical absorption edge of TiO_2 is shifted into the visible or even infrared spectral range of solar irradiance.[18]

Using a simple electrochemical anodization technique, highly ordered arrays of doped TiO_2 nanotubes with enhanced photocatalytic properties can be grown on a thin sheet of titanium.[19] X-ray photoelectron spectroscopy (XPS) results showed that the doped nanotube samples contained N, C, B, and F elements and the doped TiO_2 showed the shift in the band gap transition down to 2.98 eV. The photocatalytic activity of doped TiO_2 was 1.61 times better than undoped TiO_2.[15] Metals compounded on semiconductor materials increase charge collection efficiency due to a much slower electron–hole recombination, giving rise to longer electron lifetime, which will result in an increasing interfacial electron transfer process.[1,12]

Hitherto, the doping of TiO_2 has been widely synthesized using the sol–gel method.[20–24] However, ion implantation has now emerged as an alternative but effective doping method to improve the separation of the photogenerated

[a]Address all correspondence to this author.
e-mail: j.low@curtin.edu.au
DOI: 10.1557/jmr.2012.275

electron–hole pairs or to extend the wave length range of the TiO_2 photoresponses into the visible region.[25–30] XPS measurements revealed that the implanted nitrogen species were mainly interstitial ones. The nitrogen concentration was increased with increasing the flux of ions, which could be controlled by adjusting the gas flow rate of the ion source, resulting in improved visible light photocatalytic activities.[26] Higher visible light photocatalytic efficiency was achieved with higher implanted nitrogen concentration.[26,27]

In this paper, we present x-ray diffraction (XRD) results on the role of Cr-doping on the in situ crystallization behavior and phase stability of TiO_2 nanotubes in the temperature range 25–1000 °C. The effect of Cr-doping on the resultant microstructure, composition depth profile, and binding energy is discussed in terms of scanning electron microscopy (SEM), ion beam analysis by Rutherford backscattering spectrometry (RBS), and XPS.

II. EXPERIMENTAL METHODS

A. Sample preparation

Ti foils (99.6% purity) with dimensions of $10 \times 10 \times 0.1$ mm^3 were used for the anodizing to produce self-organized and well-aligned TiO_2 nanotube arrays. The process of potentiostatic anodization was performed in a standard two-electrode electrochemical cell, with Ti as the working electrode and platinum as the counter electrode. Before anodization, Ti foils were mechanically polished, degreased by sonicating in ethanol, isopropanol, and acetone for 5 min each, followed by rinsing with deionized water, and then drying using nitrogen stream. After drying, the foils were exposed to the electrolyte, which consists of 100 mL of ethylene glycol, 2.04 mL of water, and 0.34 g of NH_4F. The electrolyte's pH was kept constant at pH = 6 and its temperature was kept at about 25 °C. The anodization process was performed under an applied voltage of 60 V for 0.5 h.[31,32] After that, the resulting TiO_2 structures were then rinsed in ethanol, immersed in hexamethyldililazane, and dried in air.

B. Cr-doping by ion implantation

The as-anodized samples were doped with Cr ions by exposure to a flux of ions directed perpendicular to the sample surface. The Cr ions were produced using a direct extraction high flux ion source, with a charge distribution close to the theoretical prediction (9% Cr^{+1}, 75% Cr^{+2}, 13% Cr^{+3}, 3% Cr^{+4}), corresponding to an average charge of +2.1, giving an average implantation energy of 63 keV. With these implantation parameters, the depth of Cr peak in TiO_2 is close to the stopping and range of ions in matter (SRIM) prediction of 35 nm. The near-surface composition depth profiling of ion-implanted samples was measured by RBS using He^{1+} ions at 1.8 MeV and the implanted dose was $\sim 7 \times 10^{14}$ ions/cm^2. This phase of work was conducted at the Australian Nuclear Science and Technology Organisation.

C. In situ high-temperature x-ray and synchrotron radiation diffraction

The in situ crystallization behavior of as-anodized or undoped TiO_2 was characterized using high-temperature XRD up to 1000 °C in air using an Anton Paar HTK16 hot stage (Graz, Austria). The XRD patterns were acquired in steps of 100 °C from 400 to 1000 °C. The mean crystallite sizes (L) of anatase and rutile were calculated from (101) and (110) reflections, respectively, using the Scherrer equation[33]:

$$L = \frac{K\lambda}{\beta \cos\theta} \quad , \tag{1}$$

where K is the shape factor (0.94), λ is the x-ray wave length, β is the line broadening at half the maximum intensity [full width at half maximum (FWHM)] in radians, and θ is the Bragg angle. The relative abundance of anatase and rutile at each temperature was computed using the Rietveld method. The models of Djerdj and Tonejc[34] and Howard et al.[35] were used to calculate the phase abundance of anatase and rutile, respectively, using the Rietica 1.7.7 software.

The in situ crystallization behavior of Cr-doped TiO_2 was characterized using high-temperature synchrotron radiation diffraction (SRD) up to 900 °C in argon to avoid oxidation of the implanted Cr ions. The SRD measurements were conducted at the Australian Synchrotron using the Powder Diffraction beamline in conjunction with an Anton Paar HTK20 furnace and the Mythen II microstrip detector. The SRD patterns were acquired in steps of 100 °C from 100 to 900 °C at an incident angle of 3° and wave length of 0.11267 nm.

The collected XRD and SRD data were analyzed using the CMPR program/software to evaluate the integrated peak intensities of all phases present. The sum of all the integrated peak intensities in 2θ range of 10°–50° was used to calculate the relative phase content of all the phases present at each temperature as follows:

$$W_A = \left(\frac{I_A}{I_A + I_R + I_T}\right) \times 100 \quad , \tag{2}$$

where W_A is the wt% of anatase, I_A is sum integrated intensity of anatase, I_R is sum integrated intensity of rutile, and I_T is sum integrated intensity of titanium. A similar ratio method was used to calculate the wt% of rutile (W_R) or titanium (W_T). This method is expected to be more accurate than the method of Spurr and Myers[36] where only the peak intensities of anatase (101) and rutile (110) are used. The use of integrated peak intensities in Eq. (2) can minimize issues relating to preferred orientation, grain

size, and/or degree of crystallinity. The CMPR program was also used to determine the FWHM of anatase (101) and rutile (110) reflections, respectively, to calculate the crystallite size using Eq. (1).

D. Scanning electron microscopy

The morphologies of the anodized and ion-implanted samples were characterized using a focused ion beam SEM operating at working distances of 5 mm with an accelerating voltage of 5 kV. The samples were gold-coated before the microstructure examination, and the images were taken using both secondary and backscattered electrons. Energy dispersive x-ray spectroscopy (EDS) was also conducted to analyze the elemental compositions of the samples.

E. X-ray photoelectron spectroscopy

XPS with Al K_α x-ray ($h\nu$ = 1486.6 eV) radiation operated at 150 W was used to investigate the surface properties and to obtain the valence band spectra. The operating pressure of the spectrometer was typically 1×10^{-9} Torr. The x-ray spot diameter was ~500 μm. The spectra were recorded in the fixed analyzer transmission mode with pass energy of 150 eV for recording survey spectra.

III. RESULTS AND DISCUSSION

A. Crystallization behavior

Figure 1 shows the XRD plots of undoped TiO_2 before and after thermal annealing in air at different temperatures ranging between 20 and 1000 °C. The anodic TiO_2 nanotube arrays before thermal treatment were amorphous but eventually crystallized at 400 °C to form anatase, which started to decrease in abundance but persisted at up to 1000 °C. A small amount of rutile started to form at 600 °C and its abundance increased rapidly after 800 °C, which corresponds to the rapid decrease in anatase. Since anatase is well known to be metastable, it began to transform into rutile at about 600 °C. Figure 2 shows that

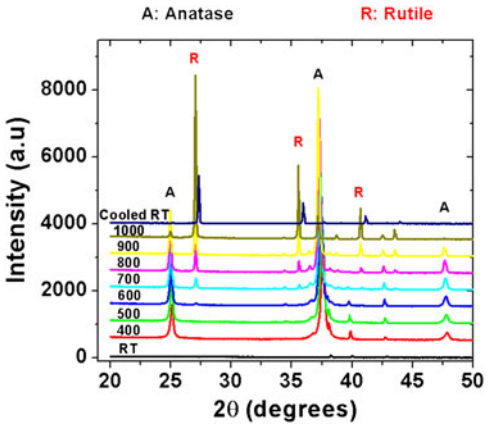

FIG. 1. High-temperature XRD plots for pure TiO_2 showing the in situ crystallization of anatase and rutile from the amorphous TiO_2 in the temperature range 20–1000 °C.

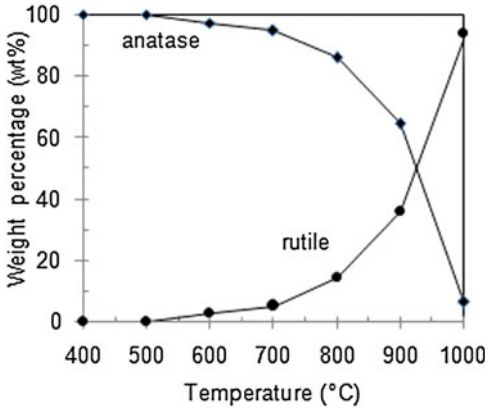

FIG. 2. Phase abundances of anatase and rutile for pure TiO_2 in the temperature range 20–1000 °C.

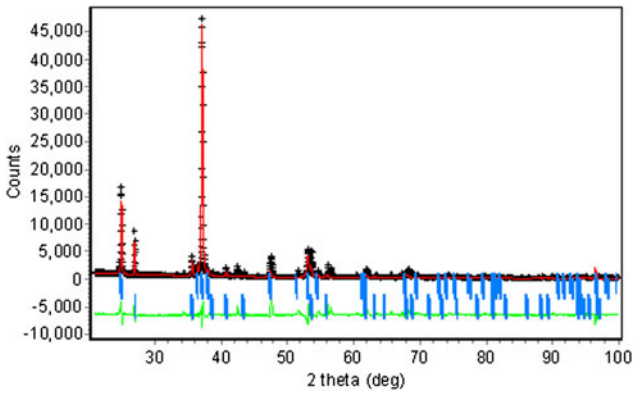

FIG. 3. XRD profile plot for pure TiO_2 nanotubes at 800 °C. Measured and calculated patterns are indicated by crosses (black) and solid line (red), respectively. Intensity differences between the two patterns are shown along the bottom of the plot (green). Vertical bars (blue) represent the allowable peak position for each of the phases (from top to bottom: anatase and rutile).

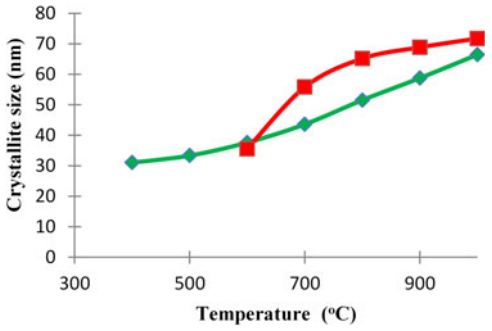

FIG. 4. Variations of crystallite size of anatase (♦) and rutile (■) as a function of temperature for pure TiO_2.

phase abundances of anatase and rutile as a function of temperature. A typical Rietveld profile fit for the XRD data at 800 °C is shown in Fig. 3. The good refinement quality of diffraction data can be discerned by the acceptable fitting parameters of $R_p = 17.4$; $R_{wp} = 26.0$; $R_{exp} = 3.5$; R_B (anatase) = 5; and R_B (rutile) = 10.

There was also a distinct narrowing and sharpening in the (101) peak for anatase and (110) peak for rutile. The corresponding increase in crystallite size calculated from the Scherrer equation is shown in Fig. 4. The crystallite size of anatase was about 30 nm at 400 °C and increased gradually with temperature to ~65 nm at 1000 °C. The crystallite size of rutile formed at 600 °C was about 35 nm, which grew rapidly and leveled off at 1000 °C with a size of 70 nm. It should be emphasized that the values of crystallite size reported here are only relative because the contribution of strains on peak broadening has been ignored in the calculation using the Scherrer equation.

The fraction of anatase-to-rutile transformation in the samples annealed at between 600 and 1000 °C can be calculated from the followed equation[36]:

TABLE I. Fractions of anatase-to-rutile transformation in pure and Cr-doped TiO_2 at various temperatures.

Temperature (°C)	x (%) TiO_2	x (%) Cr-doped TiO_2
500	...	0.6
600	4.4	3.6
700	16.4	4.6
800	30.3	5.6
900	59.6	...
1000	96.6	...

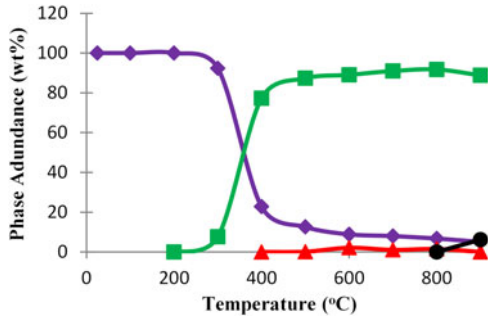

FIG. 6. Variations of phase abundances as a function of temperature for Cr-doped TiO_2 nanotubes. [Legend: titanium (♦); anatase (■); rutile (▲); TiO_{2-x} (●)].

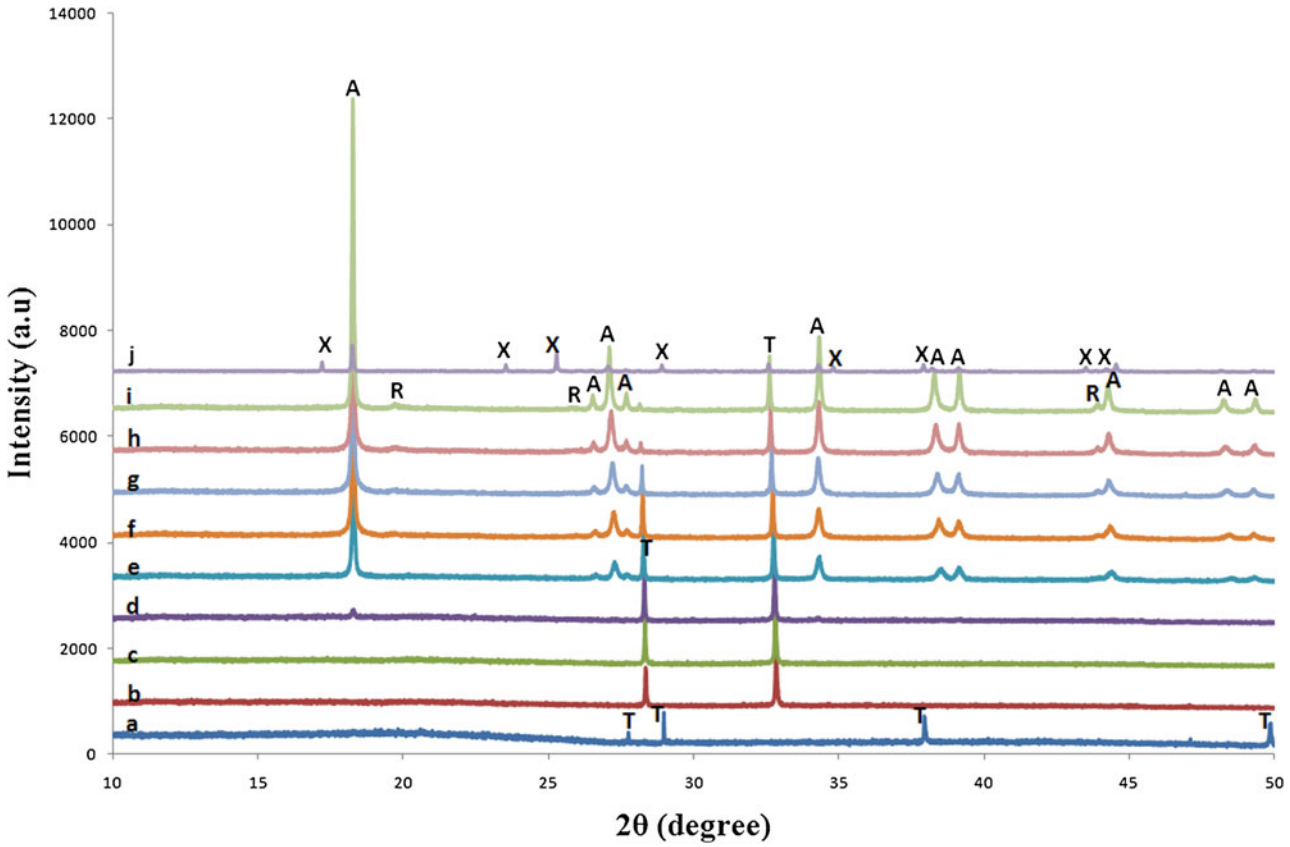

FIG. 5. In situ SRD plots of Cr-doped TiO_2 nanotubes showing the existence of anatase (A), rutile (R), Ti_5O_9 (X), and titanium (T) in the temperature range 20–900 °C. (Legend: a = 20 °C, b = 100 °C, c = 200 °C, d = 300 °C, e = 400 °C, f = 500 °C, g = 600 °C, h = 700 °C, i = 800 °C, j = 900 °C).

$$x = 1/[1 + 0.8(I_A/I_R)] \quad , \qquad (3)$$

where I_A is the x-ray integrated intensities of the (101) reflection of anatase at about 25.5°, while I_R is that of the (110) reflection of rutile at about 27.7°; x is the weight fraction of rutile in the nanotubes, which is calculated to be 4.4% for the nanotubes annealed at 600 °C, 16.4% at 700 °C, 30.3% at 800 °C, 59.6% at 900 °C, and 96.6% at 1000 °C (see Table I).

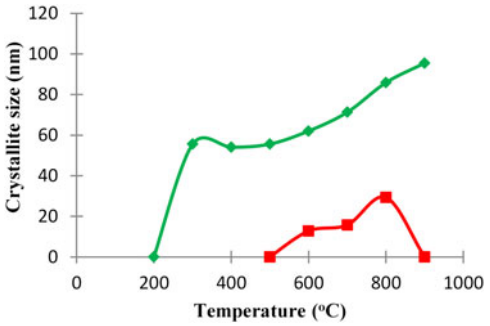

FIG. 7. Variations of crystallite size (L) of anatase (♦) and rutile (■) as a function of temperature for Cr-doped TiO_2 nanotubes.

Figure 5 shows the SRD plots of Cr-doped TiO_2 nanotubes before and after thermal annealing in argon at 20–900 °C. The TiO_2 nanotube arrays were initially amorphous but eventually crystallized to anatase at 300 °C. The peak intensities of anatase increased rapidly when the annealing temperature rises from 300 to 400 °C and continued to increase until 900 °C. The formation of rutile commenced at 500 °C but its growth was sluggish where the peak intensities increased very slightly from 500 to 800 °C. However, rutile disappeared at 900 °C with the concomitant appearance of TiO_{2-x} where $x = 0.2$ (see Fig. 6). This suggests that rutile was unstable in argon atmosphere at 900 °C and decomposed to form a non-stoichiometric titanium oxide and oxygen vacancies (O_v) as follows:

$$5TiO_2 \xrightarrow{900\,^{\circ}C/\text{argon}} Ti_5O_9 + O_v \quad . \qquad (4)$$

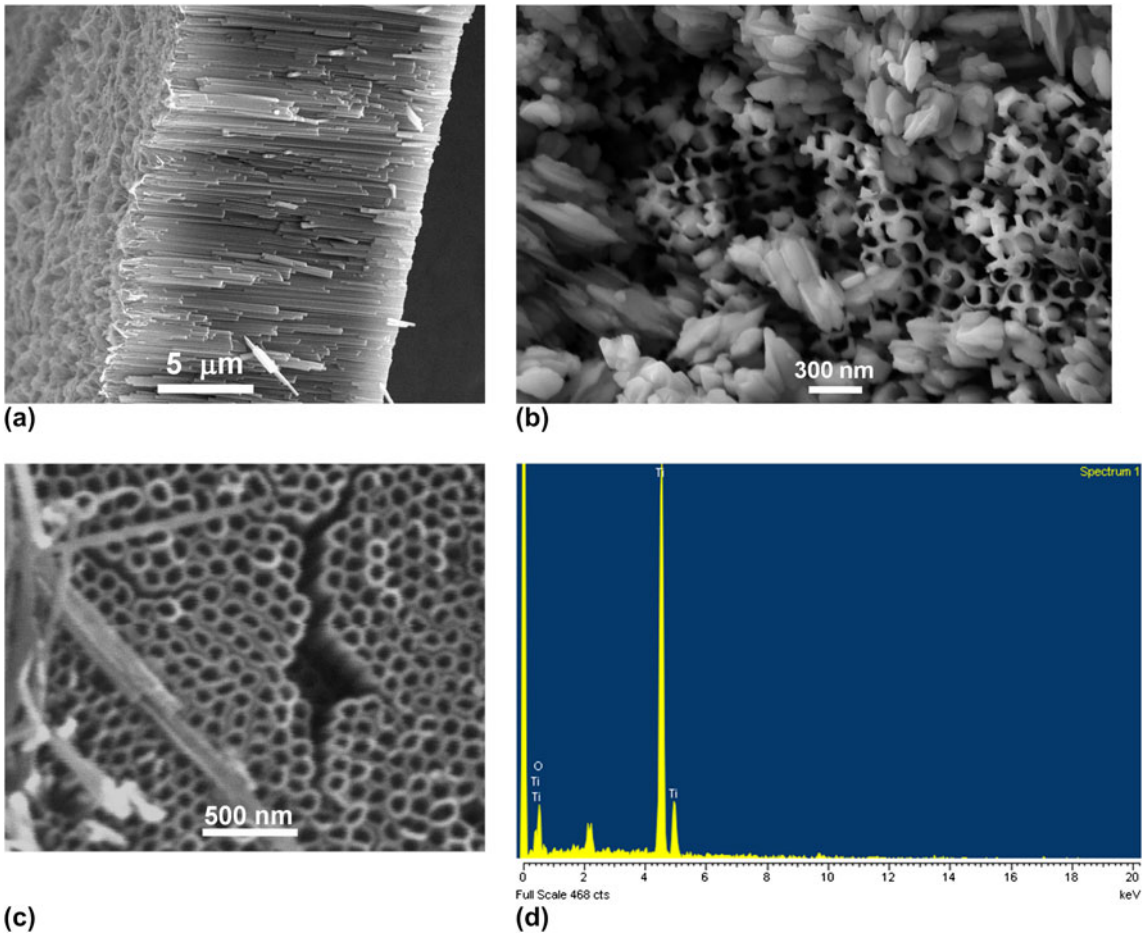

FIG. 8. Scanning electron micrographs showing the microstructure of pure TiO_2 nanotubes (a) at room temperature, (b) at 900 °C, (c) at 400 °C for 2 h, and (d) the corresponding EDS analysis of composition in Spectrum 1.

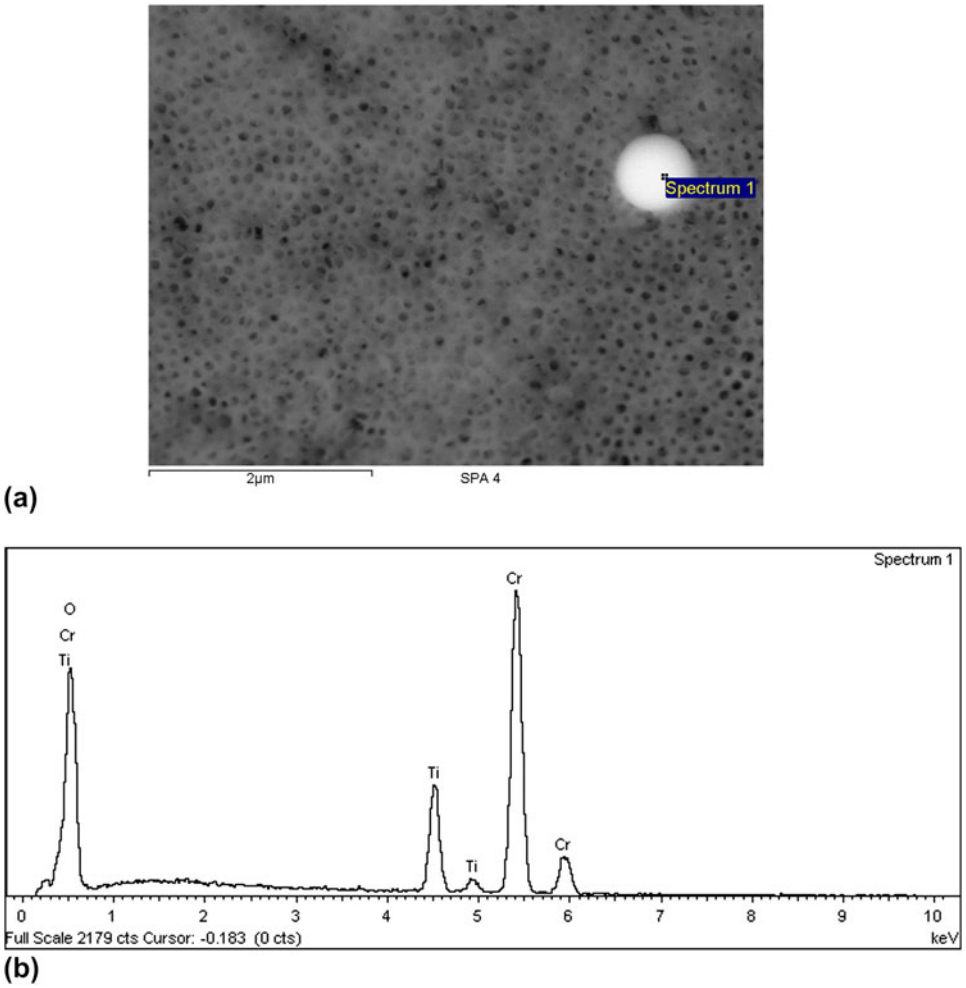

FIG. 9. Scanning electron micrographs showing the microstructure of (a) Cr-doped TiO_2, (b) EDS analysis of composition in Spectrum 1.

In contrast, no decomposition of rutile was observed in undoped TiO_2 nanotubes (see Fig. 1). When compared to Cr-doped TiO_2, both anatase and rutile in pure TiO_2 crystallized at a higher temperature, i.e., 400 and 600 °C, respectively. Using Eq. (3), the fraction of anatase-to-rutile transformation in Cr-doped TiO_2 at between 600 and 1000 °C was computed to be 0.6% at 500 °C, 3.6% at 600 °C, 4.6% at 700 °C, and 5.6% at 800 °C. As shown in Table I, these values are significantly when compared to pure TiO_2.

Figure 7 shows the influence of annealing temperature on crystallite size for anatase and rutile in Cr-doped TiO_2. The crystallite size of anatase was about 55 nm at 400 °C and increased gradually with temperature to 100 nm at 900 °C. In contrast, the crystallite size of rutile formed was much smaller than anatase and peaked at 700 °C with only 33 nm in size.

It appears that the presence of Cr-doping has accelerated the formation of anatase and rutile at a lower temperature, probably through the facilitation of defects such as vacancies. It is widely accepted that the onset temperature of the anatase to rutile phase transformation and the rate at which it proceeds can be affected significantly by dopants, firing atmosphere, microstructure, sample morphology, and the presence of impurities in the material.[1] The process of the anatase-to-rutile transformation is known to occur via (i) the nucleation of rutile at point defects, oxygen vacancies, secondary phase inclusions, particle surfaces, and/or at (112) twin interfaces in anatase and (ii) the subsequent consumption of the anatase phase by the growing rutile phase. The formation of rutile from the metastable phase anatase is reconstructive and so takes place through atomic rearrangement involving the breaking of two of the six Ti–O bonds in the TiO_6 octahedra.[37] As anatase transforms into rutile, significant grain growth takes place, resulting in lower surface area and thus poorer photocatalytic performance.

Transition metals (e.g., Cr) of variable valence are reported to enter the titania lattice and create oxygen vacancies through reduction effects as follows[1,38]:

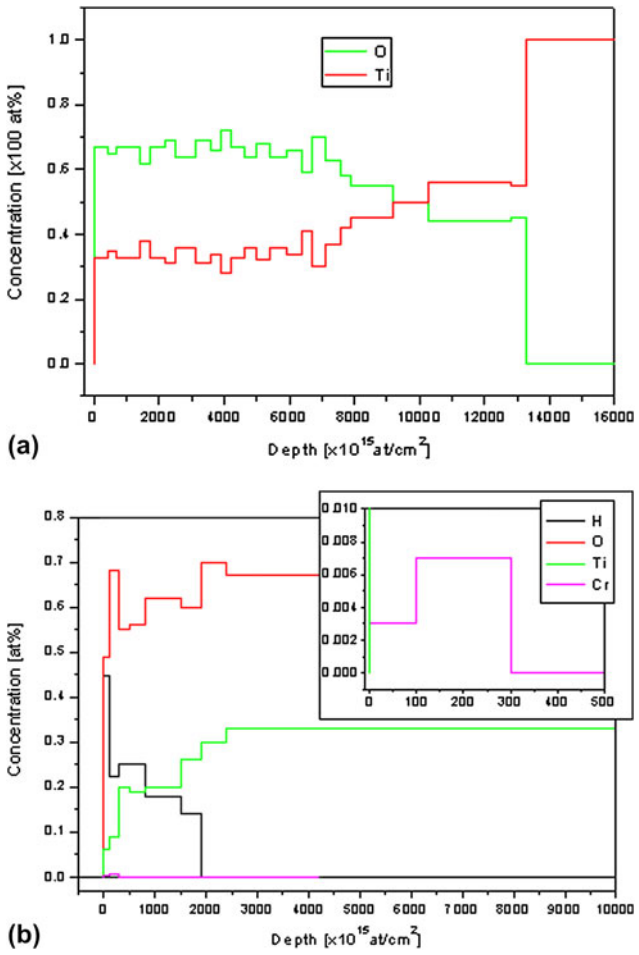

FIG. 10. Composition depth profiles in (a) pure TiO_2 and (b) Cr-doped TiO_2 nanotubes. Inset shows the close-up view of Cr concentration.

$$2M^{n+} + O^{2-} \rightarrow 2M^{(n-1)+} + \frac{1}{2}O_2 + O_v \quad , \qquad (5)$$

where M denotes a transition metal atom and O_v denotes an oxygen vacancy. Once substituted for Ti^{4+}, the reduction of such species gives rise to new oxygen vacancies and so enhances rutile formation from metastable anatase through easing of structural rearrangement. These oxygen vacancies are believed to be responsible for crystallization of anatase at a lower temperature in Cr-doped TiO_2 as well as destabilization and subsequent decomposition of rutile to form nonstoichiometric TiO_{2-x}.

B. Microstructures and formation mechanisms of nanostructured TiO_2

After anodizing in the electrolyte of NH_4F/H_2O/Ethylene glycol at 25 °C for 20 h, a homogeneous layer of TiO_2 nanotubes formed on the Ti foil. Figure 8(a) shows the SEM image of the microstructure of amorphous TiO_2 nanotubes in the as-anodized sample. Upon annealing at

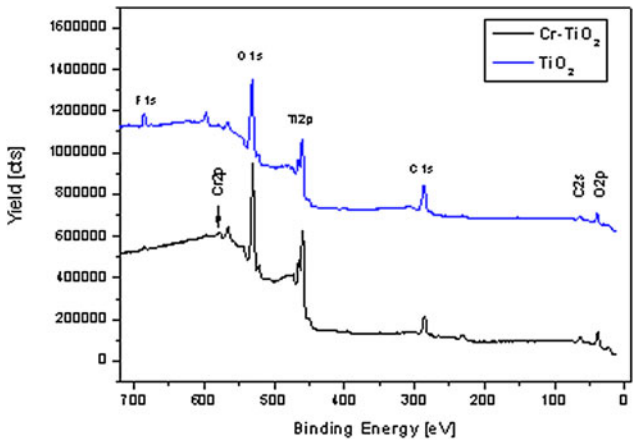

FIG. 11. XPS plots showing the chemical states and binding energies for pure and Cr-doped TiO_2 nanotubes.

400 °C for 2 h, vertically oriented and highly ordered arrays of anatase nanotubes with diameter of ~80 nm formed [Fig. 8(b)], which concur well with previous studies on anodized TiO_2.[39,40] The EDS analysis of nanotubes in Spectrum 1 of Fig. 8(c) indicated 31.04% Ti and 68.96% O, thus confirming the presence of TiO_2 in the sample. Upon annealing at 900 °C for 1 h, some anatase transformed into rutile that appeared as elongated grains randomly distributed among the nanotubes, as shown in Fig. 8(d).

The microstructure of Cr-doped TiO_2 is shown in Fig. 9(a) where the morphology of nanotubes has been retained during the process of ion implantation. The existence of implanted Cr ions has been verified by the EDS analysis of a bright region in Spectrum 1 as shown in Fig. 9(b).

C. Composition depth profiles and binding energies

The RBS results in Fig. 10 show the concentration of elements (at.%) versus depth (at./cm^2) for both the undoped and Cr-doped samples. The depth profile of Ti and O for undoped TiO_2 is shown in Fig. 10(a) where the composition at near-surface layer is fairly constant but a composition gradation in both O and Ti exists at the interface between the substrate and the oxide layer. In the Cr-doped sample [Fig. 10(b)], it is shown that a maximum Cr concentration of 0.7 at.% has been implanted in TiO_2 down to a depth of about 300 monolayers. A composition gradation also appears to exist at the interface between the substrate and the oxide layer.

The XPS plots in Fig. 11 show the binding energies of elements present in both undoped and Cr-doped TiO_2 nanotubes. The presence of Cr in the doped sample is evident by the display of Cr 2*p* peak. When compared to Cr-doped TiO_2, significantly, more fluorine is present in pure TiO_2. The cause of this diminished fluorine in Cr-doped TiO_2 is uncertain, although it is quite possible

that the process of ion implantation may have caused some fluorine to escape. Also noticeable is the slight peak shifts of Ti 2*p* and O 1*s* to the lower binding energy for Cr-doped TiO_2. Such peak shifts have also been observed for Cu-doped TiO_2.[41] This suggests that the Ti 2*p* binding energy in Cr-doped TiO_2 nanotubes increased when compared to that of pure TiO_2. The peak shift also illustrates the incorporation of Cr ions into the TiO_2 lattices. These results suggest that the Cr^{3+} ions are doped in the TiO_2 lattice forming a substitutional solid solution. When TiO_2 is doped with Cr^{3+} ions, the binding energy change in each atom occurs due to the electron transfer from Ti^{4+} to Cr^{3+}. In essence, the Fermi level of Cr_2O_3 is lower than that of TiO_2, thus resulting in the outer electron cloud density of Ti to decrease and that of Cr to increase.

IV. CONCLUSIONS

High-temperature SRD has been used to study the effect of Cr-doping on in situ crystallization of anatase and rutile in as-anodized TiO_2 nanotubes. The TiO_2 was initially amorphous but crystallized to anatase and rutile at elevated temperature. Cr-doping has lowered the crystallization temperature of anatase from 600 to 400 °C and rutile from 600 to 500 °C. In addition, it has reduced dramatically the fraction of anatase-to-rutile transformation. The rutile formed in TiO_2 was very stable after annealing at 1000 °C but became unstable in Cr-doped TiO_2, which decomposed to form TiO_{2-x} at 900 °C. Ion beam analysis by RBS has confirmed the existence of Cr ions composition gradation in doped TiO_2. The real doping of Ti lattices with Cr ions was evidenced by the analyses of surface compositions and chemical states of the nanotubes using XPS.

ACKNOWLEDGMENTS

This work was supported by funding from the Australian Synchrotron (PD-3611), the Australian Institute of Nuclear Science and Engineering (AINGRA-11134), and Spanish MAT2010-20798-C05-04. We thank Ms. E. Miller of Curtin Centre for Materials Research for assistance with the SEM work. The scientific support from the University of Oviedo SCTs, particularly to the Nanoporous Membranes Unit and Photo-electronic Spectroscopy Laboratories is also acknowledged.

REFERENCES

1. D. Hanaor and C. Sorrell: Review of the anatase to rutile phase transformation. *J. Mater. Sci.* **46**, 855–874 (2011).
2. M. Anpo, Y. Ichihashi, M. Takeuchi, and H. Yamashita: Design of unique titanium oxide photocatalysts by an advanced metal ion-implantation method and photocatalytic reactions under visible light irradiation. *Res. Chem. Intermed.* **24**, 143 (1998).
3. A. Zaleska, J.W. Sobczak, E. Grabowska, and J. Hupka: Preparation and photocatalytic activity of boron-modified TiO_2 under UV and visible light. *Appl. Catal., B* **78**, 92 (2008).
4. G.B. Saupe, T.U. Zhao, J. Bang, N.R. Desu, G.A. Carballo, R. Ordonem, and T. Bubphamala: Evaluation of a new porous titanium-niobium mixed oxide for photocatalytic water decontamination. *Microchem. J.* **81**, 156 (2005).
5. D.B. Hamal and K.J. Klabunde: Synthesis, characterization, and visible light activity of new nanoparticle photocatalysts based on silver, carbon, and sulfur-doped TiO_2. *J. Colloid Interface Sci.* **311**, 514 (2007).
6. J. Virkutyte, B. Baruwati, and R.S. Varma: Visible light induced photobleaching of methylene blue over melamine-doped TiO_2 nanocatalyst. *Nanoscale* **2**, 1109 (2010).
7. T. Umebayashi, T. Yamaki, and S. Tanaka: Visible light-induced degradation of methylene blue on S-doped TiO_2. *Chem. Lett.* **32**, 330 (2003).
8. S. Sakthivel, M. Janczarek, and H. Kisck: Visible light activity and photo-electrochemical properties of nitrogen-doped TiO_2. *J. Phys. Chem. B* **108**, 19384 (2004).
9. Y. Choi, T. Umebayashi, and M. Yoshikawa: Fabrication and characterization of C-doped anatase TiO_2 photocatalysts. *J. Mater. Sci.* **39**, 1837 (2004).
10. H. Irie, Y. Watanabe, and K. Hashimoto: Carbon-doped anatase TiO_2 powders as a visible-light sensitive photocatalyst. *Chem. Lett.* **32**, 772 (2003).
11. S. Sakthivel and H. Kisch: Daylight photocatalysts by carbon-modified titanium dioxide. *Angew. Chem. Int. Ed.* **42**, 4908 (2003).
12. R. Asahi, T. Morikawa, and T. Ohwaki: Visible-light photocatalysis in nitrogen-doped titanium oxides. *Science* **293**, 269 (2001).
13. W. Ren, Z. Ai, F. Jia, L. Zhang, X. Fan, and Z. Zou: Low temperature preparation and visible light photocatalytic activity of mesoporous carbon-doped crystalline TiO_2. *Appl. Catal., B* **69**, 138 (2007).
14. T. Ohno, M. Akiyoshi, T. Umebayashi, K. Asai, T. Mitsui, and M. Matsumura: Preparation of S-doped TiO_2 photocatalysts and their photocatalytic activities under visible light. *Appl. Catal., A* **265**, 115 (2004).
15. B.C. Bai, J.S. Im, J.G. Kim, and Y.S. Lee: Photo-catalytic degradation on B, C, N, and F element co-doped TiO_2 under visible-light irradiation. *J. Korean Ind. Eng. Chem.* **21**, 29–33 (2010).
16. G. Shao: Red shift in manganese- and iron-doped TiO_2: A DFT+U analysis. *J. Phys. Chem. C* **113**, 6800 (2009).
17. G. Shao: Electronic structures of manganese-doped rutile TiO_2 from first principles. *J. Phys. Chem. C* **112**, 18677 (2008).
18. X.H. Xia, L. Lu, A.S. Walton, M. Ward, X.P. Han, R. Brydson, J.K. Luo, and G. Shao: Origin of significant visible-light absorption properties of Mn-doped TiO_2 thin films. *Acta Mater.* **60**, 1974–1985 (2012).
19. P. Roy, S. Berger, and P. Schmuki: TiO_2 nanotubes: Synthesis and applications. *Angew. Chem. Int. Ed.* **50**, 2904–2939 (2011).
20. Y. Kuroda, T. Mori, K. Yagi, N. Makihata, Y. Kawahara, M. Nagao, and S. Kittaka: Preparation of visible-light-responsive $TiO_{2-x}N_x$ photocatalyst by a sol-gel method: Analysis of the active center on TiO_2 that reacts with NH_3. *Langmuir* **21**, 8026 (2005).
21. A. Hattori, M. Yamamoto, H. Tada, and S. Ito: A promoting effect of NH_4F addition on the photocatalytic activity of sol-gel TiO_2 films. *Chem. Lett.* **27**, 707 (1998).
22. Y. Shen, T. Xiong, T. Li, and K. Yang: Tungsten and nitrogen co-doped TiO_2 nano-powders with strong visible light response. *Appl. Catal., B* **83**, 177 (2008).
23. T.C. Jagadale, S.P. Takale, R.S. Sonawane, H.M. Joshi, S.I. Patil, B.B. Kale, and S.B. Ogale: N-doped TiO_2 nanoparticle based visible light photocatalyst by modified peroxide sol-gel method. *J. Phys. Chem. C* **112**, 14595 (2008).

24. Y. Tseng, C. Kuo, C. Huang, Y. Li, P. Chou, C. Cheng, and M. Wong: Visible-light-responsive nano-TiO_2 with mixed crystal lattice and its photocatalytic activity. *Nanotechnology* **17**, 2490 (2006).
25. T. Yamaki, T. Sumita, and S. Yamamoto: Formation of $TiO_{2-x}F_x$ compounds in fluorine-implanted TiO_2. *J. Mater. Sci. Lett.* **21**, 33 (2002).
26. H. Shen, L. Mi, P. Xu, W. Shen, and P.N. Wang: Visible-light photocatalysis of nitrogen-doped TiO_2 nanoparticulate films prepared by low-energy ion implantation. *Appl. Surf. Sci.* **253**, 7024 (2007).
27. J. Park, J.Y. Lee, and J.H. Cho: Ultraviolet-visible absorption spectra of N-doped TiO_2 film deposited on sapphire. *J. Appl. Phys.* **100**, 113534 (2006).
28. H. Yamashita, Y. Ichihashi, and M. Takeuchi: Characterization of metal ion-implanted titanium oxide photocatalysts operating under visible light irradiation. *J. Synchrotron Radiat.* **6**, 451 (1999).
29. T. Yamaki, T. Umebayashi, and T. Sumita: Fluorine-doping in titanium dioxide by ion implantation technique. *Nucl. Instrum. Methods Phys. Res., Sect. B* **206**, 254 (2003).
30. H. Yamashita, M. Harada, J. Misaka, M. Takeushi, and M. Anpo: Degradation of propanol diluted in water under visible light irradiation using metal ion-implanted titanium dioxide photocatalysts. *J. Photochem. Photobiol., A* **148**, 257 (2002).
31. V. Vega, V.M. Prida, M. Hernández-Vélez, E. Manova, P. Aranda, E. Ruiz-Hitzky, and M. Vázquez: Influence of anodic conditions on self-ordered growth of highly aligned titanium oxide nanopores. *Nanoscale Res. Lett.* **2**, 355 (2007).
32. V. Vega, M.A. Cerdeira, V.M. Prida, D. Alberts, N. Bordel, R. Pereiro, F. Mera, S. García, M. Hernández-Vélez, and M. Vázquez: Electrolyte influence on the anodic synthesis of TiO_2 nanotube arrays. *J. Non-Cryst. Solids* **354** 5233–5235 (2008).
33. B.D. Cullity and S.R. Stock: *Elements of X-Ray Diffraction*, 3rd ed. (Prentice-Hall Inc., Englewood Cliffs, NJ, 2001); pp. 167–171.
34. I. Djerdj and A.M. Tonejc: Structural investigations of nanocrystalline TiO_2 samples. *J. Alloys Compd.* **413**, 159–174 (2006).
35. C.J. Howard, T.M. Sabine, and F. Dickson: Structural and thermal parameters for rutile and anatase. *Acta Crystallogr., Sect. B: Struct. Sci* **47**, 462–468 (1991).
36. R.A. Spurr and H. Myers: Quantitative analysis of anatase-rutile mixtures with an x-ray diffractometer. *Anal. Chem.* **29**, 760 (1957).
37. S. Riyas, G. Krishnan, and P.N. Mohandas: Anatase-rutile transformation in doped titania under argon and hydrogen atmospheres. *Adv. Appl. Ceram.* **106**, 255 (2007).
38. K.J.D. Mackenzie: Calcination of titania V. Kinetics and mechanism of the anatase-rutile transformation in the presence of additives. *Trans. J. Br. Ceram. Soc.* **74**, 77 (1975).
39. V.M. Prida, M. Hernandez-Velez, K.R Pirota, A. Menendez, and M. Vazquez: Synthesis and magnetic properties of Ni nanocylinders in self-aligned and randomly disordered grown titania nanotubes. *Nanotechnology* **16**, 2696–2702 (2005).
40. O.K. Varghese, D. Gong, M. Paulose, C.A. Grimes, and E.C. Dickeya: Crystallization and high-temperature structural stability of TiO_2 nanotube arrays. *J. Mater. Res.* **18**, 156–165 (2003).
41. M. You, T.G. Kim, and Y.M. Sung: Synthesis of Cu-doped TiO_2 nanorods with various aspect ratios and dopant concentrations. *Cryst. Growth Des.* **10**, 983–987 (2010).

3.7 Effect of Indium Ion Implantation on Crystallization Kinetics and Phase Transformation of Anodized Titania Nanotubes

---

ALBETRAN, H., LOW, I. M. 2016. Effect of Indium Ion Implantation on Crystallization Kinetics and Phase Transformation of Anodized Titania Nanotubes. *Journal of Materials Research*, 31, 1588–1595.

Effect of indium ion implantation on crystallization kinetics and phase transformation of anodized titania nanotubes using *in-situ* high-temperature radiation diffraction

Hani Albetran
Department of Physics and Astronomy, Curtin University, Perth, Western Australia 6845, Australia; and Department of Basic Sciences, College of Education, University of Dammam, Dammam 31451, Saudi Arabia
It Meng Low[a)]
Department of Physics and Astronomy, Curtin University, Perth, Western Australia 6845, Australia

(Received 29 October 2015; accepted 12 February 2016)

Titania nanotube arrays were synthesized electrochemically by anodization of titanium foils, and the synthesized titania nanotubes were then implanted with indium ions. The effect of In-ions implantation on crystallization and phase transformation of titania was investigated using *in-situ* high-temperature X-ray diffraction and synchrotron radiation diffraction from room temperature to 1000 °C. Diffraction results show that crystalline anatase first appeared at 400 °C in both the non-implanted and the In-implanted materials. The temperature at which crystalline rutile temperature appeared was 600 °C for non-implanted materials and 700 °C for In-implanted materials, and the indium implantation inhibited the anatase-to-rutile transformation. Although In^{3+} is expected to increase oxygen vacancy concentration and then the rate of titania transformation, the observations are consistent with implanted In-ions occupying the Ti sublattice substitutionally and then inhibiting the transformation. The relatively difficult anatase-to-rutile transformation in the In-implanted material appears to result from the relatively large In^{3+} radius (0.080 nm). The In^{3+} partly replaces the Ti^{4+} (0.061 nm), which provides a greater structural rigidity and prevents relaxation in the Ti bonding environment.

I. INTRODUCTION

Titania is known to be a very useful nontoxic, environmentally friendly photocatalyst.[1–4] It is a stable, photodurable, inexpensive, and natural aid in the efficient realization of many applications, such as bio-application, dye-sensitized solar cells, photoelectrochemical cells, gas sensors, and hydrogen production.[5–9] Titania has three crystal structures: anatase, rutile, and brookite.[10–12] In titania phase systems transformation, amorphous titania crystallizes into the most common titania phases, namely anatase, rutile, or a mixture of them, by way of thermal treatment.[13,14] The amorphous-to-anatase and subsequent anatase-to-rutile phase transformation behaviors depend on the impurities, morphology, preparation method, dopants, heating rate, calcining temperature, calcining time, and atmospheres.[15–19]

One-dimensional (1-D) titania nanostructures, for example, nanowires, nanorods, nanobelts, nanofibers, and nanotubes provide unique electronic characteristics, such as a high surface area-to-volume ratio, high electron mobility, or quantum confinement effects, and high mechanical strength.[1,3,7,8] These characteristics increase the decomposition rate of organic pollutants significantly because photocatalytic reactions occur rapidly and intensely on the catalyst surface.[20,21] Various techniques have been used to synthesize 1-D nanostructured titania, including sol–gel,[22] microwaves,[23] electrochemical anodization,[6,24–27] hydrothermal methods,[4,28–30] and electrospinning.[31] Thus, there is a great deal of interest in synthesizing 1-D titania nanostructures using inexpensive and simple methods.

Among fabrication methods, anodization is currently one of the most commonly used method for the fabrication of 1-D titania nanostructures,[1,6,31] and the general nanostructure obtained through this process is nanotubes.[17,22] Nanotubes are 1-D nanometer scale tubes like nanowires, nanorods, and nanofiber structures. In the case of nanotubes, there is a hollow center as compared to the other 1-D structures. The anodized titania nanotube arrays are synthesized by electrochemical anodization of titanium-based alloy in an electrolyte with Pt grid used as an anode for a short period at room temperature (RT).[6,24–27]

In this paper, titania nanotube arrays were synthesized electrochemically by anodization of titanium foils, and the synthesized titania nanotubes were then implanted with indium ions. The effect of In-ions implantation on

Contributing Editor: Heli Wang
[a)]Address all correspondence to this author.
e-mail: j.low@curtin.edu.au
DOI: 10.1557/jmr.2016.83

the crystallization kinetics and phase transformations of anodized titania nanotubes were investigated using *in-situ* high-temperature x-ray diffraction (XRD) and synchrotron radiation diffraction (SRD) from RT to 1000 °C, and then were characterized by field emission scanning electron microscopy (FESEM), and associated energy dispersive X-ray spectroscopy (EDS).

II. EXPERIMENTAL METHODS

A. Sample preparation

Titanium foils (99.6% purity) with dimensions of 10 × 10 × 0.1 mm^3 were anodized to synthesize the titania nanotube arrays. The titanium foils were cleaned ultrasonically in a mixed solution of ethanol, isopropanol, and acetone for five minutes, followed by rinsing with deionized water, and were then dried using nitrogen stream. In the electrochemical anodization cell, the Ti foil acted as a cathode. Platinum was used as an anode in an electrolyte of 2.04 mL water, 100 mL ethylene glycol, and 0.34 g ammonium fluoride (NH_4F). The anodization experiment was performed in a sealed environmental chamber at a constant temperature of 25 °C, and at a pH of 6. The voltage was controlled to 60 V for 20 h using a voltage power supply between the Ti foil and the platinum located several centimeters apart. The as-anodized titania arrays were rinsed/washed after being anodized with ethanol, immersed in dimethyl sulfoxide, and dried in air.

B. Field emission scanning electron microscopy

The surface morphologies of the anodized titania nanotubes before and following the *in-situ* high-temperature measurement were investigated using field emission scanning electron microscope (FESEM; Zeiss, Neon, 40EsB, Oberkochen, Germany). Prior to the microstructure observations, the samples were sputter-coated with a 3 nm layer of platinum to avoid charging, and then the FESEM images were taken using secondary electron with an accelerating voltage of 5 kV. EDS was used to analyze the elemental compositions of the SEM-image materials.

C. In ion implantation

Details of ion implantation are given in the preliminary studies by the authors with Cr-ions implanted titania nanotube arrays and V-ions implanted titania nanofibers.[32,33] In summary, the as-anodized samples were implanted with In ions using the MEVVA ion implanter (Lawrence Berkeley Laboratory, Berkeley, California) at the Australian Nuclear Science and Technology Organization (ANSTO). The titania nanotubes were implanted by exposing a flux of indium ions perpendicular to the sample surface. The average implantation energy of indium ions was 25 keV, and the peak penetration depth of indium in the titania nanotubes was close to the 70 nm stopping and range of ions in matter prediction based on the implantation parameters. The near-surface composition depth profiling of In ion-implanted titania nanotubes was measured by Rutherford backscattering spectrometry using He^{+1} ions at 2 MeV, and the implanted dose was $\sim 4 \times 10^{15}$ ions/cm^2.

D. *In-situ* high-temperature XRD and SRD

In-situ crystallization behavior of as-anodized titania nanotubes was evaluated in an air atmosphere using XRD at temperature ranging from RT to 1000 °C using an Anton Parr HTK16 hot stage (Graz, Austria). The sample was mounted and heated at a rate of 10 °C/min, from ambient temperature to 1000 °C [See Fig. 1(a)]. The XRD patterns were collected at ambient temperature and then in steps of 100 °C from 400 to 1000 °C using Cu K_α radiation with a wavelength of 0.15419 nm, settings at 40 kV, 30 mA, and each pattern was measured over the angular range of $2\theta = 20°–125°$.

For the In-ions implanted titania nanotubes, the measurements of *in-situ* high-temperature SRD were conducted at the powder diffraction beamline at the Australian Synchrotron, Melbourne, Australia. The specimens were mounted and heated using an Anton Parr HTK16 hot platinum stage in conjunction with a Mythen II microstrip detector. The SRD patterns were acquired at ambient temperature and then in steps of 100 °C from 100 °C to 900 °C in air according to the heating protocol shown in Fig. 1(b). The SRD data were collected at an incident angle of 3° and a wave length of 0.1126 nm. The wavelength was determined accurately from a NIST 660a pattern with zero error from 0.007368283 to 0.0001243282° and sample displacement from 0.002781912 to 0.0008831296 mm. Each pattern was measured over the angular range of $2\theta = 5°–84°$.

E. Quantitative analysis

The XRD and SRD patterns were analyzed using Rietveld pattern-fitting with TOPAS (Bruker AXS, version 4.2) software, with the goodness-of-fit (GOF) being gauged from the values of the expected *R*-factor (R_{exp}), the weighted pattern *R*-factor (R_{wp}), and the derived Bragg *R*-factors (R_P). The Rietveld method is expected to be more accurate than the Spurr and Myers method, which uses only the anatase (101) and rutile (110) peak intensities.[13] The use of the Rietveld method minimizes issues relating to preferred orientation, grain size, and/or degree of crystallinity. To compute the relative crystalline phase abundances, and the lattice parameters of titanium, anatase, and rutile as a function of temperature, the parameters optimized in the Rietveld refinements were the pattern background, $2\theta_0$, sample displacement and, for each phase, the scale factor, lattice parameters,

preferred orientation, and peak shape parameters. Rietveld refinements were conducted with the crystal structures of titanium$_\alpha$ (ICSD 44872), anatase (ICSD 202242), and rutile (ICSD 64987). These phases were identified using the DIFFRAC. EVA software (released 2012, version 3.1) to search the International Center for Diffraction Data powder diffraction file database (PDF-4+2013 software version: 4.13.0.6, Database version: 4.1302).

III. RESULTS AND DISCUSSION

A. Microstructural imaging

A homogeneous white layer formed on the Ti foil after the anodizing process in the ethylene glycol/NH_4F electrolyte at 25 °C for 20 h (optical image not shown). Figure 2(a) shows a typical secondary electron FESEM image of as-anodized titania nanotubes, which were amorphous. The as-anodized nanotube arrays were more uniform and highly ordered than the titanium foil. The corresponding mean inner diameter and standard deviation for 100 nanotubes was 26 ± 4 nm.

After the *in-situ* high-temperature XRD at 1000 °C for as-anodized titania nanotube arrays, and for SRD at 900 °C for In-ions implanted titania nanotube arrays, the morphologies were re-examined at RT using the same FESEM conditions. Figures 2(b) and 2(c) illustrate the FESEM images of non-implanted and In-ions implanted materials, respectively. For the non-implanted sample, the nanotube array structures were destroyed and covered with rutile elongated grains. However, for In-ions implanted titania nanotubes, some grains were randomly

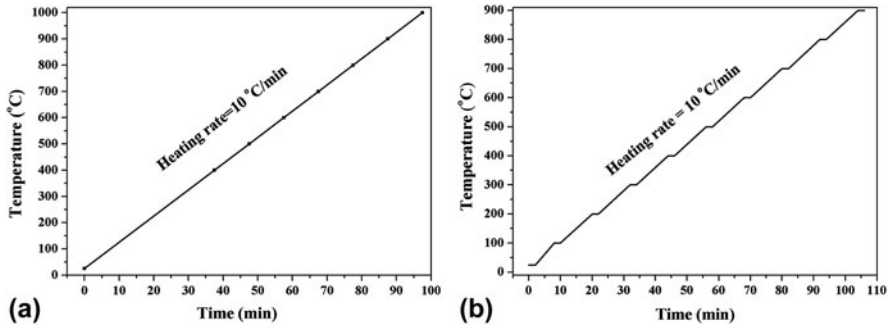

FIG. 1. Non-isothermal *in-situ* (a) XRD and (b) SRD heating protocol. Plateaus indicate the 2 min during which SRD data were acquired.

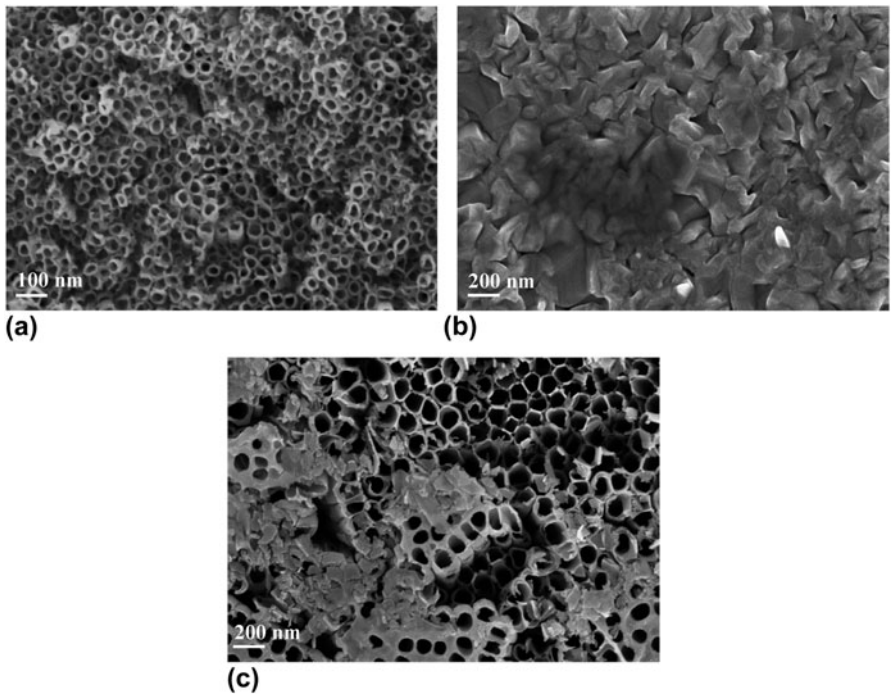

FIG. 2. FESEM micrographs of (a) as-anodized titania nanotube arrays prior to heating; (b) after thermal treatment for the XRD experiment at 1000 °C and cooling to RT; and (c) after In-ions implantation and thermal treatment for SRD experiments at 900 °C and cooling to RT.

distributed among the titania nanotubes, which indicates that implantation had inhibited or slowed the grain growth of titania nanotube arrays. These grains are crystalline rutile because metastable anatase transformed into stable crystalline rutile at elevated temperatures (see Sec. III. B).

Figure 3(a) shows the EDS spectrum for the as-anodized titania nanotube arrays in Spectrum 1, showing that strong signatures for Ti, O, and Pt, with the Pt content begin due to the platinum coating. Assuming that the Pt peak from the platinum coating is negligible, the quantitative EDS analysis indicated 66.18% O K_α and 33.82% Ti K_α, thus confirming the presence of titania. It should be noted that quantitative EDS is performed for flat samples, which is approximated for the nanotubes. The EDS for the nanotubes was collected from a small square to minimize the nonflat sample issue, using EDS software (AZtec Software, Oxford). The qualitative EDS spectrum for non-implanted and In-ions implanted nanotubes after cooling was essentially the same for the as-anodized nanotubes, whereas the quantitative EDS analysis indicated approximately 33.82% Ti K_α and 66.18% O K_α, thus confirming and providing evidence of titania with a TiO_2 chemical formula structure. The existence of In ions in-implanted titania nanotubes was verified by the quantitative EDS analysis in Spectrum 2 as shown in Fig. 3(b) that indicates 0.8(4)% In. This occurs because the surface composition is detected to a greater depth by SEM.

B. Crystallization behavior

Figures 4(a) and 4(b) show the stacked XRD and SRD plots during thermal annealing in air from RT to 1000 °C for non-implanted titania nanotubes and In-ions implanted titania nanotubes, respectively. Diffraction results showed that both titania nanotube arrays were initially amorphous, but crystalline anatase formed at 400 °C for both samples. The anatase-to-rutile transformation started at 600 °C by a small crystalline rutile peak observed for non-implanted material, compared with 700 °C for In-ions implanted material. The reason for the 100 °C delay in the initial crystallization of rutile for the In-ions implanted titania nanotubes was that the In-ions implant provided greater structural rigidity and prevented relaxation in the Ti bonding environment. This behavior of severe/difficult rearrangement of the atoms in the anatase and rutile lattices could be due to the presence of In-ions interstitially or substitutionally. The presence of interstitial ions can inhibit the anatase-to-rutile transformation, whereas substitutional ions can also inhibit phase transformation if the substitutional ion is larger and does not differ significantly from Ti^{4+}.[19,34] The In^{3+} radius (0.080 nm) is relatively larger than the Ti radius (0.061 nm). (For a discussion of whether In-ions enter the titania interstitially or substitutionally, see Sec. III. C)

The relative phase levels of crystalline titanium, anatase, and rutile in the anodized nanotubes were calculated using the Rietveld method. Figures 5(a) and

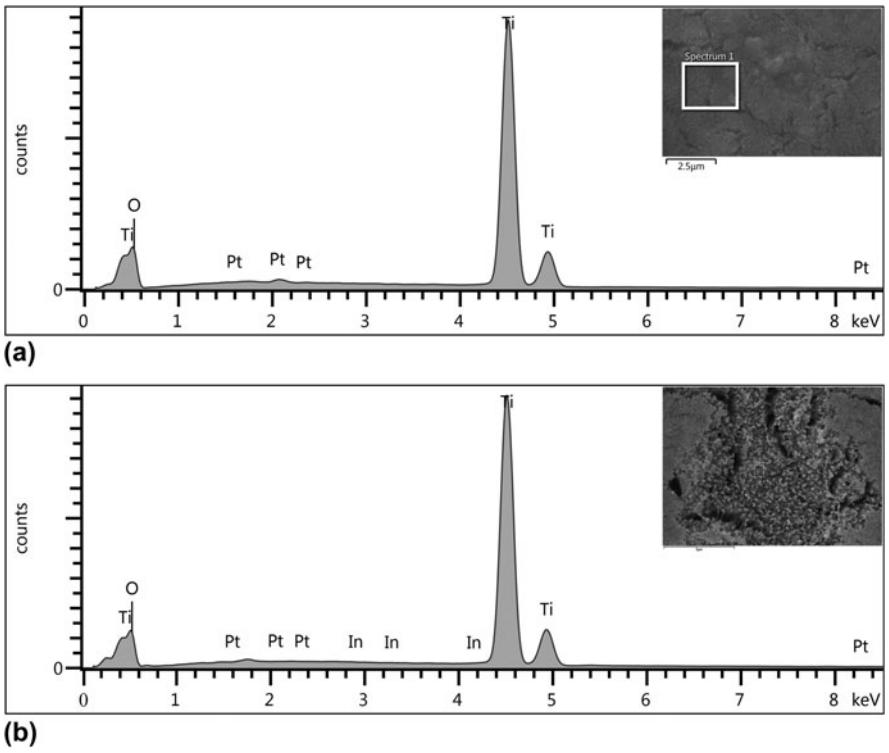

FIG. 3. EDS spectra of (a) anodized TiO_2 nanotubes prior to heating; and (b) after thermal treatment and In-ions implantation and cooling to RT.

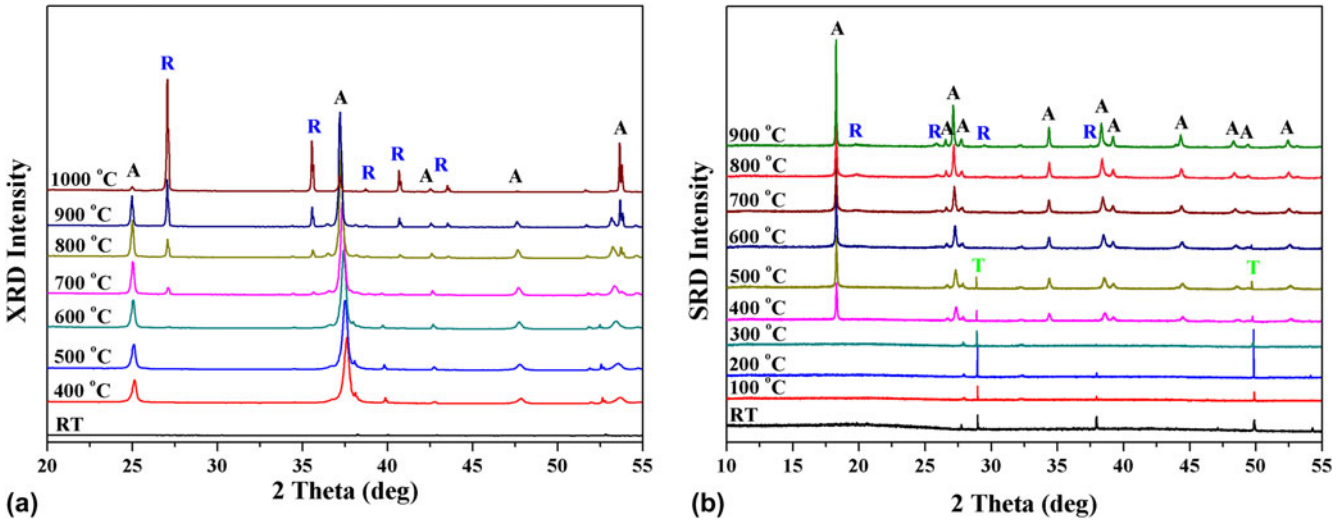

FIG. 4. Stacked XRD and SRD plots for the temperature range of RT-1000 °C of (a) non-implanted material, and (b) after In-ions implantation, respectively. [Legend: anatase (A), rutile (R), titanium peaks (T), and RT].

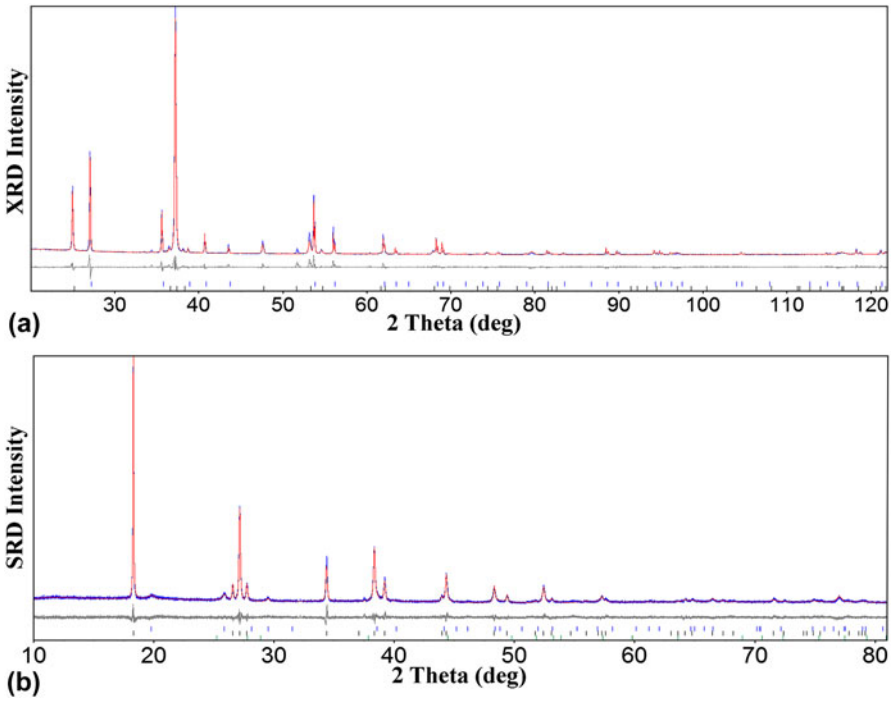

FIG. 5. XRD and SRD Rietveld difference plots for data measured in (a) non-implanted and (b) In-ions implanted titania nanotubes at 900 °C, respectively. Measured patterns are indicated by black crosses and calculated patterns by solid red lines. The Gray residual plot shows the difference between calculated and measured patterns. Peak positions for titanium, anatase, and rutile are indicated by green, black, and blue bars, respectively.

5(b) show typical XRD and SRD Rietveld residual plots at 900 °C for data measured in non-implanted and In-ions implanted titania nanotube arrays, respectively. In non-implanted material, R_{wp} = 13.23, R_{exp} = 3.75, R_B (anatase) = 4.791, and R_B (rutile) = 6.416%, and for the In-ions implanted material, R_{wp} = 12.14, R_{exp} = 9.94, R_B (titanium α) = 2.817, R_B (anatase) = 2.908 and R_B (rutile) = 2.951%. The GOF values are 3.53 for non-implanted nanotube arrays and 1.22 for In-ions implanted nanotube arrays. The ideal value for the GOF is 1.0, but 4 or higher can be accepted for abundance data analysis.[35]

Table I shows the variation of relative phase concentrations of crystalline titanium, amorphous anatase, and rutile in the temperature range of 400–1000 °C for non-implanted and In-ions implanted material. At 600 °C, the

relative phase concentrations were 1.40(12)% Ti, 96.55 (64)% anatase, and 2.05(63)% for non-implanted nanotubes, whereas they were 1.56(47)% Ti, and 98.44(47)% anatase without any crystalline rutile formed for In-ions implanted titania nanotubes. The metastable anatase crystallizes from amorphous titania, which formed from the anodized Ti foils at a relatively low temperature, and the anatase subsequently transforms into stable crystalline rutile at a higher temperature. For the non-implanted sample, it is evident that the relative phase concentration of the crystalline rutile increased dramatically as the temperature increased from 600 to 1000 °C. However,

TABLE I. The effect of In-ions implantation on the relative weight percentages of anatase and rutile as a function of temperature, using the Rietveld method.

	Nonimplantation			In-ions implantation		
Temperature (°C)	Ti (%)	Anatase (%)	Rutile (%)	Ti (%)	Anatase (%)	Rutile (%)
400	3.25(12)	96.75(12)	0	4.48(13)	95.52(13)	0
500	2.85(93)	97.15(93)	0	2.61(67)	97.63(58)	0
600	1.40(12)	96.55(64)	2.05(63)	1.56(47)	98.44(47)	0
700	0.87(11)	86.60(88)	12.53(88)	0.85(68)	85.27(58)	13.88(11)
800	0.65(16)	76.06(43)	23.29(41)	0.4202(20)	84.14(34)	15.64(56)
900	0	46.81(44)	53.19(44)	0.2194(68)	84.16(32)	15.66(31)
1000	0	5.06(62)	94.94(62)	NA	NA	NA

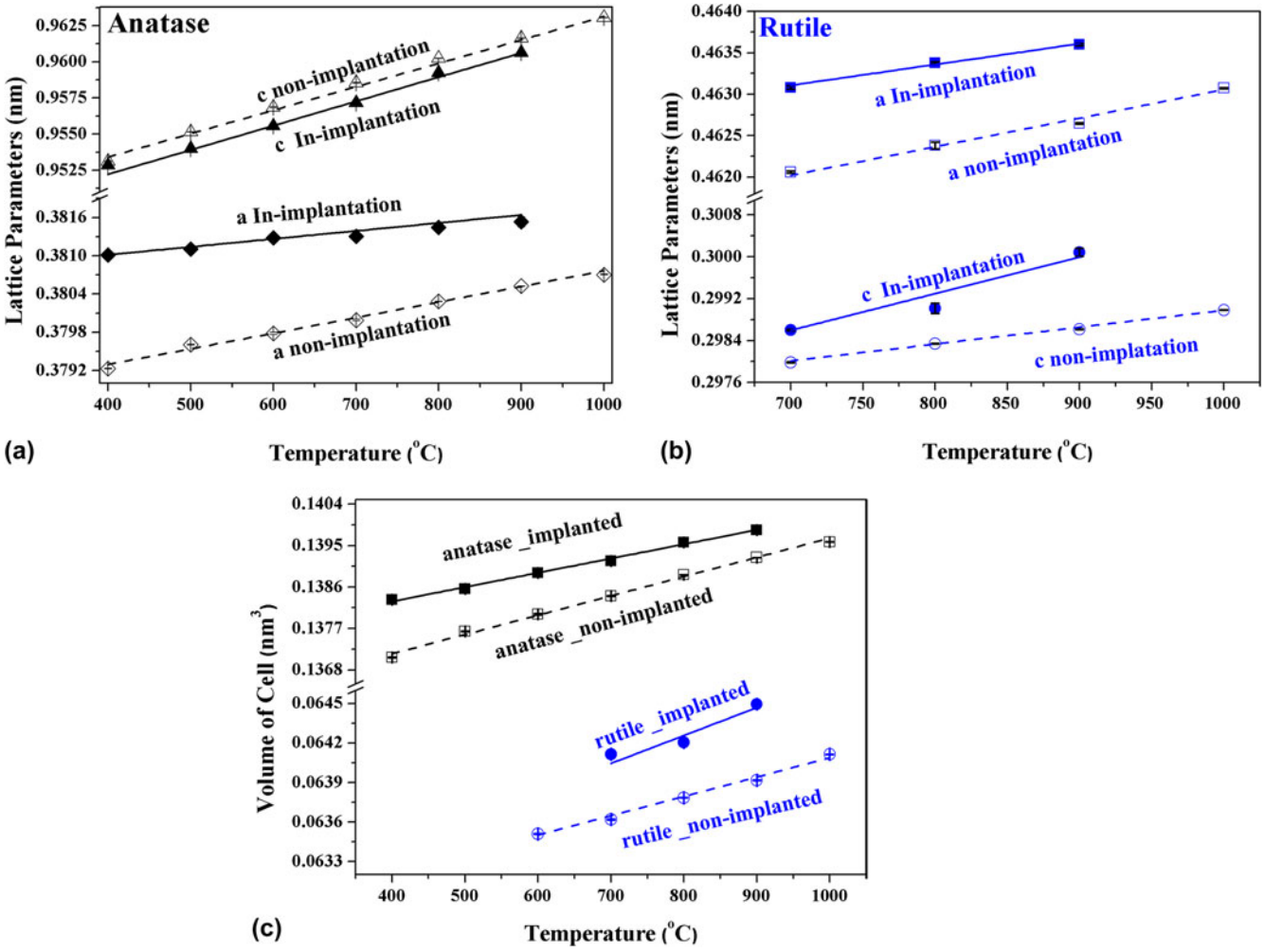

FIG. 6. Variation of the lattice parameters as a function of temperature for (a) anatase, and (b) rutile; and (c) the cell volume in non-implanted and In-ions implanted anodized titania nanotube arrays.

the titania transformations were observed to increase more slowly in In-implantation than in nonimplantation samples. At 900 °C, the relative phase concentration was 0.2194(68)% Ti, 84.16(32)%, and just 15.66(31)% rutile for the In-ions implanted nanotubes, whereas all of the crystalline Ti, and more than 53% of the crystalline anatase transformed into crystalline rutile for the non-implanted sample. The relatively larger In^{3+} than Ti^{4+} radius would inhibit the transformation of titania, since it involves greater structural rigidity and prevents relaxation in the Ti bonding environment.

C. Influence of In-ions implantation on lattice parameters

Figure 6 shows the temperature variations with the anatase and rutile lattice parameters and cell volumes for non-implanted and In-ions implanted nanotubes. The unit-cell parameters and cell volumes for both anatase and rutile in both non-implanted and In-ions implanted titania nanotube arrays increased linearly with temperature, but the lattice parameters and cell volumes showed an increase in the In-ions implanted sample relative to the non-implanted sample. For example, at 900 °C, the anatase lattice parameters ***a***, and ***c*** for the non-implanted titania nanotube arrays were 0.380523(18) and 0.961642 (26) nm, whereas they were 0.381530(75), and 0.960651 (81) nm for the In-ions implanted samples, respectively. Moreover, the rutile lattice parameters *a*, and *c* at the same temperature, were they 0.4626490 (98) and 0.2986160 (75) nm for the non-implanted sample, whereas they were 0.46360 (13) and 0.300084 (79) nm for In-ions implanted samples, respectively. Thus, the cell volumes of anatase and rutile were 0.139243(13) and 0.0639170(31) nm^3 for non-implanted samples, and 0.139838(27), 0.064495(41) nm^3 for In-ions implantation at 900 °C, respectively. As can be seen, the volume of cells for the anatase and rutile were higher for the In-ions implanted samples than the non-implanted samples. The current lattice parameter increase in the In-ions implantation suggests that added ionic In substitutes for Ti^{4+} rather than occupying interstitial sites, which causes the ions to be incorporated as dopants in the titania lattice.[19,34] The lattice deformation of both titania phases caused by the incorporation of foreign Indium dopants affects the lattice parameter of In-ions implanted samples with temperature. The relatively difficult anatase-to-rutile transformation in the In-implanted titania nanotubes appears from an In-ions radius occupying the Ti sublattice substitutionally.

IV. CONCLUSIONS

The effect of In-ions implantation on the dynamic crystallization behavior of anodized titania nanotubes was investigated using *in-situ* high-temperature XRD and SRD in the range from RT to 1000 °C. Diffraction results show that the diffraction peaks of the Ti foils were only observed before calcination until 300 °C, which indicated the amorphous titania nanotubes. The amorphous-to-anatase transformation started at 400 °C for non-implanted and In-implanted materials, including the characteristic crystalline anatase peaks. The crystalline rutile temperature increased from 600 to 700 °C for In-implantation, with the anatase-to-rutile transformation being inhibited relative to the non-implanted material. It was concluded that In-ions occupy the Ti sublattice substitutionally and then inhibit the anatase-to-rutile transformation. The relatively difficult anatase-to-rutile transformation in the In-implanted material appears to result from the relatively larger In^{3+} than Ti^{4+} radius, which provides greater structural rigidity and prevents relaxation in the Ti bonding environment.

ACKNOWLEDGMENTS

This research was supported by the funding from the Australian Institute of Nuclear Science and Engineering (AINGRA-11134), and the Australian Synchrotron (PD-3611). The authors would like to thank Prof. V.M. Prida from Department of Physics, University of Oviedo for XRD collection. Dr M. Ionescu of ANSTO assisted with work on ion-implantation.

REFERENCES

1. H. Li, L. Cao, W. Liu, G. Su, and B. Dong: Synthesis and investigation of TiO_2 nanotube arrays prepared by anodization and their photocatalytic activity. *Ceram. Int.* **38**, 5791 (2012).
2. D.V. Bavykin, A.N. Kulak, V.V. Shvalagin, N.S. Andryushna, and O.L. Stroyuk: Photocatalytic properties of rutile nanoparticles obtained via low temperature route from titanate nanotubes. *J. Photochem. Photobiol., A* **218**, 231 (2011).
3. O.K. Varghese, D. Gong, M. Paulose, C.A. Grimes, and E.C. Dickey: Crystallization and high-temperature structural stability of titanium oxide nanotube arrays. *J. Mater. Res.* **18**, 156 (2003).
4. M. Inagakia, N. Kondoa, R. Nonakaa, E. Itob, M. Toyodac, K. Sogabec, and T. Tsumura: Structure and photoactivity of titania derived from nanotubes and nanofibers. *J. Hazard. Mater.* **161**, 1514 (2009).
5. M. Senna, N. Myers, A. Aimable, V. Laporte, C. Pulgarin, O. Baghriche, and P. Bowen: Modification of titania nanoparticles for photocatalytic antibacterial activity via a colloidal route with glycine and subsequent annealing. *J. Mater. Res.* **28**, 354 (2013).
6. J.M. Macak, H. Tsuchiya, A. Ghicov, K. Yasuda, R. Hahn, S. Bauer, and P. Schmuki: TiO_2 nanotubes: Self-organized electrochemical formation, properties and applications. *Curr. Opin. Solid State Mater. Sci.* **11**, 3 (2007).
7. H. Xiong, M.D. Slater, M. Balasubramanian, C.S. Johnson, and T. Rajh: Amorphous TiO_2 nanotube anode for rechargeable sodium ion batteries. *J. Phys. Chem. Lett.* **2**, 2560 (2011).
8. D. Yanga, H. Parka, S. Choa, H. Kima, and W. Choi: TiO_2-nanotube-based dye-sensitized solar cells fabricated by an efficient anodic oxidation for high surface area. *J. Phys. Chem. Solids* **69**, 1272 (2008).

9. D. Hanaor and C. Sorrell: Review of the anatase to rutile phase transformation. *J. Mater. Sci.* **46**, 855 (2011).
10. S. Chuangchote, J. Jitputti, T. Sagawa, and S. Yoshikawa: Photocatalytic activity for hydrogen evolution of electrospun TiO_2 nanofibers. *ACS Appl. Mater. Interfaces* **1**, 1140 (2009).
11. D. Kim, N. Enomoto, Z. Nakagawa, and K. Kawamura: Molecular dynamic simulation in titanium dioxide polymorphs: Rutile, brookite, and anatase. *J. Am. Ceram. Soc.* **79**, 1095 (1996).
12. G. Liu, L. Wang, H.G. Yang, H.M. Cheng, and G.Q.M. Lu: Titania-based photocatalysts-crystal growth, doping and heterostructuring. *J. Mater. Chem.* **20**, 831 (2010).
13. H. Albetran, H. Haroosh, Y. Dong, V.M. Prida, B.H. O'Connor, and I.M. Low: Phase transformations and crystallization kinetics in electrospun TiO_2 nanofibers in air and argon atmospheres. *Appl. Phys. A* **116**, 161 (2014).
14. H. Albetran, H. Haroosh, Y. Dong, B.H. O'Connor, and I.M. Low: Effect of atmosphere on crystallisation kinetics and phase relations in electrospun TiO_2 nanofibres. *Ceram. Trans.* **246**, 125 (2013).
15. A. Ghicov, H. Tsuchiya, J.M. Macak, and P. Schmuki: Annealing effects on the photoresponse of TiO_2 nanotubes. *Phys. Status Solidi A* **203**, 28 (2006).
16. Z. Liu, X. Yan, W. Chu, and D. Li: Effects of impurities containing phosphorus on the surface properties and catalytic activity of TiO_2 nanotube arrays. *Appl. Surf. Sci.* **257**, 1295 (2010).
17. R.P. Antony, T. Mathews, P.K. Ajikumar, D.N. Krishna, S. Dash, and A.K. Tyagi: Electrochemically synthesized visible light absorbing vertically aligned N-doped TiO_2 nanotube array films. *Mater. Res. Bull.* **47**, 4491 (2012).
18. Y. Iida and S. Ozaki: Grain growth and phase transformation of titanium oxide during calcination. *J. Am. Ceram. Soc.* **44**, 120 (1961).
19. R.D. Shannon and J.A. Pask: Kinetics of the anatase-rutile transformation. *J. Am. Ceram. Soc.* **48**, 391 (1965).
20. H. Li, W. Zhang, and W. Pan: Enhanced photocatalytic activity of electrospun TiO_2 nanofibers with optimal anatase/rutile ratio. *J. Am. Ceram. Soc.* **94**, 3184 (2011).
21. J. Lee, T. Ha, M. Hong, and H. Park: The effect of porosity on the CO sensing properties of TiO_2 xerogel thin films. *Thin Solid Films* **529**, 98 (2013).
22. Z. Zainal and C.Y. Lee: Properties and photoelectrocatalytic behaviour of sol-gel derived TiO_2 thin films. *J. Sol-Gel Sci. Technol.* **37**, 19 (2006).
23. D. Monti, A. Ponrouch, M. Estruga, M.R. Palacin, J.A. Ayllon, and A. Roig: Microwaves as a synthetic route for preparing electrochemically active TiO_2 nanoparticles. *J. Mater. Res.* **28**, 340 (2013).
24. C. Arunchandran, S. Ramya, R.P. George, and U.K. Mudali: Corrosion inhibitor storage and release property of TiO_2 nanotube powder synthesized by rapid breakdown anodization method. *Mater. Res. Bull.* **48**, 635 (2012).
25. N. Baram, D. Starosvetsky, J. Starosvetsky, M. Epshtein, R. Armon, and Y. Ein-Eli: Enhanced photo-efficiency of immobilized TiO_2 catalyst via intense anodic bias. *Electrochem. Commun.* **9**, 1684 (2007).
26. K.P. Beh, F.K. Yam, S.S. Tneh, and Z. Hassan: Fabrication of titanium dioxide nanofibers via anodic oxidation. *Appl. Surf. Sci.* **257**, 4706 (2011).
27. J. Liao, S. Lin, N. Pan, D. Li, S. Li, and J. Li: Free-standing open-ended TiO_2 nanotube membranes and their promising through-hole applications. *Chem. Eng. J.* **211–212**, 343 (2012).
28. R. Sanchez-Tovar, K. Lee, J. Garcia-Anton, and P. Schmuki: Formation of anodic TiO_2 nanotube or nanosponge morphology determined by the electrolyte hydrodynamic conditions. *Electrochem. Commun.* **26**, 1 (2012).
29. D.V. Bavykin, A.N. Kulak, and F.C. Walsh: Control over the hierarchical structure of titanate nanotube agglomerates. *Langmuir* **27**, 5644 (2011).
30. D.V. Bavykin, A.A. Lapkin, P.K. Plucinski, J.M. Friedrich, and F.C. Walsh: Reversible storage of molecular hydrogen by sorption into multilayered TiO_2 nanotubes. *J. Phys. Chem. B* **109**, 19422 (2005).
31. A.W. Tan, B. Pingguan-Murphy, R. Ahmad, and S.A. Akbar: Review of titania nanotubes: Fabrication and cellular response. *Ceram. Int.* **38**, 4421 (2012).
32. I.M. Low, H. Albetran, V.M. Prida, V. Vega, P. Manurung, and M. Ionescu: A comparative study on crystallization behavior, phase stability, and binding energy in pure and Cr-doped TiO_2 nanotubes. *J. Mater. Res.* **28**, 304 (2013).
33. H. Albetran, B.H. O'Connor, and I.M. Low: Effect of vanadium ion implantation on the crystallization kinetics and phase transformation of electrospun TiO_2 nanofibers. *Appl. Phys. A* **120**, 623 (2015).
34. K. Okada, N. Yamamoto, Y. Kameshima, A. Yasumori, and K.J.D. MacKenzie: Effect of silica additive on the anatase-to-rutile phase transition. *J. Am. Ceram. Soc.* **84**, 1591 (2001).
35. E.H. Kisi: Rietveld analysis of powder diffraction patterns. *Mater. Forum* **18**, 135 (1994).

4 Conclusions and Further work

4.1 Concluding Remarks

TiO_2 is a new and preferred material for environment friendly applications, which has attracted immense attention because of its multiple advantages, especially its long-term photostability, nontoxicity, low cost, photochemical stability, strong oxidising power and so on. In the past few decades, with the development of visible light active and nanoscales surface of TiO_2 materials, a new TiO_2 generation has emerged, attracting more and more attention from researchers. This research was conducted with the specific aim of synthesising and characterising nanostructured TiO_2 so that it can utilise visible light through different methods, primarily electrospinning, sol-gel, and anodisation methods. The key objective of this research, which was to synthesise and characterise nanostructured TiO_2 for photocatalytic applications, was successfully achieved within the scheduled timeline. The following major conclusions were drawn from the findings of this research:

1. **Synthesis for nanostructured TiO_2 was achieved**
    - The study prepared the electrospun TiO_2 nanofibres within the polyvinyl pyrrolidone (PVP) polymer. It examined the effects of the combination of sol-gel and electrospinning techniques parameters on the TiO_2/PVP nanofibres' diameter, including titanium isopropoxide (TiP) concentration, flow rate, needle tip-to-collector distance, needle size and applied voltage, applying Taguchi method. It also investigated the optimum combination of factors with the highest level of the TiP concentration (60 percent), and the highest relative distance of needle tip-to-collector (11 cm) which was observed along with a flow rate of 1 ml/h and an applied voltage setting of 18 kV. The needle size's effect on the nanofibre diameter and its variation of electrospun TiO_2/PVP were also examined based on an optimal combination. It was concluded

that the needle size is not a significant factor in the nanofibre diameter of electrospun TiO_2/PVP.

- The study synthesised titania nanotube arrays electrochemically using anodisation of (with 99.6 percent purity) titanium foils. Platinum was used as the anode in the anodisation cell, and with the electrolyte consisted of 2.04 ml of water, 100 ml of ethylene glycol, and 0.34 g of ammonium fluoride (NH4F), the Ti foil acted as the cathode. The electrolyte was kept at a constant room temperature and a pH of 6, and set the anodising conditions at a constant applied voltage of 60 V for 20 h.

2. **Phase transformations in electrospun titania nanofibres: comparing the influence of argon and air atmospheres**

    - In this research, it examined how air and argon influence the dynamic crystallisation behaviour of electrospun TiO_2 nanofibres, using *in situ* SRD data measured in the temperature range 25–900 °C. Initially, the electrospun TiO_2 nanofibres were amorphous but crystallised gradually into anatase and rutile at elevated temperatures. In air, anatase was observed first at 600 °C and rutile at 700 °C. On the other hand, both phases appeared at 700 °C in argon. There was a monotonic increase in the level of crystalline TiO_2 (anatase and rutile) with the temperature increase, whereas some amorphous TiO_2 was still observed at 900 °C. The findings suggest the role of atmospheric environment in affecting the phase transformation kinetics; the rate of anatase-to-rutile transformation was quicker in argon than in air because of oxygen vacancies in the former.
    - Due to heating in argon, the initially amorphous fibres lose some oxygen, resulting in non-stoichiometry TiO_{2-x} ($x < 0.4$) on crystallising from the amorphous matrix in argon. The stoichiometry TiO_2 is observed for anatase in air and for rutile in both argon and air.
    - According to the phase analysis results, there is more anatase in air than in argon, whereas air has substantially less rutile compared to argon. These differences are due to a faster anatase-to-rutile transformation

during the heating of the samples in argon compared to air because of oxygen vacancies. The results also show that in either argon or air the fibres become mainly crystalline after heating to 900 °C. This result is consistent with FESEM and TEM imaging results.

- There is a consistency between the estimated activation energy data and the phase composition and site occupancy data. The anatase-to-rutile transformation in argon is promoted by the formation of oxygen vacancies in the anatase structure. The activation energies, 45(9) kJ/mol in argon and 69(17) in air for the amorphous-to-anatase transformation; and 97(7) kJ/mol for argon and 129(5) in air for the anatase-to-rutile transformation energies.
- It provides estimation for activation energy for amorphous-to-crystalline titania in argon, 142(21) kJ/mol by applying differential scanning calorimetry (DSC), and the estimation is consistent with the SRD results.

3. **The effect of calcination on band gap for electrospun titania nanofibres heated in air-argon mixtures was studied**
    - In order to develop titania photocatalysts that are photoactive in visible light, the study used heat treatment of amorphous titania nanofibres, instead of chemical doping. The findings, using photocatalytic titania nanofibres which can function in visible light, indicate a significant contribution in reducing the band gap for electrospun titania nanofibres. Besides, based on the findings of heating in different selected air-argon mixtures, it is found that the UV-region band gap in as-spun amorphous nanofibres, 3.33 eV, can be reduced well into the visible region with the calcination in air, argon and argon-air mixtures. When the material is heated in an air-argon mixture, the band gap value observed for heating in air, 3.09 eV, is reduced systematically, while the gap for heating in pure argon remains at 2.18 eV.
    - The gradual decrease in the band gap depends on the development of crystallinity in the fibres with the calcinations of material and the

associated development of oxygen vacancies in the case of heating in argon environment.

- The heterostructured titania phases and the formation of oxygen vacancies narrowed the band gap, creating a state below the conduction band. The increase in argon content in the air-argon mixtures contributes to the reduction of the state to below the titania conduction band, which then causes the oxygen vacancy concentration to increase, and the subsequent band gap to decrease.

4. **The effects of ion implantation on crystallisation kinetics of electrospun TiO_2 nanofibres were investigated**
    - The research examined the effect of V-ion implantation on the crystallisation of electrospun amorphous TiO_2 nanofibres using *in-situ* high temperature SRD. Based on the SRD findings, the crystallisation kinetics was studied in terms of implantation's influence on the activation energies for the anatase-to-rutile and amorphous-to-anatase transformations.
    - Whereas anatase and rutile were both initially observed at 500 °C for V-implanted TiO_2, the anatase crystalline phase was first observed at 600 °C and rutile at 700 °C for non-implanted TiO_2.
    - The implantation caused a decrease in the average activation energies for the amorphous-to-anatase TiO_2 transformation from 69(17) kJ/mol to 25(3) kJ/mol, and for the anatase-to-rutile transformation from 129(5) kJ/mol to 16(3) kJ/mol.
    - Based on XPS results, implantation reduces the concentration of Ti^{4+} ions in TiO_2 substantially, and determines the low level of difficulty transformations in the implanted material.
    - There was a steady increase of the crystallite sizes in both anatase and rutile for non-implanted, and only anatase for V-ion-implanted electrospun TiO_2 nanofibres depending on the temperature. This indicates that crystallisation of materials in the existing grains from the surrounding amorphous TiO_2 increases grain growth with increasing temperature, instead of unit cell expansion.

- According to the strain estimates, anatase has substantially higher non-linear strain than rutile for both non-implanted and implanted material. No noticeable increase was observed in strain in the implanted material at elevated temperatures for any of the two phases.
- The study indicates that the crystallisation temperatures were lowered by V-ion implantation, because it substituted relatively small V-ions for Ti in the TiO_2 crystal structure. The dramatic reductions in activation energies resulted from the implantation of V-ions.

5. **The effects of implantation on crystallisation kinetics of anodised titania nanotubes were investigated**
    - The study used high-temperature SRD to examine the effect of Cr-implantation on *in situ* crystallization of anatase and rutile in as-anodized TiO_2 nanotubes. In the beginning, the TiO_2 was amorphous but crystallised to anatase and rutile at elevated temperature. The crystallization temperature of anatase was lowered by Cr-implantation from 600 to 400 °C and rutile from 600 to 500 °C. Besides, the fraction of anatase-to-rutile transformation was reduced dramatically. Cr implanted titania nanotubes became unstable, and decomposed to form TiO_{2-x} at 900 °C.
    - The study also investigated how Cr- or In- implantation affect the dynamic crystallisation behavior of anodised titania nanotubes using *in-situ* high temperature SRD. According to the diffraction results, it is possible to observe the diffraction peaks of Ti foils only before calcination until 300 °C, indicating the amorphous nature of titania nanotubes. For both non-implanted and In-implanted materials, including the characteristic crystalline anatase peaks, at a temperature of 400 °C, the amorphous-to-anatase transformation started. As the anatase-to-rutile transformation gets inhibited compared to the non-implanted material, the crystalline rutile temperature increased from 600 °C to 700 °C for In-implantation. The major conclusion was that the Ti sub-lattice is occupied by In-ions substitutionally, which then inhibit the anatase-to-rutile transformation. The relatively larger In^{3+} radius

(relative to Ti^{4+}) can provide greater structural rigidity and thus restricts relaxation in the Ti bonding environment. A larger In^{3+} is also the source of a relatively difficult anatase-to-rutile transformation of the In-implanted materials.

4.2 Recommendations for Further Work

This thesis focused on both the synthesis and characterisation of nanostructured TiO_2 for photocatalytic applications. However, further studies are necessary to be conducted in detail to comprehensively investigate the effective mechanism of TiO_2 photocatalytic activity and the role of pure, and doped TiO_2, as well as the effect of its electronic property on photocatalysis. This study suggests the following recommendations for future research:

1. Photocatalytic activity

The photocatalytic activities of pure/undoped and implanted/doped TiO_2 nanostructures will be evaluated by the decomposition of Methylene Blue (MB) or Methyl Orange (MO) under visible light. The synthesised TiO_2 nanostructures (several mg) will be added to 1L water with the aqueous 100 ppm Methylene Blue (MB) or Methyl Orange (MO) inside a Pyrex double-jacket reactor as shown in Figure 32. The reactor will circulate cooling water in order to control the reaction temperature, and for maintaining a homogeneous solution. The obtaining of synthesised TiO_2 photocatalytic activity can be done using the following formula (Fang *et al*. 2011; Sahoo *et al*. 2012):

$$C = C_o\, e^{-kt} \qquad (4.1)$$

K: The reaction rate constant,

t: The reaction time,

C_o: The initial concentration of the MO or MB at t = 0, and

C: The concentration of the MO or MB at time *t*.

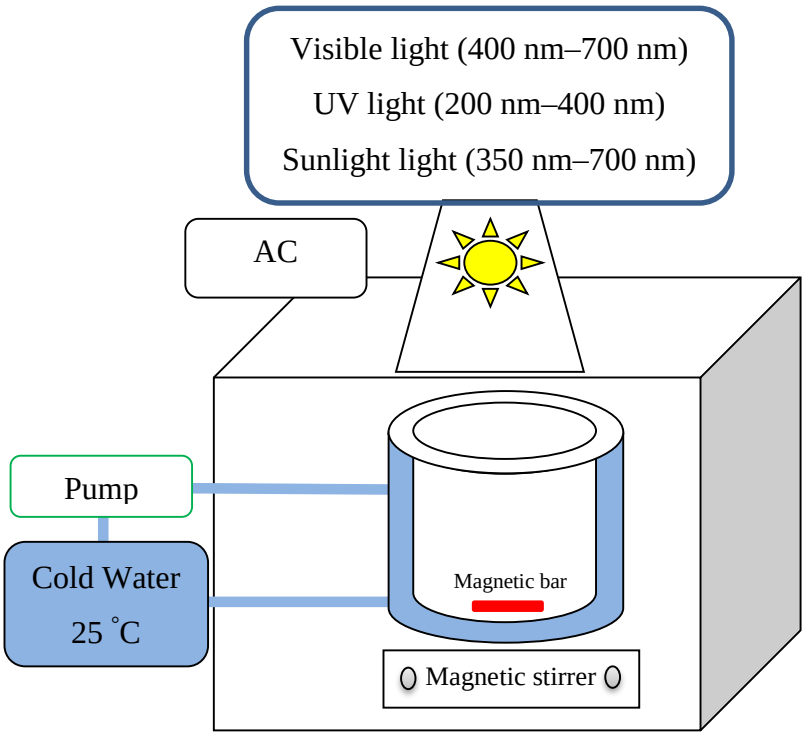

Figure 32: Experimental setup for photocatalytic oxidation.

2. Taguchi method for anodised titania nanotube arrays

During anodisation, various factors including electrolyte composition, synthesis time, applied voltage, temperature, electrode areas, the distance between electrodes, etc., affect the formation, growth rate and morphology of titania nanotubes, including wall thickness, length, and diameter of the titania nanotube arrays. It will be interesting to study these parameters using the Taguchi method, which can be used to fabricate effective titania nanotube arrays for the photocatalytic application.

3. Optimal anatase/rutile ratio

In this project, heat treatment of amorphous titania in air-argon mixtures was used as a simple method for developing pure titania to be photoactive in visible light. The progressive lowering of the titania band gap is attributed to the development of oxygen vacancies and the titania crystallinity. One way this research can be extended is to focus on the optimal anatase/rutile ratio. It is possible to find the photocatalytic activity

of pure titania with an optimal anatase/rutile ratio by calcination of amorphous titania at an optimal temperature and atmosphere. Such study will help the design of an efficient pure titania photocatalyst.

4. Optimal diameter size of electrospun TiO_2 nanofibre

The optimal diameter size of electrospun TiO_2/PVP was studied in paper five using the Taguchi Design of Experiment Method. The average diameters of thermally treated TiO_2 nanofibres will be much smaller than those observed for the as-prepared TiO_2/PVP nanofibres. The shrinkage will be attributed to the evaporation of solvent and loss of the PVP polymer. Thus, the effect of calcination temperature on the optimal diameter size of electrospun TiO_2 nanofibres will be investigated. In addition, the diameter of electrospun TiO_2 nanofibres can also play an important role in determining both phase transformation and crystallization kinetics.

5. Effect of pressure on TiO_2 phase transformations

In the case of TiO_2 phase transformation, the effect of pressure on TiO_2 phase transformations has not been well studied in the literature. Thus, it would be interesting to study the effect of pressure on titania phase transformations. TiO_2 nanopowder will be mounted in sealed quartz capillary and the mounted sample will be heated from room temperature to elevated temperature. In this study, *in-situ* high-temperature synchrotron radiation diffraction measurements will be used. The capillary gas pressure arising from sealed capillary and increasing temperature varies according to the Gay-Lussac's Law.

5 Appendix I: Supplementary Information for Publications

5.1 Synchrotron Radiation Diffraction (SRD) and X-ray Radiation Diffraction (XRD)

SRD and XRD are phase identification and quantitative analysis techniques. These two techniques were applied extensively in this thesis to study phase transformations and crystallisation kinetics in titania using *in-situ* high temperature diffraction. These techniques are based on Bragg diffraction (see Figure 33) which occurs when a wavelength of radiation comparable to atomic spacing, following Bragg's law:

$$n\lambda = 2sin\theta \qquad (5.1)$$

Where n is integer determined by the reflection order, λ is wavelength, d is interplanar distance, and θ is diffraction angle.

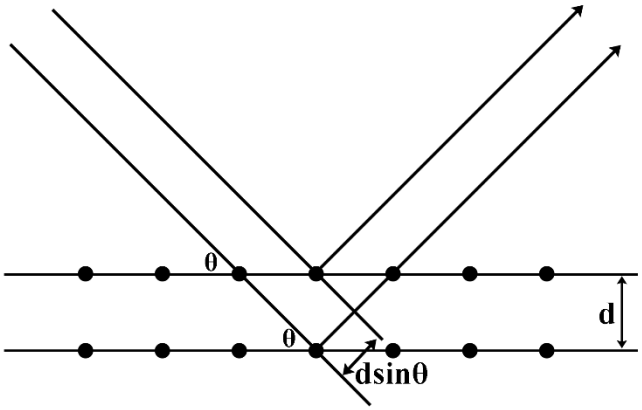

Figure 33: Bragg diffraction showing two beams with identical wavelength and phase approach a crystalline solid and are scattered off two different atoms within it.

Figure 34: Powder Diffraction beam line at the Australian Synchrotron.

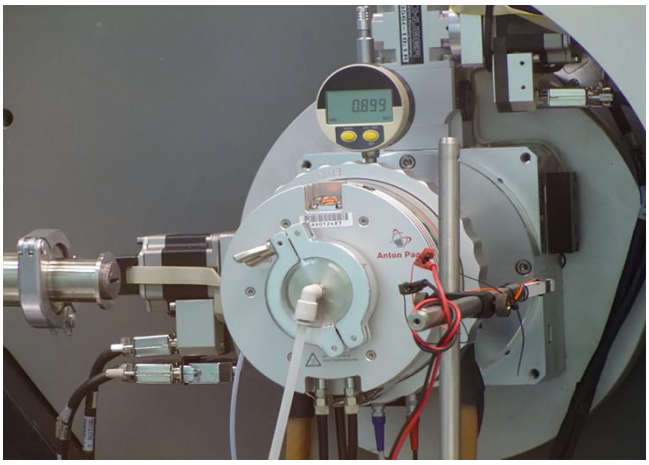

Figure 35: The Anton Parr HTK20 Furnace and the Mythen II Microstrip at the Australian Synchrotron.

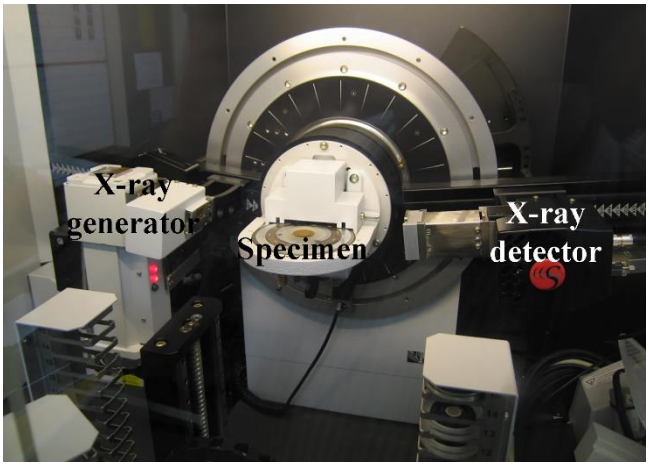

Figure 36: Bruker D8 Bragg-Brentano X-ray diffraction at Curtin University.

Table 7: Operational conditions for SRD and XRD diffractometers.

Goniometer Parameters	**XRD-**	**SRD**
Name	D8 Advance	Powder Diffraction Beamline
Location	Curtin University, Perth, WA	Australian Synchrotron, Melbourne
Figure	36	34, and 35
Radiation source	Cu	Bending magnet on a 3 GeV synchrotron
Wavelength (nm)	0.15419	4–0.077
2θ Range (°)	5–120	1.2–81
Goniometer radii (mm)	250	761.2
X-ray tubes operation voltage (kV)	40	
X-ray tubes operation current (mA)	40	
Filament length (mm)	12	
No. of strip channels	177	
Sample length in equatorial plane (mm)	25	
Receiving slit angle (mm)	17	
Primary soller slit angle (°)	2.5	
Secondary soller slit angle (°)	2.5	
Sample spinning speed (rpm)	30	Capillary spin: 15

Synchrotron radiation diffraction and laboratory X-ray diffractometer were used to collect patterns of titania nanostructure with different settings, as shown in Table 7.

5.2 Rietveld Method

Rietveld method is a well-established method for crystal structure refinement of data using X-ray diffraction (XRD), synchrotron radiation diffraction (SRD), and neutron diffraction (ND) (Rietveld. 1967; Rietveld. 1969). Moreover, it is also used in conjunction with Fourier method to assist in a crystal structure solution from powder diffraction data (Hunter and Howard. 2000).

The key components of Rietveld method include: atom parameters (atom coordinates, thermal parameters, lattice parameters), microstructural parameters (phase scale factors, phase profile parameters, texture parameters), instrumental parameter (Zero point ($2\theta_0$), specimen offset, etc.), model definition, diffraction data, and model refinement (iterative least squares).

The basic mathematics of Rietveld method is (Rietveld. 1967; Rietveld. 1969):

$$y_{i(calc)} = y_{i(bac)} + \sum_{p} \sum_{k=k_1^p}^{k_2^p} G_{ik}^p I_k \qquad (5.2)$$

where $y_{i(calc)}$ is calculated intensity at point i in the pattern, $y_{i(bac)}$ is background intensity, G_{ik} is a normalised peak profile function, I_k is k_{th} Bragg reflection intensity, $k_{1\ldots.2}$ are the reflections contributing intensity to point i, and the superscript p corresponds to the possible phases present in the sample (Hunter and Howard. 2000).

Rietveld method is a least-square-based refinement method. It is used to achieve the best fit between the calculated and the observed diffraction patterns. There are some peak profile function G_{jk} can be chosen such as:

(a) Pseudo-Voigt Function:

$$G_{ik} = \gamma \frac{C_0^{1/2}}{H_{Gk}\pi}[1 + C_0 X_{ik}^2]^{-1} + (1+\gamma)\frac{C_1^{\frac{1}{2}}}{H_{GH}\pi^{\frac{1}{2}}} exp[-C_1 X_{ik}^2] \qquad (5.3)$$

Where C_0 is 4, C_1 is 4ln2, γ is a refinable mixing parameter, H_{Gk} is the full width half maximum (FWHM) of Gaussian contribution, X_{ik} is $(2\theta_i\text{-}2\theta_k)/H_{Gk}$.

(b) Pearson VII Function:

$$G_{ik} = \frac{\Gamma(\gamma)}{\Gamma(\gamma - 1/2)} \frac{C_2^{1/2}}{H_k \pi^{1/2}} [1 + 4C_2 X_{ik}^2]^{-\gamma} \qquad (5.4)$$

Where C_2=$2^{1/\gamma}$-1, and Γ is gamma function.

(c) Voigt Function:

$$G_{ik} = \frac{C_2^{1/2}}{H_{Gk}\pi} Re\left[\omega\left(C_2^{1/2} X_{ik} + iC_3 \frac{H_{Lk}}{H_{Gk}}\right)\right] \qquad (5.5)$$

Where C_2 is 2ln2, C_3 is ln2/2, ω is the complex ere function and Re denotes its real part, and H_{Lk} is the *FWHM* of the Lorentz contribution.

The FWHM of the Lorentzian contribution (Scherrer, 1918):

$$H_{Lk} = \frac{180}{\pi} \frac{\lambda}{D} sec\theta + \frac{180}{\pi} S \tan\theta \qquad (5.6)$$

Where the λ is the wavelength of optic, *D* is the size parameter, and *S* is the strain parameter.

The FWHM of the Gaussian contribution (Caglioti *et al*., 1958):

$$H_{Gk} = (U tan^2\,\theta + V \tan\theta + W)^{1/2} \qquad (5.7)$$

Where *U*, *V*, and *W*are refinable parameters.

(d) TOF Exponential Pseudo-Voigt function:

$$G_{ik} = \frac{\alpha\beta}{2(\alpha+\beta)}\Big[(1-\eta)\big(e^u Erfc(y) + e^v Erfc(z)\big) - \frac{2\eta}{\pi} lm\big(e^p E_1(p) + e^q E_1(q)\big)\Big] \qquad (5.8)$$

Where α and β are exponential decay terms defined to vary with d-spacing. The *Erfc* is a complex error function and E_1 is a complex exponential integral function.

The first Rietveld computer program was described by Hugo Rietveld in 1969, which was written specifically for neutron diffraction data analysis from fixed-wavelength diffractometers (Rietveld, 1969). Several Rietveld programs have been developed in recent years such as Generalised Structure Analysis System (GSAS, CCP14) by Bob Von Dreele, FullProf/WinPLOTR (ILL) by Juan Rodriguez-Carvajal, Rietica (Luca Height Laboratory), and TOPAS (Bruker AXS).

Rietveld quantitative analyses were determined for both SRD and XRD data using Rietica for Windows version 2.1 (B. A Hunter 1997-2007), and TOPAS (version 4.2, Bruker AXS). The Rietveld refinement was applied to refined *in-situ* high temperature unit cell parameters, preferred orientation of titania crystallites, or rough ratios of crystalline titania phases.

5.2.1 Rietica

Rietica is a Rietveld structure refinement program developed by Luca Height Laboratory. Rietica is a Windows front end to the FORTRAN program which is derived from Hill-Howard-Hunter and known as LHPM program. This program is available for some different computer operation systems (http://www.rietica.org/features.htm).

Rietica for Windows version 2.1 features include:

- Rietveld needs two files, which are: input file (.inp) and data (.xy) file.
- Viewing the Input file and output files (main output file, bond distances and angles, bond valences and summary);
- Reading data using the format: (GSAS EDS or STD), (x, y, weight), (x, y), and (CPI).
- Reading phases easily from the input file or CIF file.
- Pattern plotting, monitoring of parameter changes and refinement indicators (χ^2 (chi-square), R_p, and R_{wp}) at each refinement cycle. This allows instant identification of problems in the refinement process;

- Peak type of Pseudo-Voigt (Riet. Asym), Pearson IV (Riet. Asym), Voigt (Riet Asym), Pseudo-Voigt (How. Asym), Pseudo-Voigt (FCJ. Asym), and Jorgensen (TOF). The Pseudo-Voigt (How. Asym) was used for a whole pattern-fitting method to refine structure parameters for nanostructured titania. The instrumental Pseudo-Voigt (How. Asym) peak shape included the refinable parameters, which are U, V, W, Asy_1, Gam_0, Gam_1, and Gam_2.
- The plot of Full Width Half Maximum (FWHM) Vs angle /TOF to see peak shape.
- Integrated Fourier plotting (no settings, no fuss);
- Easy background and excluded region input via mouse control;
- A simple database for storage and retrieval of both instrumental parameters and structural data;
- Easy to editing chart (data points, background points, calculation line, difference line, marker points, 3D plots, changing the title, font colour and size and so one).
- Export chart/plots with Metafile or Bitmap format with a wide range of size.
- Free Rietveld program.

The R-values for Rietica, which are called the figures-of-merit are as follows:

Derived Bragg, R-factors (R_B) for every phase:

$$R_B = \frac{\sum |I_{ko} - I_{kc}|}{\sum I_{ko}} \qquad (5.9)$$

where I_{ko} and I_{kc} are observed and calculated intensities for Bragg reflection k, respectively.

Profile R-factor (R_p):

$$R_p = \frac{\sum |y_{io} - y_{ic}|}{\sum y_{io}} \qquad (5.10)$$

where y_{io} and y_{ic} are observed and calculated background intensities, respectively.

Weighted pattern R-factor (R_{wp}):

$$R_{wp} = \left[\frac{\sum w_i(y_{io} - y_{ic})^2}{\sum w_i\, y_{io}^2}\right]^{1/2} \qquad (5.11)$$

Expected R-factor (R_{exp}):

$$R_{exp} = \left[\frac{N - P}{\sum w_i y_{io}^2}\right]^{1/2} \qquad (5.12)$$

The goodness of fit (GOF) for *Rietica* is determined by the following equation:

$$GOF = \chi^2 = \left(\frac{R_{wp}}{R_{exp}}\right)^2 \qquad (5.13)$$

The ideal value of GOF is suggested to be 1.0, but a value less than 4.0 during the refinement course for phase abundance data analysis is widely accepted (Kisi, 1994). However, this value is also calculated using the residual values of refinements R_{wp} and R_{exp}, but it largely depends on Rietveld program (See TOPAS, Section 5.2.2).

5.2.2 TOPAS

TOPAS stands for **To**tal **P**attern **A**nalysis **S**olutions program, which is a graphics based profile analysis program built around a general non-linear last squares fitting system.

TOPAS (version 4.2) features include (Bruker, 2008):

- TOPAS integrates various types of X-ray, synchrotron, and neutron diffraction analyses by supporting all fit profile methods;
- TOPAS templates (.pro files) contain the measurement data ((.xy) file), model and refinement parameters, evaluation results, as well as any user defined settings (input file (.inp)). The project files are ideal templates and allow easy, reliable, very fast and automatable quantifications;

- It supports two modes of operation: a graphical user interface mode for parameters input and direct editing of an input file;
- Peak type of fundamental parameters (FP), Pseudo-Voigt (PV_MOD and PV_TCHZ), Split Pearson VII (SPVII);
- Determination of accurate profile parameters (integrated intensities, line positions, peak shapes, and widths), standardless microstructure analysis, indexing in addition to lattice parameter refinement;
- Quantification of phases with partial or no known crystal structures;
- Degree of crystallinity analysis, in which calculations require the definition of at least two phases to describe the intensity contributions coming from the amorphous and the crystalline parts of a sample;
- Viewing crystal structure diagram by structure viewer window with 3-D electron densities including atom picking;
- An unlimited number of patterns set can be loaded and refined simultaneously. These can all be displayed in one single scan window;
- Using for Fourier analysis. Fourier maps can be calculated for laboratory X-ray, Synchrotron radiation or neutron single crystal or powder data.

The R-values for TOPAS, known as the figures-of-merit are presented below:

Weighted pattern R-factor (R_{wp}):

$$R_{wp} = \left[\frac{\sum w_i(y_{io} - y_{ic})^2}{\sum w_i\, y_{io}^2}\right]^{1/2} \qquad (5.11)$$

Expected R-factor (R_{exp}):

$$R_{exp} = \left[\frac{\sum N - P}{\sum w_i y_{io}^2}\right]^{1/2} \qquad (5.12)$$

The goodness of fit (GOF) for *TOPAS* is determined by the following equation:

$$GOF = \chi^2 = \left(\frac{R_{wp}}{R_{exp}}\right) \qquad (5.14)$$

5.3 Crystal Structure Data

Crystal structure data including unit cell parameters and atom coordinates were taken from crystallographic information file (CIF) available in the Inorganic Crystal Structure Database (ICSD).

Anatase

Database Code	202242					
Creation Date	1988/12/19					
Update Record	2006/04/01					
Chemical Name Systematic	Titanium Oxide					
Chemical Formula Structure	TiO_2					
Chemical Name Mineral	Anatase					
Unit Cell (nm)	***a***	0.378479(3)				
	c	0.951237(12)				
Cell Volume (nm^3)	0.13626					
Cell Angle (°)	α	90				
	β	90				
	γ	90				
Z	4					
Space Group	I_{41}/a m d z					
SG Number	141					
Crystal system	Tetragonal					
Atom position	Atom	No	Wyckoff sit	x	y	z
	Ti^{4+}	1	4b	0	0.25	0.375
	O^{2-}	1	8e	0	0.25	0.16686
Authors Name	J. K. Burdett, T. Hughbanks, G. J. Miller, J. W. Richardson, and J. V. Smith.					
Reference	(Burdett *et al*., 1987)					

Rutile

Database Code	64987					
Creation Date	1998/06/26					
Update Record	2006/04/01					
Chemical Name Systematic	Titanium Oxide					
Chemical Formula Structure	TiO_2					
Chemical Name Mineral	Rutile					
Unit Cell (nm)	***a***	0.45845(1)				
	c	0.29533(1)				
Cell Volume (nm^3)	0.06207					
Cell Angle (°)	α	90				
	β	90				
	γ	90				
Z	2					
Space Group	$P_{42}/m\ n\ m$					
SG Number	136					
Crystal system	Tetragonal					
Atom position	Atom	No	Wyckoff sit	x	y	z
	Ti^{4+}	1	2a	0	0	0
	O^{2-}	1	4f	0.3049	0.3049	0
Authors Name	H. Shintani, S. Sato, and Y. Saito.					
Reference	(Shintani *et al*., 1975)					

Titanium alpha

Database Code	44872					
Creation Date	2004/04/01					
Update Record	2006/04/01					
Chemical Name Systematic	Titanium-Alpha					
Chemical Formula **Structure**	Ti					
Unit Cell (nm)	***a***	0.29506(5)				
	c	0.46788(7)				
Cell Volume (nm^3)	0.03528					
Cell Angle (°)	α	90				
	β	90				
	γ	120				
Z	2					
Space Group	P_{63}/m m c					
SG Number	194					
Crystal system	Hexagonal					
Atom position	Atom	No	Wyckoff sit	x	y	z
	Ti		2c	0.3333	0.6667	0.25
Authors Name	I. Szanto					
Reference	(Szanto, 1955)					

Titanium beta

Database Code	76165					
Creation Date	2000/12/16					
Update Record	2006/04/01					
Chemical Name Systematic	Titanium-Beta					
Chemical Formula **Structure**	Ti					
Unit Cell (nm)	***a***	0.3283(2)				
Cell Volume (nm^3)	0.03538					
Cell Angle (°)	α	90				
	β	90				
	γ	90				
Z	2					
Space Group	I m $_{-3}$ m					
SG Number	229					
Crystal system	Cubic					
Atom position	Atom	No	Wyckoff sit	x	y	z
	Ti		2a	0	0	0
Authors Name	B. W. Levinger					
Reference	(Levinger, 1953)					

Indium titanium oxide

Database Code	74316					
Creation Date	1995/10/17					
Update Record	2011/02/01					
Chemical Name Systematic	Diindium Titanate					
Chemical Formula Structure	$In_2(TiO_5)$					
Unit Cell (nm)	***a***	0.72418(7)				
	b	0.35018(3)				
	c	1.4890(2)				
Cell Volume (nm^3)	0.3776					
Cell Angle (°)	α	90				
	β	90				
	γ	90				
Z	4					
Space Group	P n m a					
SG Number	62					
Crystal system	Orthorhombic					
Atom position	Atom	No	Wyckoff site	x	y	z
	In	1	4c	0.0978	0.25	0.0842
	In	2	4c	0.3279	0.75	0.2393
	Ti	1	4c	0.1086	0.25	0.4222
	O	1	4c	0.2323	0.25	0.3203
	O	2	4c	0.3470	0.25	0.4982
	O	3	4c	0.3635	0.25	0.1410
	O	4	4c	0.061	0.75	0.1725
	O	5	4c	0.0688	0.75	0.4531
Authors Name	T. Gaewdang, J.P. Chaminade, P. Gravereau, A. Garcia, C. Fouassier, P. Hagenmuller, and R.Mahiou					
Reference	(Gaewdang *et al*., 1993)					

Indium titanium oxide

Database Code	00-030-0640	
Creation Date	2012/01/14	
Chemical Name Systematic	Indium Titanium Oxide	
Chemical Formula **Structure**	In_2TiO_5	
Unit Cell (nm)	***a***	0.7237
	b	0.3429
	c	1.486
Cell Volume (nm^3)	0.36876	
Cell Angle (°)	α	90
	β	90
	γ	90
Z	4	
Space Group	P n m a	
SG Number	62	
Crystal system	Orthorhombic	
Authors Name	J. Senegas, J. Manaud and J. Galy	
Reference	(Senegas *et al*., 1975)	

6 Appendix II: Supplementary Information for Publications

6.1 Appendix II-A: Supplementary Information for "Phase Transformations and Crystallization Kinetics in Electrospun TiO_2 Nanofibers in Air and Argon Atmospheres." & II-B: Supplementary Information for "Activation Energies for Phase Transformations in Electrospun Titania Nanofibers: Comparing the Influence of Air and Argon Atmospheres."

Figure 37: Electrospinning machine used in this thesis.

The electrospinning method was used in this thesis to produce electrospun TiO_2 nanofibres using a commercial Nabond® electrospinning unit (standard type) purchased from Nabond Technologies Co., Ltd., Shenzhen, China (see Figure 37).

6.2 Appendix II-B: Supplementary Information for "Effect of Vanadium Ion Implantation on the Crystallization Kinetics and Phase transformation of Electrospun TiO_2 Nanofibres."

Figures 38 and 39 show the instruments for ion implantation and ion-beam analysis, respectively, at Australian Nuclear Science and Technology Organisation (ANSTO). The used average implantation energy , and peak penetration depth of ions in the TiO_2 samples were close to stopping and range of ions in matter (SRIM) prediction based on the implantation parameters Near-surface composition depth profiling of the implanted composites was measured using Rutherford Backscattering Spectroscopy (RBS). Nanostructured TiO_2 samples were implanted with several ions types such as V-ion implanted electrospun TiO_2 nanofibres, In-ions, and Cr-ions implanted titania nanotubes.

Figure 38: The MEVVA Ion-Implanter at ANSTO.

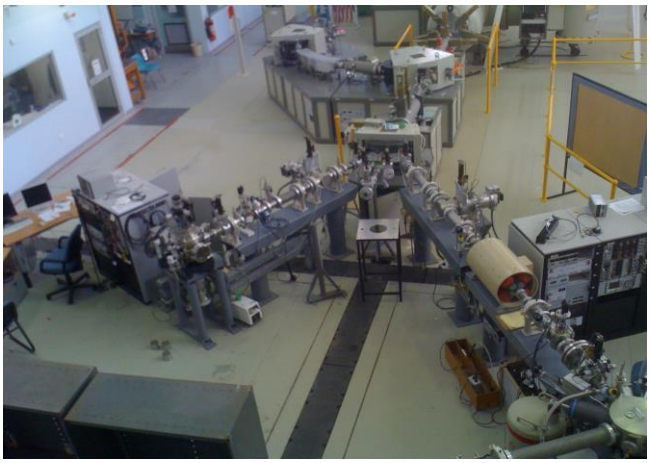

Figure 39: SIBA-2 Instrument for ion-beam analysis at ANSTO.

The absolute weight percentages of amorphous TiO_2 have been determined using the background intensities of SRD patterns at 17° (see Figure 40, and 41). The background levels for the SRD patterns at 500 °C for non-implanted TiO_2 and 400 °C for V-ion implanted TiO_2 were used as the initial background intensity B_o, corresponding to 100% amorphous TiO_2 and 0% crystalline TiO_2. The background intensities were corrected for minor variations in incident beam intensity during data collection. The SRD background level decreased with temperature due to the amorphous-to-crystalline TiO_2 transformation.

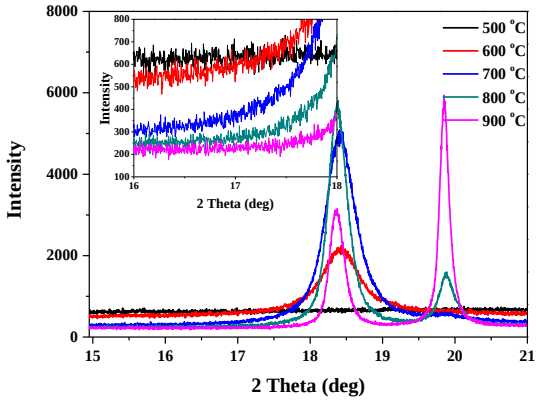

Figure 40: Variations in the SRD background intensity over the temperature ranges 500–900 °C for non-implanted electrospun TiO_2 nanofibres.

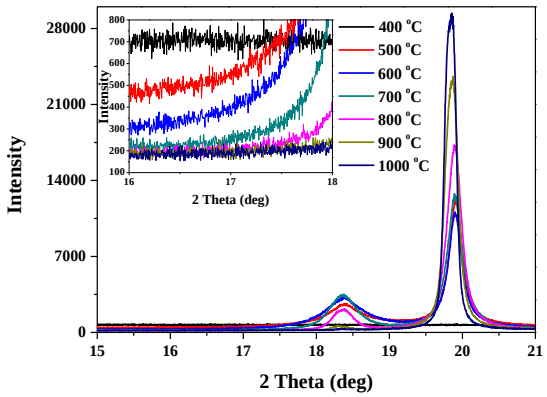

Figure 41: Variations in the SRD background intensity over the temperature ranges 400–1000 °C for non-implanted electrospun TiO_2 nanofibres.

6.3 Appendix II-D: Supplementary Information for "A comparative study on crystallization behavior, phase stability, and binding energy in pure and Cr-doped TiO_2 nanotubes." & II-H: Supplementary Information for "Effect of indium ion implantation on crystallization kinetics and phase transformation of anodized titania nanotubes."

Table 8: Figures-of-merit from Rietveld refinement using TOPAS with synchrotron radiation diffraction data for pure anodized titania nanotube arrays from 400 to 1000 °C.

Temperature (°C)	R_{exp}	R_{wp}	R_P	GOF	R_B (Titanium)	R_B (Anatase)	R_B (Rutile)
25	8.19	13.74	9.39	1.68	4.92		
400	3.22	10.12	3.57	3.15	10.39	2.10	--
500	3.20	10.66	6.99	3.33	8.53	2.43	--
600	3.15	12.64	7.79	4.01	28.61	3.14	4.80
700	3.77	13.60	8.98	3.61	19.61	6.05	4.47
800	2.96	10.05	6.53	3.39	12.99	2.26	5.73
900	3.75	13.23	9.03	3.53	--	4.79	6.41
1000	3.89	16.76	10.75	4.31	--	1.21	14.07

Table 9: Figure-of-merit from Rietveld refinement using TOPAS with synchrotron radiation diffraction data for In-ion implanted anodized titania nanotube arrays from 100 to 900 °C.

Temperature (°C)	**R_{exp}**	**R_{wp}**	**R_P**	**GOF**	**R_B (Titanium)**	**R_B (Anatase)**	**R_B (Rutile)**
100	9.98	11.13	8.65	1.12	3.18	--	--
200	9.88	11.33	8.75	1.15	2.91	--	
300	9.90	11.14	8.64	1.12	1.75	--	--
400	9.93	11.39	8.86	1.15	5.77	2.83	--
500	9.93	11.62	8.84	1.17	6.41	2.28	--
600	9.93	11.85	9.19	1.19	3.58	2.66	--
700	10.12	11.38	8.72	1.12	1.31	2.11	1.77
800	9.94	11.65	8.91	1.17	2.21	2.27	2.31
900	9.94	12.15	9.31	1.22	2.86	2.94	2.95

7 Appendix III: Statement of Contributions of Others

7.1 Appendix III-A: "Statements of Contribution of Others" for "ALBETRAN, H., HAROOSH, H., DONG, Y., PRIDA, V. M., O'CONNOR, B. H., & LOW, I. M. 2014. Phase Transformations and Crystallization Kinetics in Electrospun TiO_2 Nanofibers in Air and Argon Atmospheres. *Applied Physics A*, 116, 161–169".

Statement of Contribution of Others for “Phase transformations and crystallization kinetics in electrospun TiO_2 nanofibers in air and argon atmospheres”.

18th December 2015

To Whom It May Concern

I, Dr. H. Haroosh, contributed by specialist technical service advice and samples for electrospinning experiments to the paper/publication entitled.

ALBETRAN, H., HAROOSH, H., DONG, Y., PRIDA, V. M., O'CONNOR, B. H., & LOW, I. M. 2014. Phase Transformations and Crystallization Kinetics in Electrospun TiO_2 Nanofibers in Air and Argon Atmospheres. *Applied Physics A*, 116, 161–169.

Undertaken with ALBETRAN, HANI MANSSOR M

(Signature of Co-Author)
H. Haroosh

(Signature of First Author)
ALBETRAN, HANI MANSSOR M

Statement of Contribution of Others for "Phase transformations and crystallization kinetics in electrospun TiO_2 nanofibers in air and argon atmospheres".

18th December 2015

To Whom It May Concern

I, Dr. Y. Dong, contributed by project supervision and manuscript editing to the paper/publication entitled

ALBETRAN, H., HAROOSH, H., DONG, Y., PRIDA, V. M., O'CONNOR, B. H., & LOW, I. M. 2014. Phase Transformations and Crystallization Kinetics in Electrospun TiO_2 Nanofibers in Air and Argon Atmospheres. *Applied Physics A*, 116, 161–169.

Undertaken with ALBETRAN, HANI MANSSOR M

(Signature of Co-Author)
Y. Dong

(Signature of First Author)
ALBETRAN, HANI MANSSOR M

Statement of Contribution of Others for "Phase transformations and crystallization kinetics in electrospun TiO_2 nanofibers in air and argon atmospheres".

18th December 2015

To Whom It May Concern

I, Prof. V. M. Prida, contributed by manuscript editing to the paper/publication entitled

ALBETRAN, H., HAROOSH, H., DONG, Y., PRIDA, V. M., O'CONNOR, B. H., & LOW, I. M. 2014. Phase Transformations and Crystallization Kinetics in Electrospun TiO_2 Nanofibers in Air and Argon Atmospheres. *Applied Physics A*, 116, 161–169.

Undertaken with ALBETRAN, HANI MANSSOR M

(Signature of Co-Author)
V. M. Prida

(Signature of First Author)
ALBETRAN, HANI MANSSOR M

Statement of Contribution of Others for "Phase transformations and crystallization kinetics in electrospun TiO_2 nanofibers in air and argon atmospheres".

18th December 2015

To Whom It May Concern

I, E/Prof. B. H. O'Connor, contributed by project supervision and manuscript editing to the paper/publication entitled

ALBETRAN, H., HAROOSH, H., DONG, Y., PRIDA, V. M., O'CONNOR, B. H., & LOW, I. M. 2014. Phase Transformations and Crystallization Kinetics in Electrospun TiO_2 Nanofibers in Air and Argon Atmospheres. *Applied Physics A*, 116, 161–169.

Undertaken with ALBETRAN, HANI MANSSOR M

(Signature of Co-Author)
B. H. O'Connor

(Signature of First Author)
ALBETRAN, HANI MANSSOR M

Statement of Contribution of Others for "Phase transformations and crystallization kinetics in electrospun TiO_2 nanofibers in air and argon atmospheres".

18th December 2015

To Whom It May Concern

I, Prof. I. M. Low, contributed by project supervision and manuscript editing to the paper/publication entitled

ALBETRAN, H., HAROOSH, H., DONG, Y., PRIDA, V. M., O'CONNOR, B. H., & LOW, I. M. 2014. Phase Transformations and Crystallization Kinetics in Electrospun TiO_2 Nanofibers in Air and Argon Atmospheres. *Applied Physics A*, 116, 161–169.

Undertaken with ALBETRAN, HANI MANSSOR M

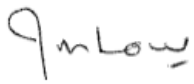

(Signature of Co-Author)
I. M. Low

(Signature of First Author)
ALBETRAN, HANI MANSSOR M

7.2 Appendix III-B: "Statements of Contribution of Others" for "ALBETRAN, H., O'CONNOR, B. H., & LOW, I. M. 2016. Activation Energies for Phase Transformations in Electrospun Titania Nanofibers: Comparing the Influence of Argon and Air Atmospheres. *Applied Physics A*, 122, 1–9".

Statement of Contribution of Others for "Activation Energies for Phase Transformations in Electrospun Titania Nanofibers: Comparing the Influence of Argon and Air Atmospheres".

18th December 2015

To Whom It May Concern

I, E/Prof. B. H. O'Connor, contributed by project supervision and manuscript editing to the paper/publication entitled

ALBETRAN, H., O'CONNOR, B. H., & LCW, I. M. 2016. Activation Energies for Phase Transformations in Electrospun Titania Nanofibers: Comparing the Influence of Argon and Air Atmospheres. *Applied Physics A*, , – . In press

Undertaken with ALBETRAN, HANI MANSSOR M

(Signature of Co-Author)
B. H. O'Connor

(Signature of First Author)
ALBETRAN, HANI MANSSOR M

Statement of Contribution of Others for "Activation Energies for Phase Transformations in Electrospun Titania Nanofibers: Comparing the Influence of Argon and Air Atmospheres".

18th December 2015

To Whom It May Concern

I, Prof. I. M. Low, contributed by project supervision and manuscript editing to the paper/publication entitled

ALBETRAN, H., O'CONNOR, B. H., & LOW, I. M. 2016 Activation Energies for Phase Transformations in Electrospun Titania Nanofibers: Comparing the Influence of Argon and Air Atmospheres. *Applied Physics A*, 122, 1–9.

Undertaken with ALBETRAN, HANI MANSSOR M

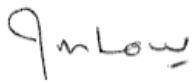

(Signature of Co-Author)
I. M. Low

(Signature of First Author)
ALBETRAN, HANI MANSSOR M

7.3 Appendix III-C: "Statements of Contribution of Others" for "ALBETRAN, H., O'CONNOR, B. H., PRIDA, V. M., & LOW, I. M. 2015. Effect of Vanadium Ion Implantation on the Crystallization Kinetics and Phase Transformation of Electrospun TiO_2 Nanofibers. *Applied Physics A*, 120, 623–634".

Statement of Contribution of Others for "Effect of Vanadium Ion Implantation on the Crystallization Kinetics and Phase Transformation of Electrospun TiO_2 Nanofibers".

18th December 2015

To Whom It May Concern

I, E/Prof. B. H. O'Connor, contributed by project supervision and manuscript editing to the paper/publication entitled

ALBETRAN, H., O'CONNOR, B. H., PRIDA, V. M., & LOW, I. M. 2015. Effect of Vanadium Ion Implantation on the Crystallization Kinetics and Phase Transformation of Electrospun TiO_2 Nanofibers" Applied Physics A, 120, 623–634.

Undertaken with ALBETRAN, HANI MANSSOR M

(Signature of Co-Author)
B. H. O'Connor

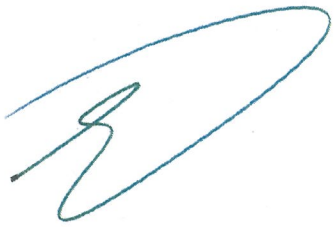

(Signature of First Author)
ALBETRAN, HANI MANSSOR M

Statement of Contribution of Others for "Effect of Vanadium Ion Implantation on the Crystallization Kinetics and Phase Transformation of Electrospun TiO_2 Nanofibers".

18th December 2015

To Whom It May Concern

I, Prof. V. M. Prida, contributed by manuscript editing and assistance with XPS measurement to the paper/publication entitled

ALBETRAN, H., O'CONNOR, B. H., PRIDA, V. M., & LOW, I. M. 2015. Effect of Vanadium Ion Implantation on the Crystallization Kinetics and Phase Transformation of Electrospun TiO_2 Nanofibers. *Applied Physics A*, 120, 623–634.

Undertaken with ALBETRAN, HANI MANSSOR M

(Signature of Co-Author)
V. M. Prida

(Signature of First Author)
ALBETRAN, HANI MANSSOR M

Statement of Contribution of Others for "Effect of Vanadium Ion Implantation on the Crystallization Kinetics and Phase Transformation of Electrospun TiO_2 Nanofibers".

18th December 2015

To Whom It May Concern

I, Prof. I. M. Low, contributed by project supervision and manuscript editing to the paper/publication entitled

ALBETRAN, H., O'CONNOR, B. H., PRIDA, V. M., & LOW, I. M. 2015. Effect of Vanadium Ion Implantation on the Crystallization Kinetics and Phase Transformation of Electrospun TiO_2 Nanofibers. *Applied Physics A*, 120, 623–634.

Undertaken with ALBETRAN, HANI MANSSOR M

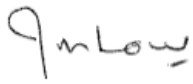

(Signature of Co-Author)
I. M. Low

(Signature of First Author)
ALBETRAN, HANI MANSSOR M

7.4 Appendix III-D: "Statements of Contribution of Others" for "ALBETRAN, H., O'CONNOR, B. H., & LOW, I. M. 2016. Effect of Calcination on Band Gaps for Electrospun Titania Nanofibers Heated in Air–Argon Mixtures. *Materials & Design*, 92, 480–485".

Statement of Contribution of Others for "Effect of Calcination on Band Gap for Electrospun Titania Nanofibers Heated in Air–Argon Mixtures".

18th December 2015

To Whom It May Concern

I, E/Prof. B. H. O'Connor, contributed by project supervision and manuscript editing to the paper/publication entitled

ALBETRAN, H., O'CONNOR, B. H., & LOW, I. M. 2016. Effect of Calcination on Band Gap for Electrospun Titania Nanofibers Heated in Air–Argon Mixtures. *Materials & Design*, 92, 480–485.

Undertaken with ALBETRAN, HANI MANSSOR M

(Signature of Co-Author)
B. H. O'Connor

(Signature of First Author)
ALBETRAN, HANI MANSSOR M

Statement of Contribution of Others for "Effect of Calcination on Band Gap for Electrospun Titania Nanofibers Heated in Air–Argon Mixtures".

18th December 2015

To Whom It May Concern

I, Prof. I. M. Low, contributed by project supervision and manuscript editing to the paper/publication entitled

ALBETRAN, H., O'CONNOR, B. H., & LOW, I. M. 2016. Effect of Calcination on Band Gap for Electrospun Titania Nanofibers Heated in Air–Argon Mixtures. *Materials & Design*, 92, 480–485.

Undertaken with ALBETRAN, HANI MANSSOR M

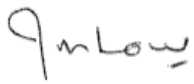

(Signature of Co-Author)
I. M. Low

(Signature of First Author)
ALBETRAN, HANI MANSSOR M

7.5 Appendix III-E: "Statements of Contribution of Others" for "ALBETRAN, H., DONG, Y. & LOW, I. M. 2015. Characterization and Optimization of Electrospun TiO_2/PVP Nanofibers Using Taguchi Design of Experiment Method. *Journal of Asian Ceramic Societies*, 3, 292–300".

Statement of Contribution of Others for "Characterization and Optimization of Electrospun TiO_2/PVP Nanofibers Using Taguchi Design of Experiment Method".

18th December 2015

To Whom It May Concern

I, Dr. Y. Dong, contributed by project supervision and manuscript editing to the paper/publication entitled

ALBETRAN, H., DONG, Y. & LOW, I. M. 2015. Characterization and Optimization of Electrospun TiO_2/PVP Nanofibers Using Taguchi Design of Experiment Method. *Journal of Asian Ceramic Societies*, 3, 292–300.

Undertaken with ALBETRAN, HANI MANSSOR M

(Signature of Co-Author)
Y. Dong

(Signature of First Author)
ALBETRAN, HANI MANSSOR M

Statement of Contribution of Others for "Characterization and Optimization of Electrospun TiO_2/PVP Nanofibers Using Taguchi Design of Experiment Method".

18th December 2015

To Whom It May Concern

I, Prof. I. M. Low, contributed by project supervision and manuscript editing to the paper/publication entitled

ALBETRAN, H., DONG, Y. & LOW, I. M. 2015. Characterization and Optimization of Electrospun TiO_2/PVP Nanofibers Using Taguchi Design of Experiment Method. *Journal of Asian Ceramic Societies*, 3, 292–300.

Undertaken with ALBETRAN, HANI MANSSOR M

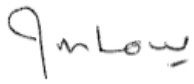

(Signature of Co-Author)
I. M. Low

(Signature of First Author)
ALBETRAN, HANI MANSSOR M

7.6 Appendix III-F: "Statements of Contribution of Others" for "LOW, I. M., ALBETRAN, H., PRIDA, V. M., VEGA, V., MANURUNG, P., & IONESCU, M. 2013. A Comparative Study on Crystallization Behavior, Phase Stability, and Binding Energy in Pure and Cr-Doped TiO_2 Nanotubes. *Journal of Materials Research*, 28, 304–312".

Statement of Contribution of Others for "A Comparative Study on Crystallization Behavior, Phase Stability, and Binding Energy in Pure and Cr-Doped TiO_2 Nanotubes".

18th December 2015

To Whom It May Concern

I, Mr. H. M. Albetran, specialist technical service advice, performing SRD data analysis, and manuscript editing to the paper/publication entitled

LOW, I. M., **ALBETRAN, H**., PRIDA, V. M., VEGA, V., MANURUNG, P., & IONESCU, M. 2013. A Comparative Study on Crystallization Behavior, Phase Stability, and Binding Energy in Pure and Cr-Doped TiO_2 Nanotubes. *Journal of Materials Research*, 28, 304–312.

Undertaken with ALBETRAN, HANI MANSSOR M

(Signature of Co-Author 1)
ALBETRAN, HANI MANSSOR M

(Signature of First Author)
I. M. Low

Statement of Contribution of Others for "A Comparative Study on Crystallization Behavior, Phase Stability, and Binding Energy in Pure and Cr-Doped TiO_2 Nanotubes".

18th December 2015

To Whom It May Concern

I, Prof. V. M. Prida, contributed by providing TiO_2 samples and assistance with XPS measurement to the paper/publication entitled

LOW, I. M., **ALBETRAN, H**., PRIDA, V. M., VEGA, V., MANURUNG, P., & IONESCU, M. 2013. A Comparative Study on Crystallization Behavior, Phase Stability, and Binding Energy in Pure and Cr-Doped TiO_2 Nanotubes. *Journal of Materials Research*, 28, 304–312.

Undertaken with ALBETRAN, HANI MANSSOR M

(Signature of Co-Author 2)
V. M. Prida

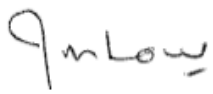

(Signature of First Author)
I. M. Low

Statement of Contribution of Others for "A Comparative Study on Crystallization Behavior, Phase Stability, and Binding Energy in Pure and Cr-Doped TiO_2 Nanotubes".

18th December 2015

To Whom It May Concern

I, Mr. V. Vega, contributed by providing TiO_2 samples and assistance with XPS measurement to the paper/publication entitled

LOW, I. M.,**ALBETRAN, H**., PRIDA, V. M.,VEGA, V., MANURUNG, P.,& IONESCU, M. 2013. A Comparative Study on Crystallization Behavior, Phase Stability, and Binding Energy in Pure and Cr-Doped TiO_2 Nanotubes. Journal of Materials Research, 28, 304–312.

Undertaken with ALBETRAN, HANI MANSSOR M

(Signature of Co-Author 3)
V. Vega

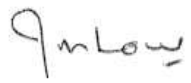

(Signature of First Author)
I. M. Low

Statement of Contribution of Others for "A Comparative Study on Crystallization Behavior, Phase Stability, and Binding Energy in Pure and Cr-Doped TiO_2 Nanotubes".

18th December 2015

To Whom It May Concern

I, P. Manurung, contributed by Performing Rietveld refinement of XRD data to the paper/publication entitled

LOW, I. M., **ALBETRAN, H**., PRIDA, V. M., VEGA, V., MANURUNG, P., & IONESCU, M. 2013. A Comparative Study on Crystallization Behavior, Phase Stability, and Binding Energy in Pure and Cr-Doped TiO_2 Nanotubes. Journal of Materials Research, 28, 304–312.

Undertaken with ALBETRAN, HANI MANSSOR M

(Signature of Co-Author 4)
P. Manurung

(Signature of First Author)
I. M. Low

Statement of Contribution of Others for "A Comparative Study on Crystallization Behavior, Phase Stability, and Binding Energy in Pure and Cr-Doped TiO_2 Nanotubes".

18th December 2015

To Whom It May Concern

I, M. Ionescu, contributed by performing ion-implantation and associated data analysis to the paper/publication entitled

LOW, I. M., **ALBETRAN, H**., PRIDA, V. M., VEGA, V., MANURUNG, P., & IONESCU, M. 2013. A Comparative Study on Crystallization Behavior, Phase Stability, and Binding Energy in Pure and Cr-Doped TiO_2 Nanotubes. *Journal of Materials Research*, 28, 304–312.

Undertaken with ALBETRAN, HANI MANSSOR M

(Signature of Co-Author 5)
M. Ionescu

(Signature of First Author)
I. M. Low

7.7 Appendix III-G: "Statement of Contribution of Others" for "ALBETRAN, H., LOW, I. M. 2016. Effect of Indium Ion Implantation on Crystallization Kinetics and Phase Transformation of Anodized Titania Nanotubes. *Journal of Materials Research*, 31, 1588–1595".

Statement of Contribution of Others for "Effect of Indium Ion Implantation on Crystallization Kinetics and Phase Transformation of Anodized Titania Nanotubes".

28th October 2015

To Whom It May Concern

I, Prof. I. M. Low, contributed by project supervision and manuscript editing to the paper/publication entitled

ALBETRAN, H., LOW, I. M. 2016. Effect of Indium Ion Implantation on Crystallization Kinetics and Phase Transformation of Anodized Titania Nanotubes. *Journal of Materials Research*. 31, 1588–1595.

Undertaken with ALBETRAN, HANI MANSSOR M

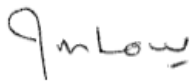

(Signature of Co-Author)
I. M. Low

(Signature of First Author)
ALBETRAN, HANI MANSSOR M

8 Appendix IV: List of Conference papers by the Candidate Relevant to the Thesis but not Forming Part of it

8.1 X-ray Diffraction Study on the *In-Situ* Crystallisation Kinetics in Electrospun PVP/TiO_2 Nanofibers

---

ALBETRAN, H., ALSAFWAN, A., HAROOSH, H., DONG, Y., & LOW, I. M. 2013. X-ray Diffraction Study on the *In-Situ* Crystallisation Kinetics in Electrospun PVP/TiO_2 Nanofibers. Nanostructured Materials and Nanotechnology VII: *Ceramic Engineering and Science Proceedings*, 34, 35–49.

Nanostructured Materials and Nanotechnology VII.
Edited by Sanjay Mathur and Francisco Hernandez-Ramirez.

X-RAY DIFFRACTION STUDY ON THE IN-SITU CRYSTALLISATION KINETICS IN ELECTROSPUN PVP/TiO_2 NANOFIBERS

H. Albetran[1], A. Alsafwan[1], H. Haroosh[2], Y. Dong[3] and I. M. Low[1]

[1]Department of Imaging and Applied Physics, Curtin University, GPO Box U1987, Perth, WA 6845, Australia
[2]Department of Chemical Engineering, Curtin University, GPO Box U1987, Perth, WA 6845, Australia
[3]Department of Mechanical Engineering, Curtin University, GPO Box U1987, Perth, WA 6845, Australia

ABSTRACT

Nanostructured TiO_2 has received much attention recently owing to their promising physical properties for photocatalytic applications. The process of photocatalysis is closely related to the electronic band gap which is controlled by shape, surface area and particle size. Elongated structures such as nanofibres are of particular importance because they can provide a high specific surface area for photocatalysis. In this paper, the effect of atmosphere and doping on the crystallisation kinetics of electrospun TiO_2 nanofibers has been investigated using high-temperature synchrotron radiation diffraction. Electrospun TiO_2 nanofibers were synthesized using titanium isopropoxide, poly (vinyl-pyrrolidone) as a polymer binder, and acetic acid and ethanol as a solvent. Diffraction results showed that the as-synthesized TiO_2 nanofibres were amorphous initially but when heated in air they crystallized to form anatase and rutile at 600 °C and 700 °C respectively. However, in argon atmosphere, anatase and rutile formed simultaneously at 700 °C. In the presence of vanadium dopant, both anatase and rutile formed in concert at 500 °C. The effects of atmosphere and doping on the crystallisation kinetics and phase stability of TiO_2 nanofibres at elevated temperature are discussed.

INTRODUCTION

Titanium dioxide (TiO_2) is an n-type semiconductor material and has two polymorphs in nature, namely anatase and rutile.[1,2] In addition to anatase and rutile, two other phases, brookite and TiO_2 (B) have been reported.[3] TiO_2 is one of the most widely studied materials due to its high photo-activity, photo-durability, mechanical robustness, low cost, chemical, and biological inertness.[4-6] Nanostructured TiO_2 has potential applications in diverse fields, such as transparent conducting electrodes for dye-sensitised solar cells, gas sensors, and photocatalysts for the purification of polluted water and air.[7-9]

Hitherto, various techniques have been used to synthesise nanostructured TiO_2 with various morphologies (e.g. nanoparticles, nanowires, nanorods, nanotubes, and nanofibers) and these include microemulsion, sol-gel, hydrothermal and vapor deposition.[2,10] Elongated structures are of particular importance, as long, thin nanotubes and nanofibers can provide a high specific surface area.[9] Furthermore, a variety of techniques, such as self-assembly, evaporation, anodisation, and electro-spinning, have been developed for fabricating one-dimensional nano-TiO_2.[11] Electro-spinning is a simple, cost-effective technique applicable at industrial levels for fabricating one-dimensional nanofibers.[12-15] For example, electrospun

TiO_2 nanofibers can be synthesized in conjunction with the sol-gel technique whereby a solution of polymer (binder) and TiO_2 precursor is ejected through a needle in a strong electric field to produce amorphous nanofibers.[16-20]

Titanium dioxide is a large band-gap semiconductor with 3.0–3.2 eV of energy, and it is photocatalytically active under UV irradiation. Considerable research has been conducted over the last two decades to develop modified TiO_2 that is active under visible light irradiation.[21-23] Metal or non-metal doping of TiO_2 is a cost-effective and efficient method for decreasing its band gap. Various methodologies have been proposed for doping TiO_2 including magnetron sputtering, oxidation of titanium nitride, sol-gel, and ion implantation.[24-27] Depending on the type and amount of metal used, ion implantation can be employed to synthesize doped-TiO_2 that is active in visible light.[28,29]

In this work, TiO_2 nanofibers were synthesized using electro-spinning, followed by doping with ion-implantation. The effect of atmosphere and doping on the in-situ crystallisation kinetics of TiO_2 nanofibres was investigated using synchrotron radiation diffraction over the temperature range of 25-900 °C.

EXPERIMENTAL PROCEDURE

Sample Preparation

A homogenous sol-gel precursor solution was prepared by mixing titanium isopropxide (M_w=284.22 g/mol, 97% purity, Sigma_Aldrich), acetic acid (M_w=60.05 g/mol, 99.7% purity, Sigma- Aldrich), and ethanol (M_w=46.07 g/mol, 99.5% purity, Sigma-Aldrich) in a fixed volume rate of 1:3:3, respectively. The sol-gel was stirred in a capped bottle for 5 min, then, 10-12 wt% of poly (vinyl pyrrolidone) (PVP) (Mw=1300000 g/mol, 100% purity, Sigma- Aldrich) was dissolved in the solution at 40 °C for one hour using a sugar stirrer. In order to achieve complete dissolution and mixing, the sol-gel solution precursor was stirred ultrasonically for 5 min before it was loaded into a 10 ml plastic syringe with a 25 gauge stainless steel needle. During the electro-spinning process, a high voltage power supply (Gamma, High Voltage Research, Ormond Beach, FL USA) was used to provide 25 KV between the needle and a mesh collector covered by an aluminium foil at a distance of approximately 12 cm. A syringe pump (Chemyx Inc. Stafford, TX USA) was used to control the flow rate at 2 ml/h.

Ion Implantation

Samples of the electrospun PVP/TiO_2 nanofibers were doped with V-ions using ion-implantation. In the process, the samples were exposed to a flux of V-ions directed perpendicular to the sample surface with a dose of ~7 $\times 10^{14}$ ions/cm^2 that corresponds to 8,500 pulses. This phase of work was conducted at the Australian Nuclear Science and Technology Organisation (ANSTO) using a MEVVA Ion Implanter.

In Situ High-Temperature Synchrotron Radiation Diffraction

In this study, the in-situ crystallisation behaviour of electrospun and ion-implanted TiO_2 nanofibers were evaluated using high-temperature synchrotron radiation diffraction (SRD) in air or argon atmosphere. The specimens were mounted and heated using an Anton Parr HTK 16 hot platinum stage. All measurements were conducted at the powder diffraction beamline in conjunction with an Anton Paar HTK20 furnace, and the Mythen II microstrip detector. The SRD data were collected at an incident angle of 3° and wavelength of 0.1126 nm.

The phase transitions or structural changes were simultaneously recorded as SRD patterns. These patterns were acquired at high temperatures over an angular range of 84°.

The SRD patterns were acquired in steps of 100 °C from 200 °C to 900 °C. The collected SRD data were analysed using the commercial Match software to compute the relative abundances of phases formed. In addition, the SRD data were analysed using the CMPR program to evaluate full-width at the maximum intensity (FWHM) for anatase (101) and rutile (110) reflections in order to calculate their crystallite sizes (L) using the Scherrer equation:[30]

$$L = \frac{K\lambda}{\beta \cos\theta} \qquad (1)$$

where K is the shape factor, λ is the x-ray wavelength, β is the FWHM in radians, and θ is the Bragg angle.

Scanning electron microscopy

The morphology of electrospun PVP/TiO_2 nanofibers were examined using an EVO 40XVP scanning electron microscope. Prior to microstructure observation, the sample was coated with platinum to avoid charging. The images were taken with an accelerating voltage of 15 kv at working distances of 4.5 mm and 4 mm for backscattered and secondary electrons, respectively.

RESULTS AND DISCUSSION

Microstructures of Electrospun TiO_2 Nanofibres

Figure 1 shows the SEM image of the as-spun PVP/TiO_2 nanofibers using secondary and backscattered electrons. The nanofibers have a smooth and an individual 1D structure with a random orientation. The diameters of the PVP/TiO_2 nanofibers are approximately 614 ± 190 nm. The nanosized TiO_2 were well-dispersed and encapsulated within the PVP matrix. As can be seen in Figure 2, the SRD patterns of both air and argon atmospheres have a large bump at the room temperature, 200 °C and 300 °C, but it disappeared at 400 °C. It was assigned to the amorphous PVP and other organic substances evaporated completely at 400 °C, which is very similar to the TGA analysis of TiP/PVP nanofibers from the room temperature to around 400 °C in the work of Park and coworkers.[8] The main decomposition of PVP occurred at between 300 °C and 400 °C. So, the PVP polymer has no effect on the crystallization kinetics of electrospun nanofibers because they crystallized to form anatase and rutile at temperatures above 400 °C.

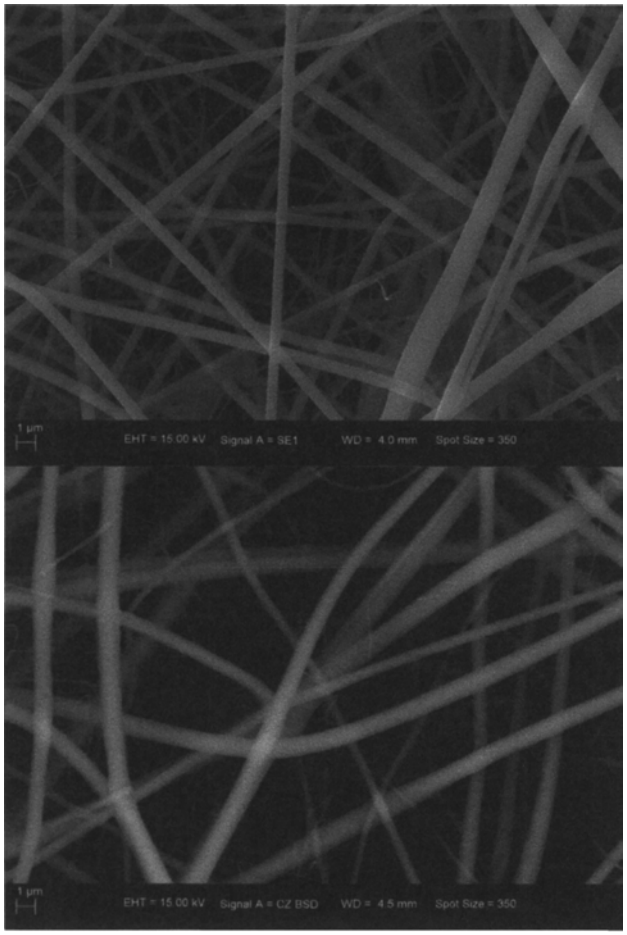

(a)
(b)

Fig. 1: SEM micrographs of as-spun PVP/TiO_2 nanofibers imaged with (a) secondary electrons (b) backscattered electrons.

Effect of Atmosphere

Figure 2 shows the effect of atmosphere on the in-situ crystallisation kinetics of as-synthesized PVP/TiO_2 nanofibers over a temperature range of 25-900 °C as revealed by synchrotron radiation diffraction. The TiO_2 nanofibers were initially amorphous but eventually crystallized to form anatase and rutile at elevated temperatures. The as-spun TiO_2/PVP fibres were amorphous, but the transformation from amorphous TiO_2 into

crystalline phases over the temperature range of 25-900 °C was studied in air and argon. Since PVP and other organic substances evaporated completely during heating in both atmospheres and thus main effect on the crystal growth of anatase and rutile was due to temperature. But, when heated in air they crystallized to form anatase and rutile at 600 °C and 700 °C respectively. However, in argon atmosphere, both anatase and rutile formed simultaneously at 700 °C. This suggests that the crystallisation of anatase was delayed by 100 °C relative to air when an argon atmosphere was used. The reason for this delay in argon atmosphere may be attributed to the lack of oxygen or presence of low oxygen partial pressure (oxygen deficient). It appears that oxygen atoms are essential to promote the transition and transformation from amorphous TiO_2 into anatase. Also, the lack of oxygen in argon atmosphere has not affected the transformation of metastable anatase into rutile. However, the lack of oxygen will inevitably lead to non-stoichiometry in the anatase and rutile formed with a composition of TiO_{2-x} where x is oxygen vacancy. In contrast, anatase and rutile formed in the air will have a stoichiometric composition of TiO_2. The corresponding phase abundances as a function of temperature are shown in Figure 3. In general, anatase dominates in abundance at between 600-800 °C whereas rutile dominates at temperatures greater than 800 °C which commensurate with the gradual transformation of the metastable anatase to rutile.

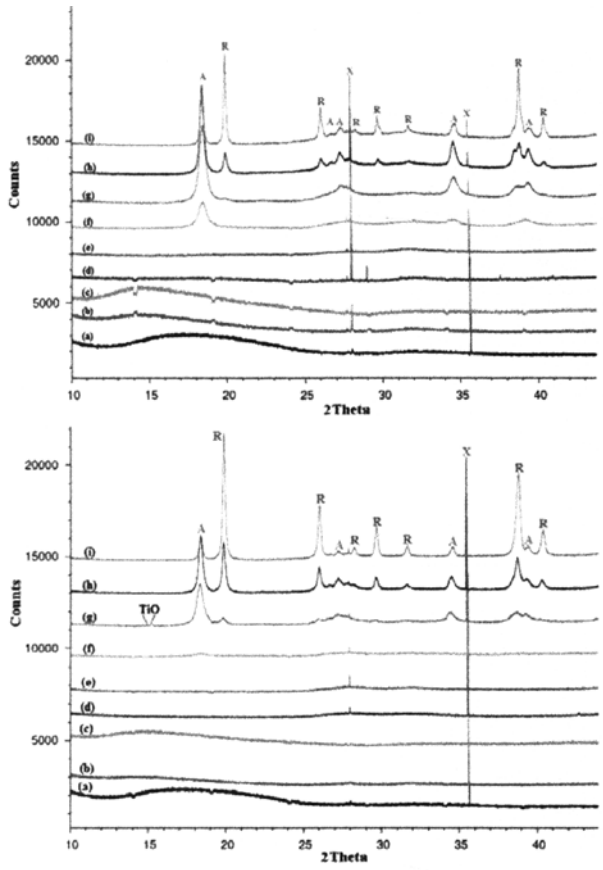

Fig. 2: In-situ synchrotron radiation diffraction plots showing the effect of atmosphere on the crystallisation behaviour of as-synthesized PVP/TiO_2 nanofibers when heated in the temperature range 25 - 900 °C (a) in air, and (b) in argon. [Legend: a = 25°C, b = 200°C, c = 300°C, d = 400°C, e = 500°C, f = 600°C, g = 700°C, h = 800°C, i = 900°C, anatase (A), rutile (R), titanium oxide (TiO) and platinum (X)].

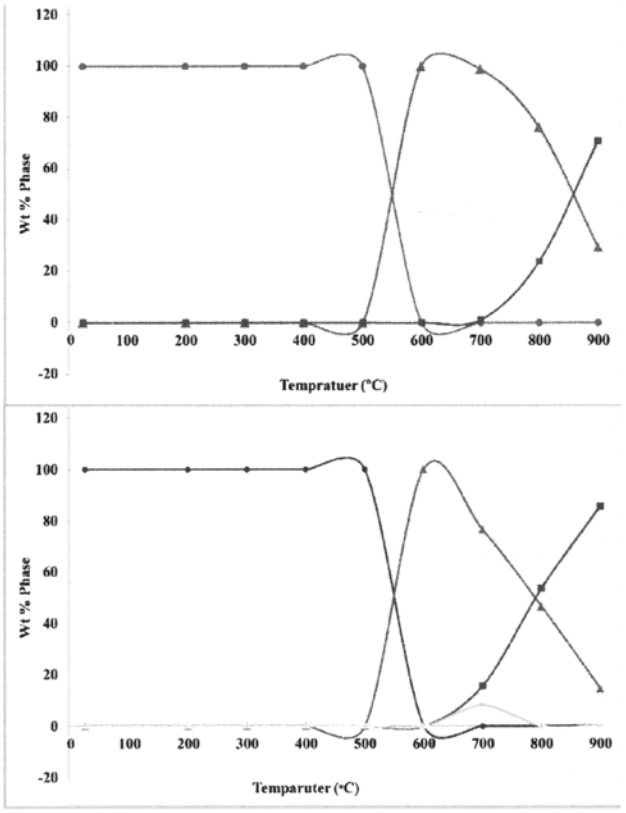

Fig. 3: Phase abundances of anatase, rutile and TiO in the temperature range 25-900 °C for as-synthesized PVP/TiO_2 nanofibers heated in (a) air, and (b) argon. [Legend: Nanofiber (●); anatase (▲); rutile (■); TiO (+)]

The fraction of anatase-to-rutile transformation (x) in the samples calcined at between 700 – 900 °C can be calculated from the following equation:[31]

$$x = 1/[1 + 0.8(I_A / I_R)] \qquad (2)$$

where I_A and I_R are the X-ray integrated intensities of anatase (101) reflection and rutile (110) reflection respectively. Table 1 shows the fraction of anatase to rutile transformation

as a function of temperature in air and in argon. It is evident that the weight fraction of rutile increased dramatically as the temperature increased by virtue of the transformation of metastable anatase to rutile at elevated temperature. The rate of anatase to rutile transformation was also observed to increase faster in argon than in air.

Table 1: Effect of atmosphere on the fraction of anatase to rutile transformation in as-synthesized PVP/TiO_2 nanofibers at various temperatures.

Temperature (°C)	*x*% (Air)	*x*% (Argon)
700	1.5	9.2
800	19.2	46.5
900	63.0	84.5

The apparent crystallite sizes of the anatase (101) and rutile (110) reflections were calculated from the Scherrer equation, where the contribution of strains on peak broadening has been ignored. Figure 4 shows the effect of atmosphere on the crystal growth of anatase and rutile at various temperatures. The crystallite size of anatase was just under 10 nm at 600 °C in the air which increased to just over 25 nm at 900 °C. However, the type of atmosphere had no appreciable effect on the crystal growth of anatase. In contrast, atmosphere had a noticebale effect on the crystal growth of rutile but only at 900 °C. The crystallite size of rutile was ~18 nm in both air and argon, but increased with the temperature to 39 nm in air and only 31 nm in argon.

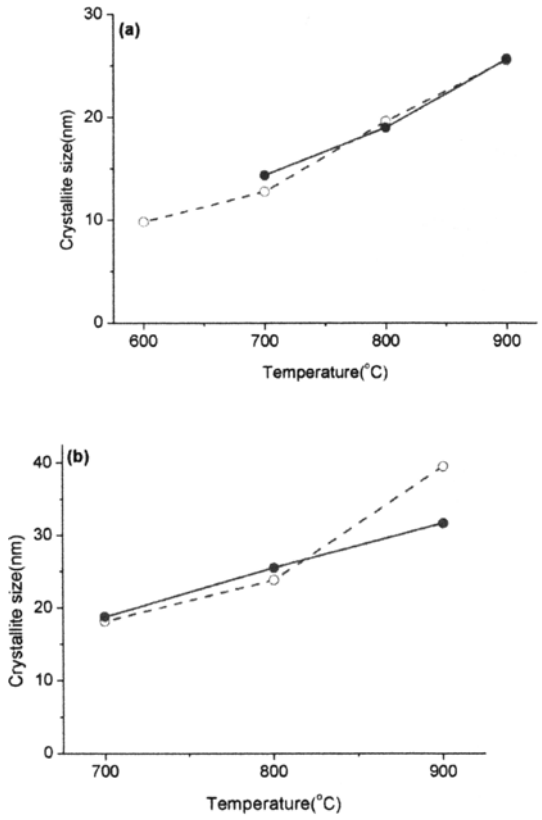

Fig. 4: Effect of atmosphere on the crystallite size of (a) anatase and (b) rutile in PVP/TiO_2 nanofibers at various temperatures. [Legend: Air (○); Argon (●)]

Effect of Doping

Figure 5 illustrates the stacked diffraction plots of V-doped electrospun TiO_2 nanofibers in air over the temperature range of 25-900 °C. The TiO_2 nanofibers were initially amorphous until 400C before they crystallized to form anatase and rutile simultaneously at 500 °C which is 100 °C lower for anatase and 200 °C lower for rutile when compared to un-doped TiO_2 nanofibers. These results are consistent with our previous observation for un-doped and Cr-doped TiO_2 nanotubes where doping lowered the crystallisation temperature of anatase from 600 to 400°C and rutile from 600 to 500°C.[4] The corresponding phase abundances as a function of temperature are shown in Figure 6. Here, rutile dominates and increases in abundance at 500-900 °C which commensurate with the gradual

transformation of the metastable anatase to rutile. At 900 °C, almost all the metastable anatse has completely transformed to rutile.

Table 2 shows the effect of doping on the fraction of anatase to rutile transformation as a function of temperature. It is evident in the presence of V-dopant, the weight fraction of rutile increased very dramatically due to the transformation of metastable anatase to rutile at elevated temperatures. It appears that V-doping has accelerated the formation of anatase and rutile at a lower temperature, probably through the facilitation of defects such as vacancies. It is widely accepted that the onset temperature of the anatase to rutile phase transformation and the rate at which it proceeds can be affected significantly by dopants, firing atmosphere, microstructure, sample morphology, and the presence of impurities in the material.[32,33] The process of the anatase to rutile transformation is known to occur via (a) the nucleation of rutile at point defects, oxygen vacancies, secondary phase inclusions, particle surfaces, and/or at (112) twin interfaces in anatase and (b) the subsequent consumption of the anatase phase by the growing rutile phase. The formation of rutile from the metastable phase anatase is reconstructive and so takes place through atomic rearrangement involving the breaking of two of the six Ti-O bonds in the TiO_6 octahedra.[33] As anatase transforms into rutile, significant grain growth takes place, resulting in lower surface area and thus poorer photocatalytic performance.

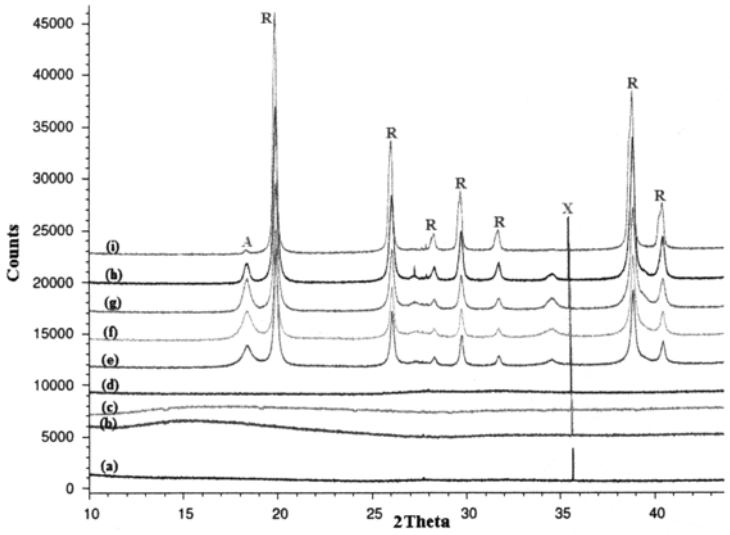

Fig. 5: High-temperature SRD in air atmosphere plots for V-doped electrospun PVP/TiO_2 nanofibers showing the in situ crystallization of both anatase and rutile from the amorphous TiO_2 in the

temperature range 25-900 °C. [Legend: a = 25°C, b = 200°C, c = 300°C, d = 400°C, e = 500°C, f = 600°C, g = 700°C, h = 800°C, i = 900°C, anatase (A), rutile (R) and platinum (X)].

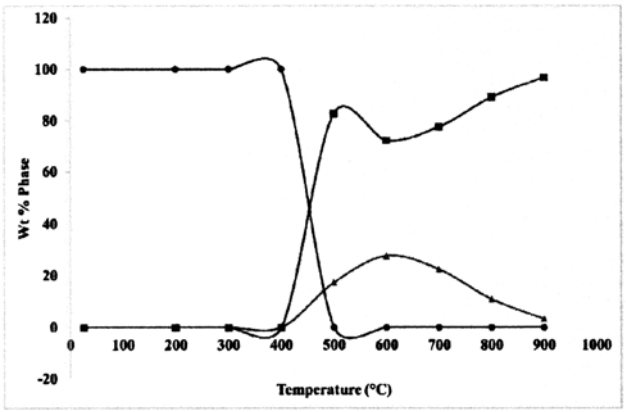

Fig. 6: Phase abundances of anatase and rutile in the temperature range 25-900 °C for V-doped PVP/TiO_2 nanofibers heated in air. [Legend: Nanofiber (●); anatase (▲); rutile (■)].

Table 2: Effect of doping on the fraction of anatase to rutile transformation in as-synthesized and V-doped PVP/TiO_2 nanofibers at various temperatures.

Temperature (°C)	*x*% (un-doped)	*x*% (doped)
500	0	76.3
600	0	66.6
700	1.5	77.4
800	19.2	91.2
900	63.0	99.2

Figure 7 shows the effect of doping on the crystal growth of anatase and rutile at elevated temperatures. The crystallite size of doped anatase was ~12 nm at 500 °C and increased rapidly to 25 nm at 900 °C. It appears that the effect of V-doping on crystallite size was only apparent at 700 and 800 °C where doping caused a moderate increase in size of anatase. Although the crystallite size of doped rutile was signifcantly larger than doped anatase at 500 °C, the crystallite size of the former remained fairly constant, indicating no crystal growth despite an increase in temperature.

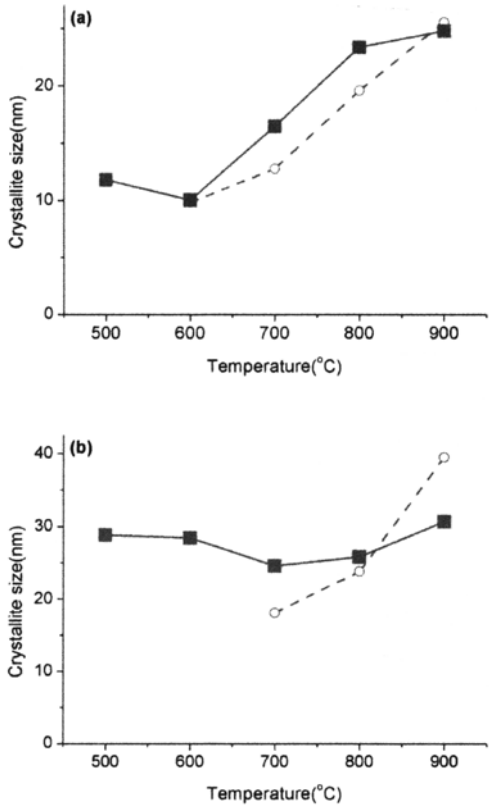

Fig. 7: Effect of doping on the crystallite size of (a) anatase and (b) rutile in PVP/TiO_2 nanofibres at various temperatures. [Legend: un-doped (○); V-doped (■)]

CONCLUSIONS

The in-situ crystallisation behaviour of electrospun PVP/TiO_2 nanofibers was investigated using high-resolution synchrotron radiation diffraction in the temperature range 20-900 °C in terms of atmosphere and doping. In all cases, PVP/TiO_2 nanofibers were initially amorphous but crystallized to anatase and rutile at elevated temperatures. Both atmosphere and doping have a significant influence on the crystallisation kinetics of anatase and rutile. In air, anatase and rutile formed at 600 °C and 700 °C respectively but in argon they formed simultaneously at 700 °C. When doped with V ions, simultaneous formation of anatase and rutile occurred at 500 °C. The crystallite sizes of anatase and rutile were only moderately affected by V-doping or argon atmosphere. In contrast, the rates of anatase to rutile transformation were significantly enhanced due to V-doping and annealing in argon atmosphere, probably through the facilitation of defects such as vacancies.

ACKNOWLEDGMENTS

We are gratefully to the Australian Synchrotron (AS122/PDFI/5075) and the Australian Institute of Nuclear Science and Engineering (ALNGRA11135) for funding this work. We thank Dr. M. Ionescu of ANSTO and Ms. E. Miller of Curtin University for assistance with ion-implantation and SEM respectively.

REFERENCES

[1]G. Liu, L. Wang, H.G. Yang, H.M. Cheng and G.Q. M. Lu, Titania-based photocatalysts-crystal growth, doping and heterostructuring. *J. Mater. Chem.* **20**, 831-843 (2010).
[2]S. Chuangchote, J. Jitputti, T. Sagawa and S. Yoshikawa, Photocatalytic activity for hydrogen evolution of electrospun TiO_2 nanofibers. *ACS Applied Materials & Interfaces.* **1**, 1140-1143 (2009).
[3]V.J. Babu, A.S. Nair, Z. Peining and S. Ramakrishna, Synthesis and characterization of rice grains like nitrogen-doped TiO_2 nanostructures by electrospinning-photocatalysis. *Materials Letters.* **65**, 3064-3068 (2011).
[4]I.M. Low, H. Albetran, V.M. Prida, V. Vega, P. Manurung and M. Ionescu, A comparative study on crystallization behavior, phase stability, and binding energy in pure and Cr-doped TiO_2 nanotubes. *J. Mater. Res.* **27**,1-9 (2012).
[5]P. Manurung, Y. Putri, W. Simanjuntak and I.M. Low, Synthesis and characterisation of chemical bath deposited TiO_2 thin-films. *Ceramics International.* **39**, 255-259 (2013).
[6]P. Zhang, C. Shao, X. Li, M. Zhang, X. Zhang, Y. Sun and Y. Liu, In situ assembly of well-dispersed au nanoparticles on TiO_2/ZnO nanofibers: A three-way synergistic heterostructure with enhanced photocatalytic activity. *Journal of Hazardous Materials.* **237-238**, 331-338 (2012).
[7]Z.R. Tang, F. Li, Y. Zhang, X. Fu and Y.J. Xu, Composites of titanate nanotube and carbon nanotube as photocatalyst with high mineralization ratio for gas-phase degradation of volatile aromatic pollutant. *J. Phys. Chem.* C **115**, 7880-7886 (2011).
[8]J.Y. Park, J.J. Yun, C.H. Hwang and I.H. Lee, Influence of silver doping on the phase transformation and crystallite growth of electrospun TiO_2 nanofibers. *Materials Letters.* **64**, 2692-2695 (2010).
[9]D.V. Bavykin and F.C. Walsh, *Titanate and Titania Nanotubes Synthesis, Properties and Applications*, RSC Publishing,. pp. 50-81 (2010).
[10]J.M. Low, B. Curtain, M. Philipps, Q.Z. Liu and M. Ionescu, High temperature diffraction study of in-situ crystallization of nanostructured TiO_2 photocatalysts. *Journal of the Australian Ceramic Society.* **48**, 198-204 (2012).
[11]A. Kumar, R. Jose, K. Fujihara, J. Wang and S. Ramakrishna, Structural and optical properties of electrospun TiO_2 nanofibers. *Chem. Mater.* **19**, 6536-6542 (2007).

[12]P. Zhu., A.S. Nair, P. Shengjie,Y. Shengyuan, and S. Ramakrishna, Facile fabrication of TiO_2-graphene composite with enhanced photovoltaic and photocatalytic properties by electrospinning. *ACS Appl Mater. Interfaces.* **4**, 581-585 (2012).
[13]C.M. Wu, H.G. Chiou, S.L. Lin and J.M. Lin, Effects of electrostatic polarity and the types of electrical charging on electrospinning behavior. *Journal of Applied Polymer Science.* **126**, E89-E97(2012).
[14]S.S. Lee, H. Bai, Z. Liu and D.D. Sun, Electrospun TiO_2/SnO_2 nanofibers with innovative structure and chemical properties for highly efficient photocatalytic H_2 generation. *International Journal Of Hydrogen Energy.* **37**, 10575-10584 (2012).
[15]M.S. Hassan, T. Amna, O.B. Yang, H. Kim and M.S. Khil, TiO_2 nanofibers doped with rare earth elements and their photocatalytic activity. *Ceramics International.* **38**, 5925-5930 (2012).
[16]Z.M. Huang, Y.Z. Zhang, M. Kotaki and S. Ramakrishna, A review on polymer nanofibers by electrospinning and their applications in nanocomposites. *Composites Science and Technology.* **63**, 2223-2253 (2003).
[17]Q. Li, D.J.G. Satur, H. Kim and H.G. Kim, Preparation of sol–gel modified electrospun TiO_2 nanofibers for improved photocatalytic decomposition of ethylene. *Materials Letters.* **76**, 169-172 (2012).
[18]W. Luo, X. Hu, Y. Sun and Y. Huang, Surface modification of electrospun TiO_2 nanofibers via layer-by-layer self-assembly for high-performance lithium-ion batteries. *J. Mater. Chem.* **22**, 4910-4915 (2012).
[19]C. Wessel, R. Ostermann, R. Dersch and B.M. Smarsly, Formation of inorganic nanofibers from preformed TiO_2 nanoparticles via electrospinning. *J. Phys. Chem.* C **115**, 362-372 (2011).
[20]H. Li, W. Zhang and W. Pan, Enhanced photocatalytic activity of electrospun TiO_2 nanofibers with optimal anatase/rutile ratio. *J Am. Ceram Soc.* **94**, 3184-3187 (2011).
[21]D. D. Guo, S. S. Lin, F. X. Zhong, Y. N. Zhu and Z. P. Meng, High-efficiency degradation sugar wastewater by Co-TiO_2 nanotube arrays. *Integrated Ferroelectrics.* **137**, 10-17 (2012).
[22]P.V. Kamat, TiO_2 nanostructures: recent physical chemistry advances. *J. Phys. Chem.* C **116**, 11849-11851 (2012).
[23]R. Kralchevska, M. Milanova, D. Hristov, A. Pintar and D. Todorovsky, Synthesis, characterization and photocatalytic activity of neodymium, nitrogen and neodymium-nitrogen doped TiO_2. *Materials Research Bulletin* **47**, 2165-2177 (2012).
[24]X.L. Yang, Z. Li, L.M. Yang, W.Y. Zhou and Y.H. Xu, Preparation and photocatalytic activity of neodymium doping titania loaded to silicon dioxide. *Trans. Nonferrous Met. Soc. China.* **21**, 335-339 (2011).
[25]V.J. Babu, M.K. Kumar, A.S. Nair, T.L. Kheng, S.I. Allakhverdiev and S. Ramakrishna, Visible light photocatalytic water splitting for hydrogen production from N-TiO_2 rice grain shaped electrospun nanostructures. *International Journal Of Hydrogen Energy.* **37**, 8897-8904 (2012).
[26]M. Samadi, H.A. Shivaee, M. Zanetti, A. Pourjavadi and A. Moshfegh, Visible light photocatalytic activity of novel MWCNT-doped ZnO electrospun nanofibers. *Journal of Molecular Catalysis A: Chemical.* **359**, 42-48 (2012).
[27]J. Xu, W. Wang, M. Shang, E. Gao, Z. Zhang and J. Ren, Electrospun nanofibers of Bi-doped TiO_2 with high photocatalytic activity under visible light irradiation. *Journal of Hazardous Materials.* **196**, 426-430 (2011).
[28]R. Zhang, H. Wu, D. Lin and W. Pan, Photocatalytic and magnetic properties of the Fe-TiO_2/SnO_2 nanofiber via electrospinning. *J. Am. Ceram. Soc.* **93**, 605-608 (2010).
[29]R.C.W. Lam, M.K.H. Leung, D.Y.C. Leung, L.L.P. Vrijmoed, W.C. Yam and S.P. Ng, Visible-light-assisted photocatalytic degradation of gaseous formaldehyde by parallel-plate reactor coated with Cr ion-implanted TiO_2 thin film. *Solar Energy Materials and Solar Cells.* **91**, 54-61 (2007).

[30]B.D. Cullity and S.R. Stock, *Elements of X-ray Diffraction*, 3rd., Prentice- Hall Inc., pp. 167-171 (2001).
[31]R.A. Spurr and H. Myers, Quantitative analysis of anatase-rutile mixtures with an x-ray diffractometer. *Anal. Chem.* **29**, 760-762 (1957).
[32]D. Hanaor and C. Sorrell, Review of the anatase to rutile phase transformation. *J. Mater. Sci.* **46**, 855-874 (2011)
[33]S. Riyas, G. Krishnan, and P.N. Mohandas, Anatase-rutile transformation in doped titania under argon and hydrogen atmospheres. *Adv. Appl. Ceram.* **106**, 255-264 (2007).

8.2 Effect of Atmosphere on Crystallization Kinetics and Phase Relations in Electrospun TiO_2 Nanofibers

---

ALBETRAN, H., HAROOSH, H., DONG, Y., O'Connor, B. H., & LOW, I. M. 2014. Effect of Atmosphere on Crystallization Kinetics and Phase Relations in Electrospun TiO_2 Nanofibers. *Ceramics for Environmental and Energy Applications II: Ceramic Engineering and Science Proceedings*, 246, 125–133.

Ceramics for Environmental and Energy Applications II.
Edited by Fatih Dogan, Terry M. Tritt, Tohru Sekino, Yutai Katoh,
Aleksander J. Pyzik, Ilias Belharouak, Aldo R. Boccaccini and James Marra.

EFFECT OF ATMOSPHERE ON CRYSTALLISATION KINETICS AND PHASE RELATIONS IN ELECTROSPUN TiO_2 NANOFIBRES

H. Albetran[a,b], H. Haroosh[c], Y. Dong[d], B.H. O'Connor[a] and I.M. Low[a]
[a] Department of Imaging and Applied Physics, Curtin University, Perth, WA 6845, Australia
[b] Department of Physics, College of Education, University of Dammam, Dammam 31451, Saudi Arabia.
[c] Department of Chemical Engineering, Curtin University, Perth, WA 6845, Australia
[d] Department of Mechanical Engineering, Curtin University, Perth, WA 6845, Australia

ABSTRACT

Titanium dioxide has received much attention as an important photocatalytic material. In this paper, the effects of air and argon atmosphere on the crystallisation kinetics and phase relations in electrospun TiO_2 nanofibres have been investigated using high- temperature synchrotron radiation diffraction. Diffraction results showed that as-synthesized TiO_2 was amorphous initially, but when heated in air or argon atmosphere they crystallized to form anatase and rutile at different temperatures and in different rates. The crystallisation of anatase was delayed by 100 °C in argon when compared to in air. However, the transform rate of anatase to rutile was faster in argon than in air.

INTRODUCTION

Titanium dioxide (TiO_2) is one of the most widely studied materials due to its high photo-activity, photo-durability, mechanical robustness, low cost, and chemical and biological inertness.[1-6] Titanium dioxide TiO_2, has three polymorphs: anatase, brookite, and rutile.[7-10] Anatase and rutile are two main polymorphs that exhibit different properties and thus different photocatalytic performances. They have the same tetragonal crystal structure, but a different space group and atoms per unit cell, which are (*I4/amd*) and 4 for anatase, and ($P4_2/mnm$) and 2 for rutile.[9,11] Moreover, at room temperature, the lattice parameters of anatase are a = b = 3.785Å and c = 9.514Å, while for rutile are a = b = 4.594Å and c = 2.9589Å.[12] These differences in the spacing between the atom and crystal structures for anatase and rutile can cause a different electronic band structure and mass densities. In general, anatase is considered more photochemically active than rutile by virtue of its lower rates of recombination and higher surface absorptive capacity.[13] However, recent work has indicated that a mixed-phase photocatalyst tends to make a better photocatalyst than single- phase titania. For example, a mixed powder of 70% anatase and 30% rutile has been found as the best photocatalyst for the wastewater treatment.[14] Similarly, commercial TiO_2 photocatalyst (P-25) that contains 80 wt% anatase and 20 wt% rutile has been observed to exhibit excellent photocatalytic reactions.[12]

The optimal composition of the photocatalyst phase of anatase and rutile can be prepared by thermal annealing. In general, metastable anatase is formed at lower temperatures than stable rutile, but it is transformed dramatically to rutile at higher temperatures.[15,16] This transformation is affected by several parameters which include the synthesis method, amount of impurities, temperature, calcination time and atmospheres.[15,17] Reaction atmospheres have been observed to have a significant influence on the thermal transformation of titania phases because oxygen defect levels

and interstitial titanium ions are influenced by the type of atmosphere.[15,18] For TiO_2 powders at a particular temperature, the effects of air, vacuum, argon, argon- chlorine mixture, hydrogen, steam and nitrogen on the anatase to rutile transformation have been studied.[18] Similarly, for titania films, the amorphous to anatase and anatase to rutile transformations were observed to occur at a lower temperature when annealed in hydrogen atmosphere than in air or vacuum.[19] The rate of anatase to rutile transformation was found to decrease in vacuum but increase in hydrogen atmosphere due to the formation of titanium interstitials that inhibited the transformation or oxygen vacancies which accelerated the transformation.[15,18]

Nanostructured titania with a noble morphology exhibit high surface area-to-volume ratio which is of great significance for increasing the decomposition rate of organic pollutants because photocatalytic reactions take place rapidly and drastically on the surface of the catalyst.[14,20] Hitherto, various techniques have been used to synthesise nanostructured TiO_2 with various morphologies (e.g. nanoparticles, nanowires, nanorods, nanotubes, and nanofibres) and these include microemulsion, sol-gel, hydrothermal and vapor deposition methods.[8,21] Elongated structures are of particular importance, as long, thin nanotubes and nanofibres can provide a high specific surface area.[9] Furthermore, a variety of techniques, such as self-assembly, evaporation, anodisation, and electro-spinning, have been developed for fabricating one-dimensional nano-TiO_2.[1,22] Among the fabrication methods, electro-spinning is a simple, and cost-effective technique applicable at industrial levels for fabricating one-dimensional nanofibres.[2] TiO_2 nanofibres can be synthesised by combining this technique with the sol-gel technique.[23] In this process, a solution of polymer (binder) and TiO_2 precursor is ejected through a needle in a high voltage electric field (kilovolts per centimetre) whereby composite nanofibres of polymer and amorphous TiO_2 nanofibres are formed.[24-28] The diameter, morphology and grain size of the TiO_2 nanofibres have optimal values for photocatalytic activity and are directly affected by the electro-spinning parameters. To the best of the authors knowledge, the effect of atmospheres on the in-situ crystallisation of anatase and rutile in electrospun TiO_2 nanofibres has not been reported.

In the present work, the effect of air and argon atmosphere on the transformation of anatase to rutile and the in-situ crystallisation kinetics of TiO_2 nanofibres was investigated using synchrotron radiation diffraction over the temperature range of 25-900 °C. TiO_2 nanofibres were synthesized using electro-spinning and their morphology, structure and composition were characterised by scanning electron microscopy and synchrotron radiation diffraction.

EXPERIMENTAL PROCEDURE

Material Synthesis

A homogenous sol-gel precursor solution was prepared by mixing titanium isopropxide (M_w = 284.22 g/mol, 97% purity), acetic acid (M_w = 60.05 g/mol, 99.7% purity), and ethanol (M_w = 46.07 g/mol, 99.5% purity) in a fixed volume ratio of 1:3:3, respectively. The sol- gel was stirred in a capped bottle for 5 min, then, 10-12 wt% of poly (vinyl pyrrolidone) (PVP) (M_w = 1300000 g/mol, 100% purity) was dissolved in the solution at 40 °C for 1h using a stirrer. In order to achieve complete dissolution and mixing, the sol-gel solution precursor was stirred ultrasonically for 5 min before it was loaded into a 10 ml plastic syringe with a 25-gauge stainless steel needle. During the electrospinning process, a high voltage power supply was used to provide 25 kV

between the needle and a mesh collector covered by an aluminium foil at a distance of approximately 12 cm. A syringe pump was used to control the flow rate at 2 ml/h.

In Situ High-Temperature Synchrotron Radiation Diffraction

In this study, the in-situ crystallisation behaviour of electrospun TiO_2 nanofibres was evaluated using high-temperature synchrotron radiation diffraction (SRD) in air or in argon atmosphere. The specimens were mounted and heated using an Anton Parr HTK 16 hot platinum stage. All measurements were conducted at the powder diffraction beamline in conjunction with an Anton Paar HTK20 furnace, and the Mythen II microstrip detector. The SRD data were collected at an incident angle of 3° and wavelength of 1.125995 Å.

The phase transitions or structural changes were simultaneously recorded as SRD patterns. These patterns were acquired at high temperatures over an angular range of 84°. The SRD patterns were acquired in steps of 100 °C from 200°C to 900°C. The collected SRD data was analysed using Rietveld refinement methods and was carried out using commercial Rietica 2.1 software to compute the relative abundances, crystallite size, and lattice parameters of anatase and rutile.[29] Rietica 2.1 and CMPR programs were used to evaluate the full-width at the maximum intensity (FWHM) to calculate their crystallite sizes (L) using the Scherrer equation:[30]

$$L = \frac{K\lambda}{\beta \cos\theta} \tag{1}$$

$$FWHM^2 = U\tan^2\theta + V\tan\theta + W \tag{2}$$

where K is the shape factor, λ is the x-ray wavelength, θ is the Bragg angle, and β is the FWHM in radians, which can be calculated from equation (2). Rietica 2.1 was used to calculate the peak shape parameters U, V, and W.

Scanning Electron Microscopy

The morphology of electrospun TiO_2 nanofibres before and after the thermal annealing was examined using an EVO 40XVP scanning electron microscope with an accelerating voltage of 15 keV. Prior to microstructure observation, the samples were coated with platinum to avoid charging. The SEM images of both as–spun and annealed nanofibres were taken using secondary electrons and backscattered at working distances of 4 mm and 4.5 mm, respectively.

RESULTS AND DISCUSSION

Microstructures of Electrospun TiO_2 Nanofibres

Figure 1 illustrates the images of as-spun pure nanofibres using secondary and backscattered electrons before thermal annealing. The nanofibres have a smooth surface and individual lengths of one-dimensional structure with random orientation. The average diameters of 30 electrospun TiO_2/PVP composite nanofibres were determined to be 614 ± 190 nm and the nanosized TiO_2 were well dispersed and embedded within the PVP matrix as shown in Figure 1b.

As shown in Figure 1(c, d), after thermal annealing at 900 °C, the average diameters of the sintered TiO2 nanofibres shrank by 48.5 % in air and 80.5% in argon because the organic

material evaporated completely during heating. The average diameters of 30 nanofibers were 298 ± 115 nm in atmospheric air and 120 ± 35 nm in argon. However, in air atmospheres, the fibres were broken and rougher while in argon they were still quite smooth, which indicated more brittleness nature of as-spun TiO_2 nanofibres in air. One possible reason is that an oxidation of the PVP polymer in air atmosphere which contains about 20% of oxygen causes damage and bond breaking in the chain. Moreover, it reduced the molecular weight of the polymer and also the mechanical properties like tensile stress to become weaker. However, argon is an ideal monatomic gas, that is, a gas containing just one atom per molecule and it is an inert atmosphere. However, it is also possible that the sample was damaged during preparation for SEM observation.

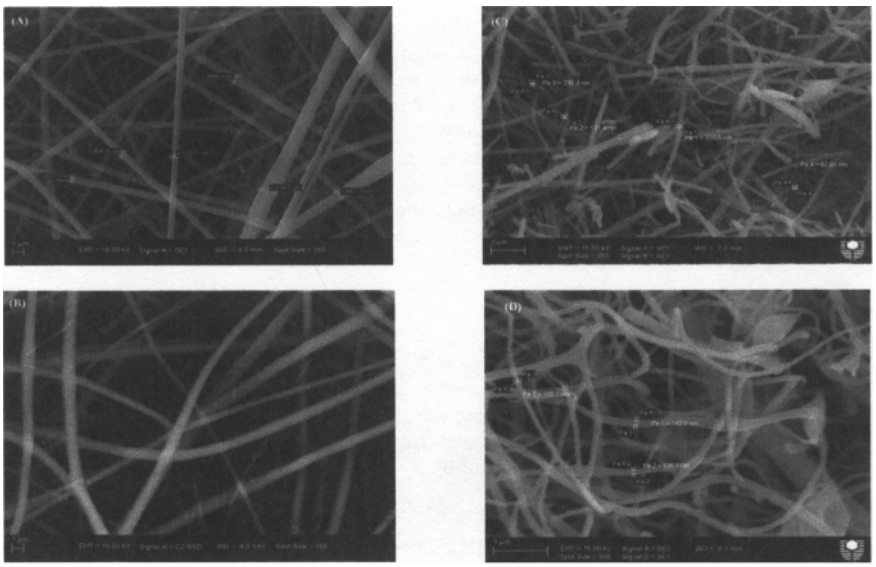

Fig. 1: SEM micrographs of as- spun pure TiO_2 nanofibres imaged with (a) secondary electrons (b) backscattered electron; and after thermal annealing in atmospheric (c) Air (d) Argon.

Effect of Atmosphere

Figure 2 shows the effect of atmosphere on the in-situ crystallisation kinetics of as-synthesized TiO_2 nanofibres over a temperature range of 25-900 °C, as revealed by synchrotron radiation diffraction. The TiO_2 nanofibres were initially amorphous but eventually crystallized to form anatase and rutile at elevated temperatures. When heated in air they crystallized to form anatase and rutile at 600 °C and 700 °C, respectively. However, in argon atmosphere, both anatase and rutile formed simultaneously at 700 °C. This suggests that the crystallisation of anatase was delayed by 100 °C relative to air when argon atmosphere was used. The reason for this delay in the argon atmosphere may be attributed to the presence of low oxygen partial pressure. It appears that oxygen atoms are essential to promote the transition and transformation from amorphous TiO_2 into anatase. But the lack of oxygen in argon atmosphere did not

affect the transformation of metastable anatase into rutile. However, the lack of oxygen will inevitably lead to non-stoichiometry in the anatase and rutile formed with a composition of TiO_{2-x}, where x is oxygen vacancy. In contrast, anatase and rutile formed in the air will have a stoichiometric composition of TiO_2.

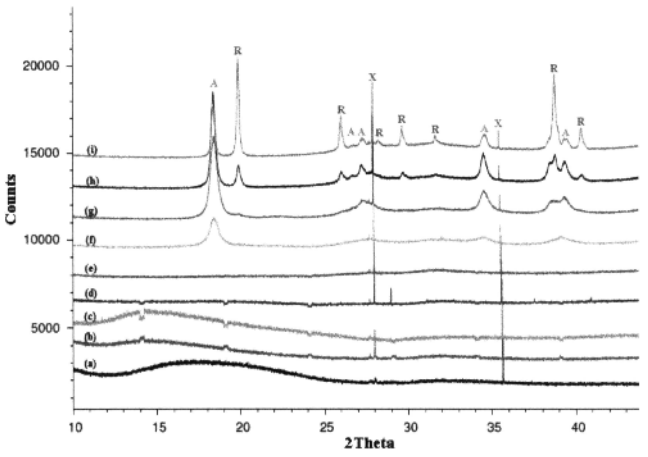

(a)

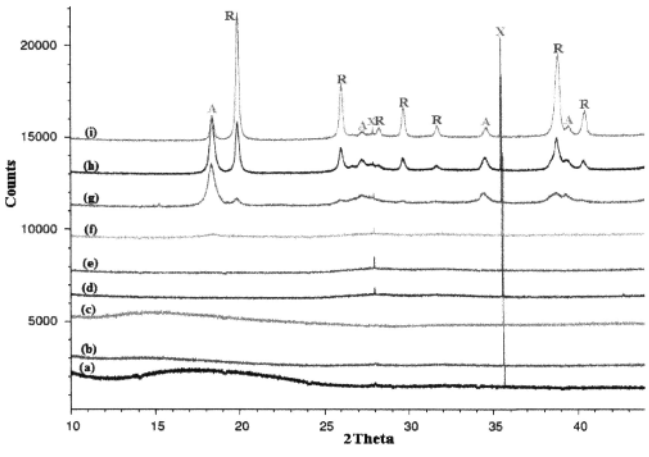

(b)

Fig. 2: In-situ SRD plots showing the effect of atmosphere on the crystallisation behaviour of as-synthesized TiO_2 nanofibres when heated in the temperature range 25-900 °C (a) in the air, and (b) in argon. [Legend: a=25°C, b=200°C, c=300°C, d=400°C, e=500°C, f=600°C, g=700°C, h= 800°C, i=900°C, anatase (A), rutile (R) and platinum (X)].

The Rietveld method was used to evaluate the phase abundance of anatase and rutile during the transformation in the air and argon atmospheres. Figure 3a shows the comparison of anatase phase content in both atmospheres as a function of temperature. At 600 °C, only anatase formed in air atmosphere. In argon atmosphere, 85% of anatase formed at 700 °C, which is 15% less than in air for the same temperature. Figure 3b shows the phase content of rutile increased dramatically as the temperature increased by virtue of the transformation of metastable anatase to rutile. Rutile formed at 700 °C in both atmospheres but with different abundances. It increased from about 15% at 700 °C to well over 85% at 900 °C in the argon atmosphere. However, in air, it increased from 4% to 65% for the same temperature range.

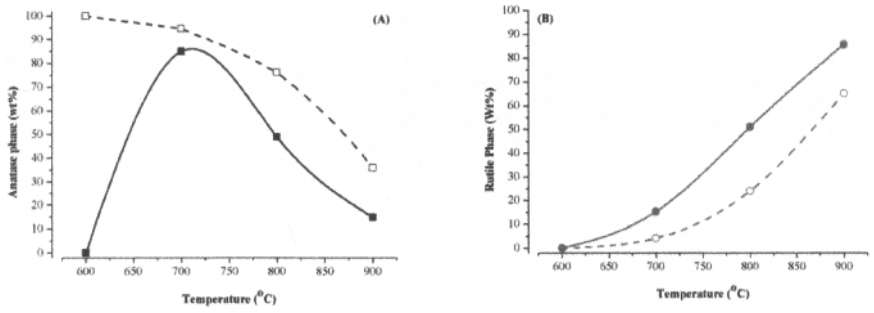

Fig. 3: Phase abundances of anatase and rutile in the temperature range 25-900 °C for as-synthesized TiO_2 nanofibres heated in (a) air, and (b) argon. [Legend: anatase in air (□); anatase in argon (■); rutile in air (○); rutile in argon (•)]

The crystallite sizes of the anatase and rutile were calculated from the Scherrer equation using Rietica 2.1 programs to evaluate the average full-width at the maximum intensity (FWHM). Figure 4 shows the effect of atmosphere on the crystal growth of anatase and rutile at various temperatures. The crystallite size of anatase was just under 10 nm at 600 °C in air and increased to just over 25 nm at 900 °C. However, atmosphere had no appreciable effect on the crystal growth of anatase. In contrast, the atmosphere had a noticeable effect on the crystal growth of rutile but only at 900 °C. The crystallite size of rutile was ~18 nm in both air and argon but increased to ~39 nm in air and 31 nm in argon.

The variations of unit-cell parameters and cell-volumes of anatase and rutile in different atmospheres with temperature and the corresponding linear and volumetric thermal expansion coefficients (TEC) are shown in Tables 1 and 2. The cell-volumes of both anatase and rutile inceased with increasing temperature by virtue of an increase of their lattice parameters. As can be seen, the cell-volumes for both anatase and rutile were affected slightly by the atmospheres which were higher in air than in argon. Thus, the linear and volumetric thermal expansion cofficients of both anatase and rutile were slightly greater in air than in argon. Moreover, the calculated unit-cell parameters, cell-volumes, and thermal expansion for anatase and rutile are comparable with results from Hummer and Heaney equations.[29]

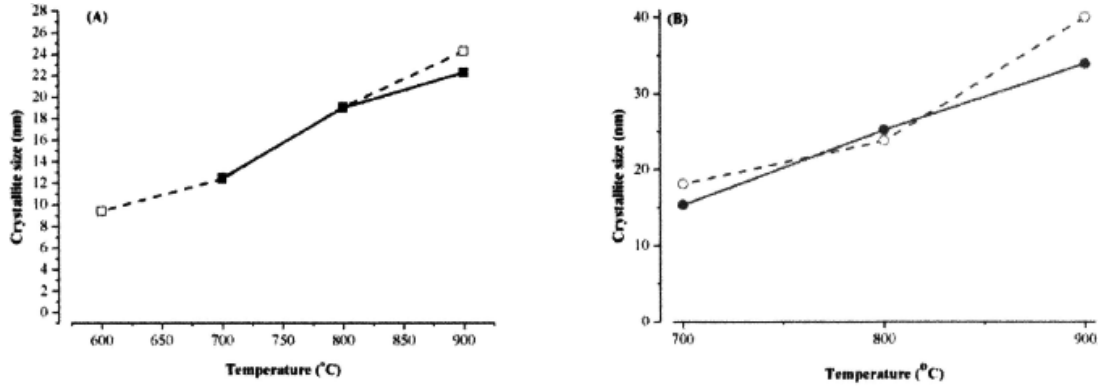

Fig. 4: Effect of atmosphere on crystallite size of (a) anatase and (b) rutile at various temperatures. [Legend: anatase in air (□); anatase in argon (■); rutile in air (○); rutile in argon (●)]

Table 1: Variation of the cell-volume of anatase and rutile in air and argon atmosphere as a function of temperature.

	Air atmosphere		**Argon atmosphere**	
Temperature (°C)	Anatase ($Å^3$)	Rutile ($Å^3$)	Anatase ($Å^3$)	Rutile ($Å^3$)
600	136.94(9)	-------	-------	-------
700	137.79(2)	63.12(4)	137.68(3)	63.41(4)
800	137.98(3)	63.67(2)	137.84(3)	63.60(1)
900	137.93(7)	64.01(1)	138.23(8)	63.95(1)

Table 2:The linear (α_a, α_c) and volumtric (β) thermal expansion coefficient at 800 °C.

Atmosphere	TEC $\times 10^{-5}$ ($°C^{-1}$)	α_a	α_c	β
Air	Anatase	0.72	0.86	2.29
	Rutile	1.95	3.03	7.07
Argon	Anatase	0.52	0.84	2.03
	Rutile	1.08	2.01	4.24

CONCLUSIONS

The effect of air and argon atmosphere on the in-situ crystallisation behaviour of electrospun TiO_2 nanofibres was investigated using high-resolution synchrotron radiation diffraction in the temperature range 25-900°C. In both cases, as-spun TiO_2 nanofibres were initially amorphous but crystallized to anatase and rutile at elevated temperatures. Both atmospheres demonstrated a significant influence on the crystallisation kinetics of anatase and rutile. In air, anatase formed at 600°C and rutile at 700°C, but in argon they formed simultaneously at 700°C. The kinetics of

transformation of anatase to rutile was also strongly affected by the atmospheric conditions. The rates of anatase to rutile transformation was faster in argon than in the air. The crystallite sizes of anatase and rutile increased with increasing temperature, and were only moderately affected by the atmospheres.

ACKNOWLEDGMENTS

We gratefully acknowledge the Australian Synchrotron (AS122/PDFI/5075) and the Australian Institute of Nuclear Science and Engineering (ALNGRA11135) for funding this work.

REFERENCES

[1]Low IM, Albetran H, Prida VM, Vega V, Manurung P, Ionescu M. A comparative study on crystallization behavior, phase stability, and binding energy in pure and Cr-doped TiO_2 nanotubes. *J Mater Res* 2013;**28**:304-12.

[2]Manurung P, Putri Y, Simanjuntak W, Low IM. Synthesis and characterisation of chemical bath deposited TiO_2 thin-films. *Ceram Int* 2013;**39**:255-9.

[3]Zhang P, Shao C, Li X, Zhang M, Zhang X, Sun Y, Liu Y. In situ assembly of well-dispersed au nanoparticles on TiO_2/ZnO nanofibers: A three-way synergistic heterostructure with enhanced photocatalytic activity. *J Hazard Mater* 2012;**237-238**,331-8.

[4]Yu C, Wei L, Li X, Chen J, Fan Q, Yu J. Synthesis and characterization of Ag/TiO_2– B nanosquares with high photocatalytic activity under visible light irradiation. *Mater Sci Eng B* 2013;**178**:344-8.

[5]Pan X, Zhao Y, Liu S, Korzeniewski CL, Wang S, Fan Z. Comparing graphene-TiO_2 nanowire and graphene-TiO_2 nanoparticle composite photocatalysts. *ACS Appl Mater Interfaces* 2012;**4**:3944-3950.

[6]Babu VJ, Nair AS, Peining Z, Ramakrishna S. Synthesis and characterization of rice grains like nitrogen-doped TiO_2 nanostructures by electrospinning-photocatalysis. *Mater Lett* 2011;**65**:3064-8.

[7]Liu G, Wang L, Yang HG, Cheng and HM, Lu GQ. Titania- based photocatalysts-crystal growth, doping and heterostructuring. *J Mater Chem* 2010;**20**:831-43.

[8]Chuangchote S, Jitputti J, Sagawa T, Yoshikawa S. Photocatalytic activity for hydrogen evolution of electrospun TiO_2 nanofibers. *ACS Appl Mater Interfa* 2009;**1**:1140-3.

[9]Kim DW, Enomoto N, Nakagawa ZE, Kawamura K. Molecular dynamic simulation in titanium dioxide polymorphs: Rutile, brookite, and anatase. *J Am Ceram Soc* 1996;**79**:1095-9.

[10]Liu R, Qiang LS, Yang WD, Liu HY. The effect of calcination conditions on the morphology, the architecture and the photo-electrical properties of TiO_2 nanotube arrays. *Mater Res Bull* 2013;**48**:1458-67.

[11]Li W, Ni C, Lin H, Huang CP, Shah SI. Size dependence of thermal stability of TiO_2 nanoparticles. *J Appl Phys* 2004;**96**:6663-8.

[12]Hanaor DA, Sorrell CC. Review of the anatase to rutile phase transformation. *J Mater Sci* 2011;**46**:855-74.

[13]Shang S, Jiao X, Chen D. Template-free fabrication of TiO_2 hollow spheres and their photocatalytic properties. *ACS Appl Mater Interfa* 2012;**4**:860-5.

[14]Li H, Zhang W, Pan W. Enhanced photocatalytic activity of electrospun TiO_2 nanofibers with optimal anatase/rutile ratio. *J Am Ceram Soc* 2011;**94**:3184-7.

[15]Shannon RD, Pask, JA. Kinetics of the anatase-rutile transformation. *J Am Ceram Soc* 1965;**48**:391-8.

[16]Eppler RA. Effect of antimony oxide on the anatase-rutile transformation in titanium dioxide. *J Am Ceram Soc* 1987;**70**:64-6.
[17]Iida Y, Ozaki S. Grain growth and phase transformation of titanium oxide during calcination. *J Am Ceram Soc* 1961;**44**:120-7.
[18]Gamboa JA, Pasquevich DM. Effect of chlorine atmosphere on the anatase-rutile transformation. *J Am Ceram Soc* 1992;**75**:2934-8.
[19]Huang JH, Wong MS. Structures and properties of titania thin films annealed under different atmosphere. *Thin Solid Films* 2011;**520**:1379-84.
[20]Lee JS, Ha TJ, Hong MH, Park HH. The effect of porosity on the CO sensing properties of TiO_2 xerogel thin films. *Thin Solid Films* 2013;**529**:98-102
[21]Low JM, Curtain B, Philipps M, Liu QZ, Ionescu M. High temperature diffraction study of in-situ crystallization of nanostructured TiO_2 photocatalysts. *J Aust Ceram Soc* 2012;**48**:198-204.
[22]Chuangchote S, Jitputti J, Sagawa T, Yoshikawa S. Photocatalytic activity for hydrogen evolution of electrospun TiO_2 nanofibers. *ACS Appl Mater Interfa* 2009;**1**:1140-3
[23]Huang ZM, Zhang YZ, Kotaki M, Ramakrishna S. A review on polymer nanofibers by electrospinning and their applications in nanocomposites. *Compos Sci Technol* 2003;**63**:2223-53.
[24]Li Q, Satur DJG, Kim H, Kim HG. Preparation of sol- gel modified electrospun TiO_2 nanofibers for improved photocatalytic decomposition of ethylene. *Mater Lett* 2012;**76**:169-172.
[25]Luo W, Hu X, Sun Y, Huang Y. Surface modification of electrospun TiO_2 nanofibers via layer-by-layer self-assembly for high-performance lithium-ion batteries. *J Mater Chem* 2012;**22**:4910-5.
[26]Wessel C, Ostermann R, Dersch R, Smarsly BM. Formation of inorganic nanofibers from preformed TiO_2 nanoparticles via electrospinning. *J Phys Chem* 2011;**C 115**, 362-72.
[27]Li H, Zhang, W, Pan W. Enhanced photocatalytic activity of electrospun TiO_2 nanofibers with optimal anatase/rutile ratio. *J Am Ceram Soc* 2011;**94**:3184-7.
[28]P. Zhu, Nair AS, Shengjie P, Shengyuan Y, Ramakrishna S. Facile fabrication of TiO_2-graphene composite with enhanced photovoltaic and photocatalytic properties by electrospinning. *ACS Appl Mater Interfa 2012*;**4**,581-5.
[29]Hummer DR, Heaney PJ. Thermal expansion of anatase and rutile between 300 and 575 K using synchrotron powder X-ray diffraction. *Powder Diffraction* 2007;**22**:352-7.
[30]Cullity BD, Stock SR. *Elements of X-ray Diffraction.* Prentice: Hall Inc; 2001.

8.3 Effect of Chromium Doping on the Crystallization and Phase Stability in Anodized TiO_2 Nanotubes

---

LOW, I. M., **ALBETRAN, H.,** PRIDA, V., MANURUNG, P., & IONESCU, M. 2013. Effect of Chromium Doping on the Crystallization and Phase Stability in Anodized TiO_2 Nanotubes. Developments in Strategic Materials and Computational Design III: *The Ceramic Engineering and Science Proceedings*, 151–158.

Developments in Strategic Materials and Computational Design III
Edited by Waltraud M. Kriven, Andrew L. Gyekenyesi, Gunnar Westin and Jingyang Wang

EFFECT OF CHROMIUM-DOPING ON THE CRYSTALLIZATION AND PHASE STABILITY IN ANODIZED TiO_2 NANOTUBES

I.M. Low[1], H. Albetran[1], V. De La Prida[2], P. Manurung[3] and M. Ionescu[4]
[1]Centre for Materials Research, Curtin University, GPO Box U1987, Perth, WA 6845, Australia
[2]Department of Physics, University of Oviedo, Spain
[3]Department of Physics, University of Lampung, Indonesia
[4]Australian Nuclear Science and Technology Organisation, Sydney, NSW 2234, Australia

ABSTRACT

Production of limitless hydrogen fuel by visible light splitting of water using the photo-electrochemical technology is cost-effective and sustainable. To make this an attractive viable technology will require the design of TiO_2 photocatalyst capable of harnessing the energy of visible light. One possible solution is the doping of TiO_2 to reduce its band gap. In this paper, the effect of Cr-doping by ion-implantation on the crystallisation and phase stability of TiO_2 nanotubes at elevated temperature is described. The effect of Cr-doping on the resultant microstructures, phase changes and composition depth profiles are discussed in terms of synchrotron radiation diffraction, scanning electron microscopy, and ion-beam analysis by Rutherford backscattering spectrometry.

INTRODUCTION

Titanium dioxide (TiO_2) is a wide band-gap semiconductor with energy of 3.0-3.2 eV. It is widely used in applications such as hydrogen production, gas sensors, photocatalytic activities, dye-sensitized solar cells and photo-electrochemical cells because of its relative high efficiency and high stability. However, due to its wide band gap energy, TiO_2 is active only under near-ultraviolet irradiation. Therefore, numerous studies have been carried out over the last 20 years to develop modified TiO_2 so that they are active under visible light irradiation (> 400 nm). One of the most studied methods is by doping the TiO_2 materials with metal ions (iron, nickel, cobalt, vanadium, and chromium)[1-4] or non-metallic elements (nitrogen, sulphur and carbon).[5-14] For instance, Cr or N-doping of TiO_2 can result in visible light response by virtue of a narrowing in the band gap due to the mixing of p states of nitrogen with O 2p states. Among these doping methods, doping with transition metals is one of the most efficient methods. X-ray photoelectron spectroscopy (XPS) results showed that the doped samples contained N, C, B and F elements and the doped TiO_2 showed the shift in the band gap transition down to 2.98 eV. The photocatalytic activity of the doped TiO_2 was 1.61 times better than undoped TiO_2. Researchers have conducted doping of bismuth into TiO_2 to enhance the photocatalytic activities in these systems. It has been reported that the metal/TiO_2 nanostructures enhance the efficiency of photocatalysis in water-splitting and dye-sensitized solar cell (DSSC). Metals compounded on semiconductor materials increase charge-collection efficiency due to a much slower electron-hole recombination, giving rise to longer electron lifetime, which will result in an increasing interfacial electron-transfer process.

Hitherto, the doping of TiO_2 has been widely synthesized using the sol-gel method.[15-19] However, ion-implantation has now emerged as an alternative but effective doping method to improve the separation of the photo-generated electron-hole pairs or to extend the wavelength range of the TiO_2 photo-responses into the visible region.[20-25] XPS measurements revealed that the implanted nitrogen species were mainly interstitial ones. The nitrogen concentration was increased with increasing ion flux which could be controlled by adjusting the gas flow rate of the ion source, resulting in improved visible-light photocatalytic activities. Higher visible-light photocatalytic efficiency was achieved with higher implanted nitrogen concentration.

EXPERIMENTAL METHODS

Sample Preparation

Ti foils (99.6 % purity) with dimensions of 10 × 10 × 0.1 mm^3 were used for the anodizing to produce self-organized and well-aligned TiO_2 nano-tube arrays. The process of potentiostatic anodization was performed in a standard two-electrode electrochemical cell, with Ti as the working electrode and platinum as the counter electrode. Prior to anodization, Ti-foils were degreased by sonicating in ethanol, isopropanol and acetone for 5 minutes each, followed by rinsing with deionised water, and then drying using nitrogen stream. After drying, the foils were exposed to the electrolyte which consists of 100 ml of Ethylene glycol + 2.04 ml of water + 0.34 g of NH_4F. The electrolyte's pH was kept constant at pH = 6, and its temperature was kept at about 25 °C. The anodization process was performed under an applied voltage of 60 V for 20 h.[26] After that, the resulting TiO_2 structures were then rinsed in ethanol, immersed in hexamethyl-disilazane (HMDS) and dried in air.

Doping by Ion-Implantation

The as-anodized samples were doped with Cr ions using a MEVVA Ion Implanter with a dose of ~$7x10^{14}$ ions/cm^2 that corresponds to 8,500 pulses. The near surface composition depth profiling of ion-implanted samples was measured by ion-beam analysis and Rutherford backscattering spectrometry (RBS) using He^{1+} ions at 1.8 MeV. This phase of work was conducted at the Australian Nuclear Science and Technological Organisation (ANSTO). The information obtained allowed the calculation of depth distribution of implanted species and the implanted dose.

The morphologies of the anodized and ion-implanted samples were characterized using a focussed ion-beam scanning electron microscope (FIB-SEM) operating at working distances of 5 mm with an accelerating voltage of 5 kV.

In Situ High-Temperature Synchrotron Radiation Diffraction

In this study, the in-situ crystallisation behaviour of as-anodized samples with or without Cr-doping was characterised using high-temperature synchrotron radiation diffraction (SRD) up to 900 °C in argon. All measurements were conducted at the Australian Synchrotron using the Powder Diffraction beamline in conjunction with an Anton Parr HTK20 furnace and the Mythen II microstrip detector. The SRD data were collected at an incident angle of 3° and wavelength of 0.11267 nm.

The phase transitions or structural changes were simultaneously recorded as SRD patterns. These patterns were acquired at high temperatures over an angular range of 100° in 2θ. The SRD patterns were acquired in steps of 100 °C from 100 °C to 900 °C. The collected SRD data were analysed using the CMPR program to evaluate the integrated peak intensities of all phases present. The sum of all the integrated peak intensities in 2θ range of 10-50° was used to calculate the relative phase content of all the phases present at each temperature as follows:

$$W_A = \left(\frac{I_A}{I_A + I_R + I_T} \right) \times 100 \qquad (1)$$

where W_A is the wt% of anatase, I_A is sum integrated intensity of anatase, I_R is sum integrated intensity of rutile and I_T is sum integrated intensity of titanium. A similar ratio method was used to calculate the wt% of rutile (W_R) or titanium (I_T). This method is expected to be more accurate than the method of Spurr & Myers[27] where only the peak intensities of anatase (101) and rutile (110) are used. The use of integrated peak intensities in equation (1) can minimise issues relating to preferred orientation, grain size and/or degree of crystallinity.

The mean crystallite sizes (L) of anatase and rutile were calculated from (101) and (110) reflections using the Scherrer equation:[28]

$$L = \frac{K\lambda}{\beta \cos\theta} \quad (2)$$

where K is the shape factor, λ is the x-ray wavelength, β is the line broadening at half the maximum intensity (FWHM) in radians, and θ is the Bragg angle.

RESULTS AND DISCUSSION

In-Situ Formation of TiO_2 at Elevated Temperature

Figure 1 shows the synchrotron radiation diffraction plots of Cr-doped TiO_2 nanotubes before and after thermal annealing in air at 20 °C – 900 °C. The TiO_2 nanotube arrays were initially amorphous but eventually crystallized into anatase at 300 °C. The peak intensities of anatase increased rapidly from 300° to 400°C and continued to increase until 900°C. The formation of rutile commenced at 600°C but its growth was sluggish where the peak intensities increased very slightly from 600 to 800°C. Surprisingly, rutile disappeared at 900C with the concomitant appearance of TiO_{2-x} where x = 0.2. This suggests that rutile was unstable in argon atmosphere at 900 °C and decomposed to form a non-stoichiometric titanium oxide and oxygen vacancies (O_v) as follows:

$$5TiO_2 \xrightarrow{900^\circ C / argon} Ti_5O_9 + O_v \quad (3)$$

In contrast, no decomposition of rutile was observed in un-doped TiO_2 nanotubes (see Fig. 2). When compared to Cr-doped TiO_2, both anatase and rutile in the un-doped sample crystallized at a higher temperature, i.e. 400 and 700°C respectively. The corresponding phase abundances as a function of temperature are shown in Figure 3. The fraction of anatase-to-rutile transformation in the samples calcined at between 600 – 1000 °C can be calculated from the followed equation:[27]

$$x = 1/[1 + 0.8(I_A / I_R]$$

where I_A is the X-ray integrated intensities of the (101) reflection of anatase at ~18.3°, while I_R is that of the (110) reflection of rutile at ~19.8°; x is the weight fraction of rutile in the nanotubes, which is calculated for the Cr-doped sample to be 2.9 wt% for the nanotubes annealed at 600°C, 4.9 wt% at 700°C, and 4.6 wt% at 800°C. The corresponding x values for the un-doped sample were 3.3 wt% at 700°C, 19.0 wt% at 800°C and 15.9 wt% at 900°C.

It appears that the presence of Cr-doping has accelerated the formation of anatase and rutile at a lower temperature, probably through the facilitation of defects such as vacancies. It is widely accepted that the onset temperature of the anatase to rutile phase transformation and the rate at which it proceeds can be affected significantly by dopants, firing atmosphere, microstructure, sample morphology, and the presence of impurities in the material.[29] The process of the anatase to rutile transformation is known to occur via (a) the nucleation of rutile at point defects, oxygen vacancies, secondary phase inclusions, particle surfaces, and/or at (112) twin interfaces in anatase, and (b) the subsequent consumption of the anatase phase by the growing rutile phase. The formation of rutile from the metastable phase anatase is reconstructive and so takes place through atomic rearrangement involving the breaking of two of the six Ti-O bonds in the TiO_6 octahedra.[30] As anatase transforms to rutile, significant grain growth takes place, resulting in lower surface area and thus poorer photocatalytic performance.

Transition metals (e.g. Cr) of variable valence are reported to enter the titania lattice and create oxygen vacancies through reduction effects as follows:[29,31]

$$2M^{n+} + O^{2-} \rightarrow 2M^{(n-1)+} + \frac{1}{2}O_2 + O_v \quad (4)$$

where M denotes a transition metal atom and O_v denotes an oxygen vacancy. Once substituted for Ti^{4+}, the reduction of such species gives rise to new oxygen vacancies and so enhances rutile formation from metastable anatase through easing of structural rearrangement. These oxygen vacancies are believed to be responsible for crystallisation of anatase at a lower temperature in Cr-doped TiO_2 as well as destabilisation and subsequent decomposition of rutile to form non-stoichiometric TiO_{2-x}.

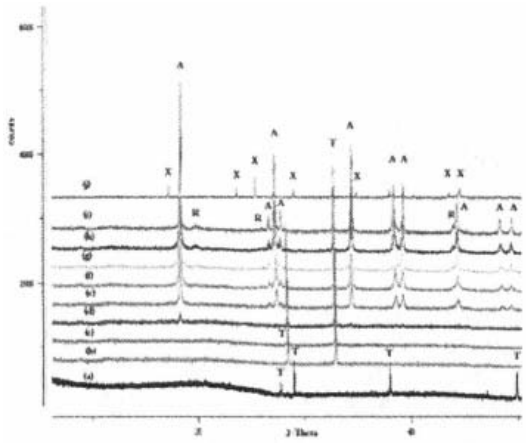

Fig. 1: In-situ synchrotron radiation diffraction plots of Cr-doped TiO_2 showing the existence of anatase (A), rutile (R), Ti_5O_9 (X) and titanium (T) in the temperature range 20 – 900 °C. [Legend: a = 20°C, b = 100°C, c = 200°C, d = 300°C, e = 400°C, f = 500°C, g = 600°C, h = 700°C, i = 800°C, j = 900°C]

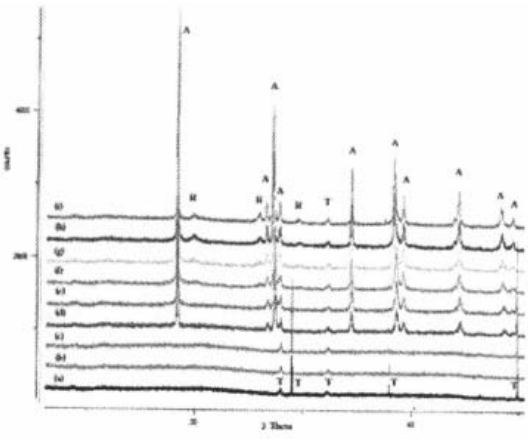

Fig. 2: In-situ synchrotron radiation diffraction plots of un-doped TiO_2 showing the existence of anatase (A), rutile (R), and titanium (T) in the temperature range 100 – 900 °C. [Legend: (a) = 100°C, (b) = 200°C, (c) = 300°C, (d) = 400°C, (e) = 500°C, (f) = 600°C, (g) = 700°C, (h) = 800°C, (i) = 900°C]

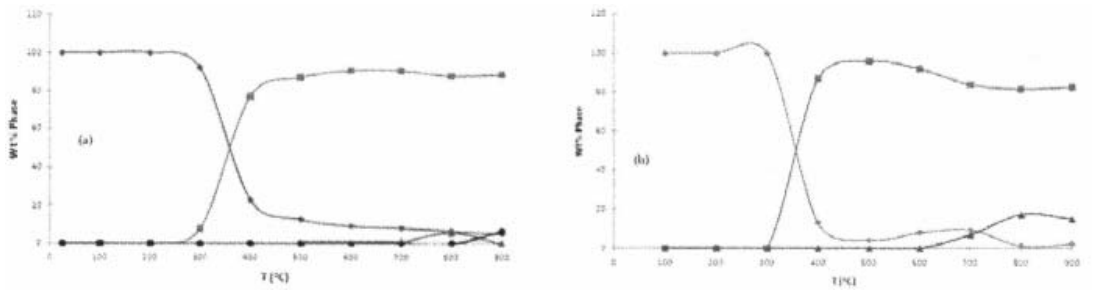

Fig. 3: Variations of phase abundances as a function of temperature for (a) Cr-doped TiO_2 and (b) un-doped TiO_2. [Legend: titanium (♦); anatase (■); rutile (▲); TiO_{2-x} (•)]

Although anatase remained stable up to 800-900 °C, there was a distinct narrowing and sharpening in the (101) peak, resulting in a corresponding decrease in the values of full-width half-maximum (FWHM) as the temperature increased. A similar sharpening of the (110) peak was observed for rutile. From the Scherrer equation,[28] a decrease in the value of FWHM implies an increase in the mean crystallite size for anatase or rutile. Figure 4 shows the influence of annealing temperature on crystallite size for anatase and rutile in both undoped and Cr-doped TiO_2. The crystallite size of anatase was just over 50 nm at 400 °C for un-doped TiO_2 but just under 50 nm in Cr-doped TiO_2 and increased gradually with temperature to 85 nm and 100 nm respectively at 900°C. In both samples, the crystallite size of rutile was much smaller than that of anatase, especially in the un-doped sample.

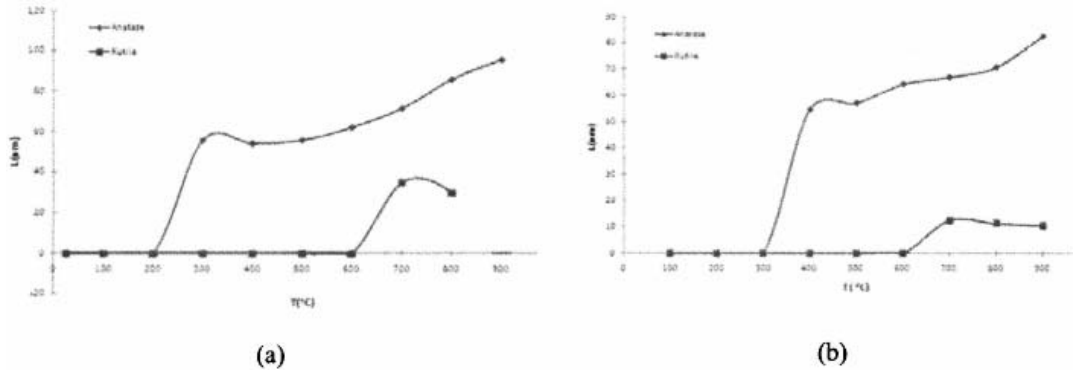

(a) (b)

Fig. 4: Variations of crystallite size of anatase (♦) and rutile (■) as a function of temperature for (a) Cr-doped TiO_2 and (b) un-doped TiO_2.

Microstructures of TiO_2 and Cr-Doped TiO_2

After anodizing in the electrolyte of NH_4F / ethylene glycol at 25 °C for 20 h, vertically oriented and highly ordered arrays of TiO_2 nanotubes with diameter of ~80 nm formed on the Ti-foil.[26] Fig. 5(a) shows the FESEM image of the amorphous TiO_2 nanotubes. Upon annealing at 900 °C for 1 h, some anatase transformed into rutile, which appeared as elongated grains randomly distributed amongst the nanotubes shown in Fig. 5 (b). The microstructure of Cr-doped TiO_2 is shown in Fig. 5 (c) where the existence of implanted Cr ions has been verified by the EDS analysis of a bright region in Spectrum 1 (see Fig. 5d).

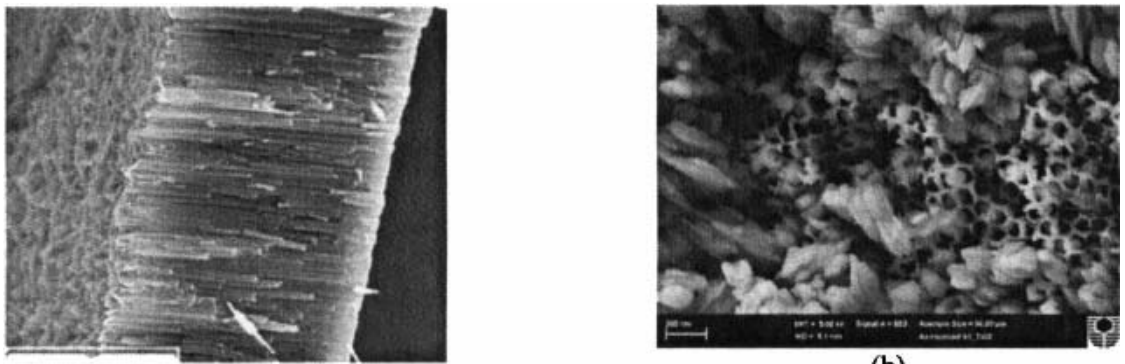

(a) (b)

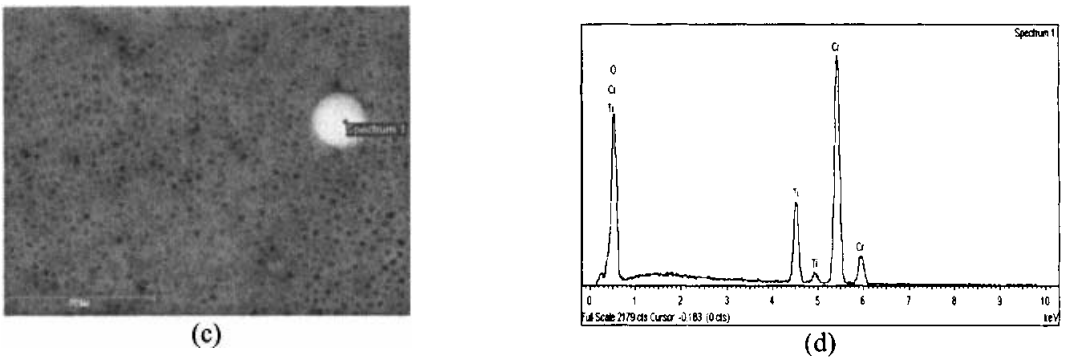

Fig. 5: Scanning electron micrographs showing the microstructure of (a) as-anodized TiO_2, (b) annealed TiO_2 at 900°C, (c) Cr-doped TiO_2 and (d) EDS analysis of composition in Spectrum 1.

Rutherford Backscattering Spectroscopy (RBS)

The RBS results in Figure 6 show the concentration of elements (at%) versus depth (at/cm^2) for both the un-doped and Cr-doped samples. In Fig. 6a, we show the depth profile of Ti and O for as-anodized TiO_2. The composition at the near surface of TiO_2 layer is fairly constant but a composition gradation in both O and Ti exists at the interface between the substrate and the oxide layer. In the doped sample (Fig. 6b), a maximum Cr concentration of 0.7 at% has been implanted in TiO_2 down to a depth of about 300 mono layers. A composition gradation also exists at the interface between the substrate and the oxide layer.

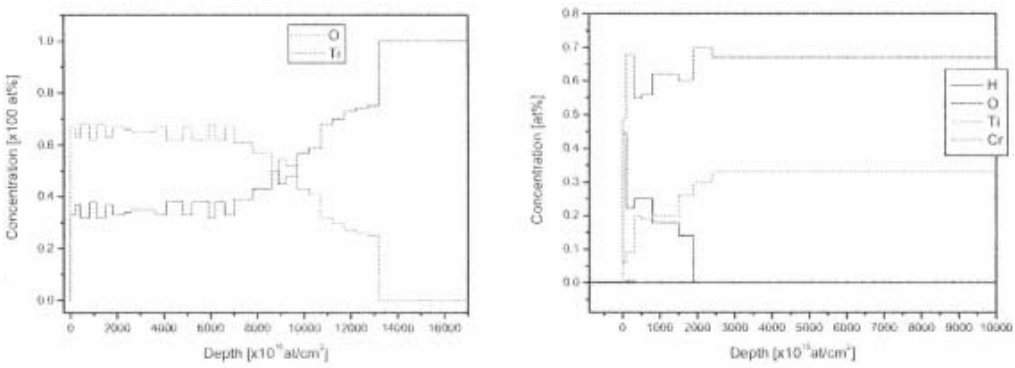

Fig. 6: Composition depth profiles in (a) un-doped TiO_2 and (b) Cr-doped TiO_2.

CONCLUSIONS

High-temperature synchrotron radiation diffraction has been used to study the effect of Cr-doping on in-situ crystallization of anatase and rutile in as-anodized TiO_2 nanotubes. The as-anodized TiO_2 was amorphous but crystallized into anatase and rutile at 400 °C and 700°C in the un-doped sample, but 300°C and 600°C in the doped sample. The rutile formed in the un-doped sample was very stable in argon after annealing at 900°C but was unstable in the doped sample and decomposed to form non-stoichiometric TiO_{2-x} at 900°C. In both cases, increasing the temperature from 300 to 900 °C caused the FWHM of anatase (101) and rutile (110) peaks to decrease, resulting in a concomitant coarsening in crystallite size. The surface of annealed sample exhibited well-aligned, uniform TiO_2 nanotubes with

an average diameter of ~80 nm and wall thickness of ~10 nm. Ion-beam analysis by RBS has confirmed the existence of Cr ions in the doped sample and composition gradation within the annealed TiO_2 sample at substrate-oxide interface.

ACKNOWLEDGMENTS

This work was supported by funding from the Australian Synchrotron (PD-3611), the Australian Institute of Nuclear Science and Engineering (AINGRA-11134) and Spanish MAT2010-20798-C05-04. We thank Ms E. Miller of Curtin Centre for Materials Research for assistance with the SEM work. The scientific support from the University of Oviedo SCT's, particularly to the Nanoporous Membranes Unit, is also acknowledged.

REFERENCES

[1]M. Anpo, Y. Ichihashi, M. Takeuchi and H. Yamashita, *Res. Chem. Intermed.* **24**, 143 (1998).

[2]A. Zaleska, J.W. Sobczak, E. Grabowska and J. Hupka, Preparation and photocatalytic activity of boron-modifled TiO_2 under UV and visible light. *Appl. Catal.* B **78**, 92-100 (2008).

[3]G.B. Saupe, T.U. Zhao, J. Bang, N.R. Desu, G.A. Carballo, R. Ordonem and T. Bubphamala, Evaluation of a new porous titanium-niobium mixed oxide for photocatalytic water decontamination. *Microchemical J.* **81**, 156-162 (2005).

[4]D.B. Hamal and K.J. Klabunde, Synthesis, characterization, and visible light activity of new nanoparticle photocatalysts based on silver, carbon, and sulfur-doped TiO_2. *J. Colloid & Interfa. Sci.* **311**, 514-522 (2007).

[5]J. Virkutyte, B. Baruwati and R.S. Varma, Visible light induced photobleaching of methylene blue over melamine-doped TiO_2 nanocatalyst. *Nanoscale* 2, 1109-1111 (2010).

[6]T. Umebayashi, T. Yamaki and S. Tanaka, Visible light-induced degradation of methylene blue on S-doped TiO_2. *Chem. Lett.* **32**, 330-331 (2003).

[7]S. Sakthivel, M. Janczarek and H. Kisck, Visible light activity and photo-electrochemical properties of nitrogen-doped TiO_2. *J. Phys. Chem.* B **108**, 19384-19387 (2004).

[8]Y. Choi, T. Umebayashi and M. Yoshikawa, Fabrication and characterization of C-doped anatase TiO_2 photocatalysts. *J. Mater. Sci.* **39**, 1837-1839 (2004).

[9]H. Irie, Y. Watanabe and K. Hashimoto, Carbon-doped anatase TiO_2 powders as a visible-light sensitive photocatalyst. *Chem. Lett.* **32**, 772-773 (2003).

[10]S. Sakthivel and H. Kisch, Daylight photocatalysts by carbon-modified titanium dioxide. *Angew. Chem. Int. Edn.*, **42**, 4908-4911 (2003).

[11]R. Asahi, T. Morikawa and T. Ohwaki, Visible-light photocatalysis in nitrogen-doped titanium oxides. *Science* **293**, 269-273 (2001).

[12]W. Ren, Z. Ai, F. Jia, L. Zhang, X. Fan and Z. Zou, Low temperature preparation and visible light photocatalytic activity of mesoporous carbon-doped crystalline TiO_2. *Appl. Catal.* B **69**, 138-144 (2007).

[13]T. Ohno, M. Akiyoshi, T. Umebayashi, K. Asai, T. Mitsui and M. Matsumura, Preparation of S-doped TiO_2 photocatalysts and their photocatalytic activities under visible light. *Appl. Catal. A* **265**, 115-121 (2004).

[14]C. Lettmann, K. Hildebrand, H. Kisch, W. Macyk and W.F. Maier, Visible light photodegradation of 4-chlorophenol with a coke-containing titanium dioxide photocatalyst. *Appl. Catal. B* **32**, 215-227 (2001).

[15]Y. Kuroda, T. Mori, K. Yagi, N. Makihata, Y. Kawahara, M. Nagao and S. Kittaka, Preparation of visible-light-responsive $TiO_{2-x}N_x$ photocatalyst by a sol-gel method: Analysis of the active center on TiO_2 that reacts with NH_3. *Langmuir* **21**, 8026-8034 (2005).

[16]A. Hattori, M. Yamamoto, H. Tada and S. Ito, A promoting effect of NH_4F addition on the photocatalytic activity of sol-gel TiO_2 films. *Chem. Lett.* **27**, 707-708 (1998).
[17]Y. Shen, T. Xiong, T. Li and K. Yang, Tungsten and nitrogen co-doped TiO_2 nano-powders with strong visible light response. *Appl. Cataly. B: Environ.* **83**, 177-185 (2008).
[18]T.C. Jagadale, S.P. Takale, R.S. Sonawane, H.M. Joshi, S.I. Patil, B.B. Kale and S.B. Ogale, N-doped TiO_2 nanoparticle based visible light photocatalyst by modified peroxide sol-gel method. *J. Phys. Chem. C* **112**, 14595-14602 (2008).
[19]Y. Tseng, C. Kuo, C. Huang, Y. Li, P. Chou, C. Cheng and M. Wong, Visible-light-responsive nano-TiO_2 with mixed crystal lattice and its photocatalytic activity. *Nanotechno.* **17**, 2490-2497 (2006).
[20]T. Yamaki, T. Sumita and S. Yamamoto, Formation of $TiO_{2-x}F_x$ compounds in fluorine-implanted TiO_2. *J. Mater. Sci. Lett.* **21**, 33-35 (2002).
[21]H. Shen, L. Mi, P. Xu, W. Shen and P.N. Wang, Visible-light photocatalysis of nitrogen-doped TiO_2 nanoparticulate films prepared by low-energy ion implantation. *Appl. Surf. Sci.* **253**, 7024-7028 (2007).
[22]J. Park, J.Y. Lee and J.H. Cho, Ultraviolet-visible absorption spectra of N-doped TiO_2 film deposited on sapphire. *J. Appl. Phys.* **100**, 113534 (2006).
[23]H. Yamashita, Y. Ichihashi and M. Takeuchi, Characterization of metal ion-implanted titanium oxide photocatalysts operating under visible light irradiation. *J. Synchrotron Radia.* **6**, 451-452 (1999).
[24]T. Yamaki, T. Umebayashi and T. Sumita, Fluorine-doping in titanium dioxide by ion implantation technique. *Nucl. Instr. & Meth. Phys. Res. B* **206**, 254-258 (2003).
[25]H. Yamashita, M. Harada, J. Misaka, M. Takeushi and M. Anpo, Degradation of propanol diluted in water under visible light irradiation using metal ion-implanted titanium dioxide photocatalysts. *J. Photochem. Photobiol. A* **148**, 257-261 (2002).
[26]V. Vega, M.A. Cerdeira, V.M. Prida, D. Alberts, N. Bordel, R. Pereiro, F. Mera, S. García, M. Hernández-Vélez and M. Vázquez, Electrolyte influence on the anodic synthesis of TiO_2 nanotube arrays. *J. Non-Cryst. Solids* **354**, 5233-5235 (2008).
[27]R.A. Spurr and H. Myers, Quantitative analysis of anatase-rutile mixtures with an x-ray diffractometer. *Anal. Chem.* **29**, 760–762 (1957).
[28]B.D. Cullity and S.R. Stock, *Elements of X-Ray Diffraction*, 3rd Ed., Prentice-Hall Inc., pp. 167-171 (2001).
[29]D. Hanaor and C. Sorrell, Review of the anatase to rutile phase transformation. *J. Mater. Sci.* **46**, 1-20 (2011).
[30]S. Riyas, G. Krishnan and P.N. Mohandas, Anatase-rutile transformation in doped titania under argon and hydrogen atmospheres. *Adv. Appl. Ceram.* **106**, 255 – 26 (2007).
[31]K.J.D. Mackenzie, Calcination of titania V. Kinetics and mechanism of the anatase-rutile transformation in the presence of additives. *Trans. J. Bri. Ceram. Soc.* **74**, 77-84 (1975).

9 Appendix V: Copyright Forms

Appendix V-A: Copyright information relating to

ALBETRAN, H., HAROOSH, H., DONG, Y., PRIDA, V. M., O'CONNOR, B. H., & LOW, I. M. 2014. Phase Transformations and Crystallization Kinetics in Electrospun TiO_2 Nanofibers in Air and Argon Atmospheres. *Applied Physics A*, 116, 161–169.

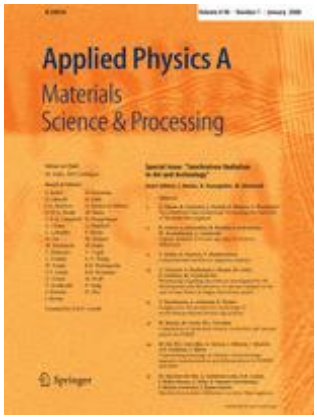

Title: Phase transformations and crystallization kinetics in electrospun TiO2 nanofibers in air and argon atmospheres

Author: H. Albetran

Publication: Applied Physics A: Materials Science & Processing

Publisher: Springer

Date: Jan 1, 2014

Order Completed

Thank you very much for your order.

This is a License Agreement between HANI ALBETRAN ("You") and Springer ("Springer"). The license consists of your order details, the terms and conditions provided by Springer, and the payment terms and conditions.

Get the printable license.

License Number	3830691019513
License date	Mar 16, 2016
Licensed content publisher	Springer
Licensed content publication	Applied Physics A: Materials Science & Processing
Licensed content title	Phase transformations and crystallization kinetics in electrospun TiO2 nanofibers in air and argon atmospheres
Licensed content author	H. Albetran
Licensed content date	Jan 1, 2014
Volume number	116
Issue number	1
Type of Use	Thesis/Dissertation
Portion	Full text
Number of copies	1
Author of this Springer article	Yes and you are the sole author of the new work
Title of your thesis / dissertation	Synthesis and Characterisation of Nanostructured TiO2 for Photocatalytic Applications
Expected completion date	Mar 2016
Estimated size(pages)	309
Total	0.00 USD

CLOSE WINDOW

Appendix V-B: Copyright information relating to

ALBETRAN, H., O'CONNOR, B. H., & LOW, I. M. 2016. Activation Energies for Phase Transformations in Electrospun Titania Nanofibers: Comparing the Influence of Argon and Air Atmospheres. *Applied Physics A*, 122, 1–9.

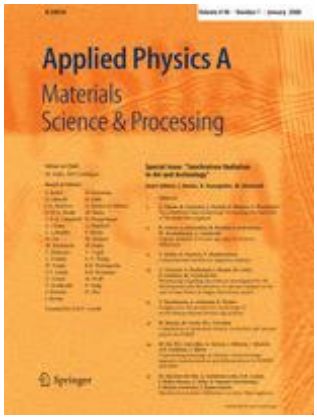

Title: Activation energies for phase transformations in electrospun titania nanofibers: comparing the influence of argon and air atmospheres

Author: H. Albetran

Publication: Applied Physics A: Materials Science & Processing

Publisher: Springer

Date: Jan 1, 2016

Order Completed

Thank you very much for your order.

This is a License Agreement between HANI ALBETRAN ("You") and Springer ("Springer"). The license consists of your order details, the terms and conditions provided by Springer, and the payment terms and conditions.

Get the printable license.

License Number	3830680893645
License date	Mar 16, 2016
Licensed content publisher	Springer
Licensed content publication	Applied Physics A: Materials Science & Processing
Licensed content title	Activation energies for phase transformations in electrospun titania nanofibers: comparing the influence of argon and air atmospheres
Licensed content author	H. Albetran
Licensed content date	Jan 1, 2016
Volume number	122
Issue number	4
Type of Use	Thesis/Dissertation
Portion	Full text
Number of copies	1
Author of this Springer article	Yes and you are the sole author of the new work
Title of your thesis / dissertation	Synthesis and Characterisation of Nanostructured TiO2 for Photocatalytic Applications
Expected completion date	Mar 2016
Estimated size(pages)	309
Total	0.00 USD

CLOSE WINDOW

Appendix V-C: Copyright information relating to

ALBETRAN, H., O'CONNOR, B. H., PRIDA, V. M., & LOW, I. M. 2015. Effect of Vanadium Ion Implantation on the Crystallization Kinetics and Phase Transformation of Electrospun TiO_2 Nanofibers. *Applied Physics A*, 120, 623–634.

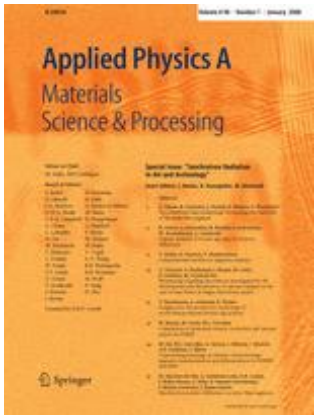

Title: Effect of vanadium ion implantation on the crystallization kinetics and phase transformation of electrospun TiO2 nanofibers

Author: H. Albetran

Publication: Applied Physics A: Materials Science & Processing

Publisher: Springer

Date: Jan 1, 2015

Order Completed

Thank you very much for your order.

This is a License Agreement between HANI ALBETRAN ("You") and Springer ("Springer"). The license consists of your order details, the terms and conditions provided by Springer, and the payment terms and conditions.

Get the printable license.

License Number	3830691120887
License date	Mar 16, 2016
Licensed content publisher	Springer
Licensed content publication	Applied Physics A: Materials Science & Processing
Licensed content title	Effect of vanadium ion implantation on the crystallization kinetics and phase transformation of electrospun TiO2 nanofibers
Licensed content author	H. Albetran
Licensed content date	Jan 1, 2015
Volume number	120
Issue number	2
Type of Use	Thesis/Dissertation
Portion	Full text
Number of copies	1
Author of this Springer article	Yes and you are the sole author of the new work
Title of your thesis / dissertation	Synthesis and Characterisation of Nanostructured TiO2 for Photocatalytic Applications
Expected completion date	Mar 2016
Estimated size(pages)	309
Total	0.00 USD

CLOSE WINDOW

Appendix V-D: Copyright information relating to

ALBETRAN, H., O'CONNOR, B. H., & LOW, I. M. 2016. Effect of Calcination on Band Gaps for Electrospun Titania Nanofibers Heated in Air–Argon Mixtures. *Materials & Design*, 92, 480–485.

Dear Dr. Albetran

Thank you for your permission request.

Please note that as one of the Authors of this article, you retain the right to include the journal article, in full or in part, in a thesis or dissertation. You do not require permission to do so.

For full details of your rights as a Journal Author, please visit:

http://www.elsevier.com/wps/find/authorsview.authors/copyright#whatrights

Your retained rights allow you to submit your article in electronic format and to post this Elsevier article online if it is embedded within your thesis. You are also permitted to post your Author Accepted Manuscript online however posting of the final published article is prohibited.

Please refer to Elsevier's Posting Policy for further information:

http://www.elsevier.com/wps/find/authors.authors/postingpolicy

Please feel free to contact me if you have any queries.

Thanks

Regards

Banita Samantray
Global Rights Department

Elsevier
(A division of Reed Elsevier India Pvt. Ltd.)

Ascendas International Tech Park | Crest Building – 12th Floor | Taramani Road | Taramani | Chennai 600 113 | India
Tel: +91 44 42994667 | Fax: +91 44 42994701
E-mail: b.samantray@reedelsevier.com | url: www.elsevier.com

Appendix V-E: Copyright information relating to

ALBETRAN, H., DONG, Y. & LOW, I. M. 2015. Characterization and Optimization of Electrospun TiO_2/PVP Nanofibers Using Taguchi Design of Experiment Method. *Journal of Asian Ceramic Societies,* 3, 292–300.

Dear Dr. Albetran

Thank you for your permission request.

Please note that as one of the Authors of this article, you retain the right to include the journal article, in full or in part, in a thesis or dissertation. You do not require permission to do so.

For full details of your rights as a Journal Author, please visit:

http://www.elsevier.com/wps/find/authorsview.authors/copyright#whatrights

Your retained rights allow you to submit your article in electronic format and to post this Elsevier article online if it is embedded within your thesis. You are also permitted to post your Author Accepted Manuscript online however posting of the final published article is prohibited.

Please refer to Elsevier's Posting Policy for further information:

http://www.elsevier.com/wps/find/authors.authors/postingpolicy

Please feel free to contact me if you have any queries.

Thanks

Regards

Banita Samantray
Global Rights Department

Elsevier
(A division of Reed Elsevier India Pvt. Ltd.)

Ascendas International Tech Park | Crest Building – 12th Floor | Taramani Road | Taramani | Chennai 600 113 | India
Tel: +91 44 42994667 | Fax: +91 44 42994701
E-mail: b.samantray@reedelsevier.com | url: www.elsevier.com

Appendix V-F: Copyright information relating to

LOW, I. M., ALBETRAN, H., PRIDA, V. M., VEGA, V., MANURUNG, P., & IONESCU, M. 2013. A Comparative Study on Crystallization Behavior, Phase Stability, and Binding Energy in Pure and Cr-Doped TiO_2 Nanotubes. *Journal of Materials Research*, 28, 304–312.

Title:	A comparative study on crystallization behavior, phase stability, and binding energy in pure and Cr-doped TiO_2 nanotubes
Author:	It Meng Low, Hani Albetran, Victor Manuel Prida, Victor Vega, Posman Manurung and Mihail Ionescu
Publication:	Journal of Materials Research
Publisher:	Cambridge University Press
Date:	Aug 29, 2012

Order Completed

Thank you for your order.

This Agreement between HANI ALBETRAN ("You") and Cambridge University Press ("Cambridge University Press") consists of your license details and the terms and conditions provided by Cambridge University Press and Copyright Clearance Center.

Your confirmation email will contain your order number for future reference.

Get the printable license.

License Number	3830700830318
License date	Mar 16, 2016
Licensed Content Publisher	Cambridge University Press
Licensed Content Publication	Journal of Materials Research
Licensed Content Title	A comparative study on crystallization behavior, phase stability, and binding energy in pure and Cr-doped TiO_2 nanotubes
Licensed Content Author	It Meng Low, Hani Albetran, Victor Manuel Prida, Victor Vega, Posman Manurung and Mihail Ionescu
Licensed Content Date	Aug 29, 2012
Licensed Content Volume	28
Licensed Content Issue	03
Start page	304
End page	312
Type of Use	Dissertation/Thesis
Requestor type	Author
Portion	Full article
Author of this Cambridge University Press article	Yes
Author / editor of the new work	Yes
Order reference number	None
Territory for reuse	World
Title of your thesis / dissertation	Synthesis and Characterisation of Nanostructured TiO2 for Photocatalytic Applications
Expected completion date	Mar 2016
Estimated size(pages)	309
Requestor Location	HANI ALBETRAN 69 C henry St East Cannington, Australia 6107 Attn: HANI ALBETRAN

Appendix V-G: Copyright information relating to

ALBETRAN, H., LOW, I. M. 2016. Effect of Indium Ion Implantation on Crystallization Kinetics and Phase Transformation of Anodized Titania Nanotubes. *Journal of Materials Research*, 31, 1588–1595.

Title:	Effect of indium ion implantation on crystallization kinetics and phase transformation of anodized titania nanotubes using *in-situ* high-temperature radiation diffraction
Author:	Hani Albetran and It Meng Low
Publication:	Journal of Materials Research
Publisher:	Cambridge University Press
Date:	Mar 11, 2016

Order Completed

Thank you for your order.

This Agreement between HANI ALBETRAN ("You") and Cambridge University Press ("Cambridge University Press") consists of your license details and the terms and conditions provided by Cambridge University Press and Copyright Clearance Center.

Your confirmation email will contain your order number for future reference.

Get the printable license.

License Number	3831061182332
License date	Mar 16, 2016
Licensed Content Publisher	Cambridge University Press
Licensed Content Publication	Journal of Materials Research
Licensed Content Title	Effect of indium ion implantation on crystallization kinetics and phase transformation of anodized titania nanotubes using *in-situ* high-temperature radiation diffraction
Licensed Content Author	Hani Albetran and It Meng Low
Licensed Content Date	Mar 11, 2016
Licensed Content Volume	-1
Licensed Content Issue	-1
Start page	1
End page	8
Type of Use	Dissertation/Thesis
Requestor type	Author
Portion	Full article
Author of this Cambridge University Press article	Yes
Author / editor of the new work	Yes
Order reference number	None
Territory for reuse	World
Title of your thesis / dissertation	Synthesis and Characterisation of Nanostructured TiO2 for Photocatalytic Applications
Expected completion date	Mar 2016
Estimated size(pages)	309
Requestor Location	HANI ALBETRAN 69 C henry St East Cannington, Australia 6107 Attn: HANI ALBETRAN
Billing Type	Invoice
Billing address	HANI ALBETRAN 69 C henry St

Appendix V-H: Copyright information relating to

ALBETRAN, H., ALSAFWAN, A., HAROOSH, H., DONG, Y., & LOW, I. M. 2013. X-ray Diffraction Study on the *In-Situ* Crystallisation Kinetics in Electrospun PVP/TiO_2 Nanofibers. Nanostructured Materials and Nanotechnology VII: *Ceramic Engineering and Science Proceedings*, 34, 35–49.

WILEY

Book: Nanostructured Materials and Nanotechnology VII

Chapter: X-Ray Diffraction Study on the In-Situ Crystallization Kinetics in Electrospun PVP/TiO2 Nanofibers

Author: H. Albetran,A. Alsafwan,H. Haroosh,Y. Dong,I. M. Low

Publisher: John Wiley and Sons

Date: Nov 22, 2013

Order Completed

Thank you for your order.

This Agreement between HANI ALBETRAN ("You") and John Wiley and Sons ("John Wiley and Sons") consists of your license details and the terms and conditions provided by John Wiley and Sons and Copyright Clearance Center.

Your confirmation email will contain your order number for future reference.

Get the printable license.

License Number	3830700183162
License date	Mar 16, 2016
Licensed Content Publisher	John Wiley and Sons
Licensed Content Publication	Wiley oBooks
Licensed Content Title	X-Ray Diffraction Study on the In-Situ Crystallization Kinetics in Electrospun PVP/TiO2 Nanofibers
Licensed Content Author	H. Albetran,A. Alsafwan,H. Haroosh,Y. Dong,I. M. Low
Licensed Content Date	Nov 22, 2013
Licensed Content Pages	15
Type of use	Dissertation/Thesis
Requestor type	Author of this Wiley chapter
Format	Print and electronic
Portion	Full chapter
Will you be translating?	No
Title of your thesis / dissertation	Synthesis and Characterisation of Nanostructured TiO2 for Photocatalytic Applications
Expected completion date	Mar 2016
Expected size (number of pages)	309
Requestor Location	HANI ALBETRAN 69 C henry St East Cannington, Australia 6107 Attn: HANI ALBETRAN
Billing Type	Invoice
Billing address	HANI ALBETRAN 69 C henry St East Cannington, Australia 6107 Attn: HANI ALBETRAN
Total	0.00 USD

CLOSE WINDOW

Appendix V-I: Copyright information relating to

ALBETRAN, H., HAROOSH, H., DONG, Y., O'Connor, B. H., & LOW, I. M. 2014. Effect of Atmosphere on Crystallization Kinetics and Phase Relations in Electrospun TiO_2 Nanofibers. Ceramics for Environmental and Energy Applications II: *Ceramic Engineering and Science Proceedings*, 246, 125–133.

WILEY

Book: Ceramics for Environmental and Energy Applications II: Ceramic Transactions, Volume 246

Chapter: Effect of Atmosphere on Crystallisation Kinetics and Phase Relations in Electrospun TiO2 Nanofibres

Author: H. Albetran,H. Haroosh,Y. Dong,B.H. O\'Connor,I.M. Low

Publisher: John Wiley and Sons

Date: Mar 1, 2014

Order Completed

Thank you for your order.

This Agreement between HANI ALBETRAN ("You") and John Wiley and Sons ("John Wiley and Sons") consists of your license details and the terms and conditions provided by John Wiley and Sons and Copyright Clearance Center.

Your confirmation email will contain your order number for future reference.

Get the printable license.

License Number	3830700620720
License date	Mar 16, 2016
Licensed Content Publisher	John Wiley and Sons
Licensed Content Publication	Wiley oBooks
Licensed Content Title	Effect of Atmosphere on Crystallisation Kinetics and Phase Relations in Electrospun TiO2 Nanofibres
Licensed Content Author	H. Albetran,H. Haroosh,Y. Dong,B.H. O\'Connor,I.M. Low
Licensed Content Date	Mar 1, 2014
Licensed Content Pages	9
Type of use	Dissertation/Thesis
Requestor type	Author of this Wiley chapter
Format	Print and electronic
Portion	Full chapter
Will you be translating?	No
Title of your thesis / dissertation	Synthesis and Characterisation of Nanostructured TiO2 for Photocatalytic Applications
Expected completion date	Mar 2016
Expected size (number of pages)	309
Requestor Location	HANI ALBETRAN 69 C henry St East Cannington, Australia 6107 Attn: HANI ALBETRAN
Billing Type	Invoice
Billing address	HANI ALBETRAN 69 C henry St East Cannington, Australia 6107 Attn: HANI ALBETRAN
Total	0.00 USD

CLOSE WINDOW

Appendix V-J: Copyright information relating to

LOW, I. M., ALBETRAN, H., PRIDA, V., MANURUNG, P., & IONESCU, M. 2013. Effect of Chromium Doping on the Crystallization and Phase Stability in Anodized TiO_2 Nanotubes. Developments in Strategic Materials and Computational Design III: *The Ceramic Engineering and Science Proceedings*, 151–158.

WILEY

Book:	Developments in Strategic Materials and Computational Design III
Chapter:	Effect of Chromium-Doping on the Crystallization and Phase Stability in Anodized TiO2 Nanotubes
Author:	I.M. Low,H. Albetran,V. De La Prida,P. Manurung,M. Ionescu
Publisher:	John Wiley and Sons
Date:	Dec 3, 2012

Order Completed

Thank you for your order.

This Agreement between HANI ALBETRAN ("You") and John Wiley and Sons ("John Wiley and Sons") consists of your license details and the terms and conditions provided by John Wiley and Sons and Copyright Clearance Center.

Your confirmation email will contain your order number for future reference.

Get the printable license.

License Number	3830700426152
License date	Mar 16, 2016
Licensed Content Publisher	John Wiley and Sons
Licensed Content Publication	Wiley oBooks
Licensed Content Title	Effect of Chromium-Doping on the Crystallization and Phase Stability in Anodized TiO2 Nanotubes
Licensed Content Author	I.M. Low,H. Albetran,V. De La Prida,P. Manurung,M. Ionescu
Licensed Content Date	Dec 3, 2012
Licensed Content Pages	10
Type of use	Dissertation/Thesis
Requestor type	Author of this Wiley chapter
Format	Print and electronic
Portion	Full chapter
Will you be translating?	No
Title of your thesis / dissertation	Synthesis and Characterisation of Nanostructured TiO2 for Photocatalytic Applications
Expected completion date	Mar 2016
Expected size (number of pages)	309
Requestor Location	HANI ALBETRAN 69 C henry St East Cannington, Australia 6107 Attn: HANI ALBETRAN
Billing Type	Invoice
Billing address	HANI ALBETRAN 69 C henry St East Cannington, Australia 6107 Attn: HANI ALBETRAN
Total	0.00 USD

CLOSE WINDOW

10 Bibliography

Akhtar, M. K., Pratsinis, S. E. & Mastrangelo, S. V. R. 1992. Dopants in Vapor-Phase Synthesis of Titania Powders. *Journal of the American Ceramic Society*, 75, 3408–3416.

Albu, S. P., Tsuchiya, H., Fujimoto, S. & Schmuki, P. 2010. TiO_2 Nanotubes–Annealing Effects on Detailed Morphology and Structure. *European Journal of Inorganic Chemistry*, 2010, 4351–4356.

Alivov, Y., Klopfer, M. & Molloi S. 2010. Effect of TiO_2 Nanotube Parameters on Field Emission Properties. *Nanotechnology*, 21, 505706–505711.

Anpo, M. 2000. Use of Visible Light. Second-Generation Titanium Oxide Photocatalysts Prepared by the Application of an Advanced Metal Ion-Implantation Method. *Pure and Applied Chemistry*, 72, 1787–1792.

Anton, F. 1934. Process and Apparatus for Preparing Artificial Threads. Google Patents.

Archana, P., Jose, Vijila, R. C. & Ramakrishna. S. 2009. Improved Electron Diffusion Coefficient in Electrospun TiO_2 Nanowires. *The Journal of Physical Chemistry C.*, 113, 21538–21542.

Armstrong, A. R., Armstrong, G. Canales, J. Garcia, R. & Bruce, P. G. 2005. Lithium-Ion Intercalation into TiO_2-B Nanowires. *Advanced Materials*, 17, 862–865.

Asahi, R., Morikawa, T. Ohwaki, T. Aoki, K. & Taga, Y. 2001. Visible–Light Photocatalysis in Nitrogen-Doped Titanium Oxides. *Science*, 293, 269–271.

Augugliaro, V., Loddo, V. Palmisano, G. Pagliaro, M. & Palmisano, L. 2010. Clean by Light Irradiation: Practical Applications of Supported TiO_2: Royal Society of Chemistry.

Bai, Y., Cao, Y. Zhang, J. Wang, M. Li, R. Wang, P. Zakeeruddin, S. M. & Gratzel M. 2008. High-Performance Dye-Sensitized Solar Cells Based on Solvent-Free Electrolytes Produced from Eutectic Melts. *Nature Materials*, 7, 626–630.

Bak, T. 2002. Photo-Electrochemical Hydrogen Generation from Water Using Solar Energy. Materials-Related Aspects. *International Journal of Hydrogen Energy*, 27, 991–1022.

Barakat, M. A., Hayes, G. and Shah, S. I. 2005. Effect of Cobalt Doping on the Phase Transformation of TiO_2 Nanoparticles. *Journal of Nanoscience and Nanotechnology*, 5, 759–765.

Barzykin, A. V., and Tachiya, M. 2002. Mechanism of Charge Recombination in Dye-Sensitized Nanocrystalline Semiconductors: Random Flight Model. *The Journal of Physical Chemistry B*., 106, 4356–4363.

Bavykin, D. V., and Walsh, F. C. 2010. Titanate and Titania Nanotubes Synthesis, Properties and Applications. Cambridge: RSC Publishing.

Bavykin, D. V., Parmon, V. N. Lapkin, A. A. & Walsh, F. C. 2004. The Effect of Hydrothermal Conditions on the Mesoporous Structure of TiO_2 Nanotubes. *Journal of Materials Chemistry*, 14, 3370–3377.

Beh, K., Yam, F. Tneh, S. & Hassan, Z. 2011. Fabrication of Titanium Dioxide Nanofibers via Anodic Oxidation. *Applied Surface Science*, 257, 4706–4708.

Beltran, A., Gracia, L. & Andres, J. 2006. Density Functional Theory Study of the Brookite Surfaces and Phase Transitions between Natural Titania Polymorphs. *The Journal of Physical Chemistry B*., 110, 23417–23423.

Benedix, R., Dehn, F. Quaas, J. & Orgass M. 2000. Application of Titanium Dioxide Photocatalysis to Create Self-Cleaning Building Materials. *Lacer*, 5, 157–168.

Bickley, R. I., Gonzalez-Carreno T. Lees, J. S. Palmisano, L. & Tilley R. J. D. 1991. A Structural Investigation of Titanium Dioxide Photocatalysts. *Journal of Solid State Chemistry*, 92, 178–190.

Bokhimi, X., Morales, A. Aguilar, M. Toledo-Antonio, J. A. & Pedraza, F. 2001. Local Order in Titania Polymorphs. *International Journal of Hydrogen Energy*, 26, 1279–1287.

Brahimi, R., Bessekhouad, Y. Bouguelia, A. & Trari, M. 2007. Visible Light Induced Hydrogen Evolution over the Heterosystem Bi_2S_3/ TiO_2. *Catalysis Today*, 122, 62–65.

Bruker, AXS. 2008. Topas V4: General Profile and Structure Analysis Software for Powder Diffraction Data. - User's Manual. Karlsruhe, Germany: Bruker AXS.

Bühler, Volker. 2005. Polyvinylpyrrolidone Excipients for Pharmaceuticals: Povidone, Crospovidone and Copovidone: Springer Science & Business Media.

Burdett, J. K., Hughbanks, T. Miller, G. J. Jr, J. W. R. & Smith, J. V. 1987. Structural-Electronic Relationships in Inorganic Solids: Powder Neutron Diffraction Studies of the Rutile and Anatase Polymorphs of Titanium Dioxide at 15 and 295 K. *Journal of the American Chemical Society*, 109, 3639–3646.

Caglioti, G., Paoletti, A. & Ricci F. P. 1958. Choice of Collimators for a Crystal Spectrometer for Neutron Diffraction. *Nuclear Instruments*, 3, 223–228.

Carp, O., Huisman, C. L. & Reller, A. 2004. Photoinduced Reactivity of Titanium Dioxide. *Progress in Solid State Chemistry*, 32, 33–177.

Chatterjee, D., & Mahata, A. 2001. Demineralization of Organic Pollutants on the Dye Modified TiO_2 Semiconductor Particulate System Using Visible Light. *Applied Catalysis B: Environmental*, 33, 119–125.

Chen, D., Jiang, Z. Geng, J. Wang, Q. & Yang, D. 2007. Carbon and Nitrogen Co-Doped TiO_2 with Enhanced Visible-Light Photocatalytic Activity. *Industrial & Engineering Chemistry Research*, 46, 2741–2746.

Choi, W., Termin, A. & Hoffmann, M. R. 1994. The Role of Metal Ion Dopants in Quantum-Sized TiO_2: Correlation between Photoreactivity and Charge Carrier

Recombination Dynamics. *The Journal of Physical Chemistry*, 98, 13669–13679.

Chu, W. 2001. Dye Removal from Textile Dye Wastewater Using Recycled Alum Sludge. *Water Research*, 35, 3147–3152.

Chuangchote, S., Jitputti, J. Sagawa, T. & S. Yoshikawa. 2009. Photocatalytic Activity for Hydrogen Evolution of Electrospun TiO_2 Nanofibers. *ACS Applied Materials & Interfaces*, 1, 1140–1143.

Cornaz, P. F., Hooff, J. H. C. Pluijm, F. J. & Schuit, G. C. A. 1966. Surface Co-Ordination of Oxygen on Oxygen-Deficient TiO_2 and MoO_3 as Revealed by E.S.R-Measurements. *Discussions of the Faraday Society*, 41, 290–304.

Cromer, D. T., & Herrington, K. 1955. The Structures of Anatase and Rutile. *Journal of the American Chemical Society*, 77, 4708–4709.

Dai, H., Gong, J. Kim, H. & Lee, D. 2002. A Novel Method for Preparing Ultra-Fine Alumina-Borate Oxide Fibres via an Electrospinning Technique. *Nanotechnology*, 13, 674–677.

Delplancke, J. L., Garnier, A. Massiani, Y. & Winand, R. 1994. Influence of the Anodizing Procedure on the Structure and the Properties of Titanium Oxide Films and Its Effect on Copper Nucleation. *Electrochimica Acta*, 39, 1281–1289.

Depero, L. E., Marino, A. Allieri, B. Bontempi, E. Sangaletti, L. Casale, C. & Notaro, M. 2000. Morphology and Microstructural Properties of TiO_2 Nanopowders Doped with Trivalent Al and Ga Cations. *Journal of Materials Research*, 15, 2080–2086.

Depero, L. E., Sangaletti, L. Allieri, B. Bontempi, E. Marino, A. & Zocchi, M. 1999. Correlation between Crystallite Sizes and Microstrains in TiO_2 Nanopowders. *Journal of Crystal Growth*, 198, 516–520.

Dholam, R., Patel, N. Santini, A. & A. Miotello. 2010. Efficient Indium Tin Oxide/Cr-Doped-TiO_2 Multilayer Thin Films for H_2 Production by Photocatalytic Water-Splitting. *International Journal of Hydrogen Energy*, 35, 9581–9590.

Ding, X. Z., Liu, X. H. & He, Y. Z. 1996. Grain Size Dependence of Anatase-to-Rutile Structural Transformation in Gel-Derived Nanocrystalline Titania Powders. *Journal of Materials Science Letters*, 15, 1789–1791.

Doh, S. J. 2008. Development of Photocatalytic TiO_2 Nanofibers by Electrospinning and Its Application to Degradation of Dye Pollutants. *Journal of Hazardous Materials*, 154, 118.

Dong, W., Zhang, T. Epstein, J. Cooney, L. Wang, H. Li, Y. Jiang, Y. B. Cogbill, A. Varadan, V. & Tian, Z. R. 2007. Multifunctional Nanowire Bioscaffolds on Titanium. *Chemistry of Materials*, 19, 4454–4459.

Dong, Y., & Bhattacharyya, D. 2008. Effects of Clay Type, Clay/Compatibiliser Content and Matrix Viscosity on the Mechanical Properties of Polypropylene/Organoclay Nanocomposites. *Composites Part A: Applied Science and Manufacturing*, 39, 1177–1191.

Dransfield, G., Guest, P. J. Lyth, P. L. McGarvey, D. J. & Truscott, T. G. 2000. Photoactivity Tests of TiO_2-Based Inorganic Sunscreens: Part 1: Non-Aqueous Dispersions. *Journal of Photochemistry and Photobiology B: Biology*, 59, 147–151.

Du, G. H., Chen, Q. Che, R. C. Yuan, Z. Y. & Peng, L. M. 2001. Preparation and Structure Analysis of Titanium Oxide Nanotubes. *Applied Physics Letters*, 79, 3702–3704.

Dzenis, Y. A. 2004. Spinning Continuous Fibers for Nanotechnology. *Science*, 304, 1917–1919.

Eppler, R. A. 1987. Effect of Antimony Oxide on the Anatase-Rutile Transformation in Titanium Dioxide. *Journal of the American Ceramic Society*, 70, 64-66.

Eufinger, K., Poelman, D. Poelman, H. Gryse, R. D. & Marin, G. B. 2007. Photocatalytic Activity of Dc Magnetron Sputter Deposited Amorphous TiO_2 Thin Films. *Applied Surface Science*, 254, 148–152.

Fan, X., Chen, X. Zhu, S. Li, Z. Yu, T. Ye, J. & Zou, Z. 2008. The Structural, Physical and Photocatalytic Properties of the Mesoporous Cr-Doped TiO_2. *Journal of Molecular Catalysis A: Chemical*, 284, 155–160.

Fang, D., Luo, Z. Huang, K. & Lagoudas, D. C. 2011. Effect of Heat Treatment on Morphology, Crystalline Structure and Photocatalysis Properties of TiO_2 Nanotubes on Ti Substrate and Freestanding Membrane. *Applied Surface Science*, 257, 6451–6461.

Fang, H. T., Liu, M. Wang, D. W. Sun, T., Guan, D. S., Li, F., Zhou, J., Sham, T. K. & Cheng, H. M. 2009. Comparison of the Rate Capability of Nanostructured Amorphous and Anatase TiO_2 for Lithium Insertion Using Anodic TiO_2 Nanotube Arrays. *Nanotechnology*, 20, 225701.

Fang, W. Q., Gong, X. Q. & Yang, H. G. 2011. On the Unusual Properties of Anatase TiO_2 Exposed by Highly Reactive Facets. *The Journal of Physical Chemistry Letters*, 2, 725–734.

Feng, L., Li, S. Li, H. Zhai, J. Song, Y. Jiang, L. & Zhu, D. 2002. Super-Hydrophobic Surface of Aligned Polyacrylonitrile Nanofibers. *Angewandte Chemie*, 114, 1269–1271.

Fridrikh, S. V., Yu, J. H. Brenner, M. P. & Gregory C Rutledge. 2003. Controlling the Fiber Diameter During Electrospinning. *Physical Review Letters*, 90, 144502–144502.

Fujishima, A. 1972. Electrochemical Photolysis of Water at a Semiconductor Electrode. *Nature*, 238, 37–38.

Fujishima, A. & Honda, K. 1972. Photolysis-Decomposition of Water at the Surface of an Irradiated Semiconductor. *Nature* 238, 37–38.

Fujishima, A., Rao, T. N. & Tryk, D. A. 2000. Titanium Dioxide Photocatalysis. *Journal of Photochemistry and Photobiology C: Photochemistry Reviews*, 1, 1–21.

Gaewdang, T., Chaminade, J. P. Gravereau, P. Garcia, A. Fouassier, C. Hagenmuller, P. & Mahiou, R. 1993. Crystal Structure and Luminescent Properties of Indium Titanate. *Materials Research Bulletin*, 28, 1051–1060.

Gamboa, J. A. & Pasquevich, D. M. 1992. Effect of Chlorine Atmosphere on the Anatase-Rutile Transformation. *Journal of the American Ceramic Society*, 75, 2934–2938.

Gao, X., Zhu, H. Pan, G. Ye, S. Lan, Y. Wu, F. & Song, D. 2004. Preparation and Electrochemical Characterization of Anatase Nanorods for Lithium-Inserting Electrode Material. *The Journal of Physical Chemistry B.*, 108, 2868–2872.

Gennari, F. C. & Pasquevich, D. M. 1998. Kinetics of the Anatase–Rutile Transformation in TiO_2 in the Presence of Fe_2O_3. *Journal of Materials Science*, 33, 1571–1578.

Ghani, J. A. Choudhury, I. A. & Hassan, H. H. 2004. Application of Taguchi Method in the Optimization of End Milling Parameters. *Journal of Materials Processing Technology*, 145, 84–92.

Ghows, N. & Entezari, M. H. 2011. Fast and Easy Synthesis of Core–Shell Nanocrystal (Cds/TiO_2) at Low Temperature by Micro-Emulsion under Ultrasound. *Ultrasonics Sonochemistry*, 18, 629–634.

Gong, D., Grimes, C. A. Varghese, O. K. Hu, W. Singh, R. S. Chen, Z. & Dickey, E. C. 2001. Titanium Oxide Nanotube Arrays Prepared by Anodic Oxidation. *Journal of Materials Research*, 16, 3331–3334.

Gratzel, M. 2001. Photoelectrochemical Cells. *Nature*, 414, 338–344.

Gratzel, M. 2005. Solar Energy Conversion by Dye-Sensitized Photovoltaic Cells. *Inorganic Chemistry*, 44, 6841–6851.

Guidi, V., Carotta, M. C. Ferroni, M. Martinelli, G. & M Sacerdoti. 2003. Effect of Dopants on Grain Coalescence and Oxygen Mobility in Nanostructured Titania Anatase and Rutile. *The Journal of Physical Chemistry B*., 107, 120–124.

Guo, D. D., Lin, S.S. Zhong, F.X. Zhu, Y.N. & Meng, Z. P. 2012. High-Efficiency Degradation Sugar Wastewater by Co-TiO_2 Nanotube Arrays. *Integrated Ferroelectrics*, 137, 10–17.

Hanaor, D. A. H. & Sorrell, C. C. 2011. Review of the Anatase to Rutile Phase Transformation. *Journal of Materials Science*, 46, 855–874.

Hao, W., Pan, F. and Wang, T. 2005. Photocatalytic Activity TiO_2 Granular Films Prepared by Layer-by-Layer Self-Assembly Method. *Journal of Materials Science*, 40, 1251–1253.

Hardick, O., Stevens, B. & Bracewell, D. G. 2011. Nanofibre Fabrication in a Temperature and Humidity Controlled Environment for Improved Fibre Consistency. *Journal of Materials Science*, 46, 3890–3898.

Hashimoto, K., Irie, H. & Fujishima A. 2005. TiO_2 Photocatalysis: A Historical Overview and Future Prospects. *Japanese Journal of Applied Physics*, 44, 8269.

Hassan, M. S., Amna, T. Yang, O. B. Kim, H. & Khil, M. 2012. TiO_2 Nanofibers Doped with Rare Earth Elements and Their Photocatalytic Activity. *Ceramics International*, 38, 5925–5930.

Hong, X., Wang, Z. Cai, W. Lu, F. Zhang, J. Yang, Y. Ma, N. & Liu, Y. 2005. Visible-Light-Activated Nanoparticle Photocatalyst of Iodine-Doped Titanium Dioxide. *Chemistry of Materials*, 17, 1548–1552.

Hoyer, P. 1996. Formation of a Titanium Dioxide Nanotube Array. *Langmuir*, 12, 1411–1413.

Hsu, S.W., Yang, T. S. Chen, T. K. & Wong, M. S. 2007. Ion-Assisted Electron-Beam Evaporation of Carbon-Doped Titanium Oxide Films as Visible-Light Photocatalyst. *Thin Solid Films*, 515, 3521–3526.

Hu, P., Du, G. Zhou, W. Cui, J. Lin, J. Liu, H. Liu, D. Wang, J. & Chen, S. 2010. Enhancement of Ethanol Vapor Sensing of TiO_2 Nanobelts by Surface Engineering. *ACS Applied Materials & Interfaces*, 2, 3263–3269.

Huang, J. H. & Ming-Show Wong. 2011. Structures and Properties of Titania Thin Films Annealed under Different Atmosphere. *Thin Solid Films*, 520, 1379–1384.

Huang, S. Y., Schlichthorl, G. Nozik, A. J. Gratzel, M. & Frank, A. J. 1997. Charge Recombination in Dye-Sensitized Nanocrystalline TiO_2 Solar Cells. *The Journal of Physical Chemistry B.*, 101, 2576–2582.

Huang, Z. M., Zhang, Y. Z. Kotaki, M. & S. Ramakrishna. 2003. A Review on Polymer Nanofibers by Electrospinning and Their Applications in Nanocomposites. *Composites Science and Technology*, 63, 2223–2253.

Hulteen, J. C. 1997. A General Template-Based Method for the Preparation of Nanomaterials. *Journal of Materials Chemistry*, 7, 1075–1087.

Hummer, D. R, Heaney, P. J. & Post, J. E. 2007. Thermal Expansion of Anatase and Rutile between 300 and 575 K Using Synchrotron Powder X-Ray Diffraction. *Powder Diffraction*, 22, 352–357.

Hunter, B. A. & Howard, C. J. 2000. Australian Nuclear Science and Technology Organization. Menai Australia, Lucas Heights Research Laboratories.

Iida, Y. & Ozaki, S. 1961. Grain Growth and Phase Transformation of Titanium Oxide During Calcination. *Journal of the American Ceramic Society*, 44, 120–127.

Iijima, S. 1991. Helical Microtubules of Graphitic Carbon. *Nature*, 354, 56–58.

Imai, H., Takei, Y. Shimizu, K. Matsuda, M. & Hirashima, H. 1999. Direct Preparation of Anatase TiO_2 Nanotubes in Porous Alumina Membranes. *Journal of Materials Chemistry,* 9, 2971–2972.

Inai, R., Kotaki, M. & Ramakrishna, S. 2005. Structure and Properties of Electrospun Plla Single Nanofibres. *Nanotechnology,* 16, 208.

Jamnongkan, T., Shirota, R. Sukumaran, S. K. Sugimoto, M. & Koyama K. 2013. Controlling Diameter of Fibers for Antibacterial Dressings. *Society of Plastics Engineers Plastics Research Online*, 1–2.

Jantawasu, P., Sreethawong, T. & Chavadej, S. 2009. Photocatalytic Activity of Nanocrystalline Mesoporous-Assembled TiO_2 Photocatalyst for Degradation of Methyl Orange Monoazo Dye in Aqueous Wastewater. *Chemical Engineering Journal*, 155, 223–233.

Jiang, J., Chen, J. & Dahn, J. R. 2004. Comparison of the Reactions between $Li_{7/3}Ti_{5/3}O_4$ or LiC_6 and Nonaqueous Solvents or Electrolytes Using Accelerating Rate Calorimetry. *Journal of the Electrochemical Society*, 151, 2082–2087.

Kamat, P. V. 2012. Manipulation of Charge Transfer across Semiconductor Interface. A Criterion that Cannot Be Ignored in Photocatalyst Design. *The Journal of Physical Chemistry Letters,* 3, 663–672.

Kandavelu, V., Kastien, H. & Thampi, K. R. 2004. Photocatalytic Degradation of Isothiazolin-3-Ones in Water and Emulsion Paints Containing Nanocrystalline TiO_2 and ZnO Catalysts. *Applied Catalysis B: Environmental*, 48, 101–111.

Kasuga, T., Hiramatsu, M. Hoson, A. Sekino, T. & Niihara, K. 1998. Formation of Titanium Oxide Nanotube. *Langmuir*, 14, 3160–3163.

Kim, B., Kim, D. Cho, D. & Cho, S. 2003. Bactericidal Effect of TiO_2 Photocatalyst on Selected Food-Borne Pathogenic Bacteria. *Chemosphere*, 52, 277–281.

Kim, D. W., Enomoto, N. Nakagawa, Z. & Kawamura, K. 1996. Molecular Dynamic Simulation in Titanium Dioxide Polymorphs: Rutile, Brookite, and Anatase. *Journal of the American Ceramic Society*, 79, 1095–1099.

Kim, J. H., Fujita, S. & Shiratori, S. 2006. Fabrication and Characterization of TiO_2 Thin Film Prepared by a Layer-by-Layer Self-Assembly Method. *Thin Solid Films*, 499, 83–89.

Kisi, E. H. 1994. Rietveld Analysis of Powder Diffraction Patterns. *Materials Forum*, 18, 135–155.

Kment, S., Kluson, P. Stranak, V. Virostko, P. Krysa, J. Cada, M. Pracharova, J. Kohout, M. Morozova, M. & Adamek, P. 2009. Photo-Induced Electrochemical Functionality of the TiO_2 Nanoscale Films. *Electrochimica Acta*, 54, 3352–3359.

Ksapabutr, B., Chalermkiti, T. & Panapoy, M. 2005. Effect of Nozzle Shapes on the Formation of Taylor Cone and the Oscillation of Fibers During Electrospinning Process. *Chiang Mai University Journal*, 4, 115–119.

Kumar, A., Jose, R. Fujihara, K. Wang, J. & Ramakrishna, S. 2007. Structural and Optical Properties of Electrospun TiO_2 Nanofibers. *Chemistry of Materials*, 19, 6536–6542.

Kuo, H. L., Kuo, C. Y. Liu, C. H. Chao, J. H. & Lin, C. H. 2007. A Highly Active Bi-Crystalline Photocatalyst Consisting of TiO_2 (B) Nanotube and Anatase Particle for Producing H_2 Gas from Neat Ethanol. *Catalysis Letters*, 113, 7–12.

Lam, R. C. W., Leung, M. K. H. Leung, D. Y. C. Vrijmoed, L. L. P. Yam, W. C. & Ng, S. P. 2007. Visible-Light-Assisted Photocatalytic Degradation of Gaseous Formaldehyde by Parallel-Plate Reactor Coated with Cr Ion-Implanted TiO_2 Thin Film. *Solar Energy Materials and Solar Cells*, 91, 54–61.

Landmann, M., Rauls, E. & Schmidt, W. G. 2012. The Electronic Structure and Optical Response of Rutile, Anatase and Brookite TiO_2. *Journal of Physics: Condensed Matter*, 24, 195503.

Latroche, M., Brohan, L. Marchand, R. & M Tournoux. 1989. New Hollandite Oxides: TiO_2 (H) and K 0.06 TiO_2. *Journal of Solid State Chemistry*, 81, 78–82.

Lee, C. K., Wang, C. C. Juang, L. C. Lyu, M. D., Hung, S. H. & Liu, S. S. 2008. Effects of Sodium Content on the Microstructures and Basic Dye Cation Exchange of Titanate Nanotubes. *Colloids and Surfaces A: Physicochemical and Engineering Aspects*, 317, 164–173.

Lee, S. S., Bai, H. Liu, Z. & Sun, D. D. 2012. Electrospun TiO_2/SnO_2 Nanofibers with Innovative Structure and Chemical Properties for Highly Efficient Photocatalytic H_2 Generation. *International Journal of Hydrogen Energy*, 37, 10575–10584.

Lee, S. S., Bai, H. Liu, Z. & Sun, D. D. 2013. Novel-Structured Electrospun TiO_2/Cuo Composite Nanofibers for High Efficient Photocatalytic Cogeneration of Clean Water and Energy from Dye Wastewater. *Water Research*, 47, 4059–4073.

Levinger, B. W. 1953. Lattice Parameter of Beta-Titanium at Room Temperature. *Transactions of the American Institute of Mining and Metallurgical Egineers*, 197, 195–195.

Li, D., Wang, Y. & Xia, Y. 2004. Electrospinning Nanofibers as Uniaxially Aligned Arrays and Layer-by-Layer Stacked Films. *Advanced Materials*, 16, 361–366.

Li, D. & Younan Xia. 2003. Fabrication of Titania Nanofibers by Electrospinning. *Nano Letters*, 3, 555–560.

Li, F., Zhao, Y. Hao, Y. Wang, X. Liu, R. Zhao, D. & Chen, D. 2012. N-Doped P25 TiO_2-Amorphous Al_2O_3 Composites: One-Step Solution Combustion Preparation and Enhanced Visible-Light Photocatalytic Activity. *Journal of Hazardous Materials*, 239, 118–127.

Li, H., Cao, L. Liu, W. Su, G. & Dong, B. 2012. Synthesis and Investigation of TiO_2 Nanotube Arrays Prepared by Anodization and Their Photocatalytic Activity. *Ceramics International*, 38, 5791–5797.

Li, H., Zhang, W. Li, B. & Pan, W. 2010. Diameter Dependent Photocatalytic Activity of Electrospun TiO_2 Nanofiber. *Journal of the American Ceramic Society*, 93, 2503–2506.

Li, H., Zhang, W. & Pan, W. 2011. Enhanced Photocatalytic Activity of Electrospun TiO_2 Nanofibers with Optimal Anatase/Rutile Ratio. *Journal of the American Ceramic Society*, 94, 3184–3187.

Li, J., Tang, Z. & Zhongtai Zhang. 2005a. H-Titanate Nanotube: A Novel Lithium Intercalation Host with Large Capacity and High Rate Capability. *Electrochemistry Communications*, 7, 62–67.

Li, J., Tang, Z. & Zhang, Z. 2005b. Layered Hydrogen Titanate Nanowires with Novel Lithium Intercalation Properties. *Chemistry of Materials*, 17, 5848–5855.

Li, L. & Liu, C. 2009. Facile Synthesis of Anatase–Brookite Mixed-Phase N-Doped TiO_2 Nanoparticles with High Visible-Light Photocatalytic Activity. *European Journal of Inorganic Chemistry*, 2009, 3727–3733.

Li, Q., Satur, D. J. G. Kim, H. & Kim, H. G. 2012a. Preparation of Sol–Gel Modified Electrospun TiO_2 Nanofibers for Improved Photocatalytic Decomposition of Ethylene. *Materials Letters*, 76, 169–172.

Li, Q., Satur, D. J. G. Kim, H. & Kim, H. G. 2012b. Preparation of Sol–Gel Modified Electrospun TiO_2 Nanofibers for Improved Photocatalytic Decomposition of Ethylene. *Materials Letters*, 76, 169–172.

Lin, C. H., Chao, J. H. Liu, C. H. Chang, J. C. & Wang, F. C. 2008. Effect of Calcination Temperature on the Structure of a Pt/ TiO_2 (B) Nanofiber and Its Photocatalytic Activity in Generating H_2. *Langmuir*, 24, 9907–9915.

Lin, H., Huang, C. P. Li, W. Ni, C. Shah, S. I. & Tseng, Y. H. 2006. Size Dependency of Nanocrystalline TiO_2 on Its Optical Property and Photocatalytic Reactivity Exemplified by 2-Chlorophenol. *Applied Catalysis B: Environmental*, 68, 1–11.

Linsebigler, A. L., Lu, G. & Jr, J. T. Y. 1995. Photocatalysis on TiO_2 Surfaces: Principles, Mechanisms, and Selected Results. *Chemical Reviews,* 95, 735–758.

Liu, G., Wang, L. Yang, H. G. Cheng, H. M. & G. Q. M. Lu. 2010. Titania-Based Photocatalysts-Crystal Growth, Doping and Heterostructuring. *Journal of Materials Chemistry*, 20, 831–843.

Liu, R., Qiang, L. S. Yang, W. D. & Liu, H. Y. 2013. The Effect of Calcination Conditions on the Morphology, the Architecture and the Photo-Electrical Properties of TiO_2 Nanotube Arrays. *Materials Research Bulletin*, 48, 1458–1467.

Liu, S. M., Gan, L. M., Liu, L. H. Zhang, W. D. & Zeng, H. C. 2002. Synthesis of Single-Crystalline TiO_2 Nanotubes. *Chemistry of Materials*, 14, 1391–1397.

Liu, S. & Chen, A. 2005. Coadsorption of Horseradish Peroxidase with Thionine on TiO_2 Nanotubes for Biosensing. *Langmuir*, 21, 8409–8413.

Low, I. M., Yam, F. K. & Pang, W. K. 2012. In–Situ Diffraction Studies on the Crystallization and Crystal Growth in Anodized TiO_2 Nanofibres. *Materials Letters*, 87, 150–152.

Low, I. M. 2012. Rutile Properties, Synthesis and Applications. New York*:* Nova Science Publishers, Inc.

Low, I. M., Curtain, B. Philipps, M. Liu, Q. Z. & Ionescu, M. 2012. High Temperature Diffraction Study of *in-Situ* Crystallization of Nanostructured TiO_2 Photocatalysts. *Journal of the Australian Ceramic Society*, 48, 198–204.

Luo, W., Hu, X. Sun, Y. & Huang, Y. 2012. Surface Modification of Electrospun TiO_2 Nanofibers via Layer-by-Layer Self-Assembly for High-Performance Lithium-Ion Batteries. *Journal of Materials Chemistry*, 22, 4910–4915.

Ma, R., Bando, Y. & Takayoshi Sasaki. 2004. Directly Rolling Nanosheets into Nanotubes. *The Journal of Physical Chemistry*, B., 108, 2115–2119.

Macak, J. M., Albu, S. P. & Patrik Schmuki. 2007. Towards Ideal Hexagonal Self-Ordering of TiO_2 Nanotubes. *Physica Status Solidi (RRL)–Rapid Research Letters*, 1, 181–183.

Macak, J. M., Tsuchiya, H. Ghicov, A. Yasuda, K. Hahn, R. Bauer, S. & Schmuki, P. 2007. TiO_2 Nanotubes: Self-Organized Electrochemical Formation, Properties and Applications. *Current Opinion in Solid State and Materials Science*, 11, 3–18.

Marchenoir, J. C., Loup, J. P. & J Masson. 1980. Etude Des Couches Poreuses Formees Par Oxydation Anodique Du Titane Sous Fortes Tensions. *Thin Solid Films*, 66, 357–369.

Marci, G., Augugliaro, V. Lopez-Munoz, M. J. Martin, C. Palmisano, L. Rives, V. Schiavello, M. Tilley, R. J. D. & Venezia, A. M. 2001. Preparation Characterization and Photocatalytic Activity of Polycrystalline ZnO/TiO_2 Systems. 1. Surface and Bulk Characterization. *The Journal of Physical Chemistry B.*, 105, 1026–1032.

Martin, C. R. 1996. Membrane-Based Synthesis of Nanomaterials. *Chemistry of Materials*, 8, 1739–1746.

Matsui, M. & Akaogi, M. 1991. Molecular Dynamics Simulation of the Structural and Physical Properties of the Four Polymorphs of TiO_2. *Molecular Simulation*, 6, 239–244.

McCann, J. T., Li, D. & Xia, Y. 2005. Electrospinning of Nanofibers with Core-Sheath, Hollow, or Porous Structures. *Journal of Materials Chemistry*, 15, 735–738.

Meagher, E. P. & Lager, G. A. 1979. Polyhedral Thermal Expansion Ln the TiO, Polymofphs: Refinement of the Crystal Structures of Rutile and Brookite at High Temperature. *Canadian Mineralogist*, 17, 77–85.

Michailowski, A., AlMawlawi, D. Cheng, G. & Moskovits, M. 2001. Highly Regular Anatase Nanotubule Arrays Fabricated in Porous Anodic Templates. *Chemical Physics Letters*, 349, 1–5.

Mills, A. & Le Hunte, S. 1997. An Overview of Semiconductor Photocatalysis. *Journal of Photochemistry and Photobiology A: Chemistry*, 108, 1–35.

Mishra, T., Wang, L. Hahn, R. & Schmuki, P. 2014. *In-Situ* Cr Doped Anodized TiO_2 Nanotubes with Increased Photocurrent Response. *Electrochimica Acta*, 132, 410–415.

Mo, S. D. & Ching, W. Y. 1995. Electronic and Optical Properties of Three Phases of Titanium Dioxide: Rutile, Anatase, and Brookite. *Physical Review B.*, 51, 13023.

Mora-Sero, I. & Bisquert, J. 2010. Breakthroughs in the Development of Semiconductor-Sensitized Solar Cells. *The Journal of Physical Chemistry Letters*, 1, 3046–3052.

Nalwa, H. S. 2004. Encyclopaedia of Nanoscience and Nanotechnology: CRC Press.

Nam, K. T., Kim, D. W. Yoo, P. J. Chiang, C. Yi. Meethong, N. Hammond, P. T. Chiang, Y. M. & Angela M Belcher. 2006. Virus-Enabled Synthesis and Assembly of Nanowires for Lithium Ion Battery Electrodes. *Science*, 312, 885–888.

Nam, S. H., Shim, H. S. Kim, Y. S. Dar, M. A. Kim, J. G. & Kim, W. B. 2010. Ag or Au Nanoparticle-Embedded One-Dimensional Composite TiO_2 Nanofibers

Prepared Via Electrospinning for Use in Lithium-Ion Batteries. *ACS Applied Materials & Interfaces*, 2, 2046–2052.

Natoli, A., Cabeza, A. Torre, A. G. Aranda, M. A. G. & Isabel Santacruz. 2012. Colloidal Processing of Macroporous TiO_2 Materials for Photocatalytic Water Treatment. *Journal of the American Ceramic Society*, 95, 502–508.

Nazeeruddin, M. K., Angelis, F. D. Fantacci, S. Selloni, A. Viscardi, G. Liska, P. Ito, S. Takeru, B. & Gratzel, M. 2005. Combined Experimental and Dft-Tddft Computational Study of Photoelectrochemical Cell Ruthenium Sensitizers. *Journal of the American Chemical Society*, 127, 16835–16847.

Ni, M., Leung, M. K. H. Leung, D. Y. C. & Sumathy, K. 2007. A Review and Recent Developments in Photocatalytic Water-Splitting Using TiO_2 for Hydrogen Production. *Renewable and Sustainable Energy Reviews*, 11, 401–425.

Nuansing, W., Ninmuang, S. Jarernboon, W. Maensiri, S. & S. Seraphin. 2006. Structural Characterization and Morphology of Electrospun TiO_2 Nanofibers. *Materials Science and Engineering*: B., 131, 147–155.

O'regan, B. & Gratzel, M. 1991. A Low-Cost, High-Efficiency Solar Cell Based on Dye-Sensitized Colloidal TiO_2 Films. *Nature*, 353, 737–740.

Ohno, T., Mitsui, T. & Michio Matsumura. 2003. Photocatalytic Activity of S-Doped TiO_2 Photocatalyst under Visible Light. *Chemistry Letters*, 32, 364–365.

Ohno, T., Sarukawa, K. & Michio Matsumura. 2001. Photocatalytic Activities of Pure Rutile Particles Isolated from TiO_2 Powder by Dissolving the Anatase Component in Hf Solution. *The Journal of Physical Chemistry B.*, 105, 2417–2420.

Okada, K., Yamamoto, N. Kameshima, Y. Yasumori, A. & MacKenzie, K. J. D. 2001. Effect of Silica Additive on the Anatase-to-Rutile Phase Transition. *Journal of the American Ceramic Society*, 84, 1591–1596.

Park, J. Y. & Kim, S. S. 2009. Effects of Processing Parameters on the Synthesis of TiO_2 Nanofibers by Electrospinning. *Metals and Materials International* 15, 95–99.

Park, J. Y., Yun, J. J. Hwang, C. H. & Lee, I. H. 2010. Influence of Silver Doping on the Phase Transformation and Crystallite Growth of Electrospun TiO_2 Nanofibers. *Materials Letters*, 64, 2692–2695.

Park, J. H., Kim, S. & Bard, A. J. 2006. Novel Carbon-Doped TiO_2 Nanotube Arrays with High Aspect Ratios for Efficient Solar Water Splitting. *Nano Letters*, 6, 24–28.

Patra, S., Easteal, A. & Bhattacharyya, D. 2009. Parametric Study of Manufacturing Poly (Lactic) Acid Nanofibrous Mat by Electrospinning. *Journal of Materials Science*, 44, 647–654.

Pauling, L. & Sturdivant, J. H. 1928. Xv. The Crystal Structure of Brookite. *Zeitschrift für Kristallographie–Crystalline Materials*, 68, 239–256.

Paulose, M., Shankar, K. Yoriya, S. Prakasam, H. E. Varghese, O. K. Mor, G. K. Latempa, T. A. Fitzgerald, A. & Grimes, C. A. 2006. Anodic Growth of Highly Ordered TiO_2 Nanotube Arrays to 134 Mm in Length. *The Journal of Physical Chemistry B.*, 110, 16179–16184.

Pfaff, G. & Reynders, P. 1999. Angle-Dependent Optical Effects Deriving from Submicron Structures of Films and Pigments. *Chemical Reviews*, 99, 1963–1982.

Plugaru, R., Cremades, A. & J Piqueras. 2004. The Effect of Annealing in Different Atmospheres on the Luminescence of Polycrystalline TiO_2. *Journal of Physics: Condensed Matter*, 16, S261.

Raja, K. S., Gandhi, T. & Misra, M. 2007. Effect of Water Content of Ethylene Glycol as Electrolyte for Synthesis of Ordered Titania Nanotubes. *Electrochemistry Communications* 9, 1069–1076.

Ranjit, R. 1990. A Primer on the Taguchi Method: van Nostrand Reinhold.

Rao, C. N. R., & Cheetham, A. K. 2001. Science and Technology of Nanomaterials: Current Status and Future Prospects. *Journal of Materials Chemistry* 11, 2887–2894.

Rao, C. N. R., Turner, A. & J. M. Honig. 1959. Some Observations Concerning the Effect of Impurities on the Anatase-Rutile Transition. *Journal of Physics and Chemistry of Solids,* 11, 173–175.

Reyes-Coronado, D., Rodriguez-Gattorno, G. Espinosa-Pesqueira, M. E. Cab, C. Coss, R. D. & Oskam, G. 2008. Phase-Pure TiO_2 Nanoparticles: Anatase, Brookite and Rutile. *Nanotechnology* 19, 145605.

Rietveld, H. M. 1969. A Profile Refinement Method for Nuclear and Magnetic Structures. *Journal of Applied Crystallography* 2, 65–71.

Rietveld, H. M. 1967. Line Profiles of Neutron Powder-Diffraction Peaks for Structure Refinement. *Acta Crystallographica* 22, 151–152.

Rupp, F., Scheideler, L. Olshanska, N. Wild, M. D. Wieland, M. & Geis-Gerstorfer, J. 2006. Enhancing Surface Free Energy and Hydrophilicity through Chemical Modification of Microstructured Titanium Implant Surfaces. *Journal of Biomedical Materials Research Part A.,* 76, 323–334.

Sahoo, C., Gupta, A. K. & Pillai, I. M. S. 2012. Photocatalytic Degradation of Methylene Blue Dye from Aqueous Solution Using Silver Ion-Doped TiO_2 and Its Application to the Degradation of Real Textile Wastewater. *Journal of Environmental Science and Health, Part A,* 47, 1428–1438.

Sakthivel, S. & Kisch, H. 2003. Daylight Photocatalysis by Carbon-Modified Titanium Dioxide. *Angewandte Chemie International Edition,* 42, 4908–4911.

Samadi, M., Shivaee, H. A. Zanetti, M. & Moshfegh, A. Z. 2012. Visible Light Photocatalytic Activity of Novel MWCNT-Doped ZnO Electrospun Nanofibers. *Journal of Molecular Catalysis A: Chemical,* 359, 42–48.

Sato, H., Endo, S. Sugiyama, M. Kikegawa, T. Shimomura, O. & Kusaba, K. 1991. Baddeleyite-Type High-Pressure Phase of TiO_2. *Science*, 251, 786–788.

Scherrer, P. 1918. Bestimmung Der Grösse Und Der Inneren Struktur Von Kolloidteilchen Mittels Röntgenstrahlen. *Nachrichten Von Der Gesellschaft Der Wissenschaften Zu Göttingen, Mathematisch–physikalische Klasse,* 1918, 98–100.

Senegas, J., Manaud, J. P. & Galy, J. 1975. Sur Un Nouveau Type D'oxydes Doubles M+ $Ivin_2O_5$ (M= Ti, V): Étude Cristallochimique. *Acta Crystallographica Section B: Structural Crystallography and Crystal Chemistry,* 31, 1614–1618.

Seo, D. S., Lee, J. K. & Hwan Kim. 2001. Preparation of Nanotube-Shaped TiO_2 Powder. *Journal of Crystal Growth,* 229, 428–432.

Serpone, N., Maruthamuthu, P. Pichat, P. Pelizzetti, E. & Hidaka, H. 1995. Exploiting the Interparticle Electron Transfer Process in the Photocatalysed Oxidation of Phenol, 2-Chlorophenol and Pentachlorophenol: Chemical Evidence for Electron and Hole Transfer between Coupled Semiconductors. *Journal of Photochemistry and Photobiology A: Chemistry,* 85, 247–255.

Shannon, R. D. & Pask, J. A. 1965. Kinetics of the Anatase-Rutile Transformation. *Journal of the American Ceramic Society,* 48, 391–398.

Sheppard, L. R. & Nowotny, J. 2007. Materials for Photoelectrochemical Energy Conversion. *Advances in Applied Ceramics*, 106, 9–20.

Shintani, H., Sato, S. & Y Saito. 1975. Electron–Density Distribution in Rutile Crystals. *Acta Crystallographica Section B: Structural Crystallography and Crystal Chemistry*, 31, 1981–1982.

Simons, P. Y. & Dachille, F. 1967. The Structure of TiO_2 II, a High-Pressure Phase of TiO_2. *Acta Crystallographica*, 23, 334–336.

Spurr, R. A. & H. Myers. 1957. Quantitative Analysis of Anatase-Rutile Mixtures with an X-Ray Diffractometer. *Analytical Chemistry* 29, 760–762.

Sun, X. & Li, Y. 2003. Synthesis and Characterization of Ion-Exchangeable Titanate Nanotubes. *Chemistry–A European Journal*, 9, 2229–2238.

Sunada, K., Kikuchi, Y. Hashimoto, K. & Fujishima, A. 1998. Bactericidal and Detoxification Effects of TiO_2 Thin Film Photocatalysts. *Environmental Science & Technology*, 32, 726–728.

Szanto, I. 1955. On the Determination of High-Purity Alpha-Titanium Lattice Parameters. *Acta Technica Academiae Scientarum Hungaricae*, 13, 363–372.

Takahashi, Y., Kijima, N. & Junji Akimoto. 2006. Synthesis, Structural Change Upon Heating, and Electronic Structure of Ramsdellite-Type TiO_2. *Chemistry of Materials*, 18, 748–752.

Tang, H., Prasad, K. Sanjines, R. Schmid, P. E. & Levy, F. 1994. Electrical and Optical Properties of TiO_2 Anatase Thin Films. *Journal of Applied Physics*, 75, 2042–2047.

Tang, Z. R., Li, F. Zhang, Y. H. Fu, X. Z. & Xu, Y. J. 2011a. Composites of Titanate Nanotube and Carbon Nanotube as Photocatalyst with High Mineralization Ratio for Gas-Phase Degradation of Volatile Aromatic Pollutant. *The Journal of Physical Chemistry C.*, 115, 7880–7886.

Tang, Z. R., Li, F. Zhang, Y. Fu, X. & Xu, Y. J. 2011b. Composites of Titanate Nanotube and Carbon Nanotube as Photocatalyst with High Mineralization Ratio for Gas-Phase Degradation of Volatile Aromatic Pollutant. *The Journal of Physical Chemistry C*., 115, 7880–7886.

Tian, Z. R., J. Voigt, A. Liu, J. Mckenzie, B. & Xu, H. 2003. Large Oriented Arrays and Continuous Films of TiO_2-Based Nanotubes. *Journal of the American Chemical Society*, 125, 12384–12385.

Thavasi, V., Singh, G. & Ramakrishna, S. 2008. Electrospun Nanofibers in Energy and Environmental Applications. *Energy & Environmental Science*, 1, 205–221.

Umebayashi, T., Yamaki, T. Itoh, H. & Asai, K. 2002. Band Gap Narrowing of Titanium Dioxide by Sulfur Doping. *Applied Physics Letters*, 81, 454–456.

Meulen, T., Mattson, A. & Osterlund, L. 2007. A Comparative Study of the Photocatalytic Oxidation of Propane on Anatase, Rutile, and Mixed-Phase Anatase-Rutile TiO_2 Nanoparticles: Role of Surface Intermediates. *Journal of Catalysis*, 251, 131–144.

Varghese, O. K., Gong, D. Paulose, M. Grimes, C. A. & Dickey, E. C. 2003. Crystallization and High-Temperature Structural Stability of Titanium Oxide Nanotube Arrays. *Journal of Materials Research*, 18, 156–165.

Vegard, L. 1916. Lv. *Results of Crystal Analysis.—III. The London, Edinburgh, and Dublin Philosophical Magazine and Journal of Science*, 32, 505–518.

Wang, J. & Lin, Z. 2009. Dye-Sensitized TiO_2 Nanotube Solar Cells with Markedly Enhanced Performance via Rational Surface Engineering. *Chemistry of Materials* 22, 579–584.

Wang, Q., Wen, Z. & Li, J. 2006. Solvent-Controlled Synthesis and Electrochemical Lithium Storage of One-Dimensional TiO_2 Nanostructures. *Inorganic Chemistry*, 45, 6944–6949.

Wang, R., Sakai, N. Fujishima, A. Watanabe, T. & Hashimoto, K. 1999. Studies of Surface Wettability Conversion on TiO_2 Single-Crystal Surfaces. *The Journal of Physical Chemistry B.*, 103, 2188–2194.

Watanabe, T., Nakajima, A. Wang, R. Minabe, M. Koizumi, S. Fujishima, A. & Hashimoto, K. 1999. Photocatalytic Activity and Photoinduced Hydrophilicity of Titanium Dioxide Coated Glass. *Thin Solid Films*, 351, 260–263.

Weir, A., Westerhoff, P. Fabricius, L. Hristovski, K. & Goetz, N. 2012. Titanium Dioxide Nanoparticles in Food and Personal Care Products. *Environmental Science & Technology*, 46, 2242–2250.

Wessel, C., Ostermann, R. Dersch, R. & Smarsly, B. M. 2011. Formation of Inorganic Nanofibers from Preformed TiO_2 Nanoparticles via Electrospinning. *The Journal of Physical Chemistry C*., 115, 362–372.

Wu, C. M., Chiou, H. G. Lin, S. L. & Lin, J. M. 2012. Effects of Electrostatic Polarity and the Types of Electrical Charging on Electrospinning Behavior. *Journal of Applied Polymer Science*, 126, 89–97.

Wu, H., Pan, W. Lin, D. & Li, H. 2012. Electrospinning of Ceramic Nanofibers: Fabrication, Assembly and Applications. *Journal of Advanced Ceramics*, 1, 2–23.

Wunderlich, W., Oekermann, T. Miao, L. Hue, N. T. Tanemura, S. & Tanemura M. 2004. Electronic Properties of Nano-Porous TiO_2 and ZnO Thin Films-Comparison of Simulations and Experiments. *Journal of Ceramic Processing & Research*, 5, 343–354.

Xie, Z. B., Adams, S. Blackwood, D. J. & Wang, J. 2008. The Effects of Anodization Parameters on Titania Nanotube Arrays and Dye Sensitized Solar Cells. *Nanotechnology*, 19, 405701.

Xu, H. & Zhang, L. 2009. Controllable One-Pot Synthesis and Enhanced Photocatalytic Activity of Mixed-Phase TiO_2 Nanocrystals with Tunable Brookite/Rutile Ratios. *The Journal of Physical Chemistry C*., 113, 1785–1790.

Yamashita, H., Harada, M. Misaka, J. Takeuchi, M. Neppolian, B. & Anpo, M. 2003. Photocatalytic Degradation of Organic Compounds Diluted in Water Using Visible Light-Responsive Metal Ion-Implanted TiO_2 Catalysts: Fe Ion-Implanted TiO_2. *Catalysis Today*, 84, 191–196.

Yang, X. L., Zhu, L. Yang, L. M. Zhou, W. Y. & Xu, Y. H. 2011. Preparation and Photocatalytic Activity of Neodymium Doping Titania Loaded to Silicon Dioxide. *Transactions of Nonferrous Metals Society of China*, 21, 335–339.

Yoganarasimhan, S. R. & C. N. Ramachandra Rao. 1962. Mechanism of Crystal Structure Transformations. Part 3. Factors Affecting the Anatase-Rutile Transformation. *Transactions of the Faraday Society,* 58, 1579–1589.

Yu, C., Wei, L. Li, X. Chen, J. Fan, Q. & Yu, J. C. 2013. Synthesis and Characterization of Ag/TiO_2-B Nanosquares with High Photocatalytic Activity under Visible Light Irradiation. *Materials Science and Engineering: B.*, 178, 344–348.

Yu, J., Dai, G. & Cheng, B. 2010. Effect of Crystallization Methods on Morphology and Photocatalytic Activity of Anodized TiO_2 Nanotube Array Films. *The Journal of Physical Chemistry C.*, 114, 19378–19385.

Yu, J. C., Yu, J. Ho, W. Jiang, Z. & Zhang, L. 2002. Effects of F-Doping on the Photocatalytic Activity and Microstructures of Nanocrystalline TiO_2 Powders. *Chemistry of Materials*, 14, 3808–3816.

Yu, J. C., Zhang, L. Zheng, Z. & Zhao, J. 2003. Synthesis and Characterization of Phosphated Mesoporous Titanium Dioxide with High Photocatalytic Activity. *Chemistry of Materials*, 15, 2280–2286.

Yun, J., Jin, D. Lee, Y. S. & Kim H. I. 2010. Photocatalytic Treatment of Acidic Waste Water by Electrospun Composite Nanofibers of pH-Sensitive Hydrogel and TiO_2. *Materials Letters*, 64, 2431–2434.

Zhang, H. & Banfield, J. F. 1998. Thermodynamic Analysis of Phase Stability of Nanocrystalline Titania. *Journal of Materials Chemistry*, 8, 2073–2076.

Zhang, H. & Banfield, J. F. 2000a. Phase Transformation of Nanocrystalline Anatase-to-Rutile via Combined Interface and Surface Nucleation. *Journal of Materials Research*, 15, 437–448.

Zhang, H. & Banfield, J. F. 2000b. Understanding Polymorphic Phase Transformation Behavior During Growth of Nanocrystalline Aggregates: Insights from TiO_2. *The Journal of Physical Chemistry B.*, 104, 3481–3487.

Zhang, H. & Banfield, J. F. 2005. Size Dependence of the Kinetic Rate Constant for Phase Transformation in TiO_2 Nanoparticles. *Chemistry of Materials,* 17, 3421–3425.

Zhang, H., Li, X. & Chen, G. 2010. Fabrication of Photoelectrode Materials. In *Electrochemistry for the Environment*, 473–513. New York: Springer.

Zhang, P., Shao, C. Li, X. Zhang, M. Zhang, X. Sun, Y. & Liu, Y. 2012. In Situ Assembly of Well-Dispersed Au Nanoparticles on TiO_2/ZnO Nanofibers: A Three-Way Synergistic Heterostructure with Enhanced Photocatalytic Activity. *Journal of Hazardous Materials*, 237–238, 331–338.

Zhang, Q., Gao, L. & Guo, J. 2000. Effects of Calcination on the Photocatalytic Properties of Nanosized TiO_2 Powders Prepared by $Ticl_4$ Hydrolysis." *Applied Catalysis B: Environmental*, 26, 207–215.

Zhang, R., Wu, H. Lin, D. & Pan, W. 2010. Photocatalytic and Magnetic Properties of the Fe-TiO_2/SnO_2 Nanofiber via Electrospinning. *Journal of the American Ceramic Society*, 93, 605–608.

Zhang, T., Ge, L. Wang, X. & Gu, Z. 2008. Hollow TiO_2 Containing Multilayer Nanofibers with Enhanced Photocatalytic Activity. *Polymer*, 49, 2898.

Zhang, Z., Shao, C. Zhang, L. Li, X. & Liu, Y. 2010. Electrospun Nanofibers of V-Doped TiO_2 with High Photocatalytic Activity. *Journal of Colloids and Interface Science*, 351, 57–62.

Zheng, J., Li, G. Ma, X. Wang, Y. Wu, G. & Cheng, Y. 2008. Polyaniline–TiO_2 Nano-Composite-Based Trimethylamine QCM Sensor and Its Thermal Behavior Studies. *Sensors and Actuators B: Chemical*, 133, 374–380.

Zheng, Z., Liu, H. Ye, J. Zhao, J. Waclawik, E. R. & Zhu, H. 2010. Structure and Contribution to Photocatalytic Activity of the Interfaces in Nanofibers with Mixed Anatase and TiO_2 (B) Phases. *Journal of Molecular Catalysis A: Chemical*, 316, 75–82.

Zhou, Y., Cao, L. Zhang, F. He, B. & Li, H. 2003. Lithium Insertion into TiO_2 Nanotube Prepared by the Hydrothermal Process. *Journal of the Electrochemical Society*, 150, 1246–1249.

Zhu, J., Deng, Z. Chen, F. Zhang, J. Chen, H. Anpo, M. Huang, J. & Lizhong Zhang. 2006. Hydrothermal Doping Method for Preparation of Cr^{3+}-TiO_2 Photocatalysts with Concentration Gradient Distribution of Cr^{3+}. *Applied Catalysis B: Environmental*, 62, 329–335.

Zhu., P., Nair, A. S. Shengjie, P., Shengyuan, Y. & Ramakrishna, S. 2012. Facile Fabrication of TiO_2-Graphene Composite with Enhanced Photovoltaic and Photocatalytic Properties by Electrospinning. *ACS Applied Materials & Interfaces*, 4, 581–585.

Zwilling, V., Aucouturier, M. & Darque-Ceretti, E. 1999. Anodic Oxidation of Titanium and TA6V Alloy in Chromic Media. An Electrochemical Approach. *Electrochimica Acta*, 45, 921–929.

"Every reasonable effort has been made to acknowledge the owners of copyright material. I would be pleased to hear from any copyright owner who has been omitted or incorrectly acknowledged"

ALBETRAN, HANI MANSSOR M

Signature:

Date: 18th March 2016